Development of Methods and Devices for Spatially and Temporally Resolved X-Ray Microscopy for Characterization in Heterogeneous Catalysis

Zur Erlangung des akademischen Grades eines
DOKTORS DER NATURWISSENSCHAFTEN
(Dr. rer. nat.)

Fakultät für Chemie und Biowissenschaften
Karlsruher Institut für Technologie (KIT) - Universitätsbereich
genehmigte

DISSERTATION

von
M. Sc. Georg Hagen Hofmann

aus
Altdöbern

Dekan: Prof. Dr. Peter Roesky

Referent: Prof. Dr. Jan-Dierk Grunwaldt

Korreferent: Prof. Dr. Christian G. Schroer

Tag der mündlichen Prüfung: 17.07.2015

DOI: 10.5445/IR/1000049565

URN: urn:nbn:de:swb:90-495658

Dedicated to my grandmother, parents, and family.

Werd ich zum Augenblicke sagen:
Verweile doch! Du bist so schön!
Dann magst du mich in Fesseln schlagen,
dann will ich gern zugrunde gehn!

(Johann Wolfgang von Goethe)

Stets findet Überraschung statt
Da, wo man's nicht erwartet hat.

(Wilhelm Busch)

Abstract

The characterization of catalyst materials and unraveling of catalytic processes requires a multitude of complementary techniques. Due to the dynamic nature of catalysts and the reaction process itself, *in situ* and spatially resolved methods like X-ray microscopy are required. To gain a deeper understanding, existing methods need to be improved in terms of spatial and temporal resolution or even need to be adapted from other scientific branches.

This work therefore addresses both, the development of analytical methods based on X-ray microscopy in the first part, namely tomography and ptychography, as well as the design of a microfluidic device and a gas phase microreactor for *in situ* experiments in the second part to enhance temporal and spatial resolution in catalytic experiments.

Preparation, measurement conditions, and analysis work-flow were developed to conduct quasi *in situ* X-ray absorption micro-computed tomography (CT) on supported catalysts. Aging effects of a 4 wt.% $Pt/\gamma{-}Al_2O_3$ catalyst were non-destructively captured with micrometer spatial resolution and as function of aging time. Therefore a single honeycomb exhaust gas catalyst channel with washcoat was prepared and investigated after several aging steps. It is demonstrated how volume segmentation and quantitative results on the aging are obtained. Growth regimes and growth rates based on individual feature (blob) size and absorption were identified and traced within the entire sample as well as for single features.

Additionally, Pt sintering found in CT on the micrometer scale was correlated to results from electron microscopy (SEM, EPMA, and TEM), X-ray diffraction (XRD), X-ray absorption spectroscopy (XAS) and CO-oxidation experiments. The results confirm a general suitability of CT for investigation of catalysts and in particular for *in situ* experiments. The results show that CT in general is suitable to investigate catalysts and useful for *in situ* experiments.

The second X-ray microscopy method used in the work, ptychography, delivered images with nanometer resolution at the beamline P06 at PETRA III (DESY, Hamburg). Hard X-ray ptychography is a scanning coherent diffraction imaging method with high penetration depth therefore well-suited for *in situ* imaging of nanoscopic catalyst samples.

A set of model samples was prepared and pre-characterized to allow systematic and quantitative evaluation of the chemical contrast between 100 nm large Au nanoparticles and a Pt marker structure while crossing the $Au\,L_3$ absorption edge. The resulting systematic variation of the phase contrast of Au in comparison to Pt allowed clear distinction between both materials. A second set of model samples with a mix of Au, Pt, and Pd nanoparticles of 10 to 100 nm in size was similarly prepared and pre-characterized. Using these samples, high resolution around 10 nm and chemical

contrasts for different types and sizes of nanoparticles were observed. These developments pave the way for *in situ* imaging with nanometer resolution, where the next step is the development and testing of *in situ* cells.

In the second part of this thesis, a microfluidic device for the investigation of gold nanoparticle (AuNP) nucleation by means of X-ray absorption spectroscopy (XAS) and small angle X-ray scattering (SAXS) was constructed to derive more rational and optimized synthesis routes to the preparation of this important class of material.

Special attention is given to the early phase of the AuNP formation in continuous flow, using $HAuCl_4$ solution and tetrakis(hydroxymethyl)phosphonium chloride (THPC) as reducing agent as this reaction provides very small AuNPs with particularly high catalytic activity. Accordingly, a microfluidic device (fluidic chip) with high time resolution and little dead time of 2 ms was developed, implemented, and finally applied.

The design of different types of cyclone mixers, and options arising from the different flow regimes, plug flow and laminar flow, were evaluated and different ways of solution feeding into the device (fluidic rack and syringe pumps) were tested. Besides the chip, a separate cyclone mixer attached to a capillary was used to extend observation times and to evaluate suitability of capillaries and a free liquid jet for time resolved measurements of gold nanoparticle formation.

However, gold deposition in the microfluidic chip and in the capillaries during the actual reaction prevented measurements of the gold oxidation state in the solution in the early stage of the reaction. Additionally, deactivation of the THPC reducing agent, as confirmed by UV-Vis lab-experiments, delayed the reaction start beyond accessible times of the entire setup. Additionally, this lowered the reaction yield, hence no kinetic data could be obtained. Possible future solution to this issue and improvements to the current setup are therefore presented at the end of the respective chapter.

In the last chapter, design and construction of a micro fabricated microreactor chip for gas phase reactions is presented. It is compatible to *in situ* X-ray spectroscopy (XAS), X-ray diffraction (XRD), and optical spectroscopies as well as on-line product analysis.

Shortcomings of the current glass capillary setup were analyzed. An improved system was designed and built accordingly, which comprises of a silicon microreactor and a support for gas connection and electrical contacts.

Major improvements as compared to the glass capillary setup are a small channel size with high mechanical stability in combination to high mechanical stability together with easy and gas-tight mounting of the gas phase chip into the support. An integrated Pt heater and Pt temperature sensor enable very fast and well-controlled temperature changes.

The setup was demonstrated to work in first *in situ* experiments using XAS and XRD acquisitions of a Pt catalyst in the partial oxidation of methane. Hence, the setup is ready to be used to study gas phase reactions in greater detail under realistic experimental conditions.

Kurzzusammenfassung

Die Charakterisierung von Katalysatormaterialien und die Aufklärung katalytischer Prozesse benötigt eine Vielzahl von komplementären Techniken. Aufgrund der dynamischen Natur von Katalysatoren und der Reaktion selbst sind *in situ* sowie ortsauflösende Analysemethoden wie die Röntgenmikroskopie notwendig. Um ein tieferes Verständnis zu erlangen, müssen die existierenden Methoden im Hinblick auf ihre räumliche und zeitliche Auflösung verbessert oder aus anderen Forschungsgebieten auf die Katalysatorforschung übertragen werden.

Diese Arbeit beschäftigt sich daher im ersten Teil mit der Entwicklung analytischer Methoden basierend auf der Röntgenmikroskopie, konkret der Tomographie und Ptychographie. Im Mittelpunkt des zweiten Teils steht die Entwicklung von Apparaten für *in situ* Experimente in der Flüssigphase und in der Gasphase mit dem Ziel katalytische Experimente mit verbesserter räumlicher und zeitlicher Auflösung verfolgen zu können.

Es wurden Präparations-, Mess- und Auswertemethodiken entwickelt, um mittels quasi *in situ* Röntgentomographie (CT) zerstörungsfrei Alterungsprozesse eines Katalysators zu verfolgen. Dazu wurden einzelne Kanäle eines Wabenkörpers für die Abgaskatalyse mit einer Beschichtung von 4 Gew.% Platin auf γ-Aluminium untersucht. Es wird gezeigt, wie eine Volumensegmentierung und quantitative Alterungsergebnisse mit Mikrometer-Auflösung erhalten werden. Darauf aufbauend wurden Wachstumscharakteristiken und Wachstumsraten sowohl für einzelne Agglomerate (Blobs) wie auch für die Gesamtheit der Bereiche mit gesintertem Platin auf der Mikrometerskala ermittelt und über das Probenvolumen hinweg verfolgt.

Das mittels Tomographie beobachtete Sintern von Platin wurde zudem mit den Resultaten aus elektronenmikroskopischen Untersuchungen (SEM, EPMA, TEM), Röntgendiffraktometrie (XRD) und Röntgenabsorptionsspektroskopie (XAS) sowie CO-Oxidationsexperimenten korreliert. Diese zeigen, dass CT im Allgemeinen für die Untersuchung von Katalysatoren und im Speziellen für *in situ* Experimente geeignet ist.

Als weitere röntgenmikroskopische Methode wurde Ptychographie für die Abbildung von Nanopartikeln mit Nanometerauflösung an der Beamline P06 bei PETRA III am DESY in Hamburg etabliert. Ptychographie mit kohärenter harter Röntgenstrahlung ist eine abrasternde, auf Beugung basierende Methode die eine große Eindringtiefe bietet und daher prinzipiell für *in situ* Experimente an nanoskopischen Katalysatoren geeignet ist.

Für diese Versuche wurde ein Satz von Modellproben hergestellt und vorcharakterisiert, welche die quantitative Ermittlung des chemischen Kontrasts zwischen 100 nm großen Gold Nanoteilchen und einer Platinmarkierung erlauben. Indem Ptychographie über die Au L_3 Absorptionskante hinweg gemessen wurde, traten systematische Variationen des Phasenkontrasts auf, welche die Unterscheidung beider Elemente erlaubte.

Ein zweiter Satz von Modellproben mit einer Mischung von Gold-, Platin- und Palladiumnanoteilchen der Größen 10 bis 100 nm wurde auf ähnliche Weise hergestellt und vorcharakterisiert. Bei der Untersuchung dieser Proben wurde eine hohe Auflösung im Bereich von 10 nm erzielt und ein chemischer Kontrast für die verschiedenen Arten und Größen der Nanoteilchen beobachtet. Damit ist die Methode prinzipiell in der Lage, die Zusammensetzung einer Probe mit Nanometerauflösung zu liefern und kann für *in situ* Fragestellungen eingesetzt werden. Hierzu ist jedoch der Bau geeigneter *in situ* Zellen im nächsten Schritt erforderlich.

Im zweiten Teil der Arbeit wurde eine mikrofluidische Zelle mit einer Totzeit von 2 ms für die Untersuchung der Bildung von Goldnanoteilchen (AuNP) mit Hilfe von XAS und Kleinwinkelstreuung (SAXS) konstruiert und realisiert. Ziel war die Bildung dieser wichtigen Materialklasse zu verstehen und darauf aufbauend die Herstellung zu verbessern. Von besonderem Interesse ist die frühe Phase der AuNP-Bildung unter kontinuierlichem Fluss auf Basis der Reduktion von $HAuCl_4$ mit Tetrakis(hydroxymethyl)phosphoniumchlorid (THPC), welche besonders kleine AuNPs liefert. Diese zeigen besonders hohe katalytische Aktivität in der CO Oxidation bei niedrigen Temperaturen.

Der Einfluss verschiedener Zyklonmischer auf die Qualität der Mischung und die Auswirkungen der zwei verwendeten Strömungscharakteristiken, laminare Strömung und Kolbenströmung, wurden erprobt. Zudem wurden verschiedene Aufbauten für die Flüssigkeitszuführung (Fluidisches Rack und Spritzenpumpen) verglichen. Neben der Mikrofluidikzelle wurde zudem ein Aufbau mit einem separaten Zyklonmischer in Kombination mit Kunststoffkapillaren und einem frei fallenden Flüssigkeitsstrahl hinsichtlich seiner Eignung für die zeitaufgelöste Untersuchung der AuNP-Bildung untersucht.

In allen getesteten Aufbauten verhinderte jedoch eine röntgeninduzierte Metallisierung der Reaktor- bzw. Kapillarenwände während der Reaktion die verlässliche Messung des Oxidationszustands des Goldes in der Reaktionslösung. Zusätzlich trat eine Deaktivierung von THPC mit dem Alter der vorgemischten Reaktionslösung auf, welche durch Laborexperimente mittels UV-Vis Spektroskopie bestätigt wurde. Dies verzögerte den Start der Reaktion so stark, dass dieser nicht mehr mit dem vorhandenen Aufbau erfasst werden konnte. Gleichzeitig führte die Deaktivierung auch zu einer starken Verminderung der AuNP Ausbeute. Es konnten daher keine kinetischen Daten für die Reaktion gemessen werden. Mögliche Lösungsansätze, welche sowohl die Metallisierung des Aufbaus wie auch die Deaktivierung des Reduktionsmittels verhindern können, werden daher am Ende des Kapitels dargestellt.

Das letzte Kapitel der Arbeit behandelt die Konstruktion und Realisierung eines Mikroreaktors für *in situ* Gasphasenexperimente. Er ist kompatibel mit Röntgenspektroskopie, -diffraktion und optischen Spektroskopien und erlaubt die Produktanalyse in Echtzeit. Schwachpunkte des gegenwärtig verwendeten Aufbaus basierend auf Glaskapillaren wurden analysiert und darauf basierend ein verbesserter Aufbau konstruiert. Dieser besteht aus einem Mikroreaktor aus Silizium und einer Halterung mit Gasanschluss und Durchführungen für elektrische Kontakte. Die Hauptverbesserungen des neuen Aufbaus sind die geringe Kanalbreite in Kombination mit hoher mechanischer

Stabilität, die schnelle und kontrollierte Temperaturänderung auf Basis des integrierten platinbasierten Heizers und Temperatursensors sowie die vereinfachte und gasdichte Installation des Mikroreaktors in der Halterung. Die Funktionsfähigkeit des Aufbaus wurde in ersten *in situ* XAS- und XRD-Experimenten eines Platinkatalysators für die partielle Oxidation von Methan gezeigt. Der Mikroreaktor ist daher bereit für den Einsatz zur Untersuchung von katalytischen Reaktionen in der Gasphase unter realen experimentellen Bedingungen.

Contents

List of Figures

List of Tables

Part I.

Introduction & Methods

1. Introduction

Catalysis in general and heterogeneous catalysis in particular are the workhorses of our economy. Around 90 % of all products from industry are prepared by at least one catalytic step, creating valuable intermediates and products from crude oil, natural gas, and biological sources [1]. Catalysts are also widely used to remove harmful byproducts from production streams as well as to remove exhaust gases forming in industry or automobiles [2]. Many reactions are only possible in industrial scale by use of the right catalyst as they were otherwise too slow or need prohibitively high temperature to overcome activation energy and thereby would be too costly [3]. To find a good catalyst and use it in large scale is a challenge.

The first modern catalyst development from lab scale to plant size was done for ammonia synthesis from its elements, nowadays known as the Haber-Bosch-process, which was invented 1906 by Haber in Karlsruhe. It was taken to industrial scale in 1913 by reactor optimization and a massive catalyst screening [4] by Bosch in Ludwigshafen. A promoted Fe catalyst is used for the synthesis of ammonia from its elements and is the base of modern agriculture, since ammonia is used as fertilizer. On the other hand, the process was unfortunately also the basis to produce explosives, *e.g.* in the first world war.

Although this empirical trial-and-error approach on catalyst development was successful, it took a long time and a lot of resources to complete. At the same time the reaction was used as a black box. Today, with demand of economical use of resources and the presence of a multitude of gradually developed catalyst systems, a more rational approach to catalyst design is needed [5].

Rational design is based on the interplay of theoretical understanding [6–9] and experimental verification of the predicted reaction steps at the elementary level as well as the identification of influencing process parameters [10]. This requires the most advanced experimental techniques and theoretical descriptions available [11] as improved or new catalysts have to be identified within a vast parameter space spanning different time and length scales, temperatures, concentrations, elements, phases and many more [12, 13].

Due to the dynamic nature of catalysts, and in addition to a multitude of *ex situ* characterization techniques [14], *in situ* investigations of catalysts are mandatory as several authors pointed out in a number of publications [15–19]. Accordingly, a variety of *in situ* techniques are used to characterize catalyzed reactions [19, 20]. Within the field of those, especially *in situ* X-ray techniques are valuable. Due to their high penetration power they allow to probe thicker, more realistic samples under relevant reaction conditions in a relatively simple and robust setup [21–24]. Thus they enable to study reactions in gas atmosphere and in liquid phase with respect to their phase

distribution, elemental composition, oxidation states, and so forth [25].

Within the continuously growing field of *in situ* characterization three main areas of development are most prominent [26]: (a) the realization of time-resolved combined spectroscopy under (near) realistic reaction conditions; (b) the development of *in situ* tools to characterize catalytic transformations in the liquid phase; and (c) the development of space-resolved and tomographic characterization approaches, ultimately allowing to perform single molecule single active site/catalyst particle *in situ* studies. All these efforts, covering different time and length scales [12, 13], are made to shed light into a multitude of different aspects of the catalyst system *in situ*. By combining results of these advanced and complementary techniques a more complete understanding of the catalyst is gained, aiding to further improve existing or even develop new systems.

Accordingly, in this work all three mentioned development aspects will be addressed with the main focus on the development of methods and devices with improved spatial and temporal resolution under *in situ* conditions using hard X-ray techniques due to the advantages given earlier. These are the key aspects and motivation of this thesis. Since the work comprises of four subtopics, this general introduction is kept short and more specific introductions to each particular field are given within the corresponding chapters, which are described in the following.

This work is divided into two main parts: First, the development of X-ray microscopy imaging methods with high spatial resolution in 2D and 3D combined with quantitative analysis in the chapters 3 and 4. And second, the development of devices for *in situ* studies of gas- and liquid-phase reactions that offer improved control over reaction conditions as well as high spatial and temporal resolution in the chapters 5 and 6.

In chapter 3 the development of quasi *in situ* X-ray absorption micro-computed tomography will be described, used to study the aging/sintering of automotive exhaust gas catalysts locally resolved and as function of aging time. This allows to quantitatively follow Pt sintering spatially resolved on single exhaust gas catalysts channel on the µm-scale. The chapter will first introduce X-ray absorption tomography in general and demonstrate potential applications in catalysis research. Afterwards, single honeycomb samples are systematically studied and the quasi *in situ* method is derived and demonstrated in detail. The extracted results are quantitatively analyzed and correlated to complementary characterization techniques.

Developments in chapter 4 concern imaging of nanoparticles with nm resolution and chemical contrast by hard X-ray ptychography. This project combines the high penetration depth of hard X-rays with high resolution imaging capabilities of ptychography and is the first step toward chemical imaging under *in situ* conditions with nm resolution. To this end, a set of well-defined model samples of gold, platinum, and palladium nanoparticles were prepared and studied, enabling progress in analysis methods and imaging resolution for this systems. This chapter will briefly introduce hard X-ray ptychography and focus on the model sample preparation and pre-characterization afterwards. Experimental results are shown for two model systems composed of the aforementioned nanoparticles, demonstrating chemical contrast as well.

In chapter 5 the development of a liquid phase setup for the investigation of the formation of gold nanoparticles using tetrakis(hydroxymethyl)phosphonium chloride (THPC) as reducing agent for $HAuCl_4$ is presented. The control over size and shape of nanoparticles is essential for their particular application. To improve the control, a good understanding of the nanoparticle formation mechanisms is valuable. Especially the initial/early phase of this process is not well understood and investigated, hence requires special attention. This is attributed here by using a continuous flow approach in combination with microfluidic devices to resolve the nanoparticle formation process with high temporal resolution using *in situ* X-ray absorption spectroscopy. The chapter will present the fundamental experimental principle for the liquid phase studies, where spatial measurements are translated to reaction times. To realize this principle different experimental setups are designed and tested. This encompasses different fluid delivery systems, microfluidic mixers, and observation techniques for the liquid stream.

In chapter 6 the development of a gas phase microreactor for *in situ* experiments with improved temperature control and spatial resolution is presented. To study gas phase reactions with high spatial resolution and in transient states, small geometrical dimensions as well as stable and fast temperature control are required. This allows to capture effects with respect to single catalyst grains and offer better reproducibility of the experimental conditions. The chapter introduces the experimental requirements and derives technical solutions based on micro structured silicon chips with integrated heater and temperature sensor. First *in situ* tests are presented proving the functionality. Furthermore, the compatibility of this versatile gas phase microreactor to various *in situ* X-ray characterization techniques is shown.

2. Methods

This chapter describes the used characterization techniques to study Pt/Al_2O_3 powders; deposited gold, platinum, and palladium nanoparticles; and gold nanoparticles in solution. In addition the relevant experimental parameters are given. The two techniques X-ray micro-computed tomography and hard X-ray ptychography, are treated accordingly in their corresponding sections 3.2 and 4.2 on page 17 and on page 82, respectively.

2.1. X-Ray Techniques

2.1.1. X-Ray Diffraction (XRD)

Powder X-ray diffraction is generally used to identify crystalline phases present in catalysts. Here it is used to estimate the size of Pt nanoparticles in Pt/Al_2O_3 samples. The principle is as follows: atoms in a crystal are periodically ordered, thus also the electron densities surrounding them. This ordering coherently scatters X-rays leading to a constructive interference when Bragg's law in eq. (2.1) is fulfilled.

$$n \cdot \lambda = 2 \cdot d_{hkl} \sin \Theta \tag{2.1}$$

In this equation λ is the X-ray wavelength, d_{hkl} the distance between given crystallographic planes, and Θ the angle of the incoming light with respect to the lattice plane. It states that the optical path difference $2 \cdot d_{hkl} \sin \Theta$ must be equal to an integer multiple of the wavelength of the radiation $n \cdot \lambda$ to obtain constructive interference, which is show in fig. 2.1.

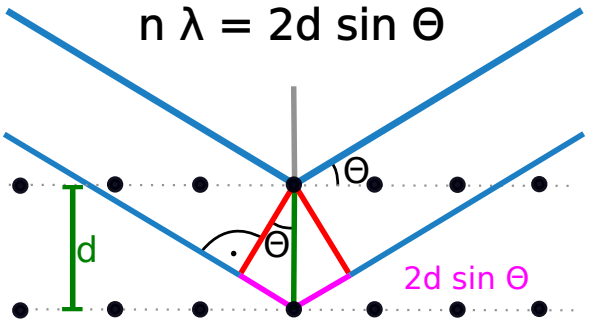

Figure 2.1.: Deviation of Bragg's law. (modified version of public domain image https://commons.wikimedia.org/wiki/File:Bragg.svg)

For the studies in this work, a *Bruker D8 Advance* X-ray diffractometer (ITCP, KIT) in Bragg-Brentano geometry equipped with Cu anode and Ni-filter was used and

operated at 35 kV and 45 mA. A variable slit setting was used to maintain a constant irradiated sample area over the scanned 2Θ range from 25 to 85° covered in steps of 0.0164°.

Diffraction patterns were recorded from uncoated fresh and aged Pt/Al_2O_3 powders to provide sufficient amounts of sample material and to avoid cordierite impurities. The flat prepared sample powder was put on a rotating sample holder to improve statistics. The peak positions in the obtained diffractogram are compared to standards or looked up in a database to identify materials and phases.

Using the Scherrer equation [27] in eq. (2.2) the average Pt crystallite size τ was estimated [28, 29] by fitting a Gaussian function to the diffraction peaks.

$$\tau = \frac{K \cdot \lambda}{\beta \cdot \cos(\Theta)} \tag{2.2}$$

From the gaussian fit, the peak full width at half maximum (FWHM) β and the cosine of half of the diffraction angle Θ in radians are used. In addition, by using Cu K_α radiation, the wavelength λ is 1.5418 Å and for a spherical shape the form factor K is 0.9 which were used as constants for the calculation of τ.

2.1.2. X-Ray Absorption Spectroscopy (XAS)

X-ray absorption spectroscopy is used to determine the oxidation state of the chemical elements in the sample compound. This is done by measuring the X-ray intensities before I_0 and after I_t the sample or the proportional fluorescence signal for a range of photon energies. As the monochromatic X-rays are passed through the sample, they are partially absorbed and cause the mentioned fluorescence. The absorption shows significant changes at characteristic absorption edges for a given chemical element, which can be used as a fingerprint. With a complete energy scan of the incoming and transmitted photon intensity the energy depended absorption coeffcient $\mu(E)$ can be calculated using the Beer's Law given in eq. (2.3).

$$I_t = I_0 \exp(-\mu \cdot d) \quad \Rightarrow \quad \mu \cdot d = \ln(I_0/I_t) \tag{2.3}$$

Besides the characteristic edge jump at E_0, the overall structure of the absorption signal $\mu(E)$ can be assigned to the oxidation state by using reference compounds. Furthermore the position of the absorption edge calibrated to a reference gives additional information on the oxidation state of the element. A shift to higher energies in E_0 is often observed for oxidized (missing outer e^-) elements, since the remaining electrons are more tightly bound and it requires more energy to eject *e.g.* a core electron (during a K-edge scan). More details can be found online at `http://xafs.org` as tutorials, *e.g.* by Newville [30], or in textbooks by Bunker [31] for example.

Exhaust gas catalyst samples based on Pt/Al_2O_3 were measured in transmission and fluorescence mode at the ANKA XAS beamline [32] in Karlsruhe. The amount (mass) of Pt/Al_2O_3 sample material was calculated by using *XAFSmass* [33] to obtain an optimal edge jump of around one and a total absorption of around two. Cellulose is added to increase the amount of powder and intermixed using a mortar. The uniform

powder is pressed into a pellet and sealed by Kapton® tape.

Absorption spectra of gold precursor and nanoparticle solutions were recorded in fluorescence mode at ANKA XAS, SLS MicroXAS [34] in Villigen Switzerland, and Petra III P06 [35] in Hamburg Germany. Solutions of gold nanoparticle have been measured in cuvettes, capillaries or in a free liquid jet without special preparation.

In every case the resulting spectra were treated using the *Demeter* software package [36] to perform energy calibration, normalization, merging, and data export for further processing.

2.1.3. Generation of X-Rays

In conventional laboratory devices X-rays are created by shooting electrons on a metal target, *e.g.* copper, to produce *Bremsstrahlung* yielding a broad energy distribution and some material characteristic X-ray emissions lines from the target.

In modern third generation synchrotron light sources [37, 38], as used for later X-ray microscopy experiments, electrons at high kinetic energy are circulated in a storage ring. The X-rays for the experiment are produced by the electrons passing through an undulator. The undulator consists of several dipole magnets with alternating orientation producing a periodic magnetic structure. As the electrons pass this magnetic field, they are radially accelerated and forced on an oscillating trajectory and emit the so-called synchrotron radiation. This coherent radiation has a very narrow energy width and very high intensity.

2.2. Electron Microscopy Techniques

By using highly accelerated and/or focused electron beams the sample is probed on the nanometer scale with high resolution. Depending on the employed technique, information on composition, topology, and crystal structure can be obtained. In the following only methods and modes are described, which have been used in this work.

2.2.1. Scanning Electron Microscope (SEM)

To gain an impression on sub-micron scale particle sizes, SEM was used. A focused electron beam is raster scanned across the sample and (forward, back)-scattered or secondary electrons are detected as well as emerging X-ray fluorescence to make up the image data for a single point. Images were taken using a *LEO 1530 Gemini* microscope equipped with a Schottky-type field-emission electron source (Laboratory for Electron Microscopy, KIT). An acceleration voltage U = 10 kV was used in combination with a 4-quadrant back-scattered electron detector (QBSD) providing high elemental (Z) contrast. Honeycomb sample fragments for inspection were obtained by manually cutting parts out of the coated honeycomb channel, yielding flat, still coated wall segments. Suitable fragments were glued to the sample holder with conductive silver epoxy and additionally carbon coated to avoid charging effects.

Pt, Au, and Pd nanoparticles have been deposited on silicon nitride windows (Si_3N_4) and were analyzed in BSE-mode using a *FEI Quant FEG 200*, hosted at the Center for

Electron Nanoscopy (CEN) at Technical University of Denmark (DTU). Additionally, the elemental composition was mapped by energy dispersive X-ray analysis (EDX).

2.2.2. Electron Probe Micro Analyzer (EPMA)

An electron probe micro analyzer (EPMA) was used to elucidate Pt distribution and create elemental mappings across the washcoat and cordierite. Similar to SEM this is a raster scan method but the focus is on wavelength dispersive X-ray micro-analysis (WDX). A diffracting crystal spectrometer is used to analyze selected peaks of the fluorescence spectrum. It provides a much higher energy (wavelength) resolution as compared to EDX thereby reducing the problem of overlapping peaks. However, it is much more time consuming and can only analyze a limited number of peaks.

A *JEOL JXA-8530F* field emission electron probe micro analyzer (Institute for Micro Process Engineering, KIT) was operated at U = 25 kV, I = 20 nA, dwell = 20 ms to investigate a honeycomb channel after the last tomography experiment.

To this end, a metallographic cross-section of the honeycomb channel was prepared. The sample was embedded in Araldit® and lapped with different SiC papers of different grain sizes and water. Final polishing was done with a suspension of diamond grains up to the size of 1 µm. Between each preparation step the sample was cleaned. For the investigation in EPMA, the sample was carbon coated to obtain a 10 nm thick conducting layer. Preparation and measurements were carried out by Uta Gerhards (IMVT, KIT).

2.2.3. Transmission Electron Microscope (TEM)

To determine the particle size distribution of Pt/Al_2O_3 samples, TEM was carried out using a *FEI Titan 80-300* aberration corrected microscope (Karlsruhe Nano Micro Facility, KIT). Images were acquired in scanning TEM mode (STEM) with 200 kV acceleration voltage. For this purpose, washcoat samples were collected by scratching off the Pt/Al_2O_3 washcoat from the honeycomb and depositing it on carbon coated Cu TEM grids. Some of the mentioned Pt, Au, and Pd nanoparticles have also been measured using a *FEI Tecnai T20 G2* (CEN, DTU) equipped with a LaB_6 electron gun, operated at 200 kV and 1.8 µA.

2.3. Further Characterization Techniques

2.3.1. Catalytic Test - CO Oxidation

By feeding a controlled gas mixture to a temperature controlled reactor with a catalyst bed and measuring the gas composition at the outlet with an Fourier transform infrared spectroscopy (FT-IR) analyzer, the catalytic conversion can be determined. The experiments were conducted in the exhaust gas centre Karlsruhe (ITCP, KIT). For the quasi *in situ* tomography of honeycomb aging in section 3.9 on page 54, reference samples have been prepared and aged in the lab. Then they were tested in CO oxidation.

Light-off curves for the fresh and aged samples were measured at $5\,\mathrm{K\,min^{-1}}$ heating ramps from 60 to 200 °C on 2.1 cm × 2.5 cm (d × h) honeycomb cylinders mounted inside a quartz glass reactor tube. Thermocouples (type K) were positioned at approx. 1 cm distance to the catalyst bed up- and downstream. The typical gas composition was 1000 ppm CO and 10 vol.% O_2 in N_2 at a gas hour space velocity (GHSV) of $30\,000\,\mathrm{h^{-1}}$ that was adjusted by mass flow controllers (Bronkhorst High-Tech BV) and continuously measured on-line by an FT-IR spectrometer (Multigas Analyzer™, MKS Instruments).

2.3.2. Brunauer–Emmett–Teller (BET) Method

The specific surface area of sample has been determined using the BET method [39]. In this approach the physical adsorption of gas molecules, *e.g.* N_2 with an surface area of $0.162\,\mathrm{nm^2}$, on a surface in multiple layers is considered.

After outgassing the sample at 300 °C for 2 h in vacuum, it is cooled to 77 K. After this portions of the nitrogen gas are dosed and the resulting pressure is measured. In this way, the adsorption and desorption isotherms are obtained, which are used to calculate the surface area of the sample.

By further increasing the gas pressure, gas is allowed to condense in the pores of the sample. After saturation, the pressure is gradually decreased and the hysteresis in the isotherm is used to estimate size, volume, and area of the pores using the Barrett-Joyner-Halenda (BJH) method [40].

For the investigation of washcoat aging a *Belsorp mini* (BEL Japan) was used to conduct a multi point measurement of the BET isotherm.

2.3.3. UV-Vis Spectroscopy

An *OceanOptics USB2000+UV-VIS* spectrometer with an *OceanOptics DH-2000-BAL* balanced deuterium tungsten halogen light source was used to estimate the size of the gold nanoparticle solutions by their plasmon resonance [41]. Measurements were performed *ex situ* in transmission mode using (plastic) cuvettes and *in situ* using a corrosion resistant dip-in probe *OceanOptics TP300 UV-VIS* made from PEEK with an adjustable-pathlength tip *RTP-2-10* from 2 to 10 mm. The formation of larger Au particles resulted in a measurable plasmon resonance at wavelengths of around 540 nm.

Samples were directly measured after preparation in solution. The data was acquired and analyzed using the *OceanOptics SpectraSuite* software. For each measurement, dark and reference measurements on a water filled cuvette have been performed in order to calculate the absolute absorption of the samples.

Part II.

X-Ray Microscopy

3. X-Ray Absorption Micro-Computed Tomography

3.1. Introduction

Exhaust gas catalysts are an inherent part in modern combustion vehicles which remove harmful components from the exhaust gas stream [42–44]. As discussed in a pertinent review article [45], the main exhaust gas pollutants are hydrocarbons (HC), carbon monoxide (CO), and nitrogen oxides (NO_x) [46, 47]. The catalytic converters are usually monolithic ceramic (cordierite) honeycomb structures, that carry a washcoat composed of a high surface area support, *e.g.* Al_2O_3, loaded with noble metals like Pt, Pd, and Rh to remove the three aforementioned gases, hence they are referred to as three-way catalyst (TWC) [47, 48].

The TWCs are optimised for gasoline-fuelled engines operated at stoichiometric air-to-fuel (A/F) ratios (by weight), *i.e.* $A/F = 14.7$ or $\lambda = 1$, that is controlled and maintained by an oxygen (λ) sensor in the exhaust gas stream [47]. In order to save fuel and lower CO_2 emissions, engines are operated at lean conditions $\lambda > 1$, *e.g.* $A/F = 20 - 60$, which results in oxygen-rich exhausts and difficulties to remove NO_x. To cope with this issue, two important technologies have been developed: (ammonia) selective catalytic reduction (SCR) of NO_x and NO_x storage/reduction (NSR) to abate lean-NO_x emissions [49, 50]. In SCR, urea $(NH_2)_2CO$ solution is added and hydrolyses to form NH_3, that reacts with NO and oxygen to form N_2 and water. In NO_x storage/reduction (NSR) or NO_x trapping catalyst, NO is converted to NO_2 in excess of oxygen over a Pt catalyst and trapped by BaO. During periodic rich-burn conditions it is released again and reduced over Pt or Rh-based catalysts [49–52]. For diesel-engines the original TWC does not work optimal, due to lower temperature of the exhaust, lean operation, and soot or particulate matter (PM) emissions. Nevertheless, diesel oxidation catalysts (DOC) are based similarly on honeycombs and Pt catalysts [53]. To reduce PM emissions special diesel particulate filters are introduced. Basically, the PM in the exhaust gas stream is filtered as it is forced to pass again through the porous honeycomb channel wall, made from cordierite or silicon carbide, before leaving [53, 54].

Since the emission limits are progressively restricted [52, 55], the ideal aftertreatment system must show very high catalytic performance, *i.e.* full conversion of all harmful components, and a very long operation time. This encompasses research and optimization of exhaust gas catalysts with respect to: surface reaction mechanisms [56], the preparation of monolithic catalysts including washcoat deposition [57, 58], and novel characterization approaches [13, 59–61].

In spite of major achievements [44, 62], the insufficient catalytic activity at low temperatures, durability of exhaust gas aftertreatment systems, and catalyst deactivation in general are still major issues for the automotive industry. According to [63], catalyst deactivation is classified into six distinct types: (i) poisoning, (ii) fouling, (iii) thermal degradation, (iv) vapor compound formation accompanied by transport, (v) vapor-solid and/or solid-solid reactions, and (vi) attrition/crushing. They can be further grouped into three categories: chemical (i,iv,v), mechanical (ii,v), and thermal (iii) deactivation. Fundamentals and mechanisms are extensively reviewed within refs. [63, 64].

Synthetic aging is usually applied, imitating real conditions in a shorter time frame and being less costly, to reproduce effects leading to catalyst deactivation [65]. However, also vehicle aged samples are investigated [66]. Real exhaust gas catalysts exhibit temperature and concentration gradients that cause non-uniform damage [53, 63]. In conventional investigations, such as X-ray diffraction (XRD) and X-ray absorption spectroscopy (XAS) as well as transmission electron microscopy (TEM), which provide atomic scale information [22, 67], this is accounted for by taking samples from inlet, middle, and outlet part of the catalyst [68]. However, most of these characterization techniques are applied postmortem, and often yield bulk averaged results so that the question of representability of samples arises. In addition, smaller changes cannot be investigated due to limited statistics.

Hence, to understand these processes, *e.g.* sintering [69], characterization across different length scales, ranging from the exhaust gas system over the monolithic structure down to the atomic scale [10, 44] is required. Especially, locally resolved techniques are desirable to capture the range of damage impact on the sample [13, 22, 70], locate *e.g.* preferred agglomeration regions and quantify their extent in 3D. This becomes even more important as selective investigation of such regions of interest may be conducted with other methods like *e.g.* SEM, known as correlative tomography [71].

To this end, X-ray micro-computed tomography (μ-CT), as non-destructive and 3D spatially resolved method, has already proved to be a valuable multi-faceted characterization technique for catalyst samples [72–78]. Sintering was shown, in general, to be accessible *in situ* for 50 µm Cu particles [79] and for sequential aging treatments of 120 µm glass spheres [80].

So far, tomography data of honeycombs was used to assist and improve simulation of temperature gradients, pore diffusion, catalytic conversion by accounting for realistic variations of the metal loading in the washcoat, and soot deposition [81–89]. Recently TEM tomography was performed to resolve the pore structure of a model sample with nm resolution [86]. In this respect tomography is well suited to examine the pore structure, which has important influence on the overall system.

Hence, the main goal is to make X-ray absorption micro-computed tomography accessible for quasi *in situ* studies and utilize it to study the aging effects on a model exhaust gas catalyst (4 wt.% Pt/Al_2O_3) to capture temperature induced structural and morphological changes spatially resolved and derive quantitative information on the µm scale.

3.2. Fundamentals of Computed Tomography

Here, a brief introduction to the most important basics of X-ray absorption computed tomography is given, as a number of books provide excellent introductions and in-depth information in this field, for example [90–92]. A comprehensive review on quantitative tomography, discussing limitations and opportunities, is found in [93].

The overall acquisition scheme is first discussed, then the interpretation of measurements, and finally the reconstruction of the investigated object, revealing its internal structure.

Tomography Workflow Overview

In fig. 3.1 the acquisition of tomographic data is shown schematically. The specimen is put on a rotation stage and illuminated by monochromatic X-rays, which are attenuated as they pass through. A scintillator converts the X-rays to visible light, which is detected afterwards. Thus, the sample is projected on the photo detector under several angles. This stack of images is used to tomographically reconstruct the object slice-by-slice for each row in the projection image, which adds up to a three dimensional representation of the object.

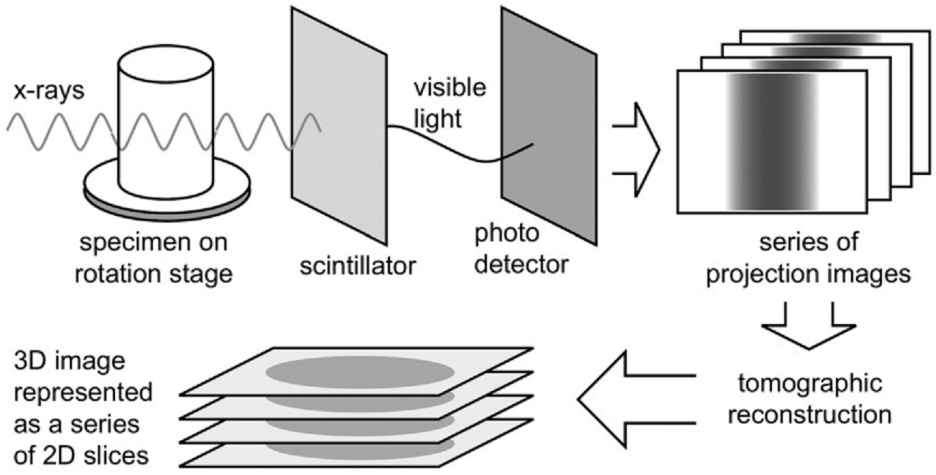

Figure 3.1.: Schematic representation of the X-ray absorption tomography workflow. Reprinted from [94] Copyright (2010), with permission from Elsevier.

Data Pre-Treatment for Absorption Tomography

To better understand the background of the tomographic reconstruction, we have a look on the processing of the acquired projection images first. The measured X-ray transmission I_{img} through the sample of thickness d and coefficient of absorption μ is used to calculate the projected absorption by Lambert-Beer's law.

$$I_{img} = I_{flat} \cdot e^{-\mu \cdot d} \qquad \Rightarrow \qquad \mu \cdot d = -\ln\left(\frac{I_{img}}{I_{flat}}\right) . \tag{3.1}$$

In tomography I_{flat} is an image recorded without the sample, called *flat field*. To compensate for detector offsets or bright pixels additional *dark field* images without X-ray illumination are recorded. Using these, the corrected projected absorption image can be calculated for each pixel of the detector by the following equation:

$$I_{abs} = -\ln\left(\frac{I_{img} - I_{dark}}{I_{flat} - I_{dark}}\right) \tag{3.2}$$

This process is shown, for already dark field corrected images, in fig. 3.2 for a 4 wt.% Pt/Al_2O_3 washcoat powder grain.

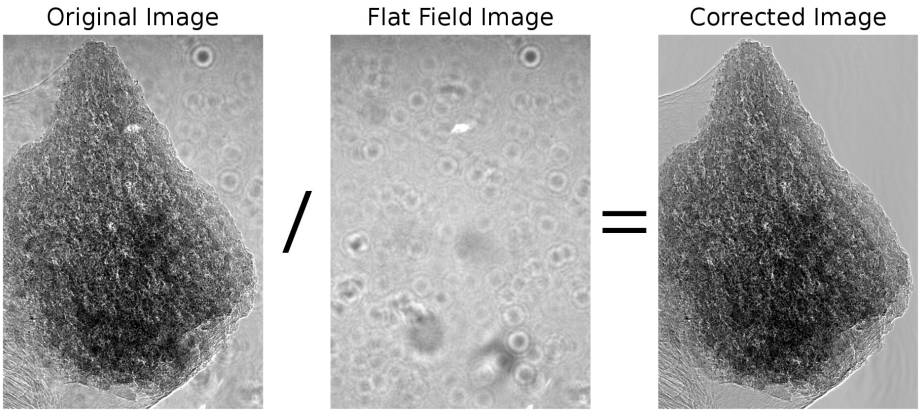

Figure 3.2.: Example for image correction by flat and dark field images.

Several effects contribute to the attenuation of X-rays in matter: the photon energy ($\mu \propto E^{-3}$), the chemical elements in the sample due to their atomic number Z ($\mu \propto Z^4$), and their density ($\mu \propto \rho$). By using coherent synchrotron radiation even phase changes of the transmitted X-rays may be used to generate images, as the phase shift is basically influenced by the same parameters [95].

After completing the processing of the raw transmission images, they contain the projection of the sample absorption on the detector plane.

Projection Data: The Radon Transform

The aim of X-ray absorption computed tomography is to spatially resolve the absorption μ within a sample $f(x, y)$. As it is continuously rotated, it is advantageous to introduce a beam-fixed coordinate system (s, r), which is centered on the rotation axis and rotated with respect to (x, y). The transformation to s, r is given by multiplication of the column vector (x, y) with the rotation matrix

$$\begin{bmatrix} s \\ r \end{bmatrix} = \begin{bmatrix} \cos\phi & -\sin\phi \\ \sin\phi & \cos\phi \end{bmatrix} \begin{bmatrix} x \\ y \end{bmatrix} \tag{3.3}$$

resulting in

$$s = x\cos\phi - y\sin\phi \qquad\qquad r = x\sin\phi + y\cos\phi\,. \tag{3.4}$$

The object $f(x, y)$ is then parametrized as $\mu(s, r)$, still referring to identical regions in the sample. The two coordinate systems are shown in fig. 3.3.

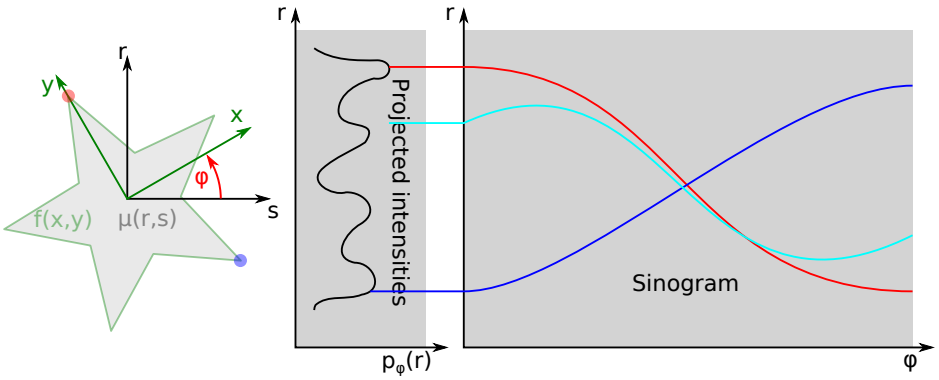

Figure 3.3.: Scheme of relations between object-fixed (x, y) (green) and beam-detector-fixed coordinate systems (s, r) (black) related by rotation ϕ. Projections $p_\phi(r)$ are taken along s as function of ϕ, which are arranged accordingly in the sinogram representing the Radon transform of the object.

When the X-rays propagate along s through the sample, they are attenuated according to the local sample composition in $\mu(s, r)$, and hit the detector at position r. This line integral along s is the **projection integral**

$$p_\phi(r) = \int \mu(s, r)\, ds \tag{3.5}$$

of $\mu(s, r)$ and assigns one projected intensity to the beam position r. Back in the object coordinate system $f(x, y)$, the same integral is expressed by

$$p_\phi(r) = \int f(s\cos\phi - r\sin\phi, s\sin\phi + r\cos\phi)\, ds \tag{3.6}$$

where (x, y) are parametrized by (s, r) and the inverted rotation $-\phi$ has to be used. This transformation of coordinates and assignment of line integrals through the sample for all rotations ϕ is the **Radon Transform** $\mathcal{R}$ of $f(x, y)$:

$$\mathcal{R}[f(x, y)] = \int_s f(x, y)\, ds = p_\phi(r)\,. \tag{3.7}$$

Recording the projections over 180°, yields the so-called sinogram, shown in fig. 3.3. It holds the projected X-ray intensities as function of (r, ϕ), since it was integrated along s. The sinogram, or Radon transform of f, is the result of the tomographic scan and starting point of the reconstruction process. Now the task is to do exactly the inverse operation and to reconstruct the object $f(x, y)$ from a series of projections $p_\phi(r)$.

Fourier Slice Theorem

The reconstruction of the object from the sinogram can be achieved in various ways, which group into iterative, Fourier Transform, and filtered back projection techniques [91]. Here the Fourier Transform (FT) based approach is presented first and the most commonly used filtered back projection method will be deduced afterwards, which is also used in the experiments performed in this work.

Firstly, the object $f(x, y)$ needs to be transformed into its 2D Fourier domain

$$\hat{f}(k_x, k_y) = \iint e^{-2\pi i(xk_x + yk_y)} f(x, y)\, dk_x\, dk_y \tag{3.8}$$

using k_x and k_y in Cartesian coordinates, similar to $f(x, y)$. In general, the Fourier transform of a projection is expressed as

$$\begin{aligned}
\hat{p}_\phi(k_r) &= \int e^{-2\pi i k_r r} \cdot p_\phi(r)\, dr \\
&= \int e^{-2\pi i k_r r} \int \mu(s, r)\, ds\, dr \\
&= \iint e^{-2\pi i k_r (x\cos\phi + y\sin\phi)} f(x, y)\, dx\, dy \\
&= \iint e^{-2\pi i (x(k_r\cos\phi) + y(k_r\sin\phi))} f(x, y)\, dx\, dy \\
&= \iint e^{-2\pi i \left(xk'_x + yk'_y\right)} f(x, y)\, dx\, dy \\
&= \hat{f}(k'_x, k'_y) \\
&= \hat{f}(k_r\cos\phi, k_r\sin\phi)
\end{aligned} \tag{3.9}$$

where the definition of the projection integral in eq. (3.5) is inserted in a first step. The object $\mu(r, s)$ in the beam-fixed system is translated to $f(x, y)$ by changing the coordinate system, which requires a variable substitution $r = x\cos\phi + y\sin\phi$. Rearranging of factors in the exponential function allows to identify the 2D Fourier transform of the object, *cf.* eq. (3.8).

This important finding is the **Fourier slice theorem**:

$$\boxed{\hat{p}_\phi(k_r) = \hat{f}(k_r\cos\phi, k_r\sin\phi)} \tag{3.10}$$

It states, that the Fourier transformed projection $\hat{p}$ under angle ϕ is equal to a radial line through the origin of the 2D Fourier space of the object $\hat{f}$ under the same angle ϕ. Thus, each projection in the sinogram adds a line into the 2D-FT domain of $\hat{f}$. This is illustrated in fig. 3.4.

Given enough projections are included, the FT domain will be sampled quite well. However, in order to directly apply the inverse 2D-FT, the Fourier coefficients on the magenta colored grid have to be known. Since sampling is done along radial lines, they are not very well sampled especially at high frequencies. Therefore, a resampling in

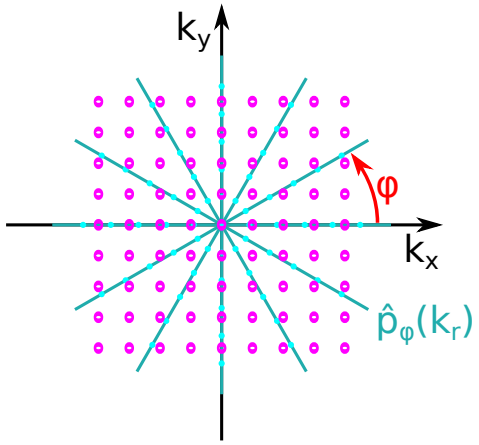

Figure 3.4.: Illustration of the Fourier Slice Theorem. Sampling of $\hat{f}(k_x, k_y)$ in the 2D frequency domain by radial lines $\hat{p}_\phi(k_r)$. Magenta circles on Cartesian grid.

FT space is required. The resampling was a major challenge for long time, but was recently tackled and demonstrated to work in the *gridrec* algorithm [96].

Filtered Back Projection

The Fourier Slice theorem shows, that the Fourier Transform of a summation/projection along s corresponds to a radial line in the 2D-FT of the object. One can use these 2D-FT lines directly to reconstruct the object without Cartesian resampling. Since $\hat{f}$ is sampled in radial lines, utilizing polar coordinates in the inverse Fourier transformation yields the coefficients without interpolation. The Cartesian coordinates in the FT domain are expressed in polar coordinates by

$$k_x = k_r \cos\phi, \qquad k_y = k_r \sin\phi, \qquad dk_x\, dk_y = k_r\, dk_r\, dk_\phi\,. \tag{3.11}$$

This introduces a factor k_r for the area of integration. The object f is obtained by the inverse FT in polar coordinates:

$$\begin{aligned} f(x,y) &= \iint e^{2\pi i \vec{k}\vec{x}} \cdot \hat{f}(k_x, k_y)\, dk_x\, dk_y && (3.12)\\ &= \int_0^{2\pi} \int_0^{\infty} e^{2\pi i (x k_r \cos\phi + y k_r \sin\phi)} \cdot \hat{f}(k_r\cos\phi, k_r \sin\phi) \cdot k_r\, dk_r\, dk_\phi && (3.13)\\ &= \int_0^{2\pi} \int_0^{\infty} e^{2\pi i k_r (x\cos\phi + y \sin\phi)} \cdot \hat{p}_\phi(k_r) \cdot k_r\, dk_r\, dk_\phi && (3.14)\\ &= \int_0^{\pi} \int_{-\infty}^{\infty} e^{2\pi i k_r r} \cdot \hat{p}_\phi(k_r) \cdot |k_r|\, dk_r\, dk_\phi\,. && (3.15) \end{aligned}$$

After transformation into polar coordinates the Fourier slice theorem is used to replace $\hat{f}$ by the corresponding Fourier transformed projection $\hat{p}_\phi(k_r)$. Substitution of $r = x\cos\phi + y\sin\phi$ and exploiting the symmetry properties of the Fourier transformation lead to the last line of the equation where an integration over the absolute value $|k_r|$ is

done. The inner integral, is the so-called **filtered projection**, which does the filtering

$$\boxed{Q_\phi(r) = \int_{-\infty}^{\infty} e^{2\pi i k_r r} \cdot \hat{p}_\phi(k_r) \cdot |k_r| \, dk_r} \tag{3.16}$$

of $\hat{p}_\phi(k_r)$ by $|k_r|$ in the Fourier domain. This becomes even more clear, when eq. (3.9) with the definition of $\hat{p}_\phi(k_r)$ is inserted into the equation yielding

$$Q_\phi(r) = \int_{-\infty}^{\infty} e^{2\pi i k_r r} \cdot \int e^{-2\pi i k_r r} p_\phi(r) \, dr \cdot |k_r| \, dk_r \, . \tag{3.17}$$

By summation and **back projection** of intensities in the filtered projections $Q_\phi(r)$ along radial lines in the image plane, the object $f(x, y)$ is reconstructed.

$$\boxed{f(x, y) = \int_0^{\pi} Q_\phi(r) \, dk_\phi} \tag{3.18}$$

The whole reconstruction process is demonstrated on a simple example in the following section.

Example of Reconstruction with Filtered Back Projection

A simple test object is shown in fig. 3.5 on the left. Horizontal projections along s are performed to obtain the Radon transform (middle), and the filtered sinogram (right) respectively.

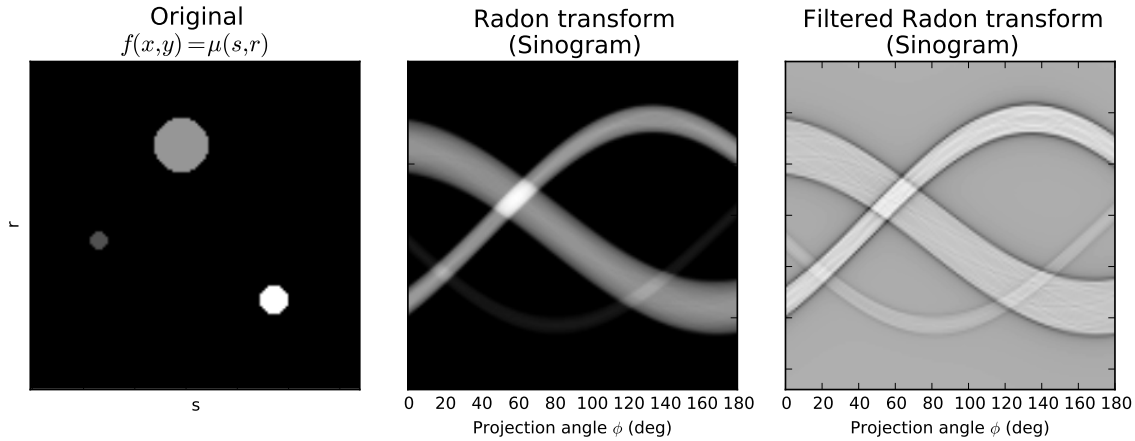

Figure 3.5.: A test object (left) is Radon transformed with integrations along s and rotation angles ϕ (middle). Finally, the sinogram is filtered (right).

The process of back projection is demonstrated in fig. 3.6. The first three panels show the back projected, filtered intensities taken from the filtered sinogram at 0, 90, and 135°, which are applied under the same angle to the image. The last panel shows the sum of all three back projections.

Finally, the original image is reconstructed in fig. 3.7. Given enough projection angles n are used, the objects becomes more defined. This also defines the number of

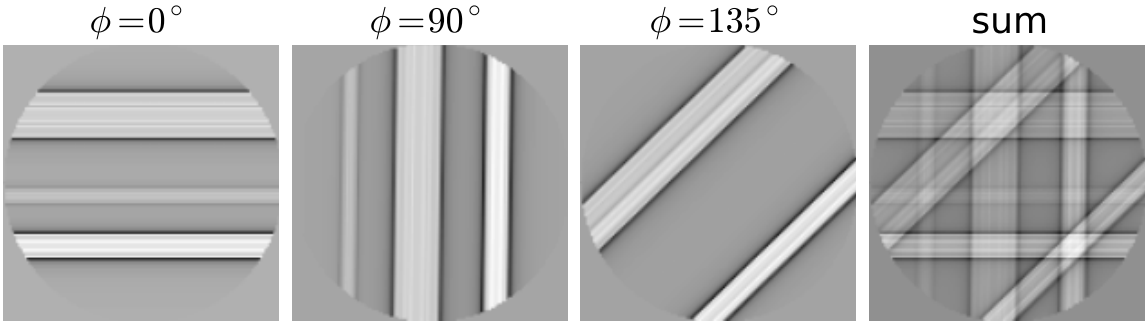

Figure 3.6.: Single filtered projections intensities extracted from the filtered sinogram and back projected across the image.

projection angles that have to be recorded in the experiment and critically determines the resolution of the tomogram. As a rule of thumb the number of projections should be around 1 to 1.5 times the object size in detector pixels [91].

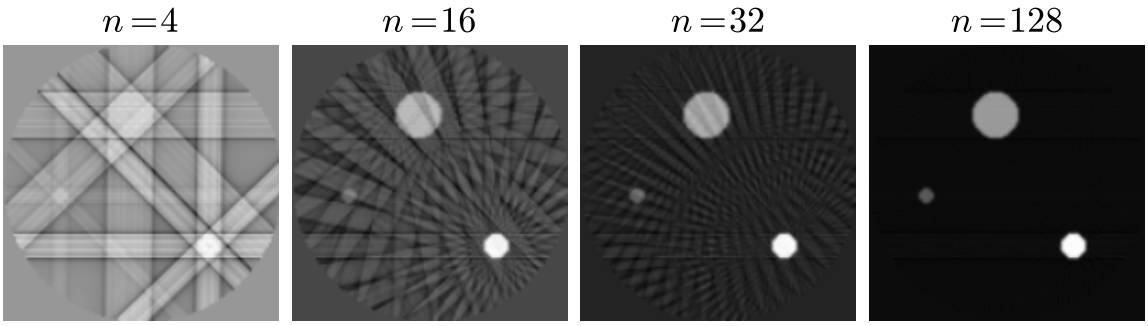

Figure 3.7.: Reconstruction of the test object with an increasing number of filtered back projections.

3.3. Quasi in situ Tomography: Experimental Approach

To enable the spatially and temporally resolved investigation of sample treatment effects by micro-computed X-ray tomography in the same sample volume, a quasi *in situ* tomography approach was developed. The fundamental principles and methods are detailed in this section.

In order to precisely identify and quantitatively evaluate changes to a specific sample due to a sample treatment the initial and final state need be known, meaning that the same sample needs to be studied by tomography before and after treatment. Since no suitable *in situ* furnace was available for the aging of the exhaust gas catalysts at up to 950 °C, temperature treatments had to be done *ex situ* using a conventional oven. Hence, the term quasi *in situ* experiment is used. The most crucial part during the measurements is the proper and careful re-installation and alignment of the sample before the next tomography scan. Altogether, repeating the described sequential tomography investigation and *ex situ* treatment of the same sample is the *experimental* key principle of the quasi *in situ* approach. This scheme is shown in fig. 3.8. However, it still requires additional computational efforts to align the virtual data sets to perform a voxel-by-voxel analysis.

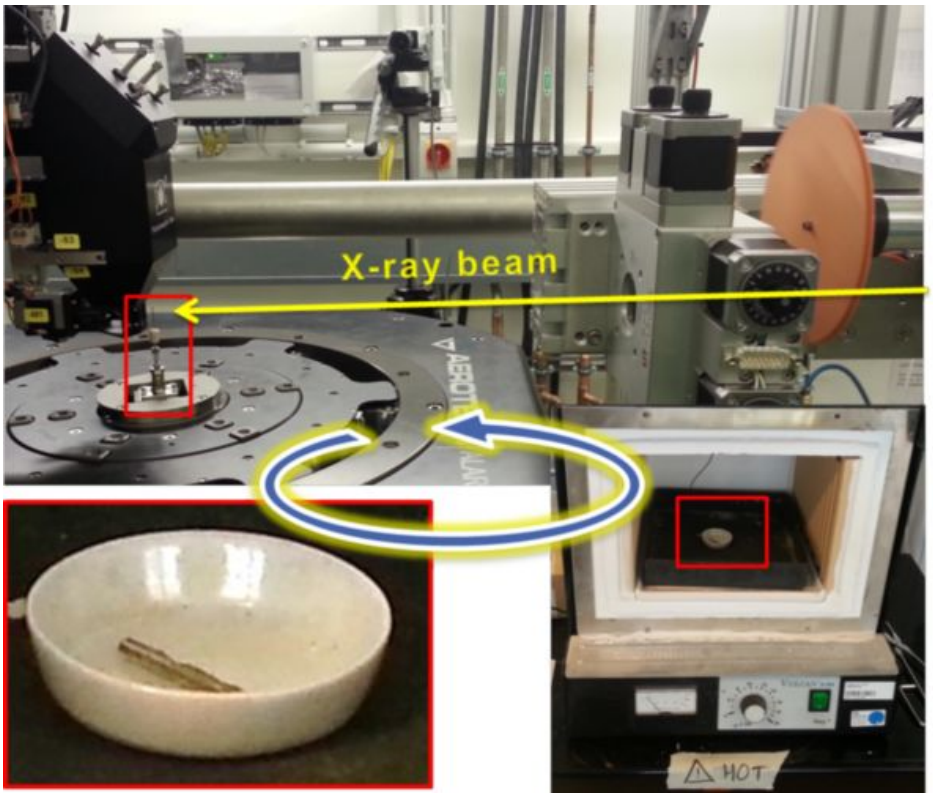

Figure 3.8.: Scheme of the quasi *in situ* tomography approach. Sample installed at the beamline (top), put in a crucible (left), and thermally aged in an oven (right). This cycle is repeated for subsequent investigations.

Notably, this quasi *in situ* approach is not limited to temperature treatments only. In fact, any sophisticated *ex situ* sample treatment can be done, provided that major features or artificial markers in the sample are preserved, since they are required for the computational alignment of the tomographic data.

3.3.1. Thermal Sample Treatment

Thermal treatments were conducted in an *ex situ* oven. For the current experiments a static air furnace (see fig. 3.8 lower right) was used, kindly provided by the Helmholtz-Zentrum Geesthacht (HZG). After the initial tomography scan, the sample was unmounted and put into a heat resistant crucible. Great care was taken to preserve the general sample orientation for later remounting of the sample. The temperature inside the oven was monitored by a thermocouple, heating and cooling ramps were run with approximately $20\,\mathrm{K\,min^{-1}}$.

3.3.2. Preparation of Honeycomb Catalyst

The sample was prepared by incipient wetness impregnation of 5 h at 700 °C calcined $\gamma{-}Al_2O_3$ ($165\,\mathrm{m^2\,g^{-1}}$, SASOL) with an aqueous solution of hexachloroplatinic acid H_2PtCl_6 (Sigma-Aldrich, cf. ref. [97]) to obtain 4 wt.% Pt loading with respect to the used $\gamma{-}Al_2O_3$ support. A slightly higher loading is used here to optimize imaging contrast in this first study. The resulting 4 wt.% $Pt/\gamma{-}Al_2O_3$ powder was dried for 12 h at 80 °C and calcined for 2 h at 500 °C in static air. Cordierite monoliths with 400 channels per square inch (cpsi) were used from which cylindrical samples of approximately 21 mm diameter, 25 mm length, and a typical weight of 3.4 g were obtained by drilling them out of larger ones. They were coated with about 1.2 g of aqueous slurry containing the catalyst powder and a commercial colloidal silica binder (Ludox AS-40, 10 % of the catalyst mass) resulting in a Pt loading of $160\,\mathrm{g\,ft^{-3}}$. After calcination in air for 5 h at 550 °C, the samples were conditioned for 4 h at 400 °C in 5 vol.% H_2/N_2.

These small coated honeycomb cylinders were directly used for catalytic tests. In addition, they were also used to obtain channels for tomography as described in the following.

3.3.3. Sample Preparation and Mounting

In general, μ-CT sample preparation is quite easy, as compared to EPMA. The sample just has to fit into the field of view or needs to be cut down accordingly. In case of the still too big cordierite monolith cylinders used here, a representative sample was obtained by cutting the catalyst using a scalpel. Since the main focus was on the washcoat layer of an intact honeycomb channel, measured at highest magnification, a single honeycomb channel was extracted, as shown in fig. 3.9 on the left.

However, since a single cordierite wall alone is quite brittle, and an intact channel can hardly be prepared directly, the preparation started from a pre-cut 3×3 honeycomb channel block, from which the central channel was prepared. Nevertheless, cutting must be done carefully to preserve integrity of the central washcoat layer. Once the

single channel was obtained, loose and overhanging wall material on the outside was removed to form a slim sample with optimal fit into the sample holder and field of view of the tomography setup, *cf.* fig. 3.9. Furthermore, this avoided large structural changes, which would have hampered the following data post-processing, *i.e.* volume registration.

Figure 3.9.: A single honeycomb channel hot glued to a plastics cap standard sample holder (left) and the cup-like holder used for mounting quasi *in situ* tomography samples (right).

The sample mounting for tomography is in principle straight forward but becomes more demanding with higher magnification, as it is harder to stay within the field of view during the rotation scan. This requires a fixed sample position in mostly upright orientation well centered on the sample holder, a shown in fig. 3.9(left), which is a crucial prerequisite to obtain good data. Generally, single *ex situ* samples are quickly hot glued to standard beamline sample holders, as shown on the left in fig. 3.9. It allows minor corrections to the sample orientation and position for a short time and produces very stable results after curing. Nevertheless, it must not be exposed directly to X-rays where it degrades, allowing the sample to move. Unfortunately, this technique cannot be used for mounting quasi *in situ* samples, since the glue is also not stable to the temperatures used for the heat treatment and the glue cannot be completely removed from the sample. Moreover, any modification of the internal washcoat layer must be avoided, which would unavoidably happen if the channel would be sticked into the hot glue.

Hence, for the quasi *in situ* tomography samples a mechanical fixation was used. One option, similar to a bench vise, makes use of two plates pushed against each other. This requires a lot of force to prevent movement parallel to the plates and is risky with brittle samples. A better solution employs the cup-like holder, shown in fig. 3.9 on the right, which was especially built for this purpose at the beamline. It features a tailored bore hole, matching the size of the honeycomb channel, with two integrated orthogonal blind set screws for fixation. The bottom part of the channel, inside the hole, is additionally wrapped into a few layers of soft laboratory tissue paper. This adds some initial stability and buffering to the fixating screws.

3.3.4. Tomography Data Post-Processing – Volume Registration

After mastering the above *experimental* aspects of the quasi *in situ* approach, tomography data was acquired, results are given in in section 3.3.6, and reconstructed. The post processing of data starts with the preparation of aligned samples that are suited for voxel-by-voxel comparison to detect sample changes.

Although done with greatest care, the manual remounting and realignment of the sample after an *ex situ* treatment, deviated from its previous position and orientation. However, by using digital volume registration, data sets were realigned. A simplified scheme, illustrating the issue and its solution is shown in fig. 3.10.

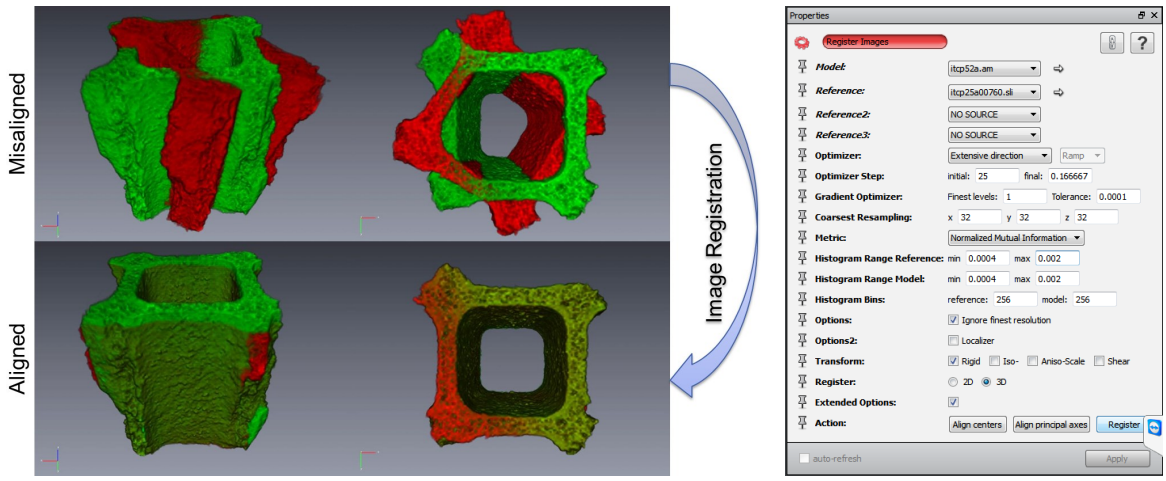

Figure 3.10.: Volume rendering of two misaligned volumes (red and green) from the same sample (top), being realigned by image registration to obtain perfectly matching volumes (bottom). Snapshot of the used Avizo Fire registration module with relevant parameters (right).

In summary, for a series of successful quasi *in situ* tomography experiments, several *experimental* (a-c) and *computational* (d) aspects have to be considered: (a) careful and reproducible mounting of the sample in the sample holder, (b) reproducible measurements of the same part of the sample under similar conditions, (c) unmounting and application of treatments without artificial modifications, and finally (d) digital alignment of the data sets as first step toward the analysis.

3.3.5. Tutorial: Data Post-Processing – Volume Registration

This brief tutorial is intended to guide new users through the volume registration process, which is divided into the following five steps. Avizo Fire 8 [98] modules are set in `typewriter` font.

(1) Create Reference Data Set

It is advantageous for practical reasons to create a reference data set, which is nicely aligned along the Cartesian coordinate system and cropped to a minimal size containing the best available data, thus reducing memory demands. In Avizo this is achieved by manually rotating the sample volume until the structure is nicely aligned to the global coordinate system. Clipping views in `Ortho Slice` are useful here. Afterwards the data is resampled by `Apply Transformation` using Lanczos interpolation, and cropping to the region of interest.

(2) Manual Search for Matches

In a first step, common characteristic features are identified and located in each volume to obtain a good initial guess. Here, the voids in the cordierite structure are very useful. Exploring the data is best done within Avizo using two `Ortho Slice` in a split screen configuration, since test rotations and zooms can be quickly performed.

(3) Manual Pre-Alignment

By using the matching regions the to-be-registered volume (model) is manually pre-aligned to the reference (1) using the `Geometry Transform` dialog. To match identical regions, it is helpful to show the corresponding `Ortho Slice` in the volume rendering during transformation to view the intersection. Some cropping of the model data, leaving enough data for later resampling, can be done to speed up processing.

(4) Invoking Registration Routine

The pre-alignment is optimized by `Register Images` used in advanced mode. Here, the histogram ranges (set to wash-coat and cordierite), resampling, and initial step size have to be adjusted, *cf.* fig. 3.10. Before invoking `Register Images`, the current model orientation and position should be saved either by the `getTransform` command or in the `Geometry Transformation` dialog. After registration, the resulting log output (console) have to be checked and whether volumes match. Finally, satisfying transformation parameters are saved for further processing of the complete, uncropped data set.

(5) Transformation and Resampling of Data

Finally, the perfectly registered model volume is transformed to the reference grid using `Apply Transformation` and Lanczos resampling, which enables voxel-by-voxel analysis later. Save the resulting volume data set.

3.3.6. Validation of the Alignment Approach

To ensure the validity of the described registration method for the quasi *in situ* approach, potential artifacts due to transformation and resampling have to be evaluated and the possible impact on the processed data as well as on the derived measurements have to be appraised.

Possible pitfalls in the quasi *in situ* process are:

1. Qualtity of transformation, interpolation, and resampling artifacts in general. How good is the interpolation and how well is the information of the experiment preserved?
2. Suboptimal volume match: The registration algorithm has not found the best possible alignment, potentially leading to artifacts in direct comparison of voxels afterwards.

Estimation of Errors from Transformation and Resampling

A volume A is transformed by operation $\mathbf{T}$ with subsequent resampling to obtain the volume A'. The transformation operation $\mathbf{T}$ is now reverted by using the inverse transformation $\mathbf{T}^{-1}$ and resampling to obtain A''. This is formally written in eq. (3.19).

$$A \xrightarrow[\text{resample}]{\mathbf{T}} A' \qquad\qquad A' \xrightarrow[\text{resample}]{\mathbf{T}^{-1}} A'' \tag{3.19}$$

Purely mathematically $A'' = A$ would hold, since $\mathbf{T}^{-1}\mathbf{T} = \mathbf{1}$. However, as the volumes are resampled in the course of transformation to the Cartesian grid used by the software, this is not true for a transformation operation performed by a computer. The impact of resampling is contained in the difference D and relative error R per voxel for the entire volume, as given in eq. (3.20).

$$D = A'' - A \qquad\qquad R = \frac{D}{A} = \frac{A'' - A}{A} \tag{3.20}$$

Graphical Representation

A central xy slice taken from the original data A, the difference D, and the relative error R are shown in fig. 3.11 for comparison. Since the values of D and R vary a lot from voxel to voxel, it is difficult to recognize a trend in the raw image directly. Therefore, a denoising box filter has been applied replacing the current voxel value by the average value of the surrounding cube of $5 \times 5 \times 5$ voxels. The resulting filtered volumes, $\bar{D}$ and $\bar{R}$, are much clearer and show only minimal blurring, if compared to the detailed statistics in table 3.1 later. The color range of the images has been adjusted to capture the relevant dynamics for A and $\bar{D}$, which is approximately 2.5 times the standard deviation around the mean value (*cf.* table 3.1).

As evident from the central xy slice in fig. 3.11 (A), the reconstructed volume consists of two distinct regions, namely homogeneous *air* (black) and a heterogeneous washcoat on cordierite *channel* (gray). These need to be analyzed separately.

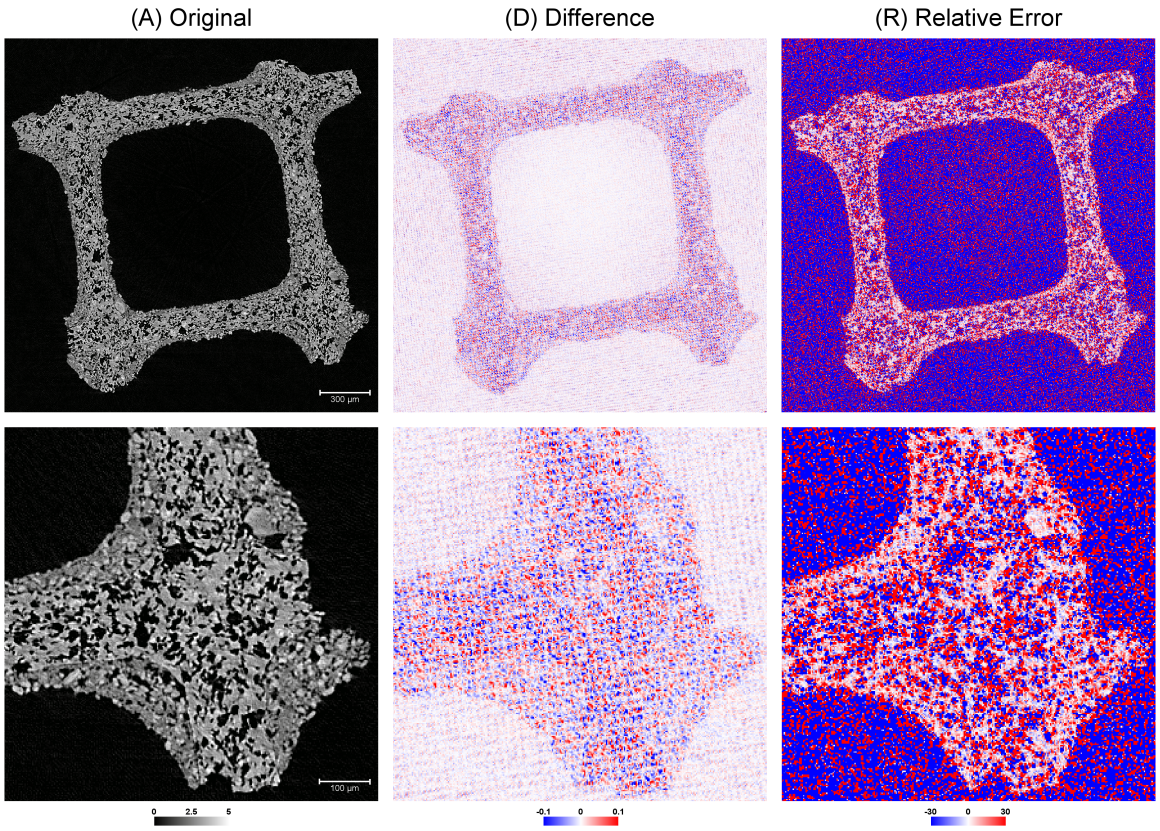

Figure 3.11.: Comparison of the original slice (A) to the box filtered difference (D) and relative error (R) after applying and reverting a sample transformation. All color scales are in units of 1×10^{-3}.

In the surrounding *air* the filtered differences $\bar{D}$, shown in fig. 3.11 (D), are close to zero (white) with little spread (hardly any dark blue or red). This indicates only minor difficulties for the resampling of homogeneous regions. However, the filtered relative error $\bar{R}$, in fig. 3.11 (R), shows mostly values apart from zero with high spread (blue and red). This can be explained by the definition of R. Although only small differences are found, they are divided by another small number and thus scaled up considerably.

Within the *channel* material larger $\bar{D}$ values are found with a magnitude of up to 1×10^{-4}, *cf.* fig. 3.11 (D). This is caused by a very inhomogeneous composition of the *channel* material in general, due to strongly varying absorption found in the washcoat and in the cordierite. Moreover, relatively sharp transitions from material to air filled pores, especially in the cordierite add pronounced changes. Both factors are more challenging for the resampling and due to the initial high absorption value of the material, deviations are on another order of magnitude. Nevertheless, considering $\bar{R}$ in fig. 3.11 (R), for the *channel* material, values very close to zero (white) with little spread are observed indicating a very good resampling performance. Larger blue and red areas within the *channel* shape correspond to pores filled with air or regions with relatively high intensity gradients.

Analysis of Material Statistics

For the two materials *air* and *channel*, comprised of 5.9×10^8 and 1.4×10^8 voxels respectively, the corresponding material statistics (min, max, median, mean, and standard deviation (StdDev)) are tabulated in table 3.1 for each volume data set: original A, back transformed A'', raw and filtered difference $D, \bar{D}$, and raw and filtered relative error $R, \bar{R}$.

Table 3.1.: Statistical results of the resampling test for materials *air* and *channel* (cordierite and washcoat) given for the respective volume data sets. All values in units of 1×10^{-3}.

	Data Set		Min	Max	Median	Mean	StdDev
Air	A	original	−17.275	30.940	0.012	−0.009	0.355
	A''	reverted	−17.459	30.980	0.012	−0.011	0.332
	D	difference	−1.708	1.513	0.000	−0.001	0.097
	$\bar{D}$	filtered	−0.931	0.523	0.000	−0.001	0.019
	R	rel. error	—	—	−167.704	−224.697	—
	$\bar{R}$	filtered	—	—	−171.130	−232.257	—
Channel	A	original	−5.046	20.564	2.687	2.547	1.161
	A''	reverted	−4.908	20.581	2.682	2.553	1.143
	D	difference	−1.495	1.798	0.003	0.006	0.172
	$\bar{D}$	filtered	−0.939	0.481	0.002	0.004	0.039
	R	rel. error	—	—	−0.416	9.540	—
	$\bar{R}$	filtered	—	—	4.158	39.729	—

The effect of box filtering D and R to obtain averaged $\bar{D}$ and $\bar{R}$ becomes evident. The StdDev (data spread) in $\bar{D}$ is reduced by about 1/5 and 1/4 in *air* and *channel* respectively. While the mean $\bar{R}$ for *air* is almost unchanged, the mean $\bar{R}$ for *channel* is increased by about a factor of 4.

For *air* both difference data sets, D and $\bar{D}$, show median and mean values close to zero with a very small StdDev. This corresponds to the observation in the above images for D in fig. 3.11. Accordingly, very high values are found for R but this is not critical for the reasons given above. Furthermore, the table provides evidence that *air* values in A'' remain well separated from *channel* material values.

Regarding the *channel* material, differences D remain very small in the order of 1×10^{-3} compared to the mean gray value of A. Thus, thresholds can be defined regardless of prior volume transformations. Considering the mean relative error R, a value of 9.540×10^{-3}, approximately 1 %, is obtained. This would in average introduce an additional gray value uncertainty per voxel of $\pm 2.54 \times 10^{-5}$ units to A. This value compared to the StdDev of A accounts to about 2 %, underlining the small effect.

Overall, the all statistical values tabulated for *air* and *channel* in the data sets A and A'', listed in table 3.1, are well preserved during the two applied resamplings. Which again underlines good resampling performance.

Conclusion: Validation of the Alignment Approach

Applying and reverting a given transformation on a honeycomb test volume data set with Lanczos resampling preserves the volumes very well as evident from overall statistical measures. Thus we can expect a quite good reproduction/preservation of the resampled tomographic volumes. This is essential for the validity of the quasi *in situ* analysis.

The surrounding *air* shows a very small mean difference D of -1×10^{-6}, indicating well working resampling on homogeneous areas. Therefore, the *air* values remain in the range of the background and do not reach typical *channel* material values, which could lead to misinterpretation. The *channel* material (including washcoat and cordierite) exhibits a small mean relative error R of 9.540×10^{-3}. Thus, the resulting additional deviation per voxel is very small compared to the mean gray value of the material. Allowing to define segmentation thresholds irrespective of applied transformations.

Consequently, for case two, the estimation of errors caused by volume registration can be briefly discussed as follows. The quality of the determined transformation $\mathbf{T}^*$ during the registration is the important parameter. By applying a known transformation $\mathbf{T}$ to a volume A, a resampled volume A' is obtained. Using the volume registration, the *computed* inverse transformation $\mathbf{T}^*$, supposed to lead from A' to A, is derived.

$$A \xrightarrow[\text{resample}]{\mathbf{T}} A' \qquad\qquad \mathbf{T}^* := A' \xrightarrow[\text{registration}]{\text{volume}} A$$

In principle, the *analytical* $\mathbf{T}^{-1}$ and the *computed* $\mathbf{T}^*$ may be compared directly, on a very abstract level. However, since resampling has no significant impact, one can calculate A^* using $\mathbf{T}^*$ and compare it directly to A.

$$\mathbf{T}^{-1} \stackrel{?}{=} \mathbf{T}^* \qquad\qquad A' \xrightarrow[\text{resample}]{\mathbf{T}^*} A^* \qquad\qquad A \stackrel{?}{=} A^*$$

Again, no significant error is produced by this operation in analogy to the aformentioned transformation case. Instead it turned out, comparing data with the same image quality is much more relevant. This is illustrated in fig. 3.12, focusing on biggest differences between two samples. Those are located in outer regions where image noise has a significant impact. The rings are artifacts from the reconstruction in the center. Hence, the following section will be dedicated to factors influencing data quality.

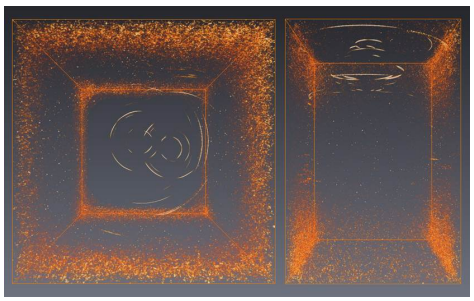

Figure 3.12.: Largest differences between two data sets shown by a volume rendering.

Parameters for optimal Tomographic Data Quality

Here we are discussing aspects for obtaining high quality tomography data of the honeycomb samples using the quasi *in situ* tomography approach.

Dynamic Range in Data Acquisition & Sample Shape

For absorption measurements, theoretical considerations yield an optimal value for the transmitted X-rays through the sample of 13.5 % or $\exp(-2)$ [99]. This can be adjusted by tuning the X-ray photon energy, the exposure time, and the amount of sample. In tomography, this is easily checked by computing the resulting absorption image at the beginning of a scan campaign.

Considering honeycomb catalysts, the area of interest is the inner washcoat layer surrounded by cordierite walls. That influences the adjustment of the above parameters considerably. The distinct rectangular geometry of the channel is responsible for high X-ray absorption each time the walls are in line with the beam. This is visible as red regions in fig. 3.13. Consequently, the full dynamic range for the washcoat could not be exploited in the angles in between. Thus, to enhance contrast an investigation of the washcoat without the cordierite structure might be prepared and measured.

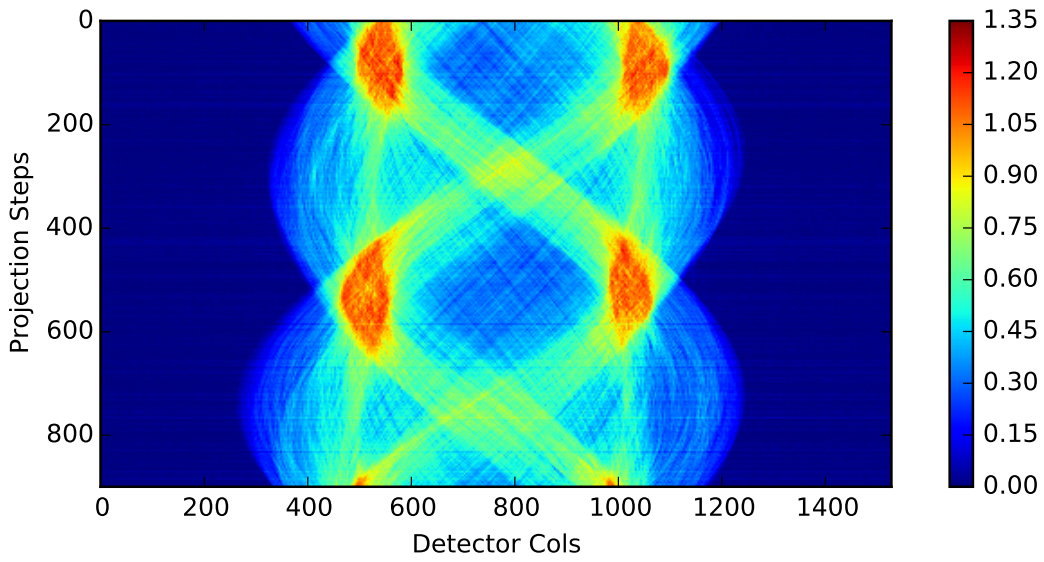

Figure 3.13.: Sinogram of a honeycomb sample, showing the dynamic range of the absorption coefficient μ across a 180° rotation.

However, the wall structure itself is important as guiding structure to register volumes in the quasi *in situ* approach. Thus, the imaging parameters need to be adjusted exactly under this highest absorption alignment to prevent reconstruction artifacts caused by full absorption.

Accordingly, the parameters are adjusted to yield a maximum attenuation of $\exp(-1.35)$ or 26 % in transmission, given that the walls are aligned with the beam. Different orientations cause around $\exp(-0.5)$ absorption or 60 % transmission, as

shown in fig. 3.13. Furthermore, the sample size and field of view is chosen to image a full single channel.

Impact of the Beam Profile

In full field tomography the beam profile typically has the shape of a 2D Gaussian. Thus highest illumination and best photon statistics are obtained in the center of the beam with a decay in horizontal and vertical directions. This is shown in fig. 3.14, where the beam illumination was averaged over all flat field images acquired during one scan.

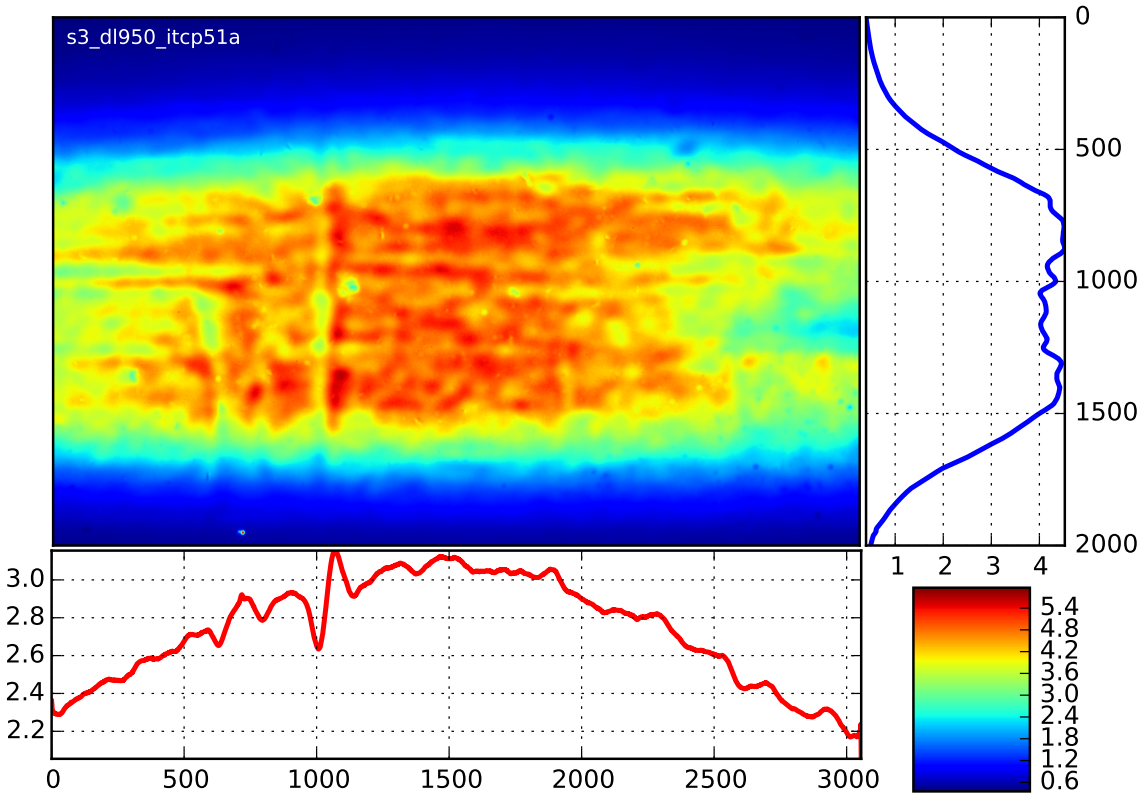

Figure 3.14.: Typical X-ray beam profile obtained from averaged flat field images. The line plots display the profile along x and y axis. Intensities $\times 10^4$.

The sample should be positioned in high intensity areas under all rotation angles, since for analysis and comparison of several data sets the signal-to-noise in the data should be comparable. For example, a suitable imaging region is found between the rows 750 and 1500 (vertically) and for columns centered around 1500 ± 750 (horizontally).

Identical Sample Region Illumination

As the quasi *in situ* approach aims to compare several tomography scans of the same sample, another constraint is put upon the setup: The same sample regions has to be placed in the best illuminated imaging region for all aging steps. This is important in order to obtain comparable reconstructions.

By plotting the average flat field beam profile and beam position for each complete scan of a series, as shown in fig. 3.15, one can ensure to compare data of similar quality and find a best common illuminated image area for cropping data.

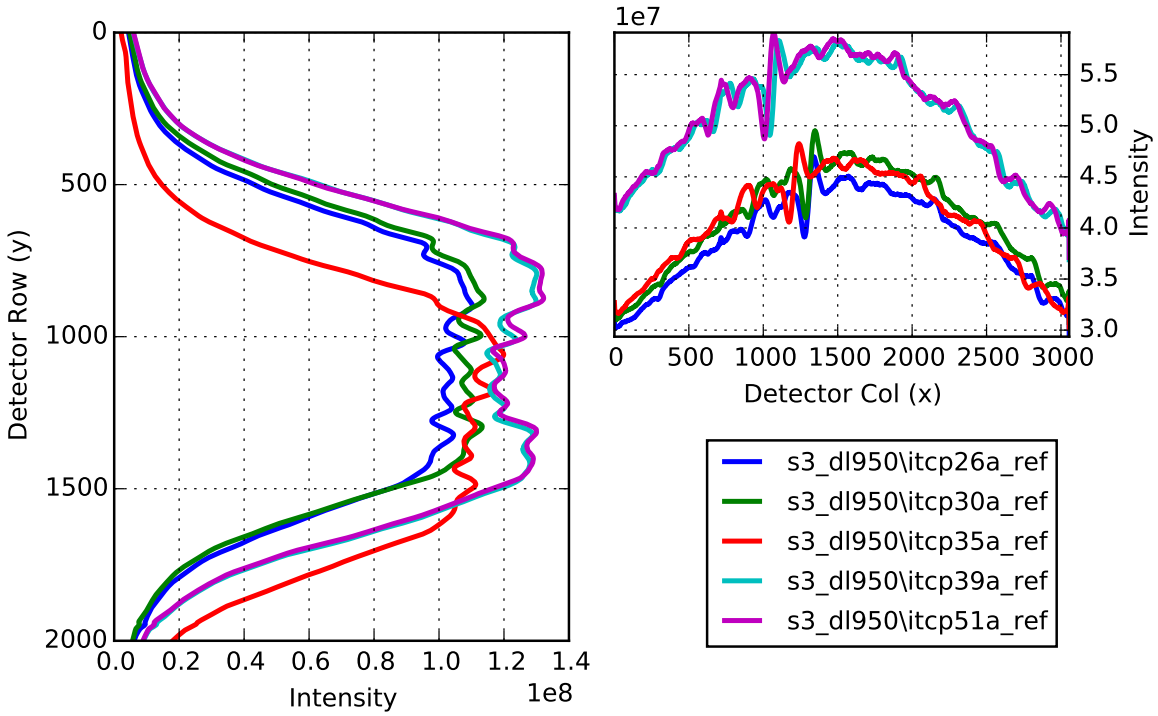

Figure 3.15.: Variation of the detector illumination by changing beam position and beam profile during a scan campaign for one specific sample (double layer aged at 950 °C). Directly consecutive scans (26+30, 39+51) are more similar than others due to changes in between.

As seen in fig. 3.15 scan itcp35a, the illumination maxium is slightly shifted down. This means, given a fixed z position of the sample, that the upper part (*e.g.* at row 600) is not as good as in the other scans, while it might have better quality in lower parts. In essence, the top part would be "missing", as compared to the other scans. Interestingly, the last two scans show a slightly higher overall intensity, which is probably related to some change of the beam during the campaign.

In the end, the task is to define regions delivering good data quality and restrict tomographic data analysis to them. As the usable sample volume is further reduced by the smallest common scan volume present in all steps of the measurement, it is paramount importance to recover the original position as close as possible. Technically, this means that xy slices that do not fulfill the above criteria are excluded from the analysis.

Noise Distribution in Reconstructions

The importance of comparable imaging regions is demonstrated by observing the noise distribution in a tomographic reconstruction. Two slices through the center of the tomographic volume along xy and xz are shown in fig. 3.16. A clear vertical dependence

on z (more at top and bottom) and horizontally as function of the distance from the center (more at the left and right border) is observed. This underlines the above reasoning to place the region-of-interest of the sample in the best imaging region for each scan, in order to obtain comparable data.

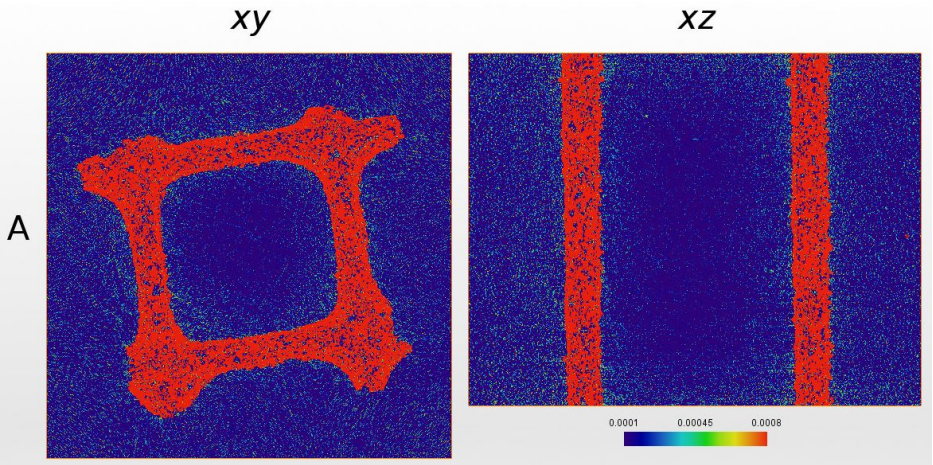

Figure 3.16.: Noise distribution in the reconstructed volume shown by 2D slices along xy and xz planes, cutting through the center of the volume.

Conclusion

It is possible to obtain high quality tomographic data from single honeycomb channels. For optimization of the sample absorption during the tomography scan, the particular sample geometry and composition has to be considered. Thus, it cannot be optimized directly to the washcoat alone, ignoring the cordierite walls.

The same sample regions have to be positioned in the center of the X-ray beam, since image quality is directly dependent on the illumination, which is changing due to the beam profile. Consequently, tomographic reconstructions are affected. For later quasi *in situ* analysis, the tomographic data has to be selected accordingly to maintain high quality and comparable reconstructions across several scans.

3.4. Results

After we have introduced theoretical and experimental backgrounds, we start with pioneering experiments. They are aimed to explore possibilities and potentials of tomography on typical exhaust gas catalyst powders and catalyst bodies. Optimal imaging conditions will be derived as well as practical experience in imaging of honeycombs will be gathered.

In the first part *ex situ* aged coated honeycomb channels will be evaluated. In the following, the quasi *in situ* approach is utilized to study the impact of treatment on the sample spatially resolved. By a series of heat treatments, proper aging conditions are determined, suitable analysis conditions are derived, and first qualitative changes are revealed by a difference method. Quantitative results are obtained by another experimental series utilizing isothermal high temperature treatments in static air using image segmentation prior to analysis. In this context, details on data interpretation, regarding the voxel size effect and Pt sintering identification are given, utilizing complementary SEM and EPMA studies.

This section uses text and images from two own first authored publications: [100] published by "IOP Publishing" and [101] published by "The Royal Society of Chemistry". Both are open access and licensed under CC BY 3.0.

3.5. Potential of Tomography in Catalysis Research

Before performing sophisticated measurement campaigns, we need to ensure that our demands can be met by the capabilities of the method. To this end some pre-tests on important properties of our catalyst systems were performed. These are comprised of: (i) investigation of different types of catalyst powders in regard to precious metal loading, composition, and type of support; (ii) development of suitable preparation routes and mounting for the inspection of honeycombs; (iii) and combination of (i) and (ii) to image coated honeycombs.

Differentiation of Catalyst Powders and Loading Effects

The differentiation between support materials and catalyst powders is important for later identification and analysis. It is also illustrative as a reference to identify typical features like local concentration variations and concentration gradients in typical tomography slices later on.

Three test samples are shown in fig. 3.17: (A) capillary with a mixture of Pt(II)-acetylacetonate pre-cursor with Al_2O_3 as 50 µm sieve fraction together with compact washcoat blocks with 120 g ft^{-3} Pt/Al_2O_3 loading (reduced). (B) capillary with the same type of washcoat blocks, with Pt/Al_2O_3 prepared by incipient wetness impregnation (IWI), compared to 1 wt.% Pt/SiO_2 produced by flame spray pyrolysis (FSP). (C) Fraction of a Al_2O_3 pellet with shell impregnated Pd−Pb of a 1:1 ratio and 2 wt.% loading.

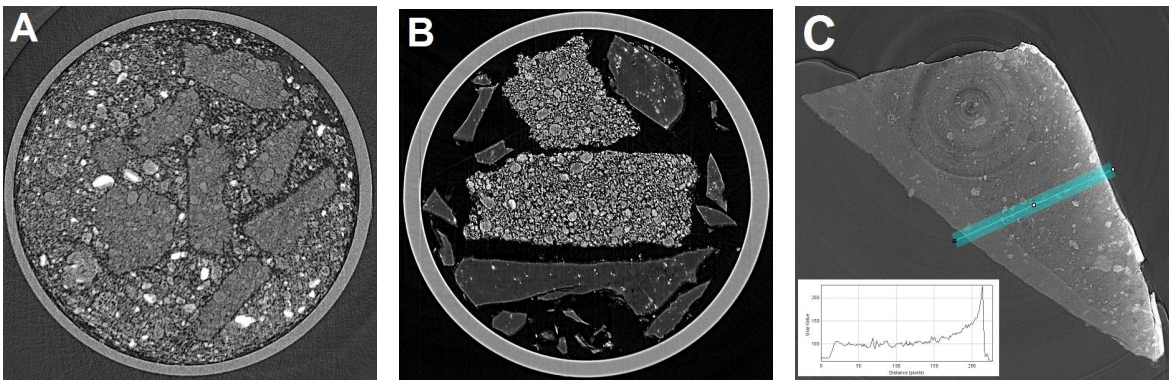

Figure 3.17.: Tomographic reconstruction of tests samples. (A) Pt/Al_2O_3 in different concentrations, (B) Pt on different supports, Al_2O_3 and SiO_2, prepared by IWI and FSP respectively, and (C) fraction of a shell impregnated $Pd-Pb/Al_2O_3$ pellet.

In the mixture of two Pt/Al_2O_3 catalyst samples in fig. 3.17(A) the two components are easily distinguished: One is concentrated in bigger lumps, the other is a fine grained, loose powder. More important is the better homogeneity of the Pt washcoat lumps in contrast to the manually mixed pre-cursor powder that shows several hot spots with very high Pt concentration. Thus it is possible to detect morphology changes and differences in Pt concentration as expected.

In fig. 3.17(B), the two supports, Al_2O_3 and SiO_2 are easily distinguished by their appearance, where SiO_2 appears smoother than Al_2O_3. Furthermore, the effect of different preparation routes was observed. While IWI produces homogeneous Pt loadings across the sample, FSP results suggest local high Pt concentration as indicated by the bright spots.

The shell impregnated pellet in fig. 3.17(C) shows a highly absorbing Pd−Pb layer on the surface and a concentration gradient into the pellet due to diffusion of the Pd−Pb solution into the pellet during impregnation. The gradient is clearly visible in a line-scan through the sample shown nearby in the 2D plot in fig. 3.17(C). Thus, tomography is able to detect metal diffusion into the bulk material and resulting gradients.

These first tests on realistic model samples successfully showed that different local Pt concentrations and concentration gradients can be resolved as well as diverse types of support material and preparation routes can be distinguished. Therefore, we can proceed to apply the method to detect changes in a sample caused by different pre-treatments.

Parameters for Honeycomb Imaging

As in every microscopy we have to compromise between the desired level of detail, hence resolution, to be resolved and the amount of sample imaged, the field of view. For full field tomography, this means that a high magnification is only obtained with a suitable X-ray energy and at cost of sample size as the complete volume has to be illuminated in the experiment. Furthermore, a capable sample preparation and mounting technique is required.

A series of coated honeycombs of different size were studied in fig. 3.18. The first two samples (A,B), imaged in a laboratory tomography setup by J. Reinhardt, were (A) a cylindrical sample with 21 mm diameter and (B) a cut down 4×4 channel structure. Another even smaller (C) fragment of a channel, imaged at a synchrotron μ-CT (P06) and was glued in a capillary.

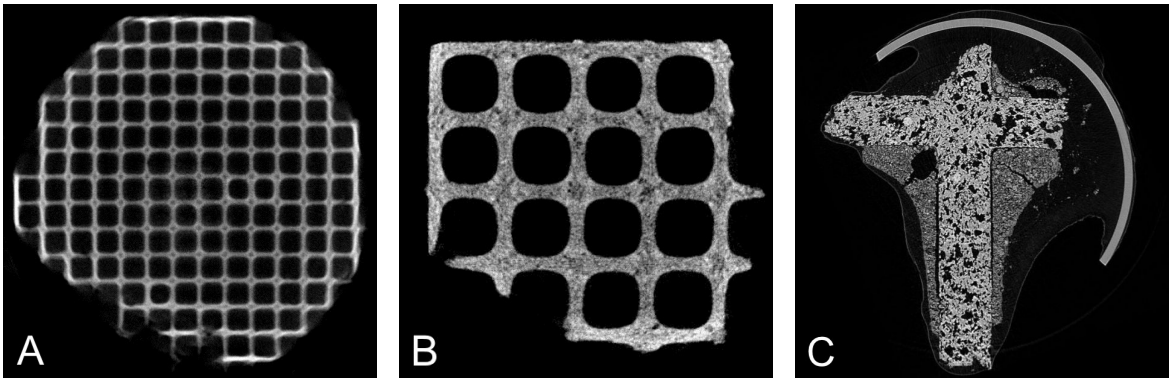

Figure 3.18.: Tomography scans of honeycombs showing increasing level of detail as sample size decreases. Scans A and B from a lab CT, C from a synchrotron CT. Wall thickness about 150 µm.

The large cylindrical sample, shown in fig. 3.18(A), can be imaged at full size in the lab CT. However, the large size required the use of low magnification and under these conditions the coating inside the channels was not visible.

In fig. 3.18(B) the 4×4 channel sample was imaged at higher magnification. Voids in the wall material became visible and the typical round shape of the channels after coating was observed. Nevertheless, the coating itself can still not be seen directly. This level of magnification would allow some coarse estimation of coating homogeneity and distribution, although the density contrast was very poor, and thus wall and coating can hardly be distinguished.

For fig. 3.18(C) a synchrotron tomography beamline was used to image the small sample at highest possible magnification (10×) resulting in 1.27 µm/voxel. This allowed to study details of the washcoat (voids, grains, cracks etc.) and the wall material. Another crucial point was only observable at high magnification: A significant gap between the wall and the washcoat exists in the lower region of the sample, as well as other detached washcoat fractions. Thus the question of sample modification due to preparation and mounting arises. It is not clear whether the gap was present in the original sample or was caused by expansion from glue that had migrated in between.

Since the sample was prepared by fracturing, it is very likely that some coating was damaged or removed. However, preparation and mounting should preserve the sample unaltered. Unintended modifications are best avoided by keeping the channel of interest intact, ensuring that the channel interior is physically protected by the cordierite wall. Therefore, for all following experiments a single channel was used as smallest sample size.

Single Honeycomb Tests: Contrast and Preparation Check

Knowing some relevant experimental parameters, a first test series of single honeycomb channels was studied at a synchrotron μ-CT (Beamline P05, PETRA III, DESY Hamburg). These yielded information whether the single channel approach provides sufficient magnification and sample preservation. Another aspect is the ability to distinguish between cordierite wall material and various types of washcoats, as their absorption may result in similar gray values rendering a subsequent analyses more challenging.

Three honeycomb cylinders, from a 400 channel per square inch (cpsi) monolith, were coated with: (A) Pt/Al_2O_3, (B) pure Al_2O_3, and (C) Pt/Al_2O_3 on top of pure Al_2O_3. A single channel of each sample was extracted and investigated by synchrotron CT.

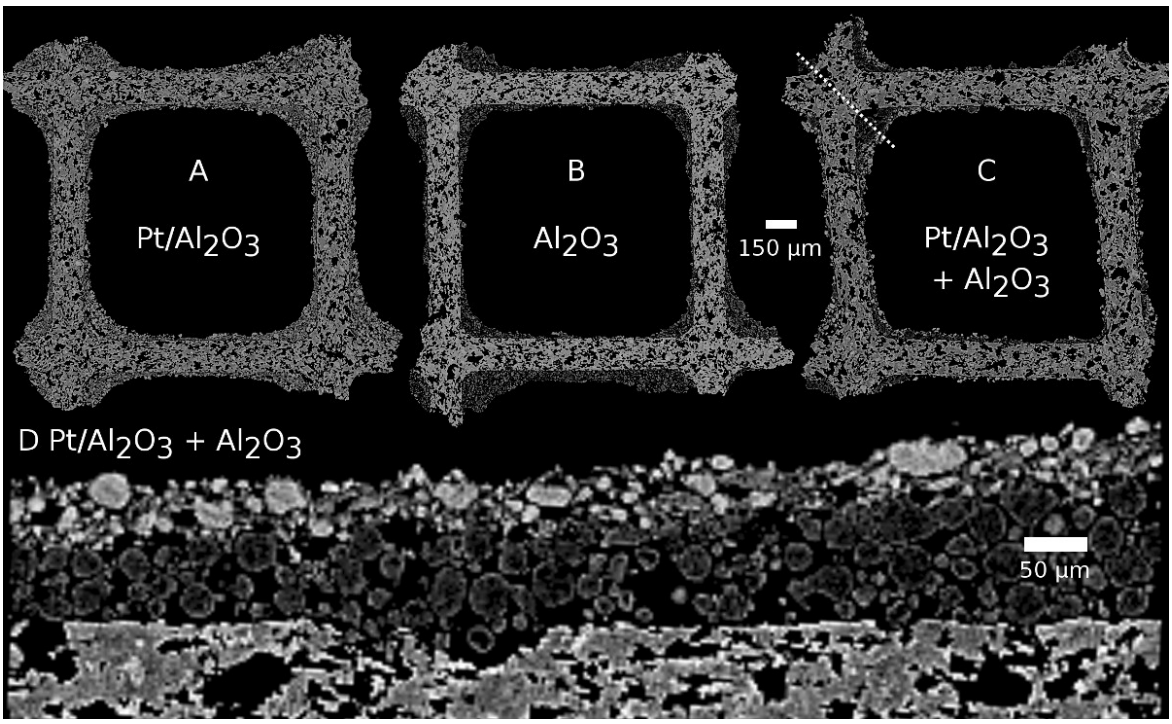

Figure 3.19.: Tomography slices of differently coated honeycombs. A: Pt/Al_2O_3, B: pure Al_2O_3, and C: double layer coating of Pt/Al_2O_3 on top of pure Al_2O_3. D: xz-slice of sample C along the dotted line. One channel has a inner diameter of $1.27\,\mathrm{mm}$

In the upper row of fig. 3.19(A-C) the three different coatings on cordierite honeycombs are shown. While the cordierite shows similar brightness in each sample, considerable brightness differences between the different types of washcoat occur. Comparing fig. 3.19(A) with Pt/Al_2O_3 and fig. 3.19(B) with pure Al_2O_3 washcoat reveals the strong difference in absorption caused by adding 4 wt.% Pt to the washcoat. This underlines the sensitivity of the method to precious metal distribution. However, it becomes more difficult to visually separate between cordierite and coating in (A) as compared to (B), since gray values are quite similar.

The double layer coating, shown in fig. 3.19(C), was clearly resolved. Due to the physical separation of the Pt/Al_2O_3 layer by the intermediate pure Al_2O_3 layer from the cordierite wall the visual separation becomes much easier. Note that the layer was not as thick and homogeneous as expected like indicated in fig. 3.18. Nevertheless, the typical coating distribution with an enrichment of material in the channel corners can be seen in detail and followed in all three dimensions. An example is given in fig. 3.19(D), where a virtual cut along the channel axis through a corner is shown. The thickness of the upper Pt/Al_2O_3 layer remains constant, while an increase from left to right was found for the lower Al_2O_3 layer. In this way the quality of the washcoat preparation can be checked.

Conclusion

The magnification used in the synchrotron μ-CT experiment, allowed to resolve the morphology of the cordierite wall with a lot of features (grains, voids etc.), which will become important for quasi *in situ* experiments later on. In the washcoat individual support grains with internal structure are resolved and well separated. At the same time, enough sample volume was investigated to obtain representative results.

A suitable compromise between field of view and resolution together with a sample preserving preparation was found. Similar contrast between Pt/Al_2O_3 coating and cordierite may complicate later analysis but is a solvable problem, since the washcoat was deposited on the wall in a separate step. Therefore no physical mixing occurs. A large contrast difference between pure Al_2O_3 and the later used Pt-rich coating Pt/Al_2O_3 demonstrates the sensitivity of μ-CT with respect to Pt loading.

In general, these preliminary studies show that tomography can be used for characterization of coated honeycomb catalysts. Subsequent μ-CT preparation checks may be used to develop advanced preparation methods, which can achieve more uniform and reproducible coating results for optimized catalyst utilization.

3.6. ex situ Tomography on Pre-Treated Honeycombs

As a next step toward monitoring aging and treatment effects on honeycombs by CT, a series of pre-treated honeycombs was investigated. The main difference between the three individual honeycomb channels should be the degree of Pt sintering originating from the "aging" pre-treatment. This will show the feasibility of possible characterization and enable more elaborated experiments later on.

These experiments were conducted during a *friendly user beamtime* at the beamline P05 at Petra III (DESY, Hamburg), which allowed early access to an experiment during its set-up phase. Thus, not every part of the experiment was already working as desired and some additional efforts were needed to acquire and process the data.

Three honeycomb cylinders were drilled out from a larger monolith and coated with the model catalyst 4 wt.% $Pt/\gamma{-}Al_2O_3$. After drying and calcination of the three samples, the first sample, a *fresh* honeycomb cylinder was obtained. Further treatments of the two remaining cylinders were conducted using a laboratory reactor. First, a conditioning at 400 °C for 4 h in a 5 % H_2/N_2 gas stream was done. Hereafter, one *conditioned* cylinder was put aside and the remaining cylinder was *hydrothermally aged* at 950 °C for 10 h in a 10 vol.% H_2O/N_2 gas stream.

Finally, a single channel was extracted from each honeycomb cylinder for the μ-CT measurements by cutting it out as explained in section 3.3.3 on page 25.

3.6.1. Data Acquisition and Reconstruction

The X-ray beamline was set to 14 keV photon energy and no decoherer was used. To minimize phase effects, the sample was put 6 mm close to the front of the scintillator screen. The microscope optics was set to 10× magnification resulting in 1.27 µm effective pixel size. The sample was rotated over 180° and scanned in $n = 1500$ steps of 0.12° with an exposure time of 2 s per projection.

Beam position variations (explained below) required to record five projection images per angle ($5 \times 1501 = 7505$) and 20 flat fields every 50th step ($31 \times 20 = 620$) during the whole scan. This resulted in extended acquisition time of 12 h per scan and large amounts of almost redundant data. Additional efforts had to be taken to correlate projections and flat field images to find the best combination before any reconstruction could be performed. The process of matching flat fields and projections is addressed in the next section.

Problems and Solutions in Data Reconstruction

Due to slow drifts and fast oscillations of the X-ray beam, the illumination was not identical for subsequently acquired images. For example, this led to a situation where the upper part of the sample was illuminated in one image whereas in the next image illumination was strongest in the lower part. This essentially resulted in poor flat field corrections with varying quality in different parts of the image, which was the major source of reconstruction artifacts, *e.g.* rings, and consequently volume data of inferior quality.

At the time of these experiments, no reconstructions could be done at the beamline and no general solution for the described problems existed. A conventional reconstruction with averaged dark and flat fields did not work for this data set, mainly due to the varying illumination, as explained above. No proper flat field correction was possible and another approach was needed. Thus, the required matching routines had to be programmed within the analysis of these experiments.

For good reconstructions, a good combination of projection and flat field images has to be found. Such combination is characterized by a smooth and almost constant background in the flat field corrected image. To obtain this best combination, the standard deviation (StdDev) of image regions without samples (background only region) was calculated. The task was then, to find this minimum in each possible combination of all 7505 projection images with all 620 flat field images.

In a first simple attempt, using a single CPU threaded `Python` program, this would have taken several days to complete. Utilizing the GPU by `PyOpenCL` and more optimized routines in `Python`, this computation was completed in a couple of minutes and an optimized set of flat field corrected projections was obtained for reconstruction.

The corrected images are then reconstructed by standard filtered back projection using the `tomo` software written and maintained by the group of Prof. Christian Schroer (DESY, Hamburg). Unfortunately, the correction did not remove all differences caused by varying/shifting brightness per slice in the volume data set, which further complicated the analysis as well as direct displaying and rendering of the tomograms. Nevertheless, a few slices of the sample could be extracted after all.

3.6.2. Results

A tomographically reconstructed slice perpendicular to the longitudinal channel axis showing the complete $1.4 \times 1.4\,\mathrm{mm}^2$ channel is presented in fig. 3.20 for each sample. As guide to the eye, the cordierite wall material and the 4 wt.% $\mathrm{Pt}/\gamma{-}\mathrm{Al_2O_3}$ washcoat are shaded in green and red respectively. Inside all three single channels an intact washcoat layer was found. A very high porosity was observed for the cordierite, which was maintained in all treatment steps, since it has been annealed at very high temperatures during fabrication.

Across the three samples variations of the coating thickness and distribution within and among the channels are visible. Furthermore, the washcoat in these samples was separated into two layers, as shown in the magnified sample corners depicted in the lower row of fig. 3.20. The first layer, close to the wall, was quite smooth and compact, while the second, on top of the first, was less compact and consisted of larger grains with higher absorption and numerous voids.

This mainly originates from the dip-coating process during sample preparation and illustrates the limitation in obtaining a very homogeneous catalyst layer with the rather simple preparation method used here. It also effects the utilization of the catalyst material in the sample [102] and especially complicates comparison between samples.

Nevertheless, treatment effects were found by XRD, XAS, and TEM (*c.f.* fig. 3.21 on page 45) and seemingly show up here as well. In the fresh sample almost no extremely bright features are found, thus the distribution of Pt was quite homogeneous in the washcoat. After the conditioning treatment, the sample showed some brighter features

and also smaller support grains. Finally, in the hydrothermally aged sample even more bright grains of slightly larger size were observed.

As higher brightness corresponds to higher X-ray absorption, this could potentially be caused by sintering of the alumina support or, more likely, by formation of bigger Pt particles. However, since different channels are scanned, it is difficult to draw a clear conclusion on the origin of the mentioned features. Only if a large number of samples were investigated, sufficient statistics could be obtained but this approach is too time consuming for a practical investigation of such a complex system. Therefore, a study of a single channel with sequential treatments, as presented in the next section, is much more promising.

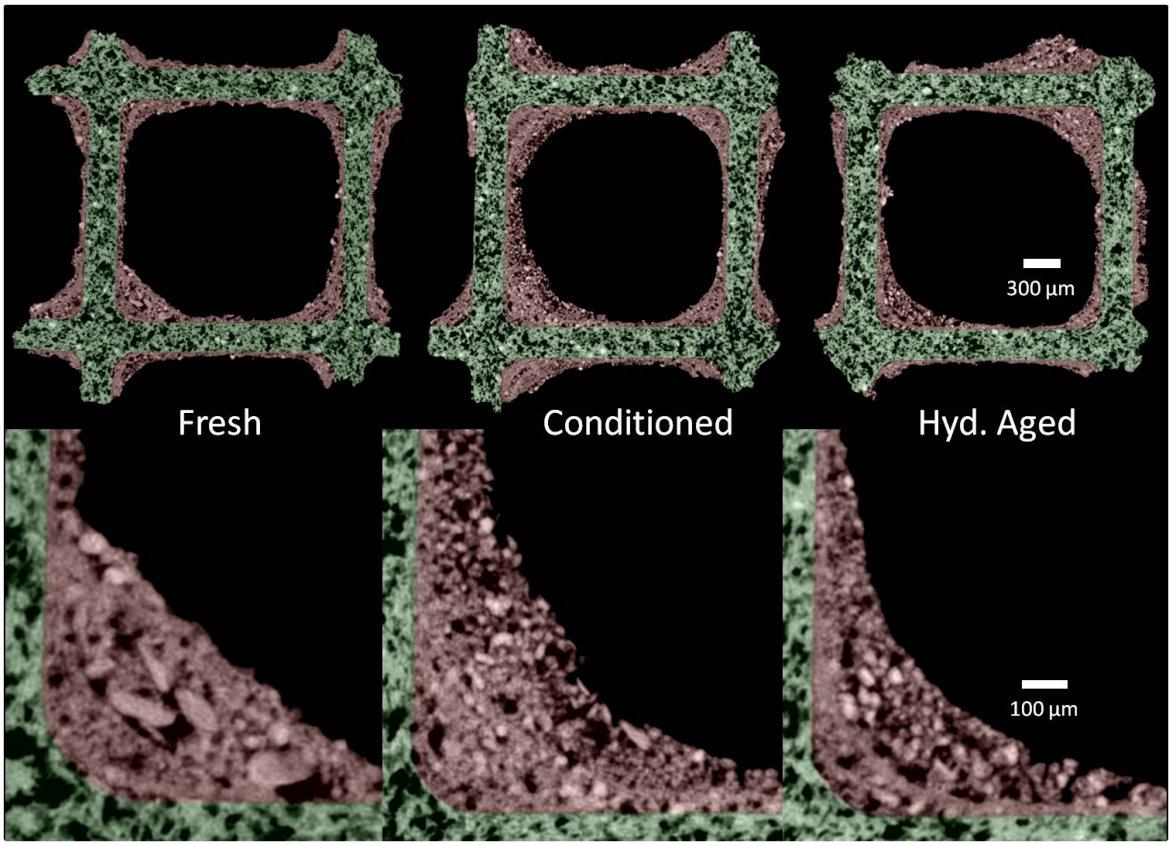

Figure 3.20.: Three different honeycomb channels in fresh, conditioned and hydrothermally aged state. Upper row: virtual cut perpendicular to the longitudinal channel axis Lower row: magnification of the lower left corner.

Complementary Characterization

The very first use of a freshly prepared sample typically involves a conditioning step where the honeycomb sample is treated with H_2. Aging is then performed in a separate step. To capture effects of both treatment steps on the sample, catalysts were prepared accordingly. Washcoat powders obtained from these samples were then studied by XRD, XAS, and TEM to cover early and short term aging effects as shown in fig. 3.21.

The three aging steps have been conducted in a laboratory reactor on three different samples and include: (i) fresh (after final calcination), (ii) conditioned: 4 h at 400 °C with 4 % H_2 in an N_2 gas stream, and (iii) hydrothermal aged: 10 h at 950 °C with additional 10 vol.% H_2O in an air gas stream.

As the washcoat powder samples have been obtained after treatment from the coated honeycomb samples by scraping with a scalpel, the amount of sample was limited and contaminants from cordierite were present, which complicated XRD analysis.

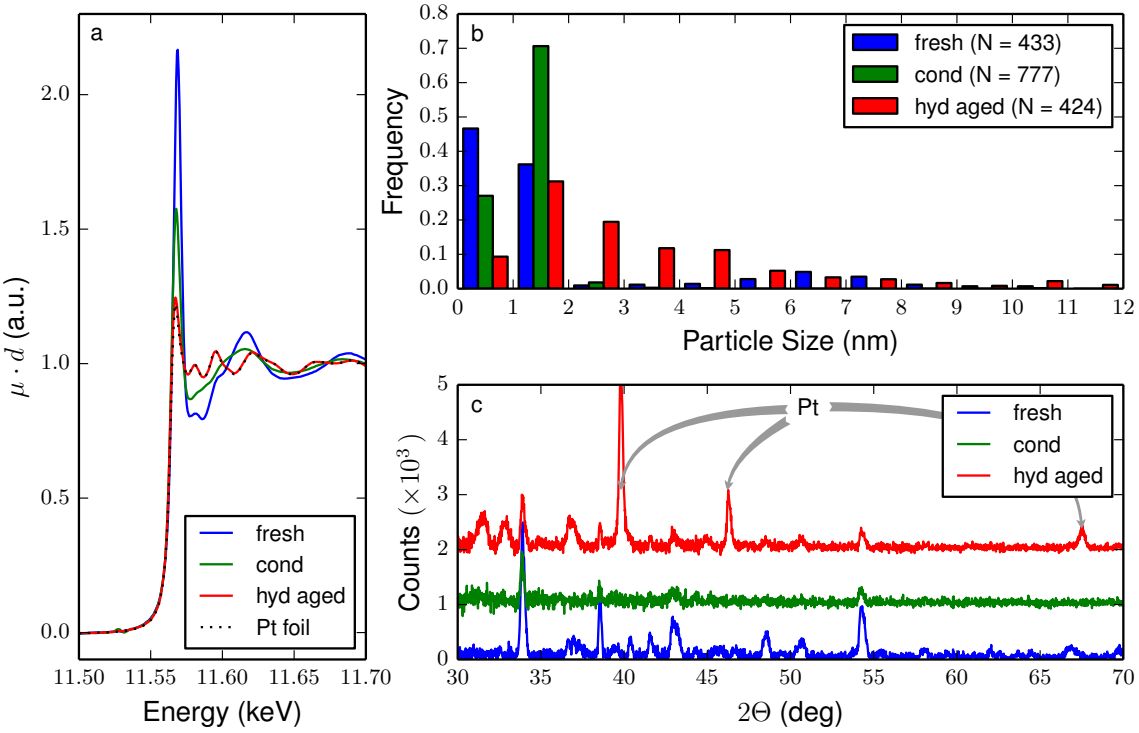

Figure 3.21.: Characterization results for the fresh, conditioned, and hydrothermally aged Pt/Al_2O_3 washcoat samples. **(a)** XANES spectra showing the Pt L_3 edge of the samples and Pt foil as reference. **(b)** Resulting particle size distribution from TEM by analyzing a total number of N Pt particles. **(c)** Corresponding X-ray diffractograms.

The X-ray absorption spectra of the Pt L_3 edge are shown in fig. 3.21(a). A pronounced white line feature revealed the presence of platinum oxide in the fresh sample. A partial reduction was observed for the conditioned sample, evident by the decreasing white line intensity and modified profile. Here a re-oxidation, may have taken place since some time lay between the H_2 treatment and XAS investigation on the beamline. Just after the first hydrothermal aging, the formation of metallic Pt was observed, which is indicated by superimposable spectra from the sample and the Pt foil reference spectra.

Transmission electron microscopy data uncovered the presence of very small particles in the fresh catalyst fig. 3.21(b). Around 80 % of the observed particles are around 1.5 nm in size. The conditioning treatment helped to narrow the particle size distribution and yielded particle sizes of mainly 2 nm. Most significant changes are observed after hydrothermal aging. Only 40 % of the Pt particles remain below 2 nm

in size. Much larger particles ranging from 12 to 350 nm were found accounting for 7 % of the total number of particles (not shown). This finding is in line with results obtained from XAS on the presence of metallic Pt and proves sintering of Pt nanoparticles.

Investigations using X-ray diffraction, shown in fig. 3.21(c), revealed the presence of more (fresh) or less (cond.) cordierite due to the above mentioned sample preparation in addition to peaks corresponding to the Al_2O_3 support. A detailed peak labeling is provided in a later experiment in section 3.9.8 on page 73. Notably, no reflections from metallic Pt are detected in the first two diffractograms due to the high dispersion of Pt as evident by TEM. Solely in the hydrothermally aged sample the characteristic reflections of metallic platinum are visible. This is in agreement with data obtained from XAS and in line with results obtained from TEM, *i.e.* the formation of large and metallic Pt particles through hydrothermal aging.

3.6.3. Conclusion

Single honeycomb channels have been successfully prepared from fresh and laboratory reactor aged honeycomb cylinders without altering the internal washcoat, leaving them intact for *ex situ* X-ray absorption tomography investigations with higher resolution. Complementary characterization by XAS, XRD, and TEM confirmed the occurrence of a sintering process during aging at high temperature on the nanoscale.

The cordierite walls showed no sign of changes under the applied treatment conditions whereas hints for Pt sintering in the washcoat layer were found, suggested by locally increased absorption values in the washcoat region for the treated samples. However, a direct proof of sample changes could not be provided since the original state, *i.e.* before aging, was not known and thus potential changes to the washcoat remain undetected.

Moreover, large variations in the amount and the distribution of the washcoat in the channels were observed, attributable to the sample preparation although they originated from the same batch. This especially complicated comparison between the different samples and additionally limits the explanatory power with respect to the impact of treatment effects.

In order to discover treatment effects, a more elaborated approach is required, since it is crucial to know the initial and the final state of the sample. Tomography in particular has the potential to spatially resolve these changes in an entire 3D volume data set, given the same sample is studied repeatedly, *i.e.* quasi *in situ*. This also avoids problems due to variations in sample morphology. Nonetheless, a sample representative of the whole honeycomb must be selected for this study.

3.7. Quasi in situ Tomography of Honeycomb Aging

In the previous experiment in section 3.6 indications for changes were observed, but an assignment of treatment effects was not possible due to strong sample-to-sample variations and thus arising ambiguities. However, due to results from complimentary analyses it is clear that the catalyst is changing under thermal aging. To study changes on a larger, a micrometer scale, the complete washcoat should be included into analysis. Therefore, the quasi *in situ* approach is utilized, which was described in detail in section 3.3. Practical examples and a first proof of principle are shown in section 3.8 on page 47 and the quantitative analysis of isothermal aging in section 3.9 on page 54.

All quasi *in situ* measurements presented here were conducted at *P05 – The Imaging Beamline* [103–105] operated by the Helmholtz-Zentrum Geesthacht (HZG) at the synchrotron radiation source PETRA III (Deutsches Elektronen-Synchrotron, DESY, Hamburg).

3.8. Quasi in situ Tomography: Proof of Principle

In this section, the first quasi *in situ* tomography experiments are presented using aging steps with increasing temperature and constant duration. This provides a proof of principle and allows to test problem specific analysis approaches of the differences induced by the treatment. Additionally, the various temperature steps, will indicate at which temperature sample changes can be detected.

In total, three single honeycomb channels were studied. Two of them carried a washcoat of 4 wt.% Pt/$\gamma-Al_2O_3$ and one had a coating of pure $\gamma-Al_2O_3$ as reference material. The channels were investigated in the fresh state and after treatment steps of 4 hours at 400, 600, 750, and 950 °C using the *ex situ* furnace as described in section 3.3 on page 24. A list of measurements and samples is gathered in table 3.2.

Table 3.2.: Overview of conducted measurements and used samples to prove the feasibility of the quasi *in situ* tomography approach.

Sample Name	Treatment		Ch1	Ch2	Ch3
	Time (h)	Temp. (°C)	Pt/Al_2O_3	Pt/Al_2O_3	Al_2O_3
fresh	—	—	✓	✓	✓
cond.	4	400	—	✓	—
aged 600	4	600	✓	✓	✓
aged 750	4	750	✓	✓	✓
aged 950	4	950	✓	✓	✓

The samples were scanned at 16 keV photon energy in 900 angular steps of 0.2° over a 180° rotation. A short distance of 3 to 5 mm from the scintillator screen was chosen and a decoherer was used to minimize coherence effects. Projection images were taken with an exposure time of 700 ms with a 10× optical magnification leading to an

effective pixel size of 1.27 µm. In total, a scan time of about 4 hours per sample was required.

Beam stability was a problem in former experiments (*cf.* section 3.6.1), but was controlled directly during acquisition in these experiments. After every 20th rotation step, along the 180° turn, 3 to 15 reference images were taken to ensure a proper beam position. When deviations from the optimal position became to large, an automatic realignment of the beam was performed. Beam position variations were treated by a correlation of sample and reference images, to match the illumination on the leftmost 100 image columns. As result the best suitable combinations for the image correction were found before invocation of the actual reconstruction. This approach is similar to the one described in section 3.6.1, except that the standard deviation of a region in the corrected image was used as optimization parameter.

Utilizing the filtered back projection with an image binning of two for the tomographic reconstruction, an effective voxel size of 2.54 µm was obtained. The reconstructions were done on a beamline computer cluster with software maintained by the P05 beamline staff.

Alignment of the subsequently acquired tomographic data was successfully conducted, as described in section 3.3.4 on page 27.

3.8.1. Evaluation

For the analysis of differences two approaches were used: (a) manual visual inspection and (b) computational aided analysis to find sample changes between two different treatment steps. The following software was used for analysis: Fiji [106] as image viewer and for quick analysis; Avizo Fire 8.1 [98] for analysis, registration, rendering of 3D data; and Python (Enthought Canopy Distribution [107]) for working with data from Avizo.

By using the direct (manual) visual inspection of virtual 2D slices, no changes could be attributed as there was no striking feature difference present in the data. This was improved by using volume renderings and slices with two different colors as overlay. In these representation, the formation of cracks and even sometimes the swapping of locations of grains on the surface became visible.

Due to the difficulties in finding changes by manual comparison, all results following were gathered by computer aided analysis as described below.

Direct Histogram Analysis for Detection of Sintering

A fast and straightforward way to detect sintering is the analysis of the full reconstructed volume histogram (without any further preparation), as plotted in fig. 3.22. With strong sintering, highly absorbing voxels should appear in the histogram. According to the plot this was not the case here. However, the histogram cannot detect changes due to displacements or surface migration of a grain. Additionally, the redistribution of material from voxel A to B is just a tiny effect in a myriad of voxels, thereby not visible in the histogram in cases of little sintering.

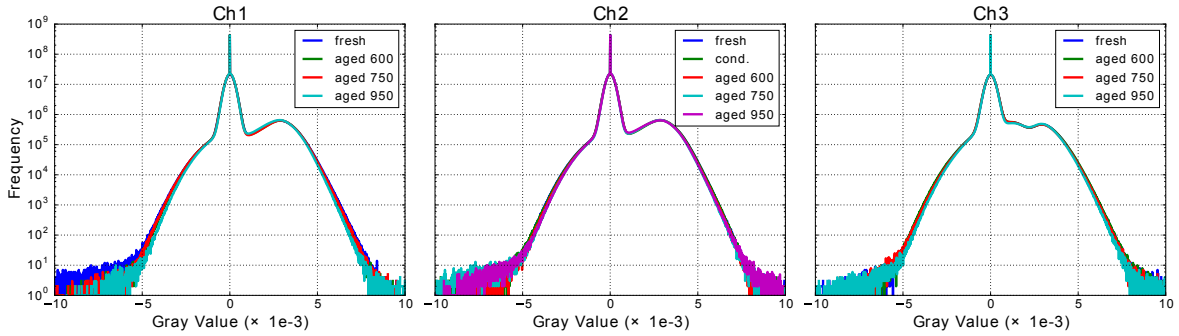

Figure 3.22.: Histograms of the full reconstructed volume for each sample and treatment step show no indication for pronounced sintering effects.

Difference Analysis Method for Sample Changes

Since manual visual inspection revealed small changes between subsequently treated samples, the difference between the subsequent steps was calculated and stored in a separate volume data set. This data set was then overlay to the original data, thereby enhancing visibility of differences caused by sample aging. However, any other difference will also show up, *e.g.* lost coating on the outer part of the channel. Thus a very careful sample handling during heat treatments was required, as well as perfectly aligned high quality volume data sets in order to obtain reasonable difference data. Details were already addressed in section 3.3.6 on page 29.

Although the difference information was available for the entire volume, the view was restricted to the washcoat on a single honeycomb wall inside the channel for the sake of visualization. This was achieved by selecting a region of interest and applying a virtual clipping to the data as shown in fig. 3.23. The resulting field of view on the channel wall in figs. 3.24 and 3.25 is $1.4 \times 1.1\,\mathrm{mm}$.

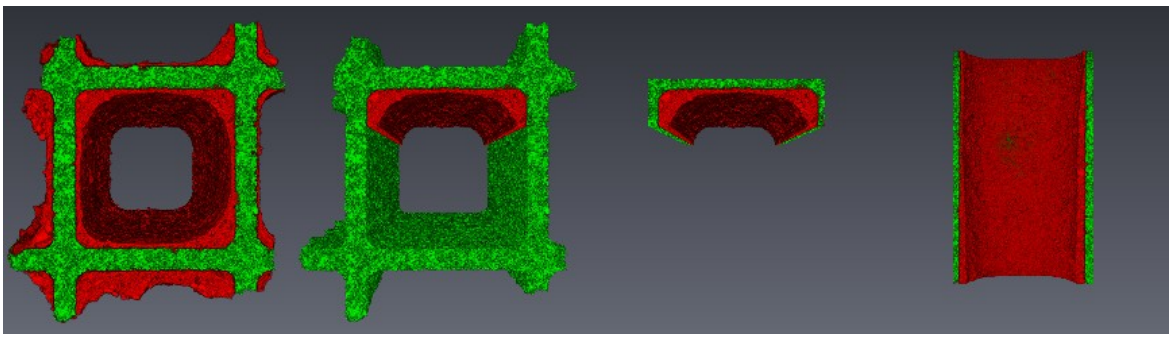

Figure 3.23.: Volume rendering of a coated honeycomb showing the selection of a region of interest: the washcoat layer inside the channel. Colors: washcoat (red), cordierite (green).

Results

To trace changes between fresh and aged samples, they are shown as two overlaid volume renderings. Additionally, the differences between them are shown as $(A - B)^2$ to obtain positive numbers and to further suppress tiny differences caused by noise.

3.8.2. Evidence for Blob Formation

The platinum loaded sample, Pt/Al_2O_3, is shown in fig. 3.24(a-c). It features a closed and intact washcoat surface in the central plane; only along the right corner an elongated crack was found. This is indicating a non-reversible movement of the washcoat in the corner after aging, while no such effects were found in the central plane, as evident from fig. 3.24(b).

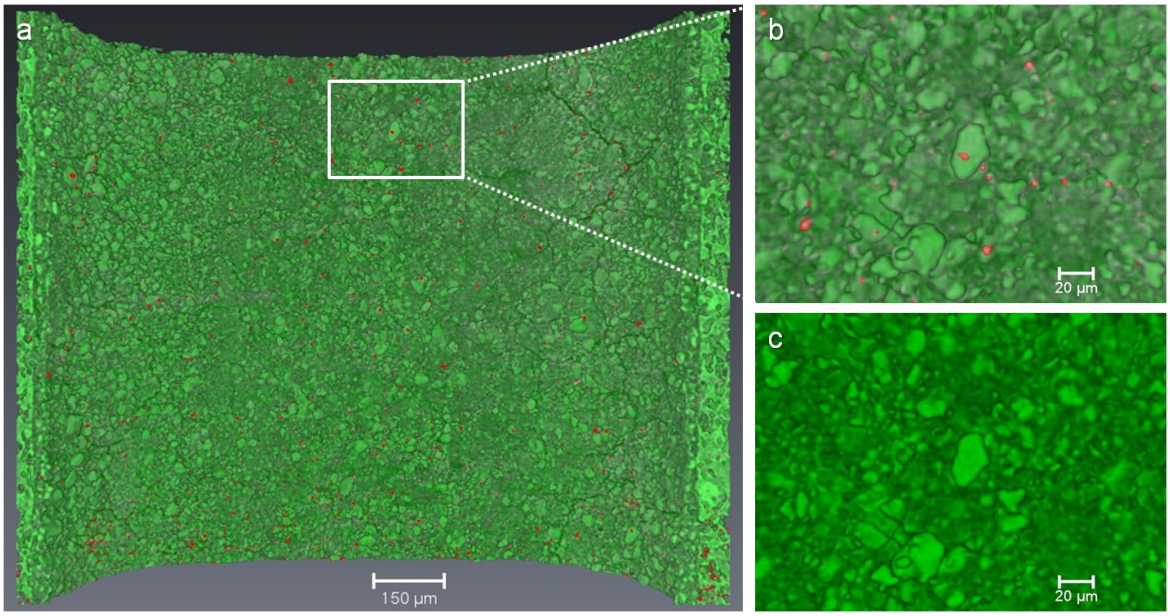

Figure 3.24.: Direct overlay of initial (fresh, green) and final (aging at 950 °C, white) state for the Pt containing sample, where large differences are colored in red. (a) View on the wall from inside the channel. (b) Zoom to a region with blob formation (red) after treatment, while the position of the micrometer sized grains remains unchanged. (c) For comparison the same area as in (b) just showing the fresh sample.

Numerous pronounced differences (marked in red) show up due to the formation of larger Pt-rich blobs. The formation of a blob on top of a larger support grain, shown in fig. 3.24(b), was clearly not related to crack formation or material displacement which is of capital importance. Hence, blobs in these regions are attributed to a significantly higher amount of Pt as consequence of the aging treatment. They were reliably detected in the whole central plane by the difference in absorption between the fresh and the aged sample. However, blobs were also found close to cracks where both, material displacement and Pt sintering might have taken place in parallel. Thus no clear assignment is possible.

The distribution of blobs was found to be mostly homogeneous across the sample, while some locally preferred regions may originate from local variations of the initial Pt distribution within the washcoat.

3.8.3. Evidence for Crack Formation

For the pure $\gamma-Al_2O_3$ washcoat reference sample, shown in fig. 3.25(a-c), a very pronounced formation of cracks and changes in the coating morphology along the entire channel was observed. This material displacement is clearly a result of the aging treatments, since the initial (fresh) washcoat was smooth and compact as depicted in fig. 3.25(c).

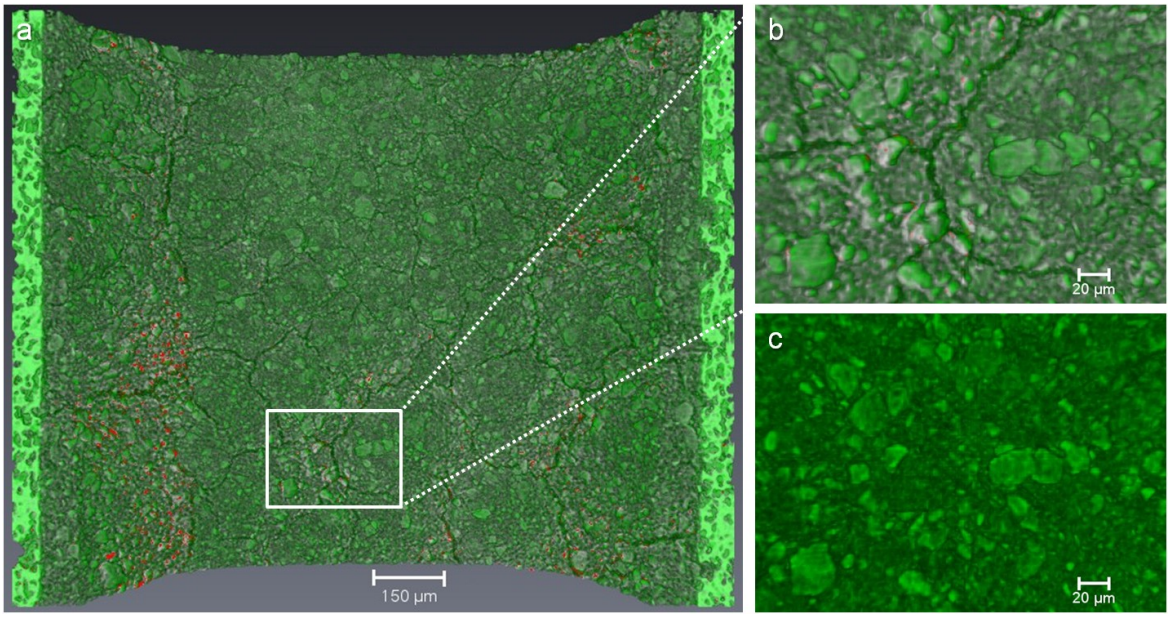

Figure 3.25.: Direct overlay of initial (fresh, green) and final (aging at 950 °C, white) state for the pure $\gamma-Al_2O_3$ coated sample, where large differences are colored in red. (a) View on the wall from inside the channel. (b) Zoom to a region with formation of cracks. The extent and direction of material displacement due to the formation of the cracks can be followed by grains partially rendered in green (initial) and white (final) indicating the movement. (c) The same area as in (b) for the fresh sample without any crack for comparison.

Most of the differences (marked in red) between the fresh and aged sample are located in the vicinity of the cracks. They are originating from the displacement of support material, occupying previously empty space and/or leaving voids consequently. This results in a significant magnitude of the calculated difference.

Notably, no formation of distinct red blobs was observed in the central plane area, as was seen in the Pt loaded sample. Hence, this supports the conclusion that blobs are a result of Pt sintering, which is ruled out in this Pt free reference sample.

From fig. 3.25(b), the amount and direction of material displacement can be derived. In the given view on the sample, the crack width is approximately 5 µm. As evident from the rendering of the support grains next to the crack, they moved around the same distance away. The direction of the movement is indicated by the white rendering relating to the final state. It is worthy to note, that the displacement was not equal on both sides of the crack and rapidly decays with increasing distance to it. A more detailed analysis is possible considering the full 3D data, which can yield 3D displacement vectors [108].

3.8.4. Feature Development as a Function of Temperature/Time

The quasi *in situ* approach enables to trace sample changes, *i.e.* the formation of cracks and blobs, over several treatment steps, as shown in fig. 3.26.

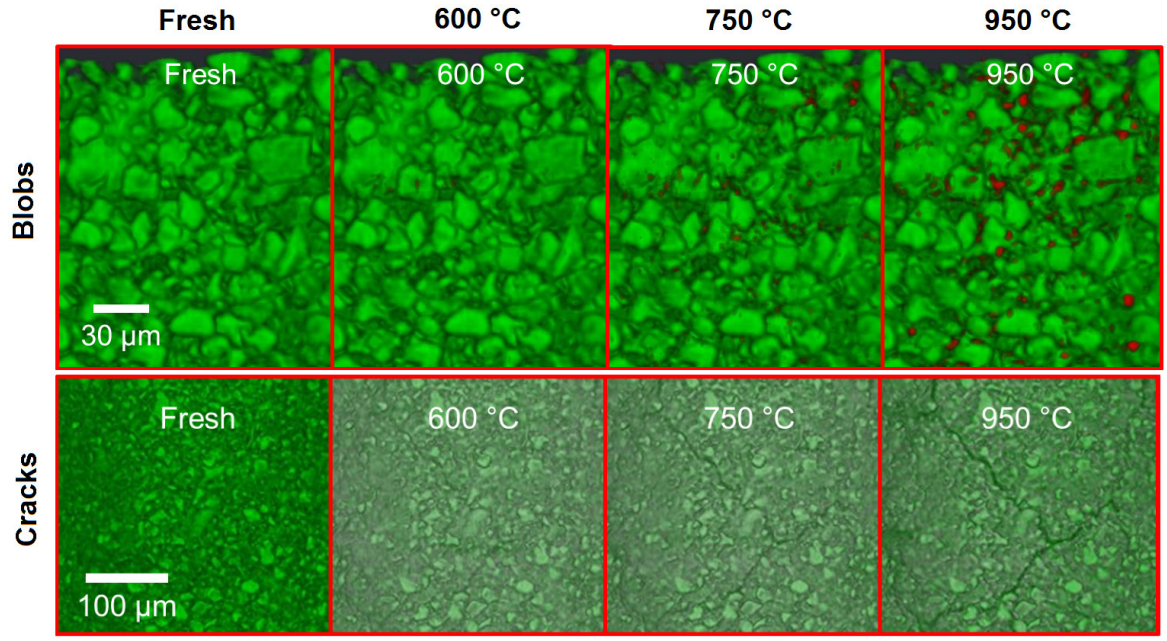

Figure 3.26.: Aging effects as function of treatment step. Top: Blob formation, showing differences in red (sintered Pt regions) on top of the fresh sample (green). Bottom: Crack formation, showing the volume renderings of fresh (green) and aged (white) sample.

Already at 600 °C the first very few indications for blobs are found in the central left area. Pt-enriched blobs are easily detected at 750 °C and the highest number was present after the treatment at 950 °C. Within the last aging step most blobs grew but a few also disappeared. They may have joined other, larger blobs or are below the detection limit of the difference method. However, the formation of new, large blobs in the last aging step is evident. This highlights the very strong impact of the high temperature aging, favoring sintering.

A careful look at the fresh sample already reveals a first tiny crack in the lower central part. It becomes more clear in the 600 °C image, due to the additional overlay, and might have slightly widened. This widening was even more pronounced with increasing temperature, as well as crack propagation and formation of new branches. Again, most distinct effects are obtained for aging at 950 °C.

The difference method worked as desired as can be concluded from the fact that the detected blobs grew after each treatment step in accordance to the results from complementary analyses. Physically meaningful sample differences were detected and the noise level was sufficiently small.

3.8.5. Conclusion

The subsequent aging treatments and measurements of single honeycomb channels have demonstrated a working quasi *in situ* tomography approach. This comprises of successful sample handling and treatment without any artificial physical modification of the channel interior as well as optimal sample registration, *i.e.* the digital alignment of subsequent tomography scans. The latter was greatly supported by the temperature stable and invariant cordierite channel walls serving as guidance. This allowed performing a voxel-by-voxel analysis, using manual inspection and computation of differences between two treatment states of the same sample.

By using the difference method, the formation of blobs and cracks as a result of the applied aging treatment were revealed. Numerous homogeneously distributed blobs, highly absorbing Pt-rich regions, were found in the Pt/Al_2O_3 sample, apart from some few cracks. The blobs were attributed to sintered Pt as no blobs of this type were observed in the pure Al_2O_3 reference sample. Cracks were visualized using volume renderings. They often caused additional differences in the direct surrounding. The close proximity of cracks has therefore to be excluded in the investigation of Pt sintering.

Moreover, the aging impact on the sample was traced over all treatment steps and confirmed systematic blob growth, attributable to enhanced sintering, as well as crack propagation and widening with increasing aging temperature. These results are in line with the sintering behavior uncovered earlier by complementary TEM and XRD results, shown in fig. 3.21 on page 45, probing the nanoscale. The observations made, using X-ray tomography, show that thermal deterioration can also be observed on the microscale, which have an impact on the catalyst efficiency.

These first results underline that the morphological and structural changes within the washcoat can be followed by X-ray absorption micro-computed tomography on the µm-scale. The potential of the technique and the paramount importance of the quasi *in situ* approach, *i.e.* monitoring the same sample repeatedly after treatments in order to draw reliable conclusions, is vividly demonstrated.

3.9. Quasi in situ Tomography: Quantitative Analysis

With a fully working quasi *in situ* approach, as shown in the last section, another series of honeycomb channels was studied under isothermal conditions at high temperatures of 750 and 950 °C for up to 34 hours using an *ex situ* oven. Tomographic reconstructions with high aging impact at 950 °C are analyzed to obtain quantitative information on the sample state and feature evolution. Complementary electron microscopy (EPMA) helped to clearly identify sintering in the washcoat volume.

In total five single honeycomb channels, prepared as described in section 3.3.2 on page 25, are studied using isothermal treatments at temperatures of 750 °C or 950 °C respectively. Besides the initial, fresh state, at zero hours, measurements are performed after 4, 8, 12, 24, and 34 hours of aging using the *ex situ* furnace as described in section 3.3 on page 24. Samples carried a washcoat of 4 wt.% Pt/$\gamma-Al_2O_3$, pure $\gamma-Al_2O_3$, and a double layer of 4 wt.% Pt/$\gamma-Al_2O_3$ on top of pure $\gamma-Al_2O_3$. A list of measurements and samples is gathered in table 3.3.

Table 3.3.: Overview of measurements and samples in the isothermal aging campaign.

Aging	950 °C			750 °C	
Duration (h)	Pt/Al_2O_3	Double Layer	Al_2O_3	Pt/Al_2O_3	Double Layer
0	✓	✓	✓	✓	✓
4	✓	✓	—	✓	✓
8	✓	✓	—	—	—
12	✓	✓	✓	—	—
24	✓	✓	—	✓	✓
34	—	—	—	✓	✓

The samples were scanned at 18 keV in $n = 1200$ steps of 0.15° over 180°. A single projection was taken using 400 ms exposure time, resulting in a total scan time of about 4 hours per aging step. Coherence effects are minimized by a close sample distance to the scintillator (300 µm $CdWO_4$) and the use of an decoherer. A CCD camera (SciCam SC09000M, EHD imaging) was used in combination with an optical microscope, which has been set to an optical magnification of 10×, yielding an effective pixel size of 1.27 µm. The large number of steps allowed a reconstruction of the tomograms without binning directly at the beamline, thus an effective voxel size of 1.27 µm was obtained. Realignment of tomographic volume data was performed as explained in section 3.3.4 on page 27.

3.9.1. Evaluation and Extraction of Sample Changes

Before a quantitative analysis of treatment effects can be tackled, potential sample changes have to be found and extracted from deviations in the histograms and in the corresponding 2D and 3D representations of the data. These differences will be correlated to electron microscopy to clarify the assignment to Pt sintering.

Evidence for Sample Changes in the Histograms

A quick and global check for sample changes was done using the volume histograms, as shown in fig. 3.27. Please note the logarithmic scaling of the frequency and recall general comments on the information contained in the histogram, as mentioned in the discussion of fig. 3.22 on page 49. For aging at 950 °C, upper row in fig. 3.27, distinct changes for the Pt loaded (Pt) and for the double layer (DL) sample are found in the histogram as a function of aging time. Whereas only little variation on the logarithmic scale for these samples at 750 °C was found, lower row in fig. 3.27. Completely unchanged histograms are observed for the reference Al_2O_3 (AL) sample, that was aged only at the highest temperature of 950 °C. This is indicating a stable support (in terms of absorption coefficient) and furthermore strongly suggesting the sintering of Platinum in the other two samples aged at 950 °C.

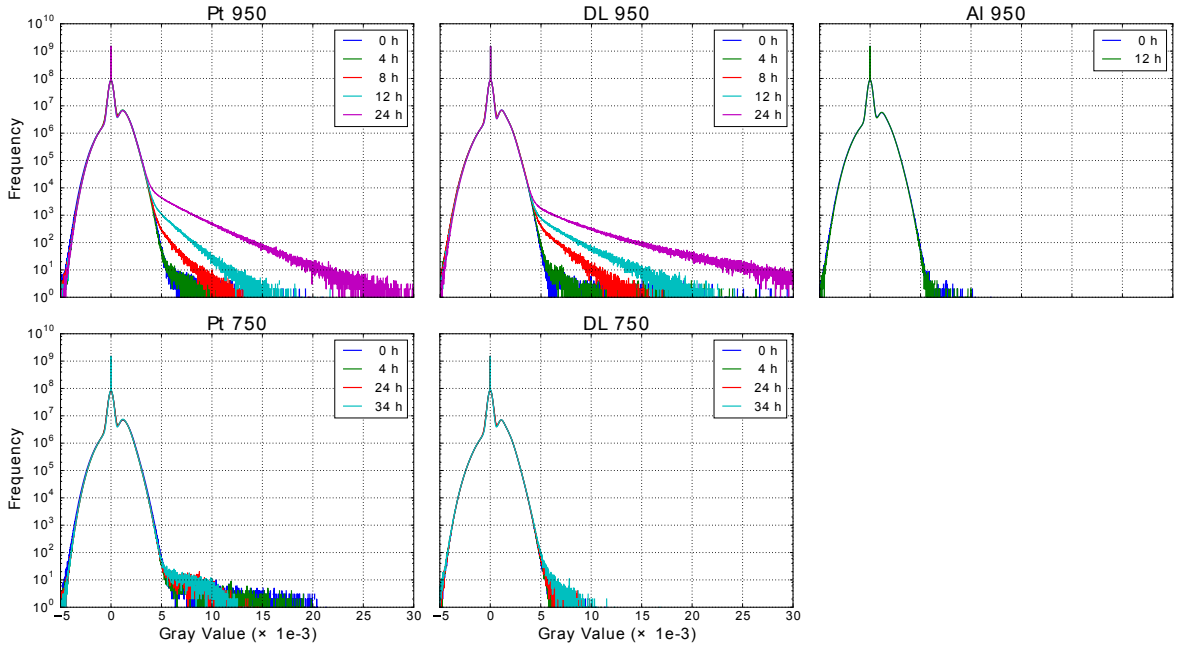

Figure 3.27.: Full histograms of all measured tomography samples for aging at 750 and 950 °C in the lower and upper row respectively. Distinct deviations from the fresh state are only observed for the double layer (DL) and the model Pt sample (Pt) at 950 °C, whereas the reference sample with a pure alumina coating (Al) remains unaffected.

Check for Changes at 750 °C Treatments

In fig. 3.27 virtually unchanged histograms are obtained for the aging at 750 °C, indicating a much weaker impact on the platinum in the washcoat. Nevertheless, changes occurred, and are found using the *difference method* as explained in the previous section. In fig. 3.28 the Pt sample is shown in fresh state and after 34 hours aging at 750 °C. The differences are colored in blue and red for regions which vanished and occurred, respectively.

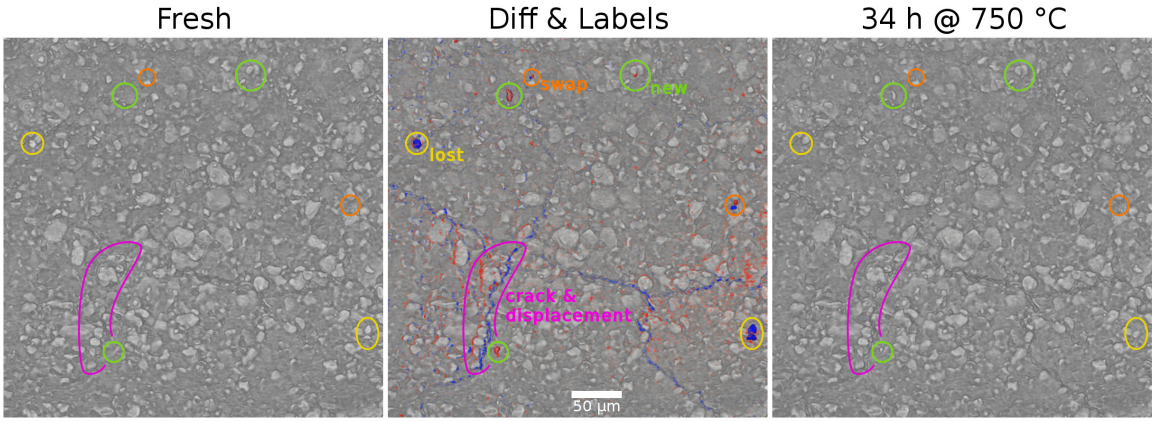

Figure 3.28.: Changes of the Pt sample at 750 °C. Differences after the treatment are observed for various reasons as indicated and color coded in blue for missing/lower and red for new/more absorption respectively.

In fig. 3.28 different sources of differences are highlighted. Besides formation of new blobs (green circles), likely due to sintering, support material was lost (yellow markings) for some reason. Most problematic are regions where support grains swap positions (orange), which must not be confused with the emergence of new particles. The formation of cracks and the resulting displacement (magenta) of support material also produces positive and negative difference signals. Again, as those differences are not due to sintered particles they have to be omitted from subsequent quantification.

For the desired quantitaive analysis, covering a large sample volume, this would require a manual verification and classification of every single difference feature. As this is impractical, the difference method is not suitable for quantitative analysis and was therefore not further pursued.

Visual Inspection and Verification of Sintering at 950 °C

According to the histograms in fig. 3.27, voxels with high gray values were present in the Pt samples aged at 950 °C. This locally increased absorption is confirmed by the image sequence in fig. 3.29. In the upper row the original xy slices of a fixed sample position are presented for each treatment step, while in the lower row the difference to the fresh state is depicted.

As evident from fig. 3.29, the formation of highly absorbing (bright) voxels was accompanied by cracks through the washcoat; opening of gaps and shifting of nearby material. However, the direct identification of sintered particles is possible by exploiting

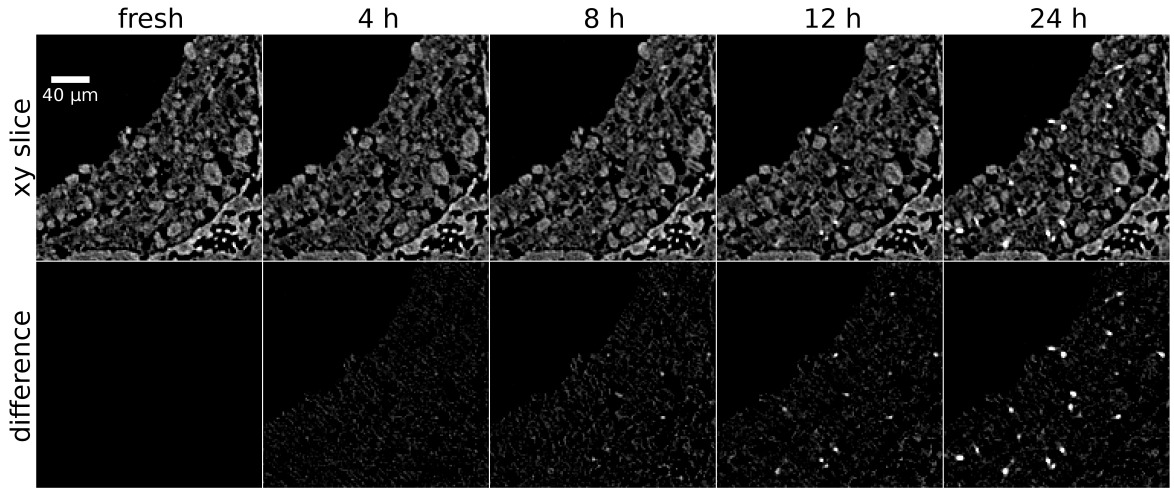

Figure 3.29.: Series of xy slices for the 950 °C aged Pt sample with differences to the fresh state in the lower row.

their absorption (gray value), independently from their current position. This is in contrast to the difference method, which is heavily affected by position changes, as already mentioned.

Before any further analysis was done, the assignment of blobs to sintered Pt was checked by EPMA. Based on the results of the EPMA measurement a comment on interpretation of voxel intensities is given.

3.9.2. Correlation of Tomography Data and EPMA Results

To ensure the correct correlation of blobs to sintered Pt in the 950 °C aging, an Electron Probe Micro Analyzer (EPMA) was employed on a mechanical cross section of the samples after finishing the μ-CT experiments. This approach worked quite well, and is known in the community as Tomography Assisted Chemical Correlation (TACCo) [109].

Scanning electron microscopy provides highly resolved images of the exterior sample surface, as shown previously, but naturally fails to image internal surfaces or sub-surface regions except with the application of further preparation, *e.g.* by FIB, polishing, or crushing. Hence, the prior aged tomography sample (24 h at 950 °C) was embedded and mechanical cross sectioned, *cf.* section 2.2.2 on page 10, to obtain a region, which was scanned by tomography before and investigated with respect to structure and Pt distribution. The EPMA result and the corresponding μ-CT slice are shown in fig. 3.30.

Imaging has been achieved using a high resolution EPMA, *cf.* section 2.2.2 on page 10, in combination with wavelength-dispersive X-ray spectroscopy (WDX) for mapping the chemical composition of the cross section. The complete honeycomb cross section, as shown in fig. 3.30(a), was imaged at 40× magnification (2.33 μm/px). At this scale, the porous cordierite structure and the distribution of washcoat in this cross section was visible. At the same resolution, using a close up of fig. 3.30(a) given in (c), pores and some bright features are observed in the washcoat.

A complementary slice of the same region (dashed box) taken from the beforehand

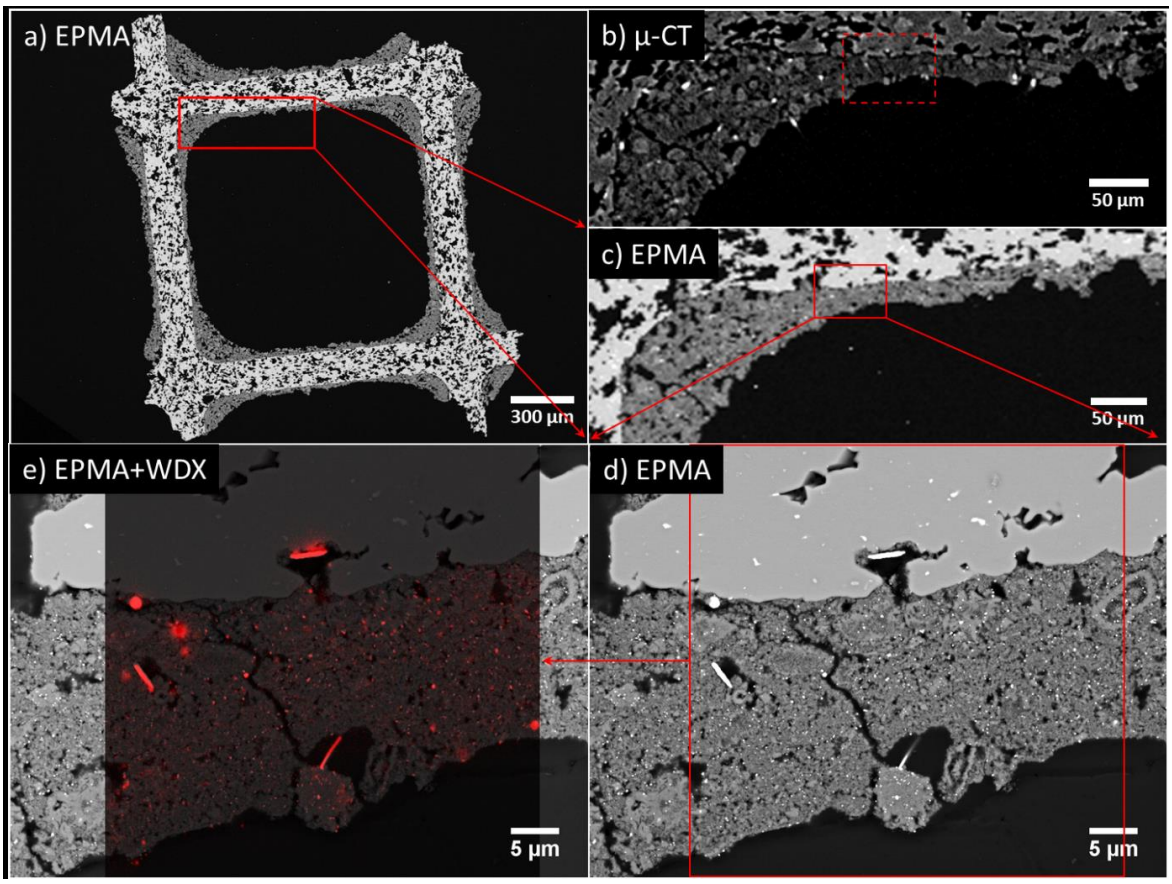

Figure 3.30.: Mechanical cross section of an embedded sample, aged 24 h at 950 °C in static air, imaged by EPMA and μ-CT. Back-scattered electron images of (a) the complete embedded honeycomb channel and (c) close up to the part containing the ROI box for the (d) high resolution EPMA with additional (e) WDX map of Pt overlaid. For comparison a (b) μ-CT slice of the same sample part before embedding is shown with a dashed box indicating the ROI measured in (d, e).

conducted μ-CT experiment, fig. 3.30(b), is presented to compare features and image contrast. Both images exhibit very similar image contrast and show the same characteristic sample features, *e.g.* the cordierite structure, voids, and most important: bright features within the washcoat layer. Notably, some grains with internal structure (bright rim, dark core) are found, indicating variation of Pt loading within these structures.

High resolution EPMA with 2000× magnification, resulting in a resolution of 47 nm/px, has been performed on the marked region in fig. 3.30(c) and corresponds to the dashed box in (b). The resulting image is shown in fig. 3.30(d). It provides a detailed view on the cordierite wall (upper image area with constant brightness) and the Pt/Al_2O_3 washcoat layer (lower image area) in the sample. The aged washcoat was discontinuous with cracks and numerous voids of different sizes and shapes, providing high porosity. Moreover, the washcoat grains were heterogeneous in size, compactness, and Pt distribution, which is convoluted in the pixel brightness and was partially disentangled later by using WDX.

Regarding Pt sintering, fig. 3.30(d) shows distinct micrometer-sized Pt single crystals within the washcoat volume. This is in direct agreement with previously taken SEM

images from the washcoat surface, shown in fig. 3.44 on page 75. In fact, fig. 3.30(d) provides even more insight, since it shows that Pt crystals are preferentially found in sample areas close to voids and cordierite pores providing sufficient space for growth. As shown before, a lot of small Pt particles are found distributed all over the washcoat in accordance to XRD results in section 3.9.8 on page 73.

The Pt loading and distribution was resolved in detail by the WDX mapping shown as overlay in fig. 3.30(e). Platinum was found to be confined to the washcoat layer, *i.e.* no Pt was detected in the bulk cordierite, which would potentially further deactivate the catalyst. Furthermore, Pt was identified as the origin of the bright tomography features visible in the washcoat by comparison of fig. 3.30(d) with the Pt mapping in fig. 3.30(e). Other bright features in the bulk cordierite visible in EPMA are clearly not related to presence of Pt.

In summary, the observed similar contrast and distribution of bright features both in μ-CT and EPMA confirm the assignment of those features to sintered Pt.

Interpretation of Voxel Intensities

As was just shown, large Pt single crystals in SEM/EPMA correspond to bright features in tomographic slices. It is tempting to assume that the latter are single crystals too, which is not necessarily true. Thus a note on the interpretation of voxel gray values is given to prevent misleading conclusions. The example in fig. 3.31 will clarify this issue with an SEM image (backscattering electron (BSE) image, 10k× mag.) showing several features marked by boxes on a grid that indicates size of the voxels in tomography of 1.27 µm. Based on the SEM image, a pixelated "low resolution" image was calculated simulating the tomography result with the given voxel size.

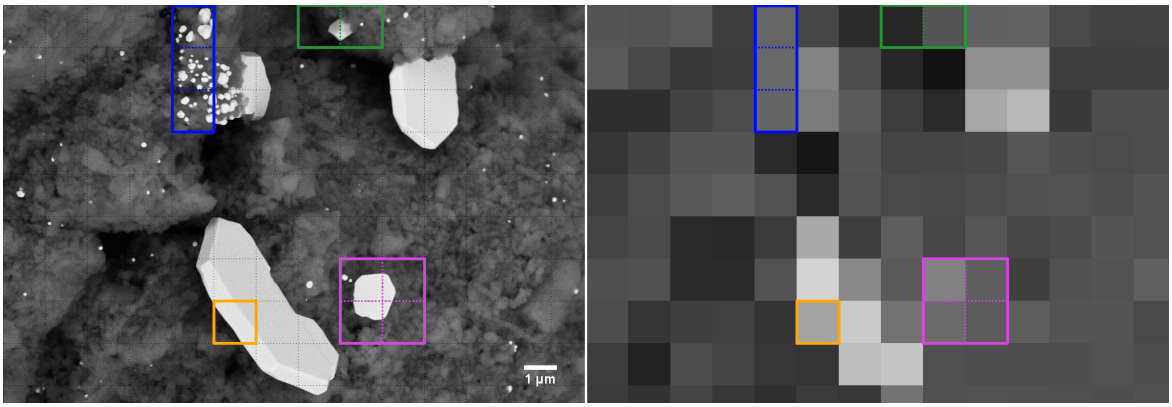

Figure 3.31.: Comparison of pixel and voxel sizes in SEM and μ-CT images relevant for data interpretation. (a) SEM image of a Pt/Al_2O_3 sample (aged 24 h at 950 °C) reveals various platinum crystals. (b) Simulation of the measurement outcome by box averaging of (a) with a pixel size of 1.27 µm, being the μ-CT voxel size.

As shown in the SEM image in fig. 3.31, Pt single crystals can fully, partially, or cumulatively contribute to the gray value as indicated by the colored boxes, which make up the total voxel absorption in fig. 3.31(right). Voxels with a different number of

Pt crystals inside but with a very similar total amount of Pt (blue box) have the same average absorption. Hence, we cannot distinguish whether one of them was composed of just one large single crystal or several small crystals. Volume averaging in combination with a very structured support, *e.g.* voids and inhomogeneous in Pt loading etc., may even cause µm sized crystals (green box) to disappear since the overall density within the voxel is close to that of the support. Similarly, a µm-sized crystal (magenta box) may become hard to distinguish from the support due to unfavorable sampling across several voxels. Even the large plate-like crystal in the lower left of the SEM image might not completely fill a single 3D voxel (orange box) due to its small thickness, which results in low absorption although the voxel is part of a huge crystal. Altogether this complicates the correlation of gray value to platinum loading.

In summary, tomography allows the observation of sintered Pt on a µm-resolved scale. However, the voxel brightness encodes the total absorption, proportional only to the total amount of Pt, regardless of size, shape, and number of Pt particles present.

3.9.3. Feature Extraction by Segmentation using Thresholding

In order to extract and further analyze the bright features (blobs) observed in the Pt loaded sample aged at 950 °C, shown in fig. 3.29, they need to be separated from the remaining (unchanged) sample. Since the blobs are represented by the highly absorbing voxels in the corresponding histogram, *cf.* fig. 3.32, an image segmentation based on thresholding was performed. By manually selecting the washcoat volume and calculating the material statistics the following mean gray value and corresponding standard deviation was found.

$$\text{mean} = (1.1 \pm 0.5) \times 10^{-3} \qquad \text{threshold} = 3.0 \times 10^{-3}$$

The threshold value is three and six times larger than the mean and standard deviation of the entire washcoat, respectively. Both values are indicated by lines in the histogram shown in fig. 3.32. The voxels in the yellow shaded regions represent voxels due to the newly formed features.

The histogram is taken from the entire sample volume containing air, cordierite, and washcoat. Hence, at the selected threshold value of 3.0×10^{-3} also some bright voxels in the cordierite might be included. A higher threshold, *e.g.* 10×10^{-3}, would avoid this, but would at the same time significantly decrease sensitivity to very early stages of Pt sintering in the washcoat. Thus, it was necessary to manually remove falsely marked voxels belonging to the cordierite before proceeding with quantification.

To keep the visualization simple, memory footprint moderate, and computation time reasonable just a single corner with dimensions $800 \times 300 \times 300\,\mu\text{m}$ was analyzed. This is indicated by the colored region on the right side of fig. 3.32. Nevertheless, an extension to the full sample volume is straight forward.

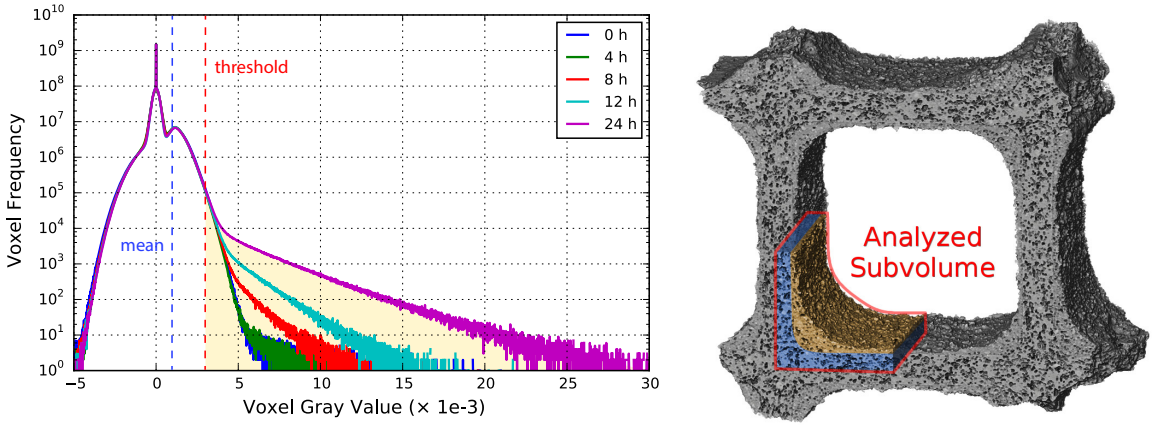

Figure 3.32.: Rendering of the entire sample volume (right) and corresponding histogram (left) for each aging step. Newly emerged features are found above the threshold in the yellow shaded area.

Applying Segmentation and Generation of Labels

The segmented washcoat was obtained after applying the threshold and fixing outliers, yielding two types of "material" to analyze: "normal" and "sintered" washcoat, as shown in blue in the middle of fig. 3.33. In a next step all disconnected voxels clusters in the sintered washcoat, *e.g.* separated spheres, were identified and individually labeled (indexed). This resulted in numerous independent blobs of sintered Pt, displayed as colored objects in the volume rendering in fig. 3.33 on the right.

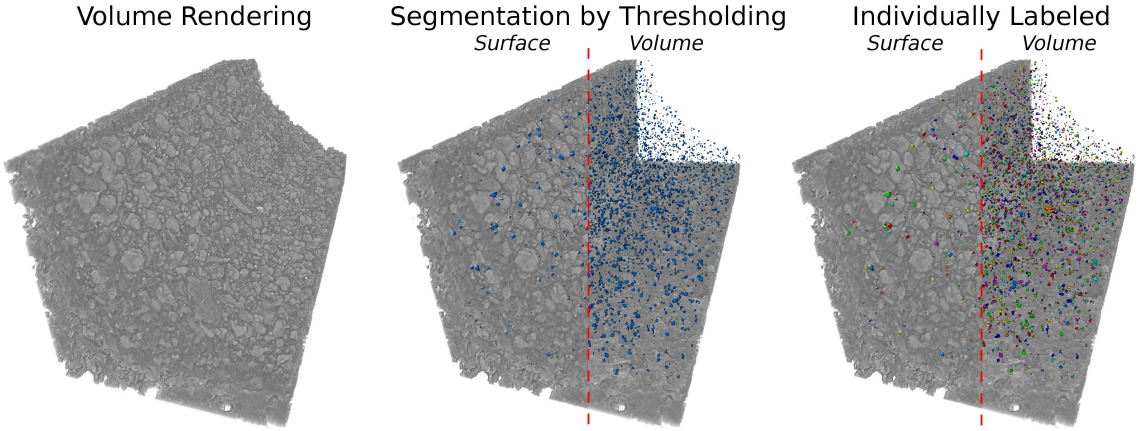

Figure 3.33.: Volume Rendering of the analyzed honeycomb corner (left). Overlay of sintered washcoat (blue) found by segmentation (middle), and individually labeled blobs in various colors (right). The unchanged washcoat was removed on the right hand side of the red line to reveal bulk features.

To give a better impression on the whole process, fig. 3.33 shows the original volume rendering of the corner aged for 12 h at 950 °C in gray scale, the result of segmentation, and the labeling separately.

Technical Note: All this was done using `Avizo Fire`. The initial segmentation by thresholding was done by the `Interactive Thresholding` module, which was applied to the volume of interest. Outlier were removed using the `Segmentation Editor` and filtered volumes to coarsely select cordierite and washcoat. No label smoothing was used to avoid removal of tiny blobs. Individual blobs are determined using the `Labeling` module with 3D interpretation and 26 Neighborhood criteria.

Correlation of Blobs between Subsequent Data Sets

The labeling process provides a unique `id` for any given blob within the sample volume. It is assigned to the blobs by sequentially numbering them from one end of the data set to the other. Obviously, in case of increasing blob numbers, additional labels need to be assigned, which do not match `ids` from previous aging steps. Nevertheless, the position of the blob within the sample volume remains rather constant and can be used to correlate `ids` across different data sets.

A mapping of `ids` from sample volume **A** to **B** was performed by evaluating the positions (center of mass) of the blobs given in Cartesian coordinates (x, y, z). The resulting positions are stored as $\mathbf{a}$ and $\mathbf{b}$ and the Euclidean distance d, given in eq. (3.21), between them is calculated.

$$d(\mathbf{a}, \mathbf{b}) = \sqrt{(a_x - b_x)^2 + (a_y - b_y)^2 + (a_z - b_z)^2} \tag{3.21}$$

Since blobs may merge, grow, or move in the sample a simple comparison of positions, *e.g.* $a = b$, does not work.

Consequently, a valid `id` mapping is present when $d \leq \sqrt{2}$. This limit allows a shift of ca. 1.4 voxel in the center of mass of a blob. Usually the d-values were much smaller, indicating little shift and a perfect match. Potential candidates within a certain volume from the original blob position, *e.g.* within $d \leq 10$, are gathered and further checks and filtering could be introduced to find valid successors in case of ambiguous results.

As a result, a list of individual blobs, *e.g.* for $(\mathbf{r}, \mathbf{s}, \mathbf{t})$, across different sample volumes, *e.g.* $\mathbf{A}, \mathbf{B}, \mathbf{C}$, was built containing the mapping of blob `ids`, *e.g.* $\mathbf{r} : \mathrm{id}_{\mathbf{A}}, \mathrm{id}_{\mathbf{B}}, \mathrm{id}_{\mathbf{C}}$. Thus, a single blob can be identified and tracked over several aging steps.

3.9.4. Results

After extracting the blobs, containing sintered Pt, from each honeycomb volume in the fresh and aged states, after 4, 8, 12, and 24 hours at 950 °C, the quantitative analysis begins.

3.9.5. Evolution of Washcoat Sintering

A considerable increase in the number of blobs as function of aging time was observed, which reflects earlier observations in the raw slices in fig. 3.29 and in the corresponding histogram in fig. 3.32. This increase is visible in fig. 3.35, which shows the full corner (original), blobs on the surface (surface), and blobs in the entire volume (full) at which the washcoat below the threshold was removed for inspection.

Global Analysis

The ensemble of individual blobs present in each aging step, as depicted in the last column of fig. 3.35, was analyzed in terms of total blob number, mean blob absorption (gray value), mean blob volume, and occupied washcoat volume fraction in fig. 3.34.

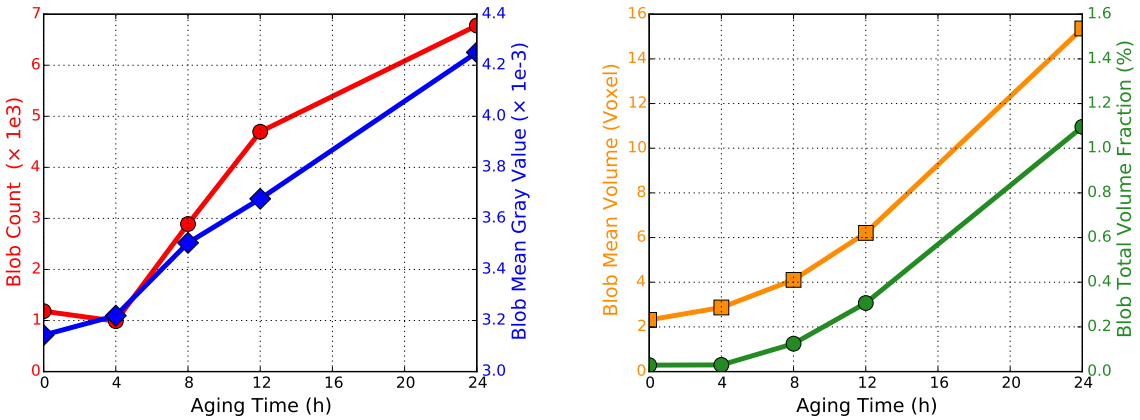

Figure 3.34.: Evolution and analysis of the blob ensemble over aging time by the total blob number (red), average blob gray value (blue), average blob volume (orange), and resulting occupied washcoat volume fraction (green).

The total number of blobs fig. 3.34 (red) in the fresh and 4 h aged sample was quite similar and slightly decreases in this first step. Further aging steps, 4 to 8 and 8 to 12 hours, caused a rapid increase in the total number with constant slope. In the last aging step from 12 to 24 h the blob number still increased to around 7000 blobs but the growth rate became smaller. This indicates a slowing down of sintering after long aging duration although the final state was not yet reached.

The platinum concentration per voxel is encoded in the mean gray value fig. 3.34 (blue). Already after the first treatment of 4 h this value increased. After 8 h an almost linear increase of the average voxel absorption over aging time was observed. This implies continuous accumulation of additional platinum into the blobs. Finally, after 24 h an average absorption of 4.2×10^{-3} was reached, which is four times higher

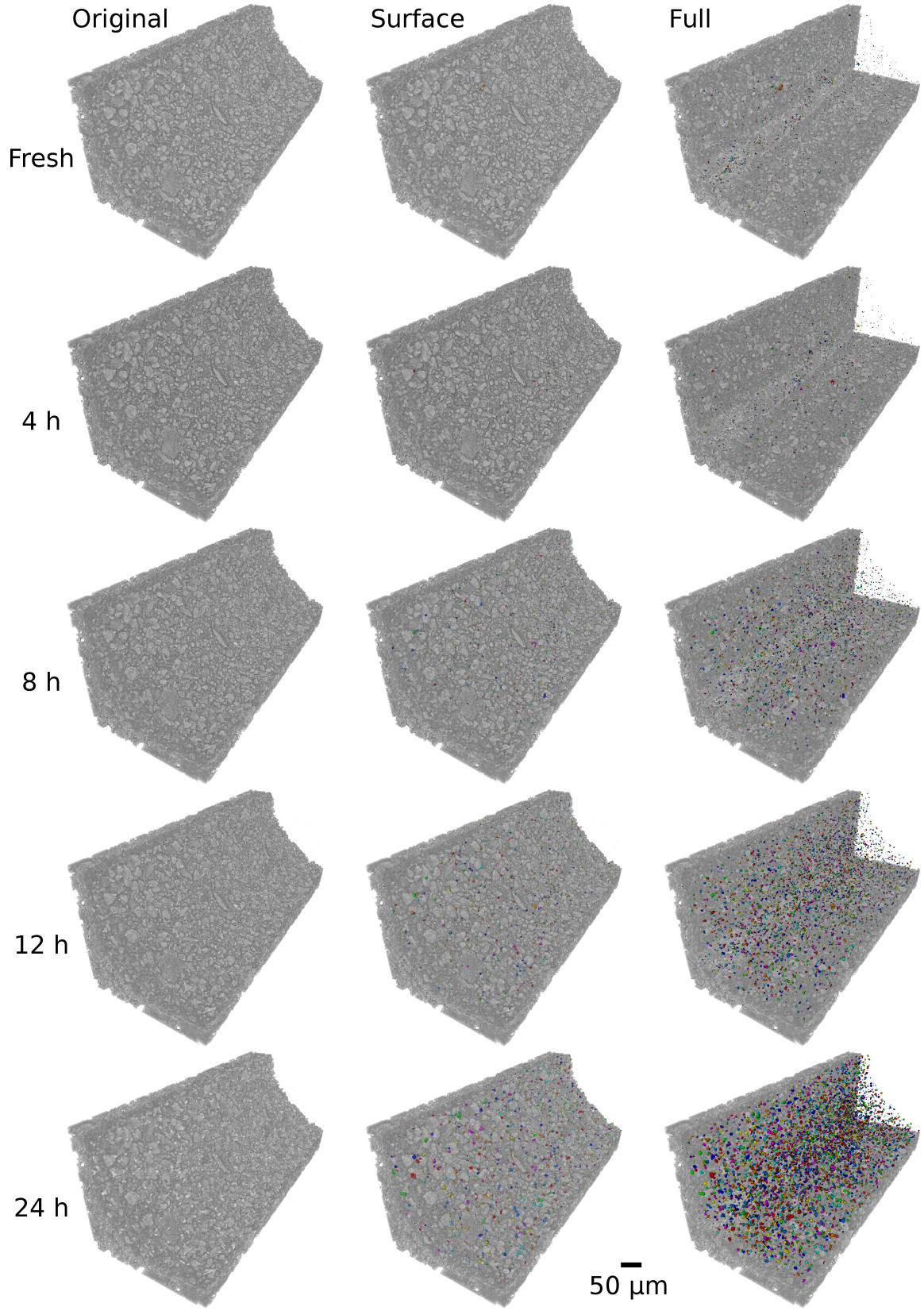

Figure 3.35.: Volume renderings of the $800 \times 300 \times 300\,\mu\mathrm{m}$ large honeycomb corner aged at $950\,^{\circ}\mathrm{C}$ as original rendering, with colored surface blobs visible, and all blobs in the entire corner without the "normal" washcoat for volume inspection.

than the mean washcoat gray value. Simultaneously with the initial drop in the total blob number (red), a slight increase in absorption was found. This could indicate a densification of the initially present blobs.

The average blob volume fig. 3.34 (orange), grew non-linearly with increasing rate toward extended aging duration. The same trend was observed for the total occupied volume fig. 3.34 (green) of all blobs that finally reached 1.1 vol.%.

As the mean blob volume (orange) and the mean blob absorption (blue) increased in parallel, a very pronounced transfer of platinum from other grains into those containing rather large Pt-particles must have occurred. Hence, there is evidence for platinum redistribution/accumulation (mass transfer) into the marked blobs even visible on the micrometer scale.

Correlation of Blob Volume and Blob Absorption

The observed simultaneous growth of mean blob absorption and mean blob volume was further examined by using 2D histograms, shown in fig. 3.36. In this representation of the blob ensemble contributions from every individual blob are accounted without the need to use ensemble averages. The frequency of blobs meeting a certain combination of gray value and volume is denoted by colors using a logarithmic scale. Note that the blob gray value is still averaged across several voxels, since a blob is usually composed of several voxels with varying absorption.

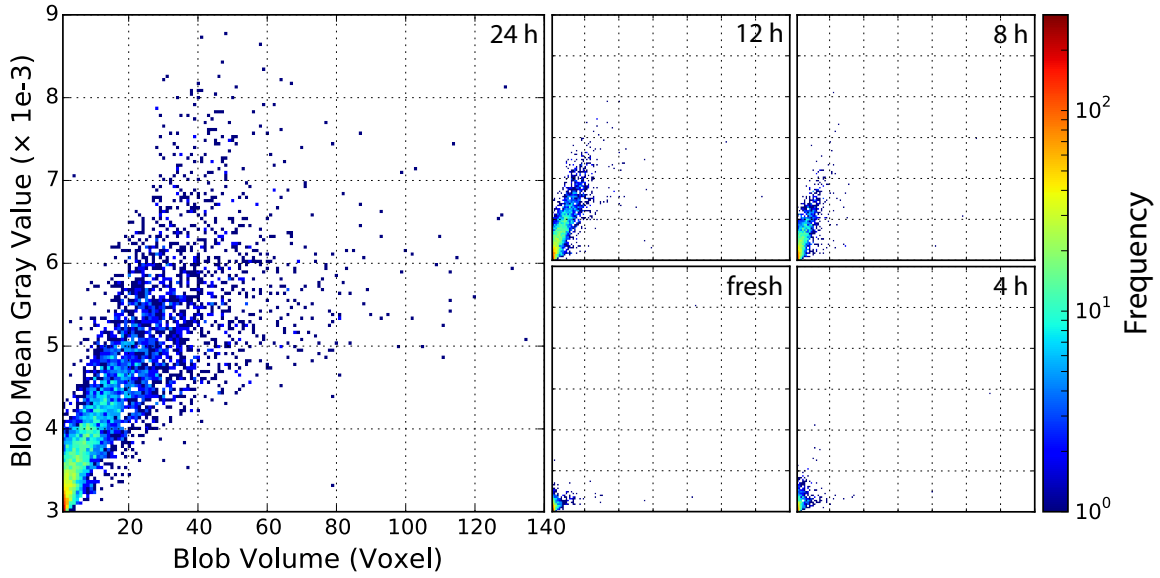

Figure 3.36.: Correlated growth of blob absorption and blob volume from fresh to 24 aging at 950 °C.

By plotting the 2D histograms for every treatment step, a spread of the blob gray values and volumes can be seen. A strong correlation was found as most blobs are positioned along one straight line with little scattering. Most features are located in and emerge from the lower left corner, *i.e.* starting with a small volume and low absorption. As aging proceeds, the majority of blobs first fans out toward higher absorption, meaning higher Pt content, and later on also toward larger volumes. This

observation is in line with general sintering mechanisms described in literature [63, 64, 110–112]. Most highly absorbing blobs with very high volumes are found after 24 h aging, although a few are already found at earlier stages of aging.

3.9.6. Tracking and Clustering of Individual Blobs

The individual blob labels allow to pinpoint and select any number of blobs. These can be tracked across the different aging steps and clustered into different growth regimes, as shown below. Blobs in the different aging steps were identified and tracked as described on page 62.

Single Blob Tracking

The tracking of ten randomly chosen individual blobs is demonstrated in fig. 3.37(left). Each trace belongs to a single blob, where circles are marking states at 8, 12, and 24 hours of aging. The individual blob volume and absorption are used for plotting, similar to the correlation plot in fig. 3.36. This representation shows again the growth that was observed for the complete ensemble: a growth of average absorption and later on a volume increase.

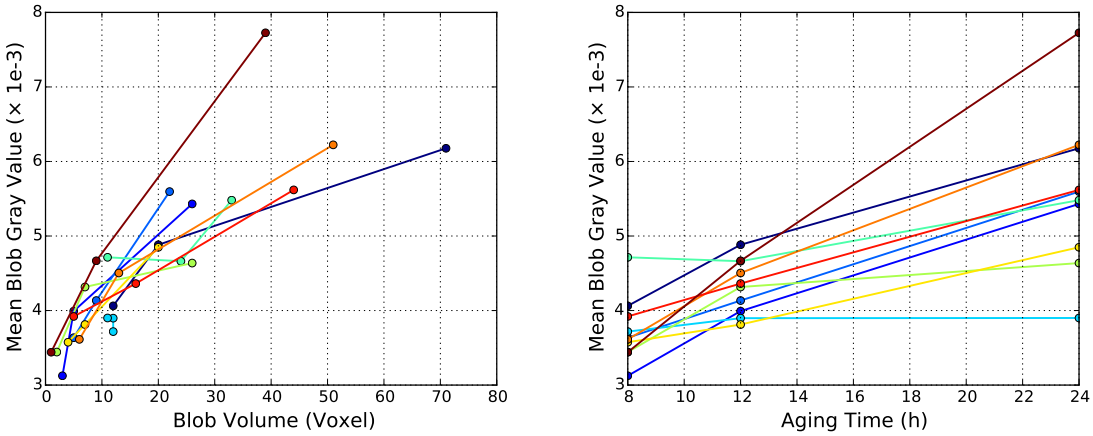

Figure 3.37.: Tracking the evolution of 10 individual randomly chosen blobs over aging time. In the left panel the blob gray value and volume are shown, circles correspond to aging times of 8, 12, and 24 h. The same data is shown directly as function of time in the right panel.

Moreover, any blob attribute that is accessible from tomography data can be plotted directly as function of aging time, as done in the right panel in fig. 3.37. Please note, that lines between the data points are used as guide to the eye only.

A tracking of this small number of blobs already revealed some differences in the individual growth behavior: While some blobs were quickly growing, some others remained almost constant in the mean gray value for example. A more comprehensive analysis is given in the next section.

Clustering of Temporal Blob Evolution

After the blob tracking analysis for a few individual blobs in the previous section, this idea is generalized and applied to a subset of the entire blob ensemble. This will allow to describe the ensemble evolution by individual growth rates. A subset of in total 964 blobs was analyzed, which allowed unambiguous tracking across all aging steps. That means that no newly emerging, merging, or separating blobs are considered. The temporal derivative $\frac{d}{dt}$ of the blob volume and gray value was calculated for each entity. This allowed a clustering of the blob ensemble into four different growth regimes with respect to the blob parameters volume (x axis) and absorption (y axis), which are indicated by four different colors:

- compacting with shrinking volume and increasing Pt loading
- growing with increasing volume and increasing Pt loading
- vanishing with shrinking volume and decreasing Pt loading
- diluting with increasing volume and decreasing Pt loading

The color coded diagram in fig. 3.38 directly visualizes the distribution of grow types. A clear majority of growing blobs (green) was present in the first step from 8 to 12 hours. This growth regime became even more dominant in the second aging step from 12 to 24 hours. This is also underlined by a calculation of the fraction of blobs in each branch, in eq. (3.22).

$$8\,\mathrm{h} \Rightarrow 12\,\mathrm{h} = \begin{bmatrix} 3.1 & 83.9 \\ 3.8 & 9.2 \end{bmatrix} \cdot \% \qquad 12\,\mathrm{h} \Rightarrow 24\,\mathrm{h} = \begin{bmatrix} 4.1 & 91.3 \\ 0.6 & 4.0 \end{bmatrix} \cdot \% \tag{3.22}$$

Especially the regimes with decreasing gray value (red, yellow) have lost population, which mostly shifted to the growing branch (green).

Since, some points in the graphs in the left panel of fig. 3.38 may overlap, it was difficult to judge the ensemble behavior and the center of mass. Hence, a 2D histogram is provided in the right column of fig. 3.38 to determine the frequency, encoded in gray levels, and the center of mass denoted by the red cross. In average, the gray level increased by 1.17×10^{-4} and $0.92 \times 10^{-4}\,\mathrm{h}^{-1}$ for the aging steps 8 to 12 and 12 to 24 hours respectively. For the same aging steps, the volume increased by 1.37 and 1.46 voxel/h respectively. Thus we observed a decreasing tendency in Pt accumulation within the blob (gray value) but an increasing blob expansion. This confirms the observations made previously using the 2D histogram in fig. 3.36 on page 65. A formally decreasing rate of Pt accumulation may be explained by addition of new voxels to an existing blob, which are just above the threshold and in turn lower the average blob absorption. However, Pt agglomeration continuous and no saturation in absorption was observed.

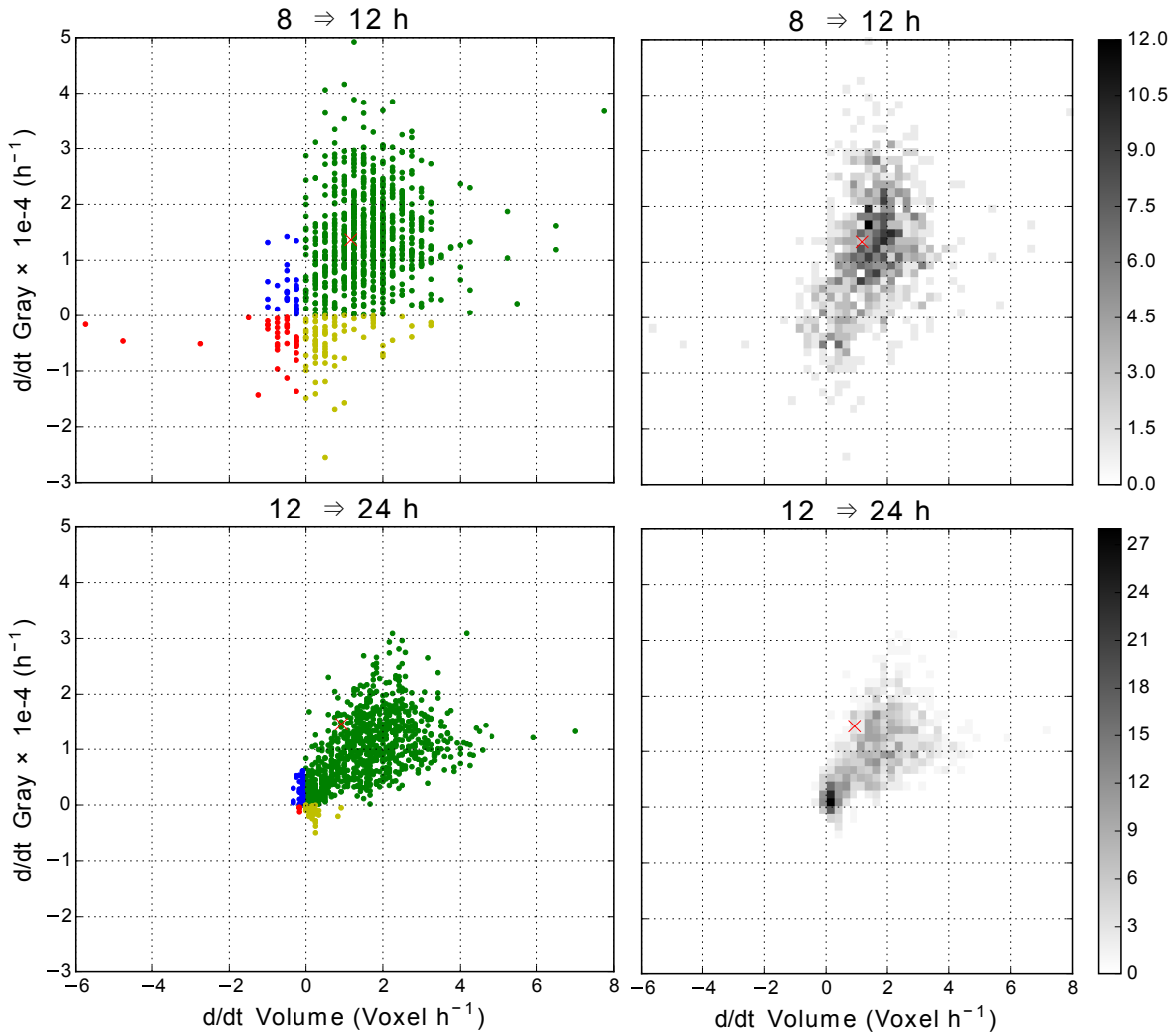

Figure 3.38.: Cluster analysis and evolution of the temporal derivative of the blob volume and blob gray value for aging between 8 to 12 and 12 to 24 hours. The analyzed ensemble consists of 964 individual blobs. The left column presents the clustering of individual blobs into growth regimes: growing (green), compacting (blue), vanishing (red), and diluting (yellow), where each entity is represented by a single point. The right column shows the corresponding 2D histograms of the blob distribution to account for overlapping of single points. The red cross denotes the center of mass in all plots.

3.9.7. Inspection of Sintering in a Washcoat Sub-Volume

The effect of aging, influencing the distribution and concentration of Pt, is reflected in the absorption of the voxels. Prior analysis revealed, in general, the emergence of initially small regions with an increased platinum content, which further grew as aging proceeded. Hence, a specific region of the washcoat was visualized in detail to follow absorption and morphology changes directly.

In fig. 3.39 volume renderings of a small washcoat portion are presented to give a quick overview, the full size image in fig. 3.40 provides more details. A color scale was used to encode different absorption values within the sample, it was chosen to reflect characteristic properties of the washcoat, which have already been used for the segmentation above in section 3.9.3 on page 60. It essentially spans from the mean washcoat gray value (1.0×10^{-3}, dark blue partially transparent) to the threshold value (3.0×10^{-3}, orange) with both limits additionally extended by one σ (0.5×10^{-3}).

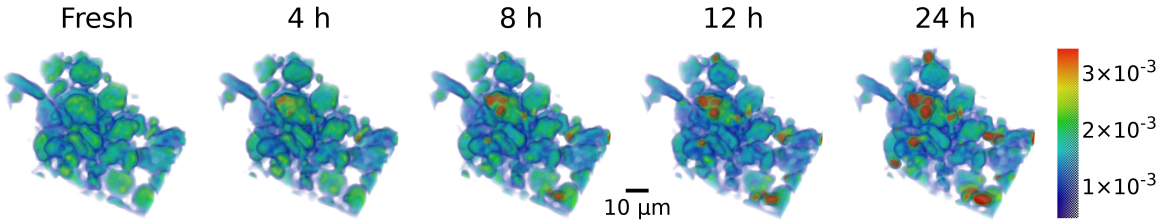

Figure 3.39.: Color rendering of a small washcoat portion demonstrating local sintering and material transport.

The agglomeration and redistribution of platinum after each treatment step is clearly visible and consistent with the above-mentioned results. In the full-size fig. 3.40, a quite homogeneous fresh state (greenish) was observed.

After 4 h aging, first spots (orange) became visibly. Some areas with considerably higher Pt loading (red) had formed after 8 h and remained at their initial position. They continued to extend and intensify with increasing aging duration, as evident in the 12 and 24 h renderings. Simultaneously to the formation of Pt agglomerates, depicted in red, decreasing Pt concentration was observed in the surrounding area around the agglomerates, evident by color changes from greenish to light blue and dark/transparent violet. This gives indirect proof of the sintering process, where some regions continuously grow into bigger feature as they deplete Pt from the nearby area.

Hardly any sintering of alumina particles and no loss of porosity was found. The redistribution of Pt was visible on single Al_2O_3 grains, but was more pronounced across different grains. This suggests diffusion of Pt on top of the alumina grains in agreement with earlier observations.

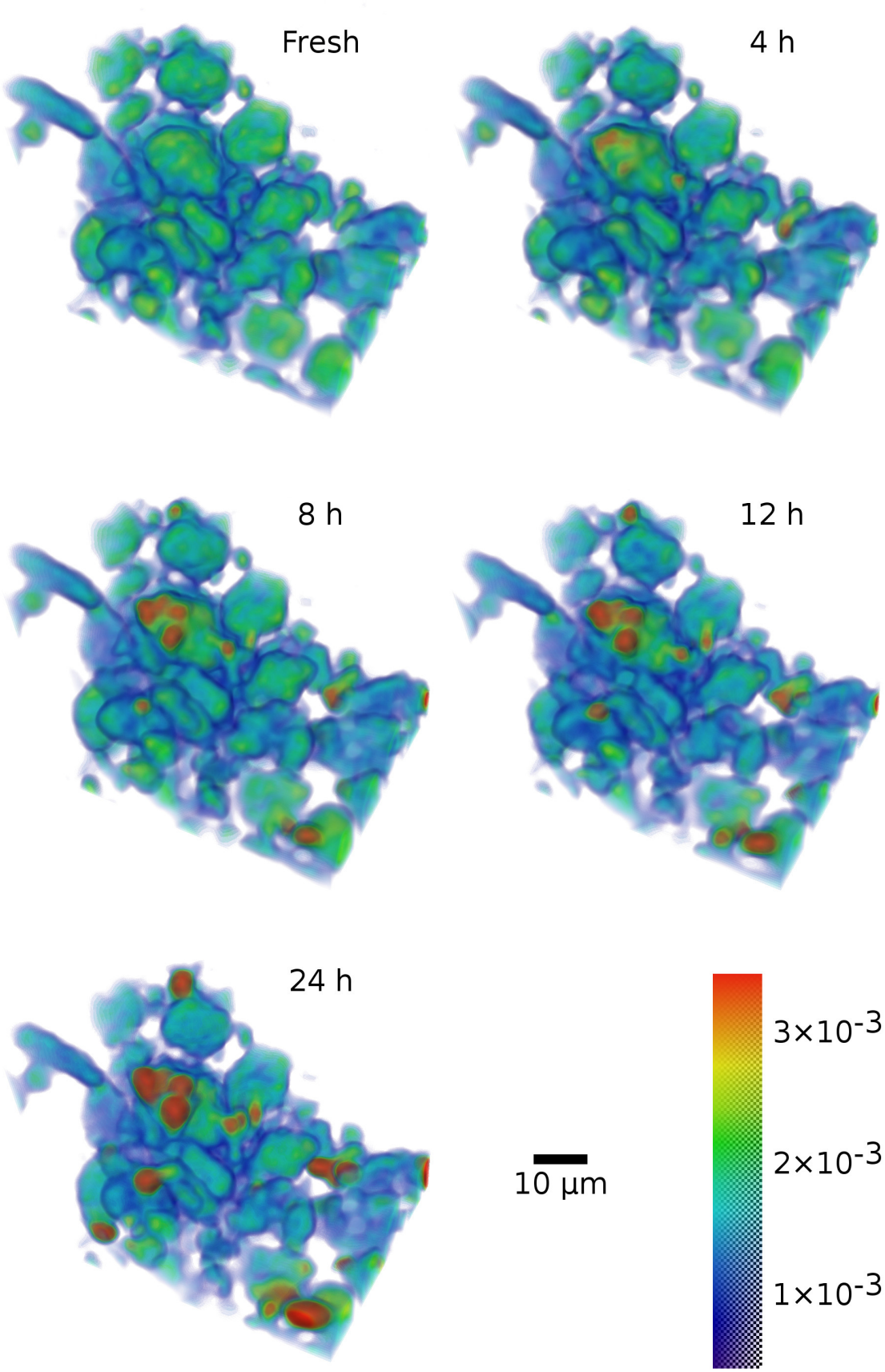

Figure 3.40.: Large scale color rendering of a small washcoat portion demonstrating local sintering and material transport.

3.9.8. Complementary Characterization

CO Oxidation

CO oxidation was used as model reaction to study the effect of the applied aging conditions on the catalytic performance. The influence of treatment temperature, time, and gas atmosphere on the thermal deactivation of supported Pt/Al_2O_3 catalysts has been frequently discussed in literature [113] as well as for similar systems [114]. A decrease of the washcoat surface area and the increase of the noble metal particle size due to sintering are reported with increasing temperature and exposure time. Already at 600 °C the sintering process starts [115] and for Pt it seems to be accelerated especially by oxidizing environments [53, 116]. Therefore, aging in static air, similar to the conditions used in the quasi *in situ* experiments has been used in addition to aging under more realistic conditions using 10 vol.% water vapor in the gas stream.

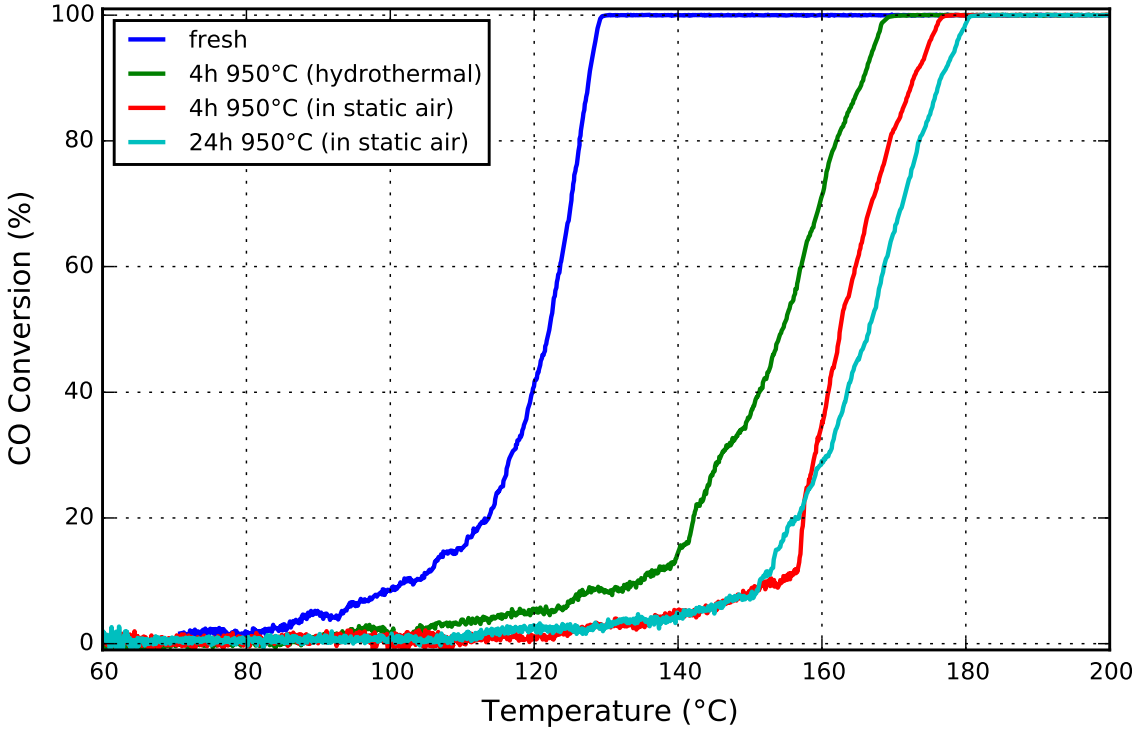

Figure 3.41.: Light-off curves for CO oxidation for the Pt/Al_2O_3 honeycomb samples aged either (i) in static air for 4 and 24 hours, or (ii) with 10 vol.% H_2O in the gas stream for 4 hours.

The fresh catalysts used in this study featured highly dispersed Pt nanoparticles with a narrow particle size distribution. Mean particle size was below 2 nm [100]. This was reflected in the CO oxidation activity which corresponded to a light-off temperature of about 120 °C, as shown in fig. 3.41. After 4 h of aging at 950 °C, a pronounced shift in the light-off temperature from 120 °C to 162 °C (in static air) and to 154 °C (hydrothermal) was observed. This is in line with recent catalytic and modeling studies by Chan *et al.* [113]. Although the catalyst deactivates under both aging conditions, the effect of aging in static air was significantly stronger for the given parameters and

catalyst. This is maybe due to differences in surface energy and hence wettability of the Pt/PtO_x particles on the Al_2O_3 surface resulting from the interaction with the wet or dry atmosphere. These might change the inclination of Pt to sinter. Another source of the differences might be the extent of Oswald ripening due to mobile PtO_x species, as found by *in situ* electron microscopy [116–118]. Additionally, the presence of chlorine traces from the hexachloroplatinic acid precursor and of water at the same time could result in possible partial redispersion of Pt via hydroxychloride platinate in addition to oxychloride platinate species [119–121]. However, a more systematic study at such extreme aging temperatures would be needed to conclude on these hypotheses, since the influence of water during sintering and especially redispersion of noble metal is still controversially discussed [25, 121, 122].

The elongation of aging time to 24 h in static air affected the catalytic activity just slightly, as evident by a small shift to about 165 °C light-off temperature. This is in line with the two reported regimes of the sintering processes for such high Pt loadings. A very steep loss of the noble metal surface occurs in the first hours of aging at temperatures above 700 °C in oxidizing atmospheres, which is followed by a slow almost linear increase of the Pt particle size [64, 112, 113]. Furthermore, the increase of the turnover rate for CO oxidation over larger Pt particles will compensate the decrease of the total number of active sites [97]. As previously demonstrated [113, 123], this is caused by the different CO adsorption and desorption kinetics and adsorbate-adsorbate interactions as a function of morphology and particle size distribution. Moreover, the agglomeration of Pt as observed by μ-CT (*cf.* section 3.9 on page 54), may additionally compensate the loss of active sites, since increased activity can be expected [124]. On the other hand, at high temperatures deactivation may not only be due to sintering of the very small Pt particles but also due to changes in the catalytically active porous washcoat layer, which was an additional focus of this study.

In this regard, a general enhancement of the thermal stability may be achieved either by addition of dopants that improve the stability of the alumina support or by modifications influencing the noble-metal support interaction, which result in reduction of the noble metal sintering rate [53]. In addition, sintering of metal particles can be prevented by application of synthesis routes that result in high initial dispersion and uniform distribution of the metal particles. This is part of ongoing research [53, 125–127].

X-Ray Diffraction

Further evidence for changes in the sample due to isothermal treatment were found by recording X-ray diffraction patterns. To obtain sufficient amounts of sample and to avoid contaminations from cordierite, the pure (uncoated) 4 wt.% Pt/$\gamma-Al_2O_3$ catalyst powders have been used and aged in static air at 950 °C for 4 and 24 hours. The results are presented in fig. 3.42.

In the fresh sample, no characteristic reflections of metallic Pt, *e.g.* at $2\Theta = 81°$, were detected due to the high dispersion of Pt. Already after 4 h of aging at 950 °C four very intense reflections at 39, 46, 63, and 81° became visible, which correspond to the (111), (200), (220), and (311) diffraction planes of metallic fcc platinum (labeled by ♦). This finding is in line with earlier studies under oxidizing conditions [128].

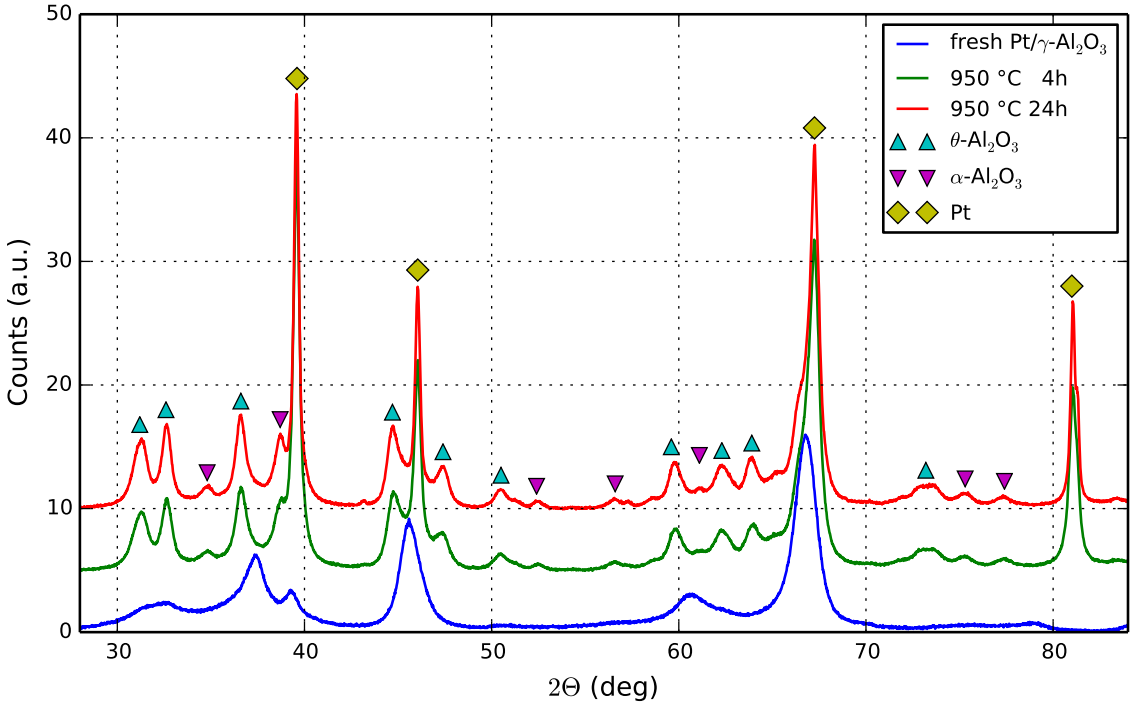

Figure 3.42.: Diffraction patterns of 4 wt.% Pt/$\gamma-Al_2O_3$ powder: (a) fresh, (b) aged at 950 °C in static air for 4 h, and (c) aged for 24 h under the same conditions. Markers are added for metallic fcc phase of Pt (♦), $\theta-Al_2O_3$ (▲), and $\alpha-Al_2O_3$ (▼) while $\gamma-Al_2O_3$ was the only detected phase in (a). The plots are unscaled and stacked for comparison.

Further aging up to 24 h resulted in narrower and more intense reflections, indicating continuation of crystallite growth due to sintering. Peak fitting allows estimation of the average Pt crystallite size by using the Scherrer formula [27]. Results were obtained accordingly, and are summarized in table 3.4. The average size increased from 24 nm after 4 h by 25 % to 30 nm after 24 h aging at 950 °C. Although this average growth rate was much smaller as compared to the initial fresh-to-4-hours rate, the effect was still present and correlates with the observed slightly deteriorated catalytic activity obtained after extended aging periods [64, 112, 113].

The support material, $\gamma-Al_2O_3$, was found to be responsible for all reflections present in the fresh sample [129]. Aging likewise affected the support, thus $\theta-Al_2O_3$

Table 3.4.: XRD fit results of lab aged powders.

Peak Position	Diffraction Plane	4 h @ 950 °C		24 h @ 950 °C	
		FWHM	Size	FWHM	Size
(2Θ)	(hkl)	(mrad)	(nm)	(mrad)	(nm)
39.57	111	5.88	25	4.87	30
46.05	200	6.63	22	5.15	29
67.27	220	9.00	19	7.70	22
81.06	311	6.18	30	4.45	41
average			24		30

was found (marked by ▲) as well as some weaker contributions of $\alpha-Al_2O_3$ (indicated by ▼) [130] for the aged samples. Hence, the question arises to which extent the phase transformation as well as the macro-porosity and possible cracks in the coated catalyst layer in addition to the sintering of Pt particles have an impact on the catalyst performance. The effect of cracks and cavities was investigated by Novák *et al.* [84], who found that enhanced diffusion improves catalyst performance as long as the adhesion and mechanical durability of the washcoat layer is preserved.

BET Surface Area

The surface area was studied by Brunauer–Emmett–Teller physical adsorption (BET) measurements, using the samples from XRD. The results are shown for 950 °C, according to the XRD measurements, and for 750 °C as additional information from separate samples.

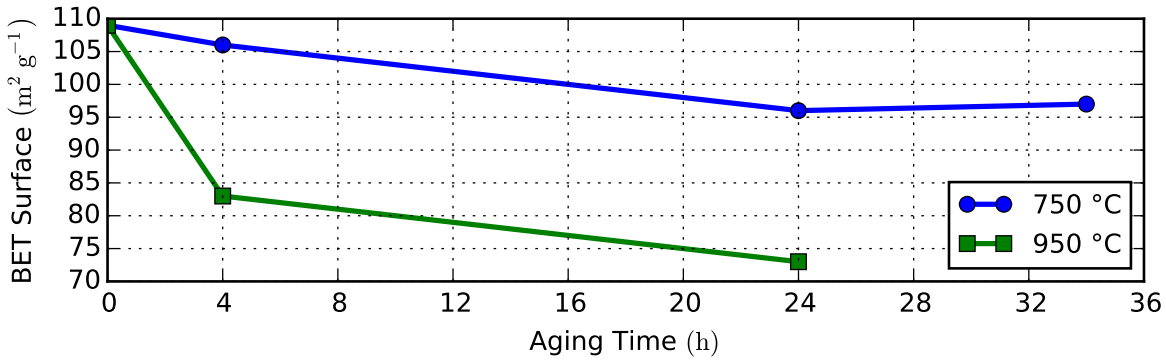

Figure 3.43.: BET surface area of uncoated Pt/Al_2O_3 sample powder aged at 750 and 950 °C.

The initial BET surface was around 109 $m^2\,g^{-1}$ and decreased rapidly to 73 $m^2\,g^{-1}$ after 24 h at 950 °C. A similar, but less pronounced effect was observed for aging at 750 °C. After 34 h a surface area of 97 $m^2\,g^{-1}$ was obtained.

The results are in line with observations made by XRD and cited literature [64, 112, 113], stating a rapid early phase and slow almost linear effects at later stages and longer time scales.

Electron Microscopy of Pt/Al_2O_3

The fresh sample was studied by TEM to detect highly dispersed platinum nanoparticles supported on $\gamma-Al_2O_3$ as shown in fig. 3.44(a). The analysis of several high resolution TEM images revealed a particle size distribution with the majority of particles below 2 nm in size, *cf.* fig. 3.21 on page 45.

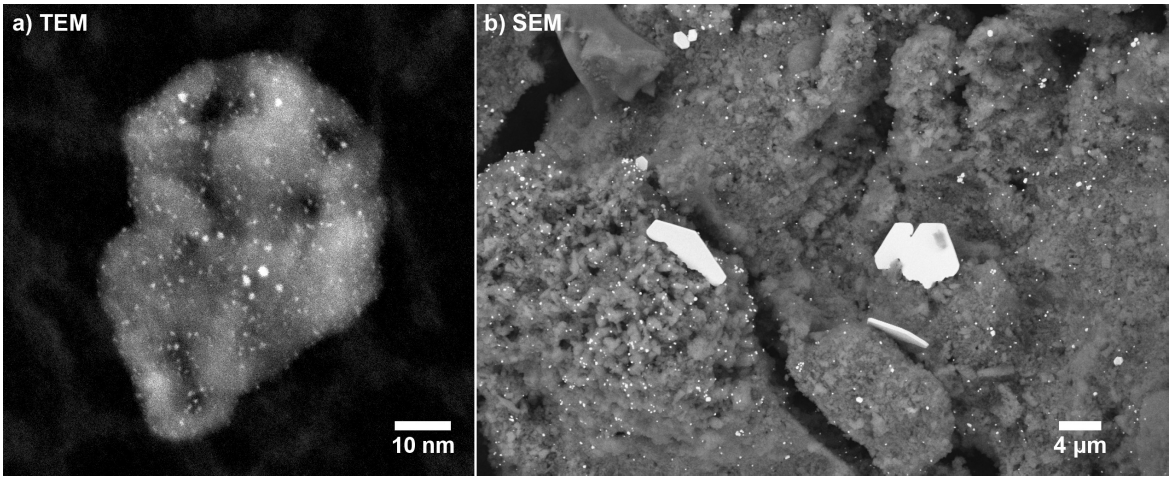

Figure 3.44.: Electron microscopy images of the Pt/Al_2O_3 sample. (a) TEM image of the fresh sample (STEM, 910k× magnification). (b) SEM image of the sample after aging for 24 h at 950 °C (BSE, 8k× magnification).

After finishing the last aging for 24 h at 950 °C and a subsequent tomography scan, the sample was studied by SEM. The surface of the aged washcoat, still attached to the honeycomb wall, is presented in fig. 3.44(b). The two images directly prove the sintering of initially small well dispersed Pt particles into very large, micrometer-sized plate-like platinum single crystals, as detected by XRD. Nevertheless, still numerous small particles are observed with sizes in agreement with the results obtained by XRD.

3.9.9. Summary & Conclusion

The isothermal aging of multiple single honeycomb channels was studied by quasi *in situ* X-ray absorption micro-computed tomography (μ-CT). As honeycomb coating 4 wt.% Pt/Al_2O_3, pure Al_2O_3, or a double layer with 4 wt.% Pt/Al_2O_3 on top of Al_2O_3 was used. Samples were aged in air *ex situ* at 750 and 950 °C for up to 34 and 24 hours respectively.

By evaluation of the voxel gray value histograms, no deviation due to aging was observed for the pure Al_2O_3 at 950 °C nor for any other sample at 750 °C. Nevertheless, increasing numbers of voxel high gray values were observed with time for aging at 950 °C in all samples with a Pt coating. This indicates pronounced Pt sintering at 950 °C. Nonetheless, it does not exclude Pt sintering at 750 °C. The conclusions given in the following are drawn on the results found for the Pt/Al_2O_3-sample.

For aging at 750 °C, the difference method was used to detect various sample changes caused by the treatment, *e.g.* widening of washcoat cracks, displacements of washcoat material, and newly emerging features due to Pt sintering (blobs). However, "only" qualitative statements are made, since the origin of each difference feature, needs to be checked and verified to avoid ambiguities. Such ambiguities might arise for example from grains that just swap their position or are displaced in any other manner. They can easily be confused with newly formed blobs.

Aging at 950 °C for up to 24 h induced tremendous augmentations of local absorption within the sample volume. This was already evident in the histogram and was demonstrated for single slices. These highly absorbing voxels were assigned to sintered platinum, which was confirmed by a direct correlation of a mechanical cross section investigated by EPMA and WDX to a virtual slice of the same region from μ-CT. The sintering was further confirmed by increased Pt crystallite size in XRD and the observation of large single crystals in SEM. Accordingly, the light-off temperature for CO oxidation was increased, and the BET surface area of the support was decreased, due to the treatment.

Prior to quantitative analysis, the digital volume was segmented into non-sintered washcoat and regions containing sintered and agglomerated platinum. As the latter volume possessed an increased absorption, this was exploited by a thresholding operation to yield an automatic segmentation. In a next step, the whole sintered volume was split into individual clusters, referred to as blobs. This enabled quantitative analysis of individual blob properties, *e.g.* volume and absorption, or quantification across the entire blob ensemble, *e.g.* total number and average volume, per aging step.

Quantitative analysis of the blob ensemble yielded an almost linear increase in absorption, growing total numbers, and non-linearly enlarging average volumes with aging time. Consequently, a steady raising washcoat volume fraction containing sintered platinum was observed. In accordance with general sintering mechanisms, a correlated growth of blob absorption and blob volume was observed.

For individual blobs, the tracking of blob characteristics over aging time was demonstrated. Moreover, the individual growth behavior was clustered into four regimes based on the temporal evolution of blob volume and absorption. In the aging steps

from 8 to 12 h and 12 to 24 h 84 % and 91 % of the 964 considered blobs were found in the growth regime with simultaneously increasing absorption and volume. The mean absorption increase was 1.17×10^{-4} and $0.92 \times 10^{-4}\,\mathrm{h}^{-1}$, while the average volume increased by 1.37 and 1.46 voxel/h for the two stated aging steps. Notably, these growth rates are obtained for each individual blob and thus may also be analyzed spatially resolved to unravel different dynamics in different locations of the sample.

Finally, volume renderings were employed to directly visualize the described aging effects. They revealed a homogeneous distribution of blobs in the washcoat, whereupon largest blobs were found in voids and on the surface providing sufficient space for growth.

By rendering a small washcoat sub-volume, an almost homogeneous Pt distribution was found in the initial state. However, with proceeding aging highly absorbing regions emerged and continued to grow in size and absorption. At the same time, the absorption was found to decrease in the direct surrounding. This graphically represents the quantitatively captured redistribution and sintering of Pt and underlines the strength of spatially resolved quasi *in situ* X-ray absorption micro-computed tomography.

Quasi *in situ* X-ray absorption micro-computed tomography was routinely and successfully applied to single coated honeycomb channels. Isothermal aging at 950 °C caused strong sintering effects and allowed segmentation based on thresholding with subsequent quantitative analysis for the first time. This demonstrates the feasibility to reliably detect and analyze sintering features within the entire sample volume in absorption mode. It also emphasizes the need for a possibility to perform segmentation in order to conduct further quantitative analysis. Although manual segmentation is possible, it should be avoided since it is very time consuming and not very well reproducible. This is especially critical if a batch of samples is investigated and sample changes shall be tracked, which should be based on measurable properties like absorption changes.

Sintering was found to proceed with aging time according to results from μ-CT and complementary XRD and SEM. However, a direct correlation to the CO oxidation light-off temperature seems to be more difficult. A shift in the light-off temperature was observed just after the first aging and remained almost unchanged in the sample aged for 24 h. This might be caused by compensating effects like enhanced diffusion due to cracks and cavities and the presence of locally high Pt concentrations, both leading to an improved catalytic activity [84, 124]. Further deviations may originate from aging a single channel at the beamline in contrast to aging a complete cylindrical cordierite monolith in the laboratory reactor as the coating per channel varied considerably, see section 3.6. In essence, more systematic studies are required, preferentially on the same sample measured by μ-CT and in the catalytic test.

The current status of the technique encourages to perform *in situ* experiments with even better resolution to optimize quantitative analysis and obtain better correlation to catalytic tests.

3.10. Conclusion & Outlook

In general, *ex situ* X-ray absorption micro-computed tomography (μ-CT) is useful for the characterization of pellets and coated honeycomb samples. Major benefits are the non-destructive investigation and sampling of large volumes to obtain a more representative picture. The coating homogeneity and distribution in the channel and the outcome of different preparation routes affecting metal distribution were checked. Different metal loadings on the washcoat and concentration gradients were detected too.

These capabilities may be utilized to study potential sintering and deterioration gradients in vehicle aged samples, which might be quantified and correlated to complementary studies. Moreover, regions of interest identified by μ-CT may be selected for further investigation by higher resolution μ-CT or complementary methods like *e.g.* SEM. In this way conducting correlative tomography [71].

A quasi *in situ* X-ray absorption micro-computed tomography approach was developed, in which subsequent tomography scans and treatments of the same sample are performed. This added the ability to detect, trace, and quantitatively analyze sample changes on the µm-scale due to thermal treatments.

The obtained quantitative results are important to compare different samples and treatments. Moreover, such quantification is needed for correlation of tomography results with complementary techniques and thus helps to obtain a more complete understanding. Vice versa input from, *e.g.* electron microscopy, is valuable to assist data interpretation in tomography. This is in agreement with Maire *et al.* [93], stating that 3D imaging is often best considered as part of a multi-scale imaging strategy. Furthermore, a comprehensive review on quantitative tomography, discussing limitations and opportunities, is found in [93].

Considering other treatments and sample systems for use with the quasi *in situ* approach, limitations may arise, since the registration of subsequent tomography scans is required. Hence, some treatment invariant structure or marker is needed. Otherwise *in situ* experiments need to be conducted to prevent major changes in sample orientation and positioning between the different scans.

Besides the determination of the local absorption, different sample characteristics can be addressed by choosing suitable tomographic contrasts. These are for example: fluorescence for mapping of the elemental distribution and diffraction to distinguish crystalline phases. Moreover, a direct tomography based on inelastic X-ray scattering with sensitivity to light elements such as carbon may be applied to study soot deposits [131]. In this context, the capabilities of modern laboratory μ-CT devices should be evaluated, since µm-sized voxels can be obtained in such systems. These might be sufficient to study coating and preparation properties and are more readily available than synchrotron beamtime [132]. To perform more realistic and/or sophisticated experiments, the development of suitable cells for *in situ* μ-CT is required. It would be highly desirable to connect such experiments either directly or separately to catalytic performance tests and other complementary characterization techniques of the same sample.

Current reactors in our laboratory usually employ honeycomb cylinders with 21 mm diameter for catalytic tests. When measurements of such samples were possible with μ-CT, an easy transfer between experiments would allow a direct comparison of reactivity and sample changes. As these samples are too big to enable full μ-CT with high resolution, local μ-CT or stitching might be an option [93, 133], but as measurement time and the amount of data to be analyzed rapidly increases in such an experiment, that approach has to be tested yet. In case it worked, it would be even possible to directly implement a laboratory reactor into a tomography setup to perform *in situ* experiments. However, presumably a compromise between both experimental setups has to be found.

On the analysis part, digital volume correlation may be used to quantify displacements and resolve sample strain [108]. This and other quantitative analysis methods, however require special analysis software, as discussed by Ketcham [134], and analysis efforts may be considerable.

To improve the correlation of absorption values in μ-CT with the Pt loading of the washcoat, a test volume containing a suitable set of differently loaded Pt reference samples could be measured. Such a sample and measurement would be additionally useful to compare and calibrate data from different μ-CT devices or synchrotron experiments, thereby providing an absolute quantification of Pt distribution in the studied honeycomb channels.

Higher spatial resolution of the aging effects in the washcoat can be obtained by preparing a small capillary with samples. In combination with *in situ* treatments, effects of temperature and gas atmosphere can be studied tomographically. On a larger scale, the preparation of shell-impregnated extrudates can be followed during impregnation, calcination, and after being used in a catalytic reaction. This will reveal changes of the catalyst distribution in the pellet and help to optimize coating parameters.

The obtained volume data may serve as input for simulations with realistic pore structure and spatial variations in Pt concentration, especially after aging. The pore structure is important for the mass transport to the catalytically active sites and for estimating tortuosity, porosity, and thus the effective diffusion coefficient. A better resolution in this respect using TEM or ptychography as introduced in the next chapter, could thus improve simulations, especially after aging.

By a combination with TEM tomography similar to the work of [86] spatial resolution of such a model can be increased beyond the limits of μ-CT. This can be used, *e.g.*, to investigate mass transport and optimize other devices, such as gas phase reactors.

Altogether, the μ-CT technique is very versatile and capable of providing spatially resolved 3D information complementary to other characterization techniques, *e.g.* electron microscopy or other bulk averaging methods.

4. X-Ray Ptychography

4.1. Introduction

Recent advances at synchrotron light sources and in X-ray microscopy provide higher resolution, routinely in the nanometer range, and enable new imaging techniques, *e.g.* coherent diffraction imaging, which offer new possibilities [135, 136]. With respect to catalysis, the imaging of catalyst particles itself and the changes to the catalyst sample are important aspects [12, 70, 137], here X-ray microscopy on the nanometer-scale is essential [138].

Nanoscale imaging of Fe catalysts with oxidation state contrast was demonstrated *in situ* with 40 nm resolution using soft X-ray scanning transmission X-ray microscopy (STXM) [139], but with restrictions to sample thickness and gas atmosphere. By using hard X-ray full-field transmission X-ray microscopy (TXM) and a special *in situ* cell, catalyst particles have been imaged in 3D with 15 nm resolution at 600 °C at pressures up to 30 bar [140]. Further details and examples on TXM are found in [141–144]. A decisive parameter for the resolution in TXM are high quality lenses, which are sill challenging to fabricate and are used to form the image on the detector [145, 146].

However, in coherent X-ray diffraction imaging (CXDI) methods, *e.g.* ptychography, no such imaging lens is required. Thus they are refereed to as lensless X-ray imaging [147–149]. Accordingly, the resolution can be further increased [147, 150–152]. CXDI methods and associated experiments in materials science have been excellently and comprehensively reviewed by Nugent [153].

Ptychography is a scanning CXDI method, that enables to image non-compact samples larger than the beam size and with resolutions much smaller than the beam size. Since hard X-ray ptychography experiments showed a resolution of 10 nm for patterned test objects [154], it is appealing for the imaging of nanoparticles as used in life science and catalysis [155, 156]. Nanoparticles are weakly scattering objects, thus challenging for ptychography. Nonetheless, recently progress was made to successfully image them [150, 157]. Chemical contrast in soft X-ray ptychography was recently demonstrated for 2 µm large SiO_2 and PMMA beads at multiple energies [158]. First experiments in the hard X-ray regime have reported on chemical contrast at fixed X-ray energies to distinguish chemical elements present in a microchip [159] and on exploiting contrast differences in the ptychographic images for 220 nm large Au/Ag nanoparticle scanned at two X-ray energies below the Au L_3 edge to reveal Au rich regions in cubes [160].

By virtue of these inspiring and exciting TXM results and the potential of higher resolution by using ptychography (or CXDI in general), the final aim is to further

increase the spatial resolution of hard X-ray ptychography to well below 10 nm in combination with chemical imaging capabilities during *in situ* or favorable operando experiments. Extending the repertoire of complementary characterization techniques for a variety of research fields including catalysis.

As a first milestone, and in close collaboration with the group of Christian Schroer (DESY), imaging of nanoparticles with high resolution and chemical contrast had to be achieved at the newly-built ptychography experimental setup at the *"Hard X-Ray Micro-/Nano-Probe Beamline P06"* [35] at PETRA III in Hamburg. To this end, a set of well-defined model samples has been prepared, pre-characterized, and partially Pt tagged by high resolution electron microscopy, X-ray fluorescence mapping, and dual beam focused ion beam SEM respectively. This work was enabled and greatly supported in a collaboration with Christian D. Damsgaard (CEN, DTU).

4.2. Principle of Ptychography

Ptychography is a scanning coherent diffraction imaging method first described by W. Hoppe in 1969 [161]. In ptychography a transmissive sample is illuminated by a confined coherent beam and diffraction patterns are collected in the far field. The illumination is raster scanned across the sample, ensuring enough overlap between subsequent scan points, which is essential and influences the final image quality [162]. The size of the object can be larger than the beam size. Remarkably, the illumination might come from an optical laser, an electron beam, or a coherent X-ray beam. In general, the wave field is characterized by amplitude and phase. However, the measured diffraction pattern is only the magnitude of the transmitted wave field. Thus the phase information cannot directly be accessed, this is the so-called phase problem.

Essentially, ptychography is about retrieving the lost phase information to reconstruct the scattering object. The ptychographic data, presented herein, was reconstructed using the extended ptychographical iterative engine (ePIE) [163]. Historic background and well explained physical details can be found in a book chapter by Rodenburg [164].

4.3. Model Sample Preparation

All Ptychography samples were prepared by Juliane Reinhardt and myself in the *Center for Electron Nanoscopy* (CEN) hosted at the *Technical University of Denmark* (DTU) in Lyngby Denmark. Instrument time and training to inspect and characterize the samples was kindly provided by CEN. Further help on site was supplied by Christian D. Damsgaard (CEN) in the initial deposition trials and machine training. For the development of the ptychography method in the direction of chemical contrast and imaging of weakly scattering objects, it is essential to have well defined samples. To this end, great care was taken on the deposition and throughout pre-characterization of produced nanoparticle clusters.

Colloidal nanoparticles were used, as listed in table 4.1, to create diluted solutions (milli-pore water) for deposition on silicon nitride TEM grids, type TEM Windows SN100-A20Q33, having 20 nm thick Si_3N_4 windows eight of 100×100 and one of 100×350 µm in size. The TEM grids were attached to the sample holder by a carbon pad.

Table 4.1.: List of used colloidal nanoparticles for the preparation of the Au and Pt-Au-Pd mixed model samples.

Nanoparticle	Cat. No.	CAS	Size nm	Concentr. mg L^{-1}	Buffer	Supplier
Pt	78-1404	7440-06-4	10–15	100	acetone	Strem
Pt	78-1414	7440-06-4	50–70	100	acetone	Strem
Au	EM.GC100	7440-57-5	100±8	57	water	BBI
Pd	46-4012	7440-05-3	10–15	100	acetone	Strem
Pd	46-4022	7440-05-3	50–70	100	acetone	Strem

A single drop of nanoparticle solution was added to a Si_3N_4 window using an Eppendorf µL pipette. The liquid showed good wetting on plasma cleaned chips, spreading so fast that it left little time for the particles to move and thus often poor dispersion resulted. This could be compensated by addition of more droplets if needed. At the as-delivered chips, the liquid formed a drop on the surface and had to be moved around manually to distribute the nanoparticles and aid sedimentation/deposition. After successful deposition, drying was done at room temperature under an infrared light bulb.

The dried samples were studied by an optical microscope to quickly visualize the particle distribution and check for damaged Si_3N_4 windows due to deposition and handling. It this context, switching between bright and dark field images is useful, as shown in fig. 4.1. The detailed distribution of particles on a single windows was revealed by combining bright and dark field images to enhance the image contrast.

The most promising chips were studied by SEM to precisely locate the most suitable clusters for ptychography. For samples with more than one metal or multiple sizes, further in-depth characterization was done using EDX to determine composition of the nanoparticle clusters. For selected samples TEM was applied to measure sizes of the single nanoparticles with highest resolution, *cf.* fig. 4.2. This screening was aided by the 6-fold sample holder shown in fig. 4.2, which allowed mounting of multiple TEM grids at once.

For the ptychography experiment two types of samples were prepared and are described in the following: a simple mono-metallic Au nanoparticle sample and a multi-metallic Pt-Au-Pd nanoparticle sample.

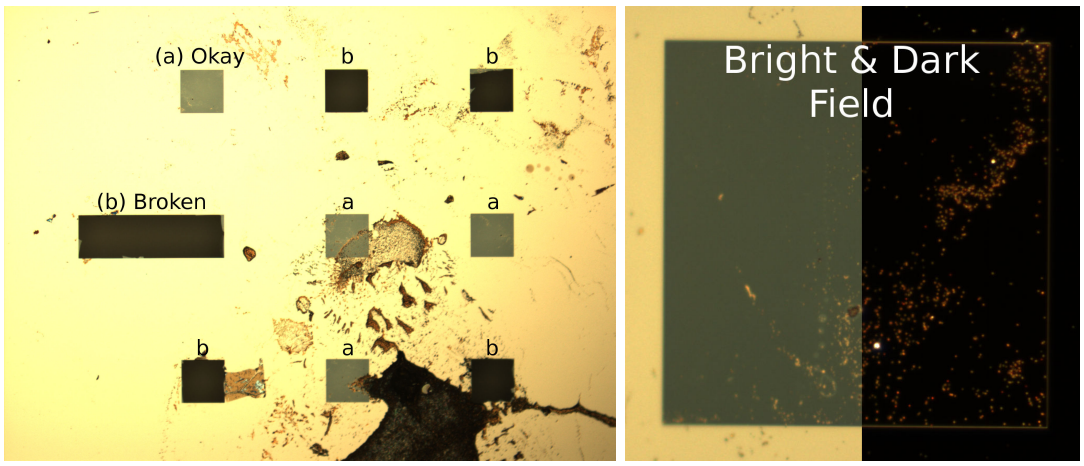

Figure 4.1.: Si_3N_4 chips inspected by an optical light microscope for quick sample inspection. Windows may be okay (a) or already broken (b) after handling and deposition solutions. Bright and dark modes are used to enhance image contrast. Square window size $100 \times 100\,\mu m$.

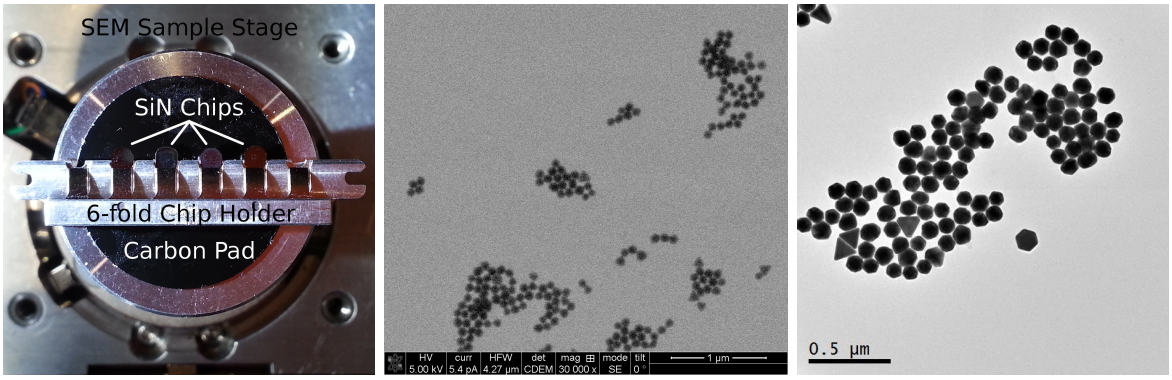

Figure 4.2.: Characterization of nanoparticle samples on silicon nitride windows. Left: 6-fold sample holder from SEM, middle: SEM image of Au nanoparticle clusters, and right: TEM of an AuNP cluster.

4.3.1. Gold Nanoparticles with Pt Marker

The first samples for XANES ptychography should provide a simple non-ambiguous system to develop analysis algorithms to extract elemental (chemical) contrast from ptychography experiments. Thus 100 nm large gold nanoparticles (*cf.* table 4.1) were selected, that had arranged in a simple cluster pattern and allowed easy identification as well as localization in the ptychography measurement. A single gold cluster near a Si_3N_4 window edge was found to be suitable and located by SEM.

Dual beam FIB-SEM was then used to additionally mark the most promising clusters by a Pt ring as shown in fig. 4.3. This allows to study effects of the chemical element on the ptychographic contrast, as the two elements are well separated and their distribution is well-known beforehand. Finally, the cluster was carbon coated to prevent charging of the sample in the X-ray beam.

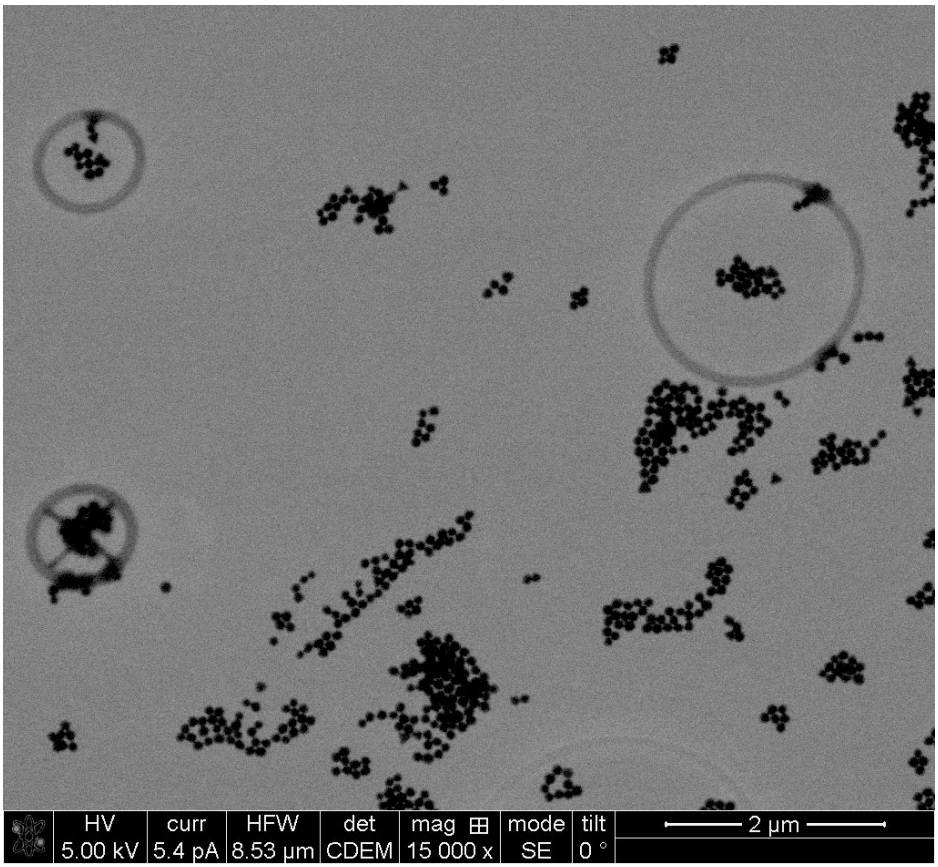

Figure 4.3.: SEM image of gold nanoparticle clusters deposited on a Si_3N_4 window and marked by Pt rings using a dual beam FIB-SEM. The upper left cluster was used for ptychography as shown in fig. 4.7.

4.3.2. Mix of Pt-Au-Pd Nanoparticles

A more complex system, to benchmark ptychography, was prepared from colloid solutions (*cf.* table 4.1) after successful ptychography imaging of the first sample type. It consisted of a mix of platinum (Pt), gold (Au) and palladium (Pd) nanoparticles, as shown in fig. 4.4, with individual particle size distributions between 10 and 100 nm.

A glass vial was filled with 1 ml of each nanoparticle solution. To aid thorough mixing of the solutions, it was rigorously shaken for some minutes, as well immediately before solution was retrieved from it for deposition.

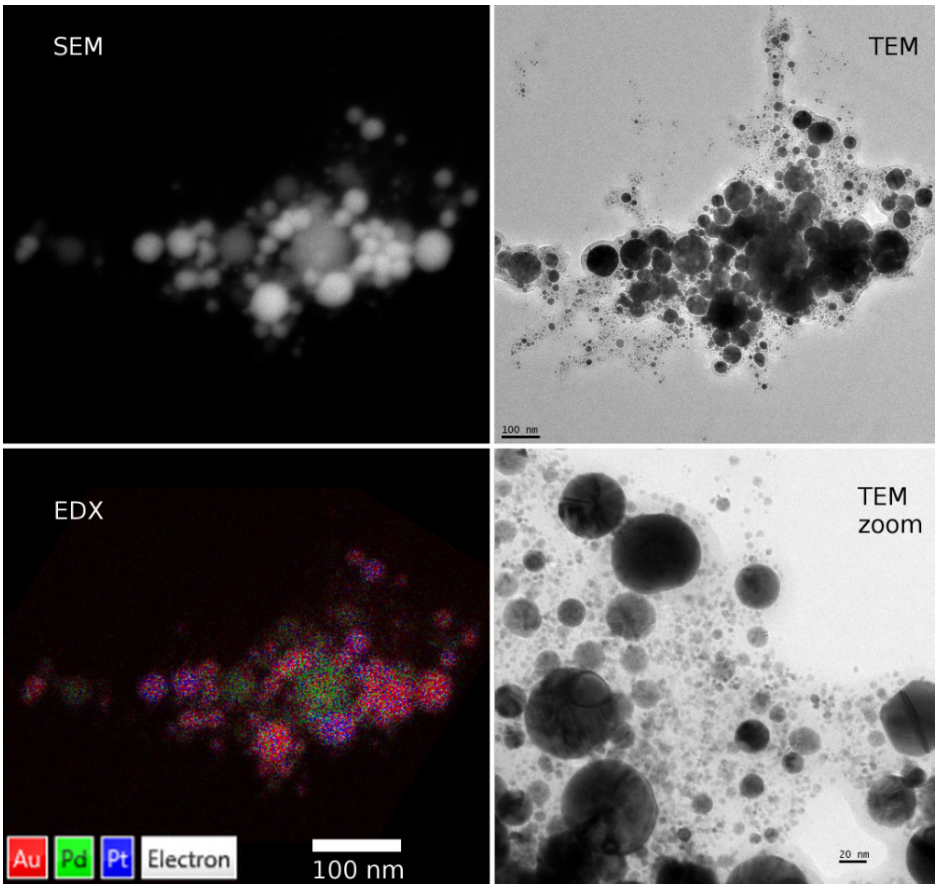

Figure 4.4.: Pre-characterization of a sample cluster composed of Pt, Au, and Pd nanoparticles by SEM, EDX, and TEM. Note: mixed colors in EDX are due to overlapping Pt and Au peaks [165] and not related to alloying.

Most important for this type of sample is a proper elemental mapping of Au, Pt, and Pd to enable correlation of size and type of the nanoparticles to ptychography. This was achieved using SEM in combination with EDX (CEN, DTU). A comprehensive characterization was done on several chips in order to find a suitable agglomerate containing all three chemical elements and preferentially all available particle sizes. An example of such a mixed nanoparticle cluster is shown in fig. 4.4. SEM indicates the presence of different types of nanoparticles based on the different gray values in the back scattered electron image. In TEM, the same sample was imaged on a similar scale and then further magnified to investigate smallest particles not observed by SEM.

4.4. Chemical Contrast in Ptychography

In this chapter, ptychography experiments are discussed that employed the specially crafted samples from section 4.3 on page 82. Besides pushing the current resolution limits for nanoparticle imaging by optimizing the acquisition protocols and experimental conditions (*e.g.* raster scan scheme, beam stops, flight tube), a focus was laid on probing and developing a methodology for imaging with chemical contrast suitable for applications in catalysis.

All measurements have been done at the *"Hard X-Ray Micro-/Nano-Probe Beamline P06"* at PETRA III in Hamburg [35]. In fig. 4.5 (a) the complete experiment inside the "Nano Hutch" is shown including CCD detector, flight tube, and fluorescence detector. In (b) we see a close-up of the 6-fold sample holder on the scanner table in front of the lens box and pinhole. Finally, the fluorescence detector and the entrance to the flight tube are put very close to the sample, as shown in (c) with view from the top.

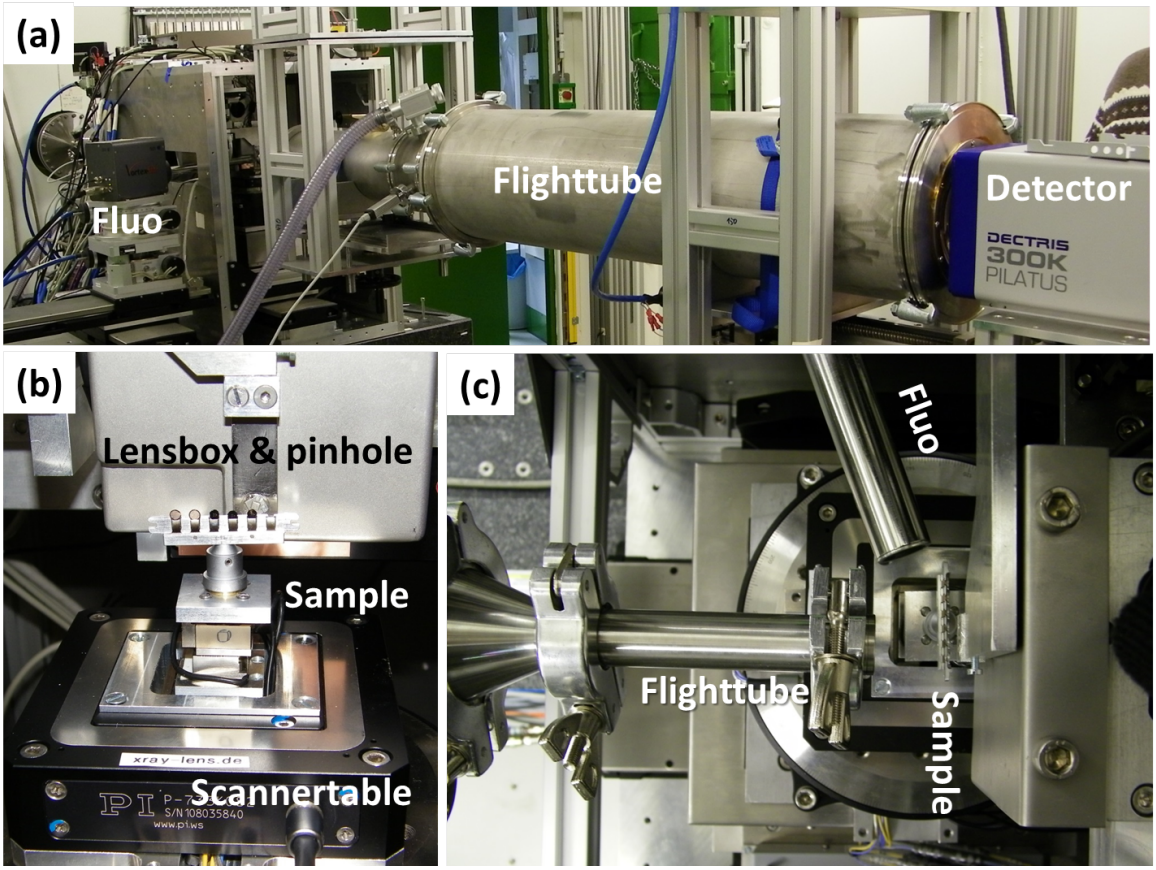

Figure 4.5.: Ptychography beamline setup at P06 with mounted 6-fold sample holder.

4.4.1. Au Cluster with Pt Ring

The gold nanoparticle cluster encircled by a deposited Pt ring, *cf.* section 4.3.1 on page 84, was used to develop a method to gain chemical contrast from hard X-ray ptychography. This was mainly conducted by Juliane Reinhardt within her diploma thesis. Further experimental details and results are reported in the corresponding publication [166].

Fluorescence Sample Mapping on Si_3N_4 Window

The first challenge was to relocate the desired nanoparticle cluster in the X-ray microscope. By using an optical microscope, the location on the TEM grid was roughly adjusted based on the position of the Si_3N_4 frame where it was found earlier and aligned to the assumed beam position. Then the Si_3N_4 frame was searched by raster scanning with the nano-focused X-ray beam (approx. 100 nm) to find the cluster. The initial alignment of the beam on the cluster is difficult as a too coarse raster might miss the cluster and a too fine raster is not feasible for large areas due to prohibitive scan duration. The fluorescence detector was used in a last step to get a map of composition and location of the sample, given a photon energy above a corresponding absorption edge.

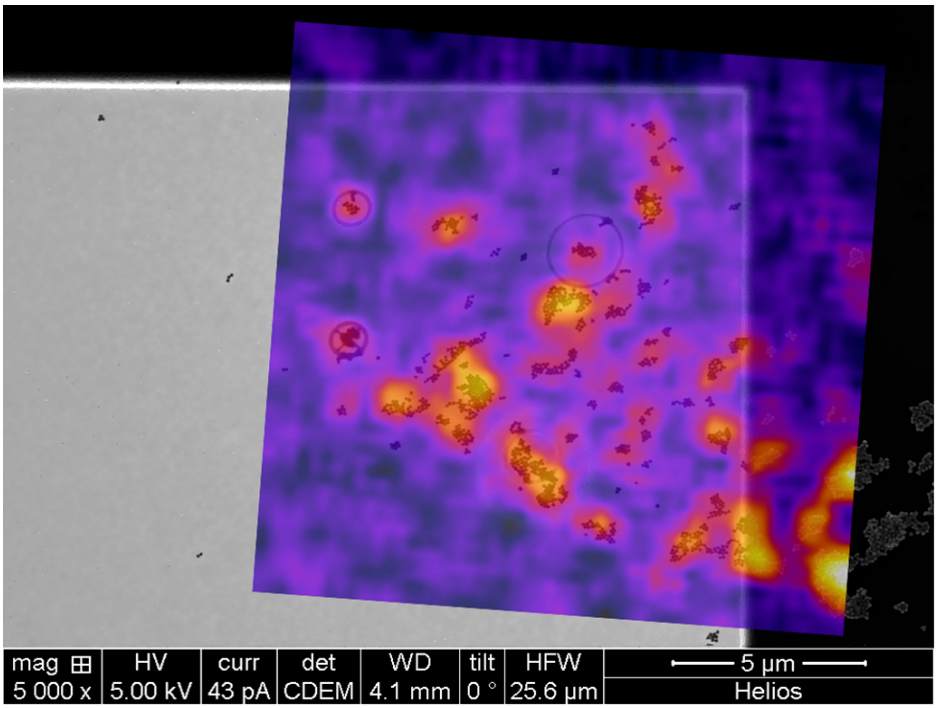

Figure 4.6.: SEM image and superimposed X-ray fluorescence map of Au nanoparticle clusters on the Si_3N_4 frame partially marked with Pt rings. The cluster of interest is found in the upper left corner of the fluorescence map.

An example of such a fluorescence map is shown in fig. 4.6 as an overlay to the previously acquired SEM image of the sample. In the latter, several Pt marked clusters can be seen in the gray scale SEM image. Distinct fluorescence signals are only detected

from the larger, more extended clusters which still requires to perform additional finer maps of the target region to resolve the structure of the cluster further. The cluster used for ptychography is located in the upper left corner of the fluorescence map in fig. 4.6.

Ptychographic Reconstruction and Chemical Imaging

The reconstructed data in fig. 4.7(c) shows that 100 nm gold nanoparticles can be resolved with a resolution of 19 nm using an exposure time of 1.5 s. This result is already the first success, since nanoparticles are weak scatterers do to the little mass contained within their volume.

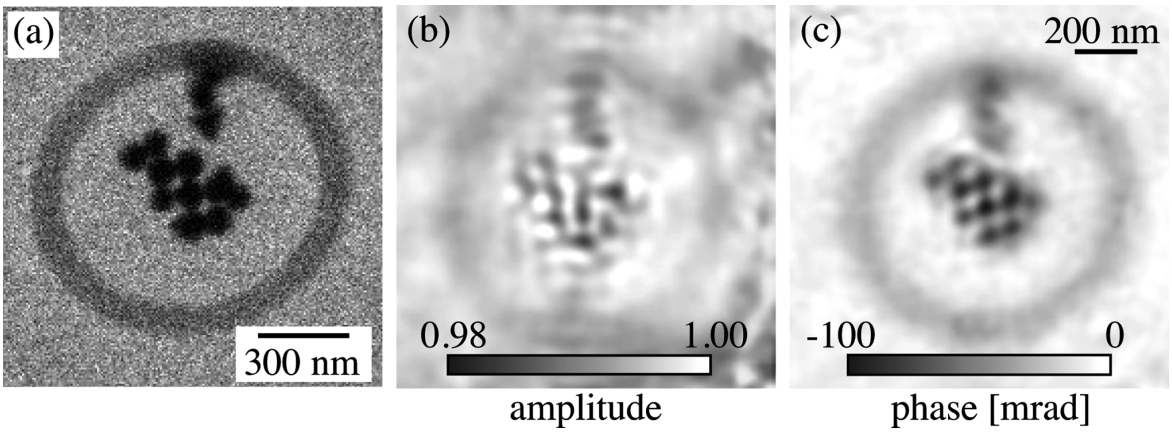

Figure 4.7.: SEM image and ptychographic reconstructions of amplitude and phase of the AuNP sample framed by a Pt ring. Reprinted with permission from [166]. Copyright 2013, AIP Publishing LLC.

The spectroscopic part was addressed next by recording a series of ptychographic scans as function of the photon energy, sampling across the Au L_3 absorption edge. An elaborated analysis of the phase shift as function of energy and sample position in each single reconstruction was carried out by J. Reinhardt. It was found, that the phase shift of the deposited Pt ring is almost constant, as expected. In contrast, the gold nanoparticles produce a significant dip in the phase shift signal as the Au L_3 absorption edge is approached. Hence one can discriminate the surrounding Pt from the Au nanoparticle cluster. More details can be found in the corresponding publication [166].

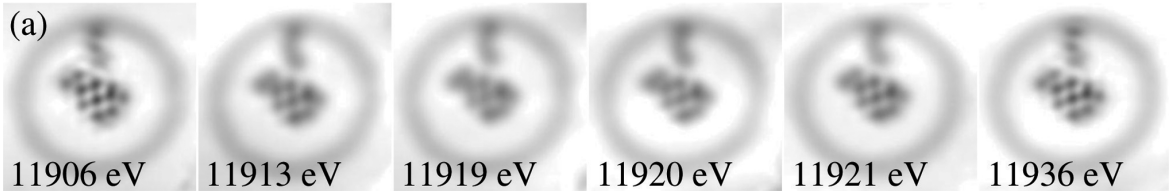

Figure 4.8.: Ptychographic reconstruction of the objects phase shift at selected energies crossing the Au L_3 edge at 11919 eV. Note that the resolution for image 2-4 is slightly decreased from 19 nm to 27 nm because a shorter exposure time of 0.3 s was used instead of 1.5 s. Reprinted with permission from [166]. Copyright 2013, AIP Publishing LLC.

The change in phase shift as function of energy can directly be seen in the image sequence in fig. 4.8, where darker gray values represent stronger phase shifts. Please note, that the left and right most images were acquired at 1.5 s with a slightly higher resolution as compared to 0.3 s for the others with slightly lower resolution, hence they are a bit more blurry. Nevertheless, the gray value for the Pt ring remains constant, the gray value for the Au nanoparticles changes with increasing energy from a darker gray below the absorption edge, to a brighter gray at the absorption edge, and back to darker gray for energies above. Thus, the experiment and analysis proves the ability to obtain chemical contrast and spectroscopic information in ptychography.

4.4.2. High Resolution Imaging of Pt-Au-Pd Nanoparticles

For the next sample, composed of platinum, gold, and palladium nanoparticles, *cf.* section 4.3.2 on page 86, the data is currently evaluated. Therefore only a first snapshot of the reconstruction is presented below.

In fig. 4.9 the cluster of Pd, Au, and Pt nanoparticles is imaged by SEM (middle) using the back scattered electron detector. The image clearly shows the different particle sizes and shapes, as well as characteristic gray values for the particular type of nanoparticle. This elemental distribution is further elucidated by an energy dispersive X-ray spectroscopy (EDX) mapping of the sample in fig. 4.9 (left), which identifies all three types of nanoparticle.

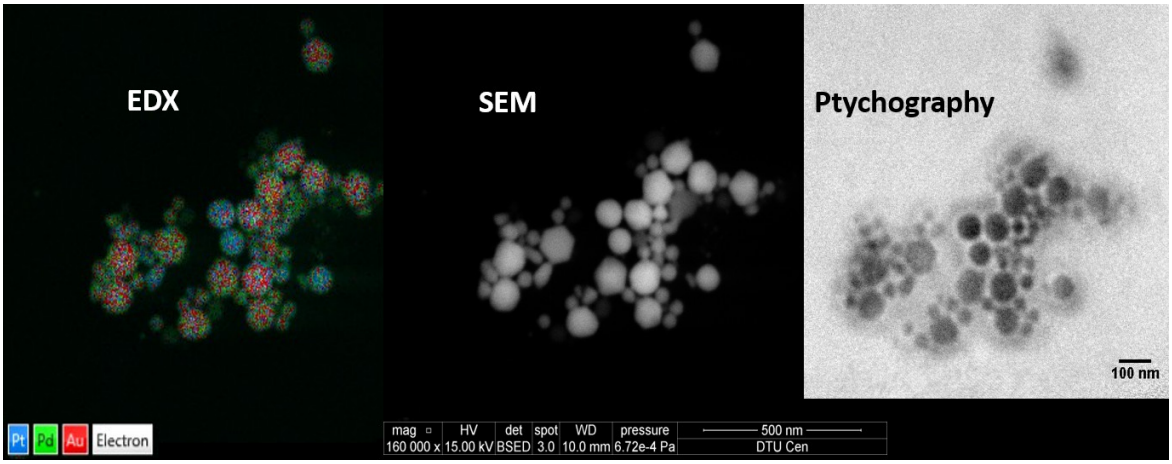

Figure 4.9.: Imaging of the mixed nanoparticle sample by SEM, X-ray ptychography, and elemental mapping by energy-dispersive X-ray spectroscopy (EDX).

A ptychographic reconstruction of the phase shift of the cluster is shown in fig. 4.9 (right). The image resolution is almost comparable to the SEM image, facets of larger particles as well as small particles are clearly resolved. In agreement with the SEM and EDX results, the ptychogram also shows similar grey values for similar types of nanoparticles.

Overall, these preliminary results demonstrate already a significantly higher resolution of around 10 nm in the ptychogram. In addition, the suitability of ptychography for chemical contrast imaging is again confirmed by observing a different brightness for different types of nanoparticles at a fixed energy.

4.5. Conclusion & Outlook

Well-defined model samples composed of Au nanoparticles with a Pt ring marker and a mix of Pt-Au-Pd nanoparticles have been prepared and pre-characterized by electron microscopy to further develop ptychographic imaging at the beamline P06 at PETRA III DESY. The focus was laid on nanoparticle imaging with chemical contrast, aiming at *in situ* experiments in a later stage.

The samples have been measured by ptychography and data analysis was carried out within the group of Prof. Schroer, that successfully yielded nanoparticle reconstructions with resolutions of 30 nm and 10 nm for the first (AuNP + Pt ring) and the second (Pt-Au-Pd NP mix) experiment respectively. Additionally, chemical contrast as function of the X-ray energy was exploited and quantitatively analyzed for the first sample, to clearly distinguish Au and Pt on the sample, that was greatly supported by the simple and well-defined sample design. Similar contrast was available for the second sample, where analysis is work in progress.

Within the two presented experiments, separated by one year, the resolution for nanoparticle imaging has evolved from approximately 30 nm to around 10 nm, due to steady improvements of the experimental setup and the reconstruction software developed by the group of Prof. Schroer. Both cases show the desired chemical contrast, which makes ptychography a promising tool for catalysis related studies.

In catalysis, spatially resolved *in situ* or *operando* methods are valuable tools that provid new insights on reaction mechanisms and kinetics [60, 61, 137]. Although environmental TEM and transmission X-ray microscopy offer excellent spatial resolution they cannot be used for *operando* studies due to limits in gas pressure, sample holders, and temperature ramps.

Hence, it is desirable to increase the spatial resolution of hard X-ray microscopy techniques and to work under operation conditions at the same time. The next step toward *in situ* imaging is the development of a reactor cell. This cell should be suitable for ptychography as well as for complimentary techniques like TEM, to ensure comparable experimental conditions. Thus alloying of nanoparticles and changes in oxidation state can be studied. In case of samples with pronounced topography it becomes necessary to perform tomography from ptychographic data sets to disentangle overlapping or stacked structures or to resolve volume effects as shown by refs. [167–171], done at the cSAXS beamline (PSI, Switzerland). This 3D ptychographic imaging was recently shown at P06 in pioneering work on polymers for solar cells [172]. In general, in such experiments thermal drift of samples and sample loss due to the gas stream can be anticipated and have to be compensated. Furthermore, numerous projections may be required to obtain highest 3D resolution. This results in long scan times and high X-ray dose on the sample [171], which has to be considered, *i.e.* with respect to sample damage.

Further improvements can be expected from a more stable scanner setup avoiding sample drifts, new detectors with smaller pixel increasing the resolution of the scattering pattern, combinations of flight tube and beam stops, and a more stable monochromator minimizing variations of the beam position.

Part III.

Device Design for in situ Experiments

5. Liquid Phase Experiments

5.1. Introduction

Gold nanoparticles (AuNPs) have found various applications in a broad spectrum of scientific fields like medicine and catalysis. This versatility and suitability to many different application aspects is provided by a big range of sizes and shapes [173]. Due to their versatile surface chemistry, they can easily be surface functionalized by well-established routes, for example based on linkage via thiols [174], or by electrostatic bonding of amines [175], either stabilizing the particles or load them with biologically active functionalities and drugs.

This makes them an ideal tool for a variety of applications ranging from engineering [176] and electronics [177] to medicine [178] and biology [179]. For example, AuNPs have been used in tumor detection [180, 181] as drug carrier [182], for photothermic tumor therapy [183], and as dose enhancer in tumor radiotherapy [184]. Besides their widespread use in these fields, they are also used as sensors [185], for example in the detection of heavy metal ions, water pollutants, toxins, and surface antigens. A comprehensive review on this topic was given by Saha *et al.* [179]. Their color properties also render them useful as probes for dark-field microscopy [186] and in transmission electron microscopy [187], as well as in tomography [188]. Another outstanding property of AuNPs is their catalytic activity at low temperatures, even below room temperature, when deposited on metal oxide surfaces or carbon [189]. The reactivity of gold is likely related to the amount of low coordinated sites such as edge or corner atoms as suggested by density functional calculations [190, 191] as well as their interaction with a transition metal oxide support [192], making AuNPs extremely reactive. Gold nanoparticles are used for various reactions like oxidation of CO to CO_2 [193], selective oxidation of alkynes in the presence of alkenes [194], as well as reduction of nitrogen oxide [195]. An overview about this broad field is given in several reviews [155, 189, 196–198].

Depending on the reaction of interest, the size of the AuNPs has to be adjusted to ensure maximum reactivity and/or selectivity. For example, for the oxidation of benzyl alcohol, it was found that a particle size of 6.9 nm was best [199], whereas for CO oxidation smaller particles in the range of 1.3 nm show the best performance in relation to total gold loading of the catalyst [200].

These few examples demonstrate the diversity of AuNPs, where size and shape are tailored to fit the particular application. Accordingly, a number of synthesis routes exists, with a multitude of variations in order to obtain the desired nanoparticle properties. A very elaborate overview on the state of the art in gold nanoparticle synthesis is given in [201] and similarly but with additional focus on various applications

in [155]. Moreover, recent development in seed mediated growth of AuNPs was reported, enabling a variety of shapes like dendrimers, rods, nanourchins, cubes or even flat membranes [202–204].

In general, the preparation of AuNPs with a well-defined size and narrow distribution down to almost monodispersity is desired, especially when AuNPs are used as seed for further growth and for catalysis. A prominent route of AuNP synthesis in liquid phase is the reduction of $HAuCl_4$ by a reducing agent, usually in presence of a surfactant or other surface active chemical that prevents uncontrolled growth of the formed AuNPs. There exist several routes for the preparation of AuNPs in the range < 30 nm. Most commonly used is citrate [205–207] in the Turkevich reaction and its variations, which produces around 10-20 nm spherical-like particles with medium dispersity in a slow reaction at high temperatures. Here, citrate both acts as a reducing agent as well as a stabilizer. Another often used reducing agent is $NaBH_4$ activated by NaOH in a two-phase system with water in the Brust-Schiffrin Method [208], which yields functionalized AuNPs. In a modified one-phase-reaction, developed by Martin [209], nearly monodisperse, non-functionalized spherical particles of 3-6 nm diameter can be synthesized with $NaBH_4$ depending on the stoichiometry of the educts in the solution. A third method to generate very small nanoparticles without additional surface functionalization is the use of tetrakis(hydroxymethyl)phosphonium chloride (THPC), as proposed by Duff *et al.* [210], which routinely yields 0.9-5 nm particles with very low dispersity in a very fast reaction (within seconds) at room temperature. This method was later successfully used in catalysis [199, 211, 212]. However, it is relatively new and therefore not investigated in-depth yet as much as the other methods.

Although this great variety of shapes and applications already exist, the synthesis conditions are usually optimized based on the outcome of the synthesis in a trial-and-error manner. However, the need for extremely well defined AuNPs calls for an even better control of the process, aided by knowledge of the particular reaction mechanisms and kinetics. Especially, the understanding of nanoparticle synthesis in the early phase of nucleation and their further growth is important to derive new rational synthesis routes for well-defined and tailored reaction products.

This requires *in situ* observation of these reactions [213] to verify theories of growth mechanisms and kinetics as given in [214, 215]. Typical methods to study such mechanisms are reviewed in [216, 217], while *in situ* methods to capture the relevant dynamics, for example ensemble averaging characterization techniques like X-ray absorption spectroscopy (XAS), small angle X-ray scattering (SAXS) and UV-vis spectroscopy, are discussed elsewhere [213, 218, 219]. Notably, complementary approaches were reported, using a liquid cell TEM or single particle spectroscopies to track individual particle formation and kinetics [220–222].

In the context of *in situ* characterization the use of microfluidic devices for rapid and thorough mixing is well established. Such devices not only allow the preparation of nanoparticles but also the investigation of early reaction states, given a suitable, controlled flow regime is used [223, 224]. In general, microfluidic devices provide improved reaction control [225–230]. Naturally, this leads to a growing field for application of microfluidic devices in nanoparticle synthesis in general [223, 231–236] and for AuNPs [237–243] in particular.

The formation of AuNPs in such devices was successfully studied by Polte *et al.* [244–246] and Abécassis *et al.* [247, 248] using XAS, SAXS, and UV-vis for citrate and BH_4^- based synthesis routes. Notably, a fast gold reductions was observed within the first 200 ms. However, observations of the first 100 ms of reaction were not possible due to the experimental setup or acquisition time of the spectroscopic method used in the stopped flow apparatus, respectively. An outcome of this work is the need for a fast data acquisition in case of stopped flow or measurements in continuous flow to enhance time resolution at the very early stage of the experiment to cover the initial growth kinetics or to correlate time and measurement position to enhance resolution.

As the reaction of THPC with $HAuCl_4$ was not yet studied in such a setup, the AuNP formation using THPC as reducing agent shall be investigated in the following, to understand this rapid reaction yielding very small spherical nanoparticles. To best knowledge, only the late growth phase of AuNPs from THPC was studied yet from 10 to 700 minutes [249]. To this end, a setup with very short dead times, high time resolution, and compatibility to *in situ* XAS and SAXS measurements is presented.

5.2. Experimental Approach

The basic idea of the liquid phase experiment is depicted in fig. 5.1. The educts are provisioned by a fluid storage and a delivery system, which supplies material at desired volumetric flow rates into a micro mixer device. Here a rapid and thorough mixing of the two liquid streams is achieved by utilizing turbulent flow conditions in specially designed and custom-built micro mixer devices. Ultimately, the reaction mixture arrives in an observation line where it is, for example, measured by X-ray absorption spectroscopy.

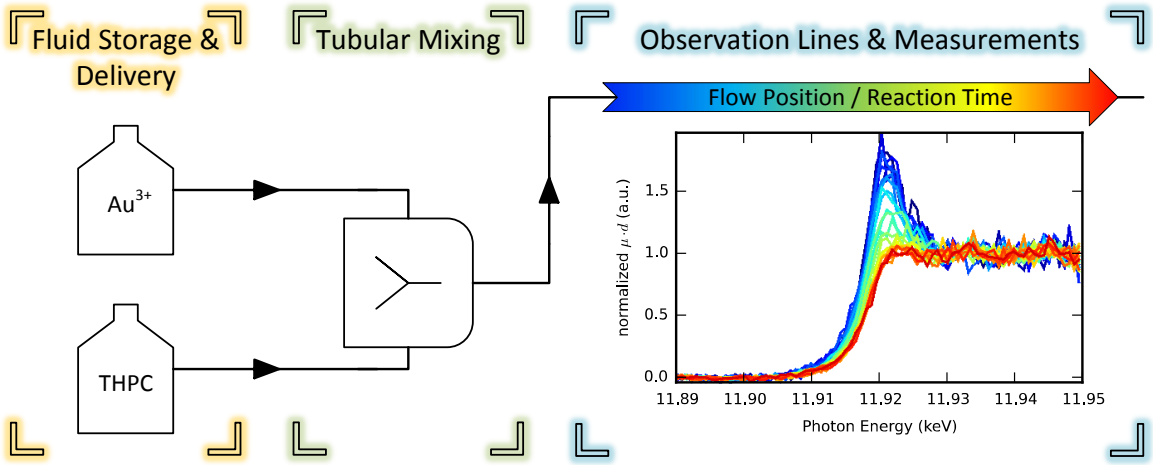

Figure 5.1.: Fundamental experimental principle for the investigation of liquid phase reactions.

As indicated in fig. 5.1, measurements at given flow positions x are mapped and correlated to a specific reaction time t, which yields individual snapshots of the reaction progress. By making use of a turbulent flow in the observation line, a plug flow is formed resulting in short residence times of the liquid. This allows to calculate the

reaction time t by using eq. (5.1), where A is the channel cross section, x the position along the flow, and Q the volumetric flow rate.

$$t = \frac{A \cdot x}{Q} \tag{5.1}$$

It must be emphasized that this simple calculation demands a flat flow profile as present in a turbulent plug flow. In case of laminar flow, the resulting parabolic flow profile would produce a convolution of residence times, thereby degrading temporal resolution considerably.

5.2.1. Gold Colloid Synthesis using THPC

As model reaction for the liquid phase experiments, the synthesis of gold nanoparticles from $HAuCl_4$ solution and tetrakis(hydroxymethyl)phosphonium chloride (THPC) solution as reducing agent was chosen. This route was found to produce small gold nanoparticles of around 2 nm in diameter within a few seconds at room temperature [210, 211].

The preparation follows the protocols given in the above literature. The following chemicals have been used: Gold(III) chloride hydrate, $HAuCl_4 \cdot xH_2O \geq 49\,\%$ Au basis (Sigma-Aldrich), tetrakis(hydroxymethyl)phosphonium chloride ($[P(CH_2OH)_4]Cl$) solution 80 % in H_2O (Sigma-Aldrich), and 1.0 M NaOH solution (Sigma-Aldrich).

To produce the gold sol two beakers were put on a magnetic stirrer. The first beaker was filled with 46.3 ml dest. water and 1.2 ml of 43 mM $HAuCl_4$ solution. The second beaker, was filled with 1.5 ml of 0.2 M NaOH solution and 1.0 ml of diluted THPC solution (1.2 ml of 80%-THPC in 100 ml water). After adding THPC, 2 minutes are allowed for mixing, then it was added to the Au solution in the other beaker. An immediate color change from pale yellow to dark brown orange took place, indicating the formation of nanoparticles. Decisive are pure reaction vessels, cleaned normally by aqua regia, and fresh solutions.

For continuous flow experiments a 1:1 volumetric mixing of the two solutions was used by distributing the water accordingly. A similar fast reaction and colored solution as in the original route was found in laboratory tests.

5.3. Fluid Storage & Delivery

As shown in fig. 5.1, the first part of the experimental setup is the fluid storage & delivery system. For a proper design of this part, the requirements of the reaction under observation and the other parts of the experiment have to be considered.

For turbulent flow experiments high volumetric flow rates and potentially high feeding pressures are needed. To maintain steady flow conditions and to mix a pulsation free flow a long or even continuous operation is desirable. A remote controlled flow setup and logging is needed. Additionally, all parts in contact with the reaction fluids need to be chemically stable under operation. In case of the Au-reduction reaction this means that the $HAuCl_4$ carrying branch must be resistant to corrosion.

Based on these design requirements two possible realizations were identified and are presented in the next section: a purely commercial setup based on syringe pumps and a home made fluidic rack.

5.3.1. Syringe Pump Setup

The above-mentioned design requests are met by a system from *cetoni GmbH*, which was purchased and tested. It consisted of a base unit providing power supply, motor controller, and Ethernet port (via external CAN bus to Ethernet converter from *IXXAT CAN@net II/VCI*), four mid-pressure dosing modules (max. pusher force 1000 N), and four 50 ml glass syringes. According to the manual, a single syringe and dosing unit can cover flow rates from 1.519 µl min^{-1} to 269.533 ml min^{-1} with a single dosing step of 16.516 nl and up to 10.39 bar pressure.

The pump was controlled by cetonis *neMESYS User Interface* software, which allows to set flow speeds and running a continuous mode combining the movement of two or more drivers. Remote control was possible, since the device was connected over Ethernet via existing LAN infrastructure or own cables. The syringe pump setup is shown in fig. 5.2, mounted for experiments at the SLS. According experiments using the syringe pump are found in section 5.6 on page 107. Due to shortcomings of this setup, which became evident during these experiments, an alternative solution, the fluidic rack, was developed.

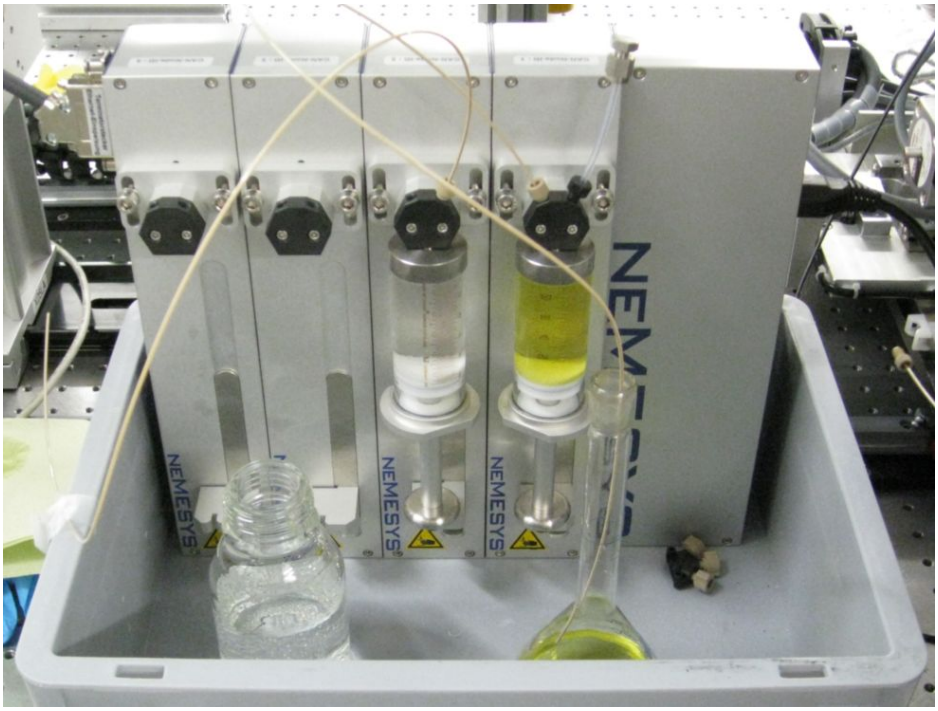

Figure 5.2.: Syringe pump setup from centoni GmbH used at the MicroXAS beamline at SLS for *in situ* XAS experiments on the AuNP formation. The syringes are loaded with the gold precursor solution (yellow) and THPC+NaOH reducing agent (colorless) respectively.

5.3.2. Fluid Delivery Rack

A home made solution, meeting the above design requests, is the fluidic rack. It has been designed and constructed in cooperation with the group of Dr. Rinke (IMVT KIT) at IMVT. The basic idea is to use hydrostatic pressure to achieve pulsation free and continuous pumping of the liquids. As shown in fig. 5.3 a set of vessels is used to store the educt liquids, which can be pressurized independently to set-up the desired flow rates per branch. The particular gas pressure per vessel for a given target flow rate depends strongly on the back pressure present in the whole system and has to be adjusted individually. Finally, the desired total flow rate and mixing ratio can be adjusted. In a last step, the two flows are mix rapidly in a microfluidic mixer and the product stream is fed into observation lines to trace the reaction.

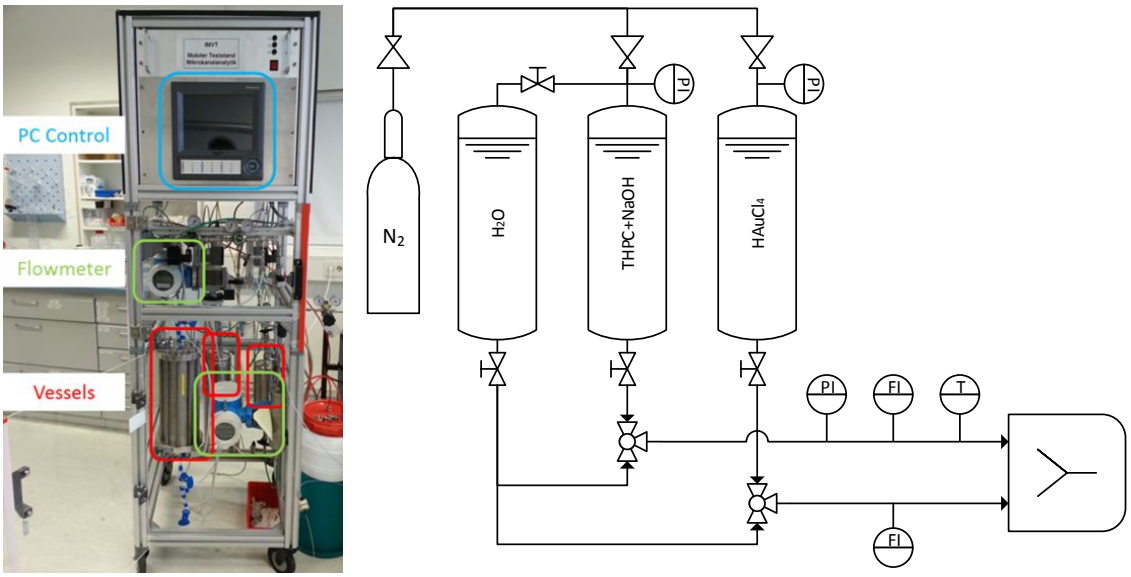

Figure 5.3.: Photograph of the fluidic rack with PC logging, flow meters, and liquids vessels (left) and a simplified flow scheme of the setup (right). Symbols are: pressure indicator (PI), flow indicator (FI), and temperature sensor (T).

The rack frame measures $0.6 \times 0.6 \times 2.0$ m and is assembled from commercial aluminium profiles. It consists of three modules, as shown in fig. 5.3 on the left. The PC module is positioned on the top, flow meters, valves, and pressure regulators in middle module, while fluids are stored in the bottom module in two 2 l vessels for water and reducing agent (Festo CRVZS-2). They are pressure tight up to 16 bar. Furthermore, a 2.5 l custom made corrosion resistant vessel with high-density polyethylene (HD-PE) inlay (Tri System GmbH, Waghäusel-Kirrlach) for the gold precursor solution is situated there. It is also pressure tight up to 15 bar. The flow was measured by a *Promag* and a *Promass* flowmeter (Endress+Hauser AG) on the Au and on the water/THPC branch respectively. Experiments using the rack are presented in section 5.7 on page 113.

5.4. Turbulent Mixing using Stand Alone Cyclone Micro Mixer

The second part of the setup are the mixers, providing rapid and thorough mixing under turbulent conditions *cf.* fig. 5.1. Two different designs were realized based on cyclone-type mixers.

A stand-alone cyclone mixer made of PEEK had been developed and manufactured at IMVT KIT recently [250], which is shown in fig. 5.4. It is well suited for the purpose of preliminary experiments. PEEK, polyether ether ketone, is a semicrystalline thermoplastic material widely used for chemical and analytical applications such as chromatography columns due to its excellent mechanical and chemical stability across a wide temperature range and against most aqueous acids and bases [251].

The mixer was built into a five cent sized PEEK disk and mounted inside a support block. It was used for pioneering experiments and as fall back solution, since several mixers were produced and laid in stock to replace clogged ones.

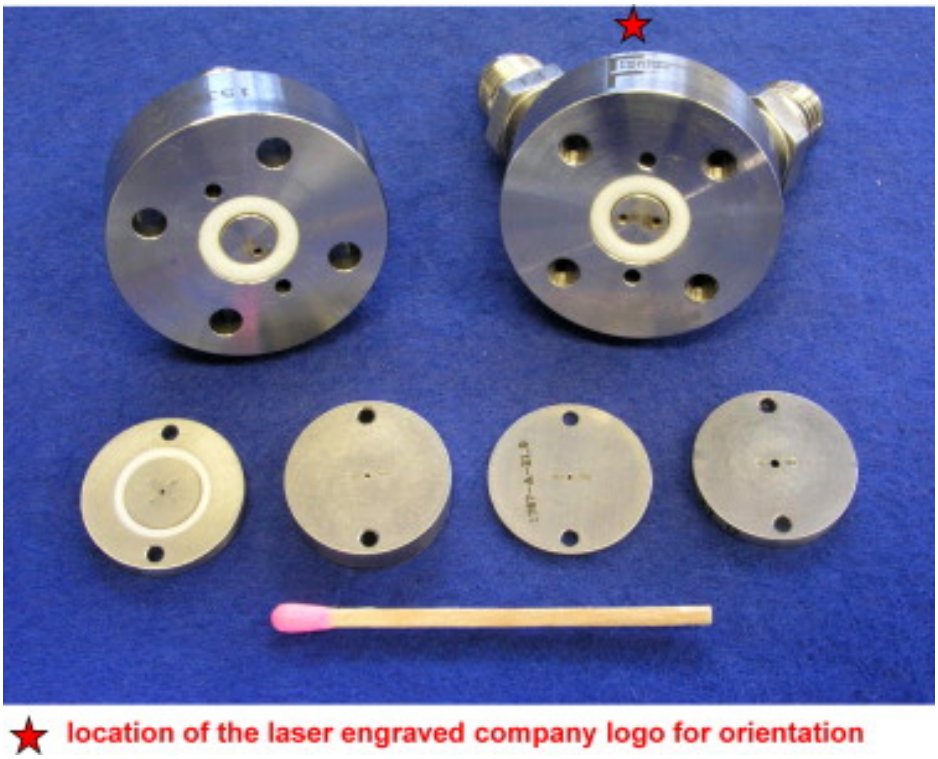

Figure 5.4.: Example of PEEK mixers (brown disks in the front row), as used in this work. Reprinted from [250] with permission from Elsevier.

The mixer outlet was then connected to commercial PEEK capillaries, that acted as observation lines. These are standard components for high performance liquid chromatography (HPLC). In the experiments, capillaries with an outer diameter (OD) of 1/16 inch (1.5875 mm) and inner diameters (ID) ranging from 0.5 to 1.0 mm were used.

However, observation times below 20 ms and without dead-time cannot be achieved using this setup, since the fittings that are used for the connection prevent a measure-

ment in that region. Further reduction of the inner diameter decreases the minimal observation times a little but also reduces the amount of sample, which in turn decreases the sensitivity of the experiment.

5.5. Liquid Phase Chip – Design and Fabrication

An alternative approach is the combination of mixer and observation line, minimizing dead-times due to the compact dimensions of the device and a more precise and rapid measurement of different points along the observation line, as a meandering structure is more compact than a linear capillary.

As the device is working in turbulent flow with potentially high liquid feeding rates and high flow back pressures, a pressure tight fabrication is of utmost importance. Moreover, geometrically precise fluid channels are required to exclude variations of the channel cross-section. Too large or too small cross-sections might lead to a laminar flow or increased back pressure respectively. It also enables a precise mapping of spatial coordinates to reaction times.

The optimal design of the liquid phase chip is not only determined by fluidics but also by the restrictions set by the spectroscopic method used to follow the reaction, in this case X-ray spectroscopy.

For the investigation of gold nanoparticles, X-ray stable and transparent materials for photon energies around 12 keV are needed. In addition, no fluorescence signal should be emitted from the window material itself to minimize background in the spectra. The chip thickness has to be compatible with the detection of fluorescence signals from the liquid. Since observation of the channel is not possible under 90° to the chip surface, a geometry factor has to be taken into account, that further limits the maximal thickness of the device. Additionally, the inner diameter of the channels must be large enough to allow enough absorption of radiation by a sample. No beam or detector blocking parts should be present either in the chip nor the support.

The support itself should ensure leak free feeding of the liquids to and from the chip. Connections on the support should be standard fluid parts, *e.g.* compatible with HPLC ports and fittings.

Additionally, to probe reactions at very early stages, dead-time has to be as low as possible. This means that rapid and perfect mixing of educts by a specially designed built-in mixer should be directly followed by the observation line. Finally, the materials used, need to be chemically inert against reaction solutions and cleaning solutions.

Liquid Phase Chip Layout

The liquid phase chip was realized in close collaboration with GeSiM GmbH, IMVT KIT, and IHM TUD who shared construction tasks. The liquid phase chip was based on a 1500 µm thick Si wafer with a diameter of 4 inch. This was obtained by Si fusion bonding of two 750 µm wafers. These contained an integrated microfluidic mixer

(cyclone type) and fluidic channels for observation. Hence, all fluidic parts were realized by structuring the silicon wafer by deep reactive ion etching.

In fig. 5.5 a design drawing of the chip and a schematic cross-section is shown. A tailored stainless steel support sandwiched the chip and carefully pushed an O-ring tightened fluid connection on the chip. Details are provided in the following sections.

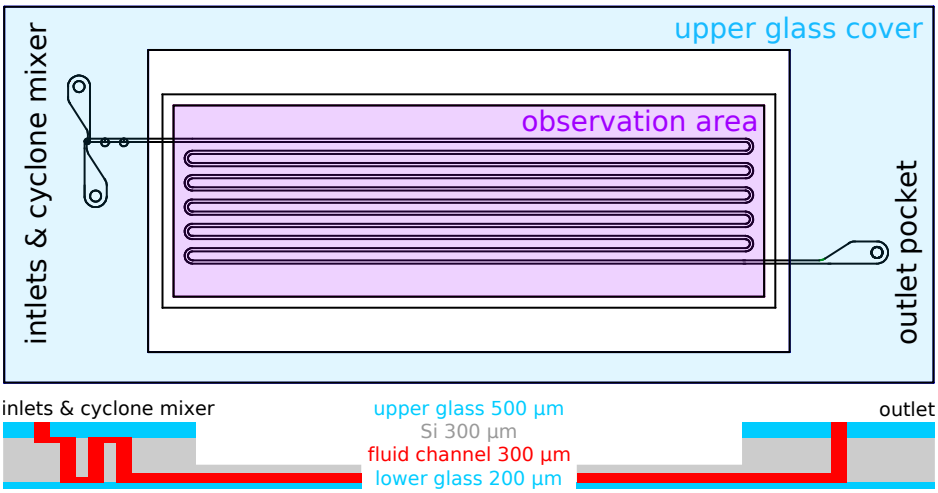

Figure 5.5.: Design drawing of the liquid phase chip (top) with outer dimensions of 34×84 mm (src.: modified GeSiM drawings). The observation area of 19×55 mm is thinned down as can be seen in the schematic chip cross-section (bottom).

The upper side of the chip was partially covered by 500 µm thick glass (blue shades) and hosted inlet and outlet ports. In the central area of the chip the observation area was located, on the opposite side of the meander structure, which was especially thinned down to allow experiments in transmission mode. Thus, only 300 µm of Si had to be passed in addition to 200 µm of the lower glass layer and 300 µm of sample in the fluid channel.

The bottom side of the chip was completely covered by a 200 µm thick glass and acted as lid for the fluid channels in the meander, which had a dimensions of 300×300 µm. In fluorescence measurements, X-rays were guided to the bottom side and fluorescence is detected from it as well.

Laser drilling was used to manufacture the holes in the top glass layer for the inlet and outlet ports. Furthermore it was used to create the cylinders for the cyclone mixer in the silicon chip. The meander channels and fluid pockets were produced by Si etching conducted at IHM TUD. Anodic bonding was used for the glass-Si parts and fusion bonding for the two 750 µm Si wafers to achieve the desired thickness of 1.5 mm.

Please note, the chip used later on had only 3 meander lanes as shown in fig. 5.9. In the initial configuration it was designed for a total flow of $2.5\,\mathrm{kg\,h^{-1}}$ resulting in a Reynolds number of 2350 (turbulent flow), a pressure drop of 12 bar, and an observation time ranging from 1 to 15 ms. Thus, an additional pressure drop of 2 bar for the fluidic rack is still within the operating conditions.

Integrated Cyclone Mixer Design

To achieve the desired rapid and thorough mixing, a design based on cyclone type mixers was chosen [250]. The best mixing was found for a series of three cyclones, *cf.* fig. 5.6, confirmed by computational fluid dynamics (CFD) simulations. These have been conducted by A. Wenka (IMVT KIT) using ANSYS Fluent 14 [252]. In this design each cylinder had a height of 1500 µm and diameters of 500 µm for first and 700 µm for the following two cylinders. They were connected by 300×300 µm large channels attached tangentially to the cylinder. Assuming a total flow rate of $2.0\,\mathrm{kg\,h^{-1}}$ this cyclone structure will emit the mixed fluids after a residence time of 2.9 ms and cause a pressure drop of 1.92 bar.

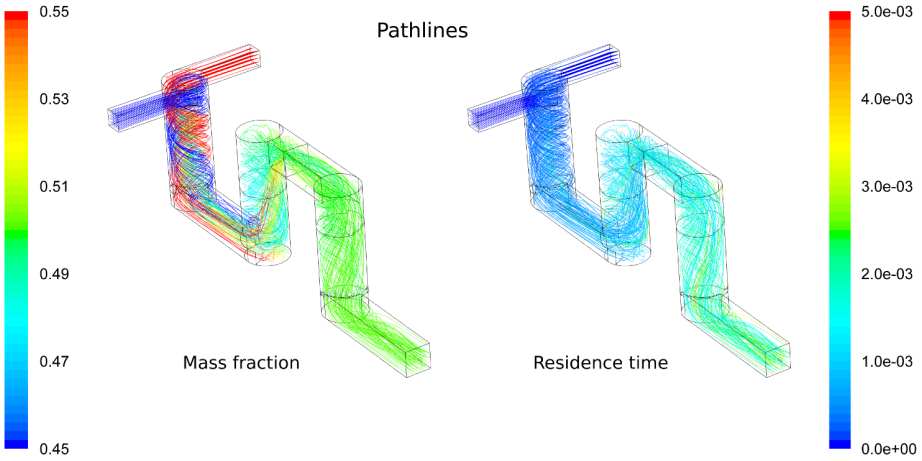

Figure 5.6.: Simulation results for the triple cyclone mixer, showing the mass fraction (left) and residence time in seconds (right). Total flow $2.0\,\mathrm{kg\,h^{-1}}$, residence time 2.9 ms, pressure drop 1.92 bar, cyclone height 1500, diameter 500, 700, and 700 µm, channel width $300 \times 300\,\mu\mathrm{m}$. CFD simulation by IMVT KIT.

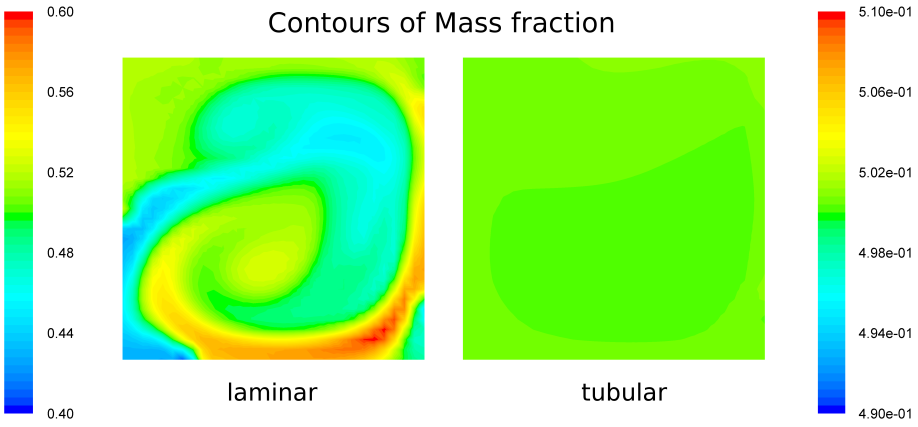

Figure 5.7.: Results of simulated mass fractions at the mixer outlet. Cross-section are shown for laminar (left) and turbulent flow (right). Total flow $2.0\,\mathrm{kg\,h^{-1}}$, channel width $300 \times 300\,\mu\mathrm{m}$. CFD simulation by IMVT KIT.

The simulation result, shown in fig. 5.6, displays the pathlines of the mixing fluids along the mixer structure in terms of mass fractions (left) and residence time (right). A good mixing (green) is not achieved before the third cyclone column. After the third cyclone a perfect mixing is created at the outlet, as shown in fig. 5.7 on the right. The stream leaves the mixing structure after 2.9 ms and the residence time pathlines show no significant residence time distribution of the emitted stream.

To underline how crucial the turbulent flow is to achieve optimal mixing results, fig. 5.7 is shown for laminar and turbulent flow conditions. While in the turbulent flow no changes are visible in a mass fraction range of 0.50 ± 0.01 ($\pm 2\%$) the laminar flow shows significant mixing inhomogeneities on a 0.5 ± 0.1 ($\pm 20\%$) scale.

Chip Support

The Si chip was mounted inside a frame-like support made from stainless steel consisting of two parts sandwiching the chip, as shown in fig. 5.8. It was designed and fabricated with respect to the above requirements in collaboration with GeSiM.

The upper frame, left image in fig. 5.8, provides two centered screws (gray cylinders) at both ends to tightly connect the two frames. In total, five ports with $1/4 - 28$ UNF threads are present to connect tubings for fluid delivery, three of them were actually used, indicated by the blue screw nuts. As can be seen on the lower frame, several alignment pins are integrated to hold the chip in place and align both frames properly.

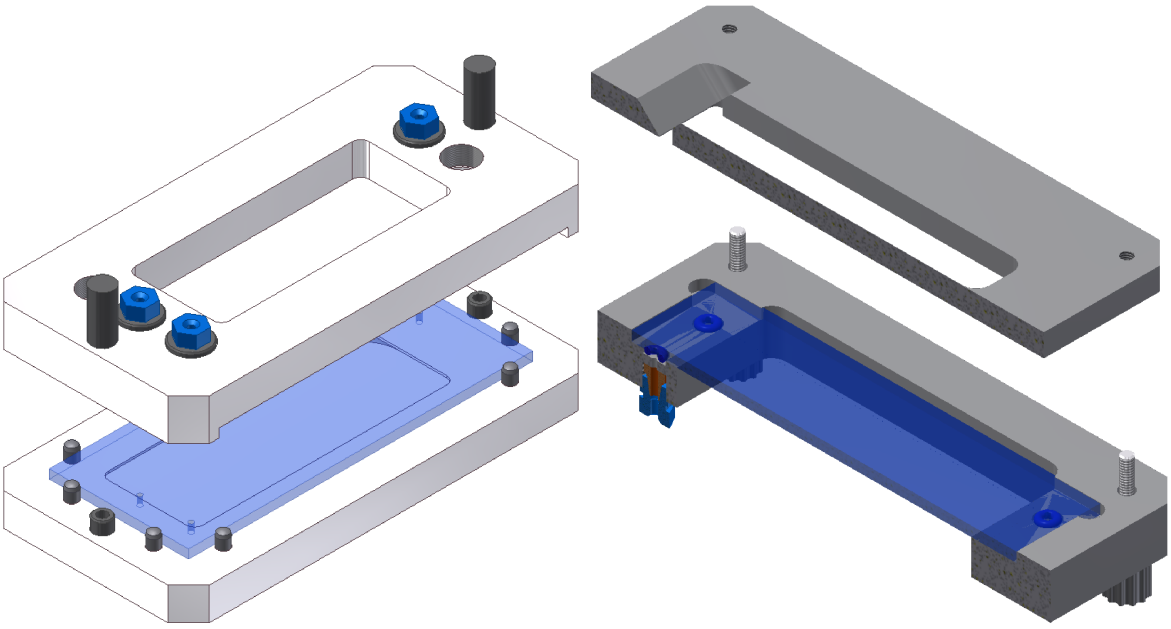

Figure 5.8.: Design of the liquid phase chip support. View on the upper side with connectors (left) and on the lower side (right). The chip is indicated by the blue shaded plate between the two frames. Images by GeSiM.

A leak-tight installation of the chip was achieved by placing O-rings between the upper side of the chip and the inner side of the upper support frame fig. 5.8, lower right. Please notice the remaining layer of Si between the ferrule (red) and the O-ring (blue).

Therefore frame and chip thickness as well as the alignment have to fit precisely to avoid leaking or breaking of the chip. This approach was used for all fluid connections to the chip.

To prevent blocking of emerging fluorescence close to the frame border, the window is machined under an angle of 45°, *cf.* fig. 5.9, while the top frame is cut-out straight under 90°. Furthermore, the outer side of the lower frame is kept flat to allow close positioning of detectors, see top right pane in fig. 5.8. The dead-time is minimized by placing the mixer outlet in the chip as close as possible to the edge of the frame. The total residence time of the fluid in the device is limited to 15 ms, thereby bridging the dead-time present in the experiments done with the PEEK cyclone mixer.

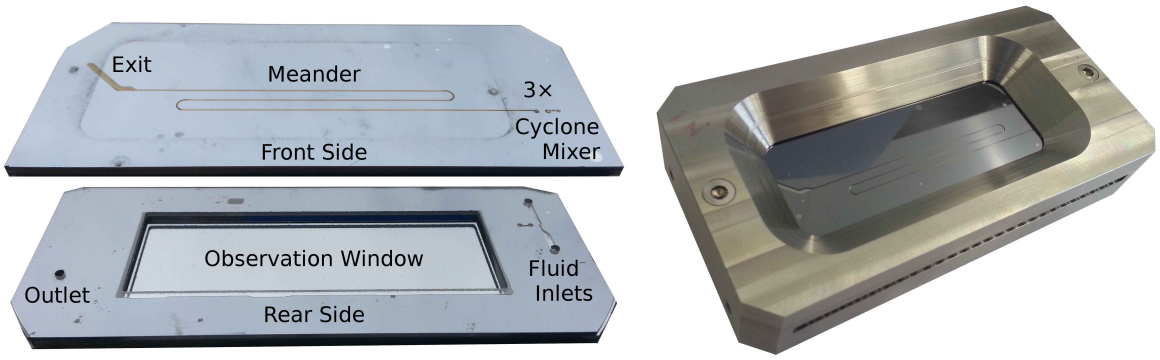

Figure 5.9.: Photographs of microfluidic chip (left) and the assembled support (right).

In fig. 5.9 a manufactured microfluidic chip is shown separately as well as installed into the stainless steel support. The entire setup for liquid phase experiments, was then tested *in situ* with the aforementioned test reaction, the formation of gold nanoparticles from $HAuCl_4$.

5.6. Syringe Pump in situ Experiments

A brief two days test experiment was conducted at the MicroXAS beamline at the Swiss Lightsource (SLS) [34]. During this time, the syringe setup as introduced in section 5.3.1 on page 99, various mixers, and XAS measurement protocols were tested. The experimental setup is shown in fig. 5.10.

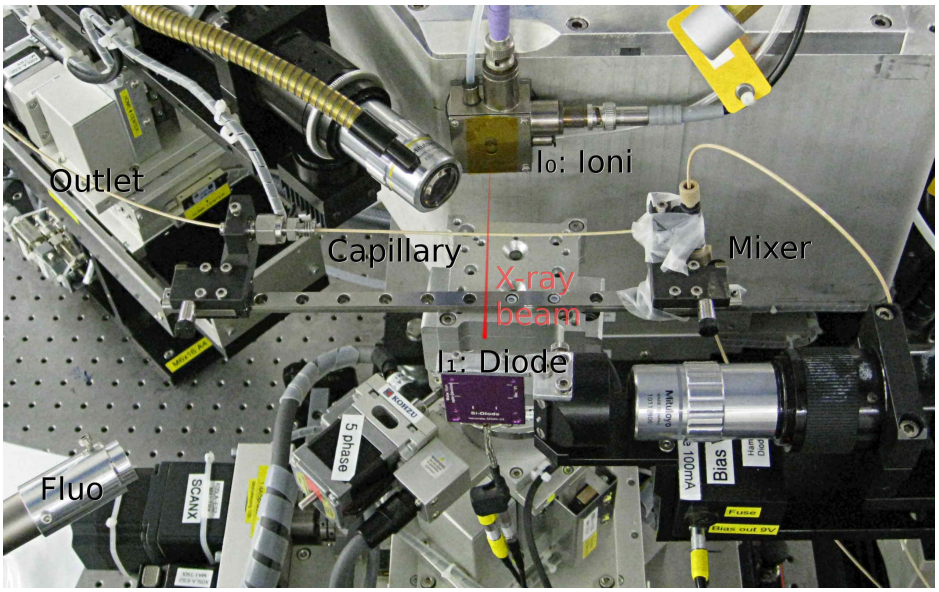

Figure 5.10.: Setup at the MicroXAS beamline with a mounted capillary, attached to a T-type mixer, between ionization chamber (I_0) and diode (I_1) for transmission experiments. The distance of the fluorescence detector (Fluo) is adjusted later during experiments.

In fig. 5.10 the capillary is mounted horizontally in the center of the image on top of motor stages for sample movements. Thus the capillary can be scanned between the two brackets of the capillary holder (left to right) and in vertical direction (up and down). The capillary holder maintains the capillary in a fixed position during operation. Since the mixer is attached directly to the right bracket it is possible to maintain short dead times for the investigation of the early reaction phase. The X-ray beam intensities are measured by an ionization chamber and a diode before and after the capillary respectively. The fluorescence detector (lower left) was later positioned closer to the capillary to increase the count rate.

Beam Size Effects

To improve the temporal resolution of the reaction progress, it is advantageous to work with a small beam and high flow velocities, which translates into smaller time steps. Therefore, a micro focused X-ray beam (MB) of $2 \times 3\,\mu m$ (v×h) is *in principle* preferred over an unfocused $300 \times 300\,\mu m$ large beam (LB) shaped by slits. The effect of the different beam sizes is discussed in the following and shown in fig. 5.11 for $HAuCl_4$–water solution in a conventional $10 \times 10\,mm$ cuvette and gold foil as reference.

At first glance, the results, shown in fig. 5.11, obtained from the $AuCl_3$ solution differ significantly by using the micro beam or the large beam. In the latter case, two

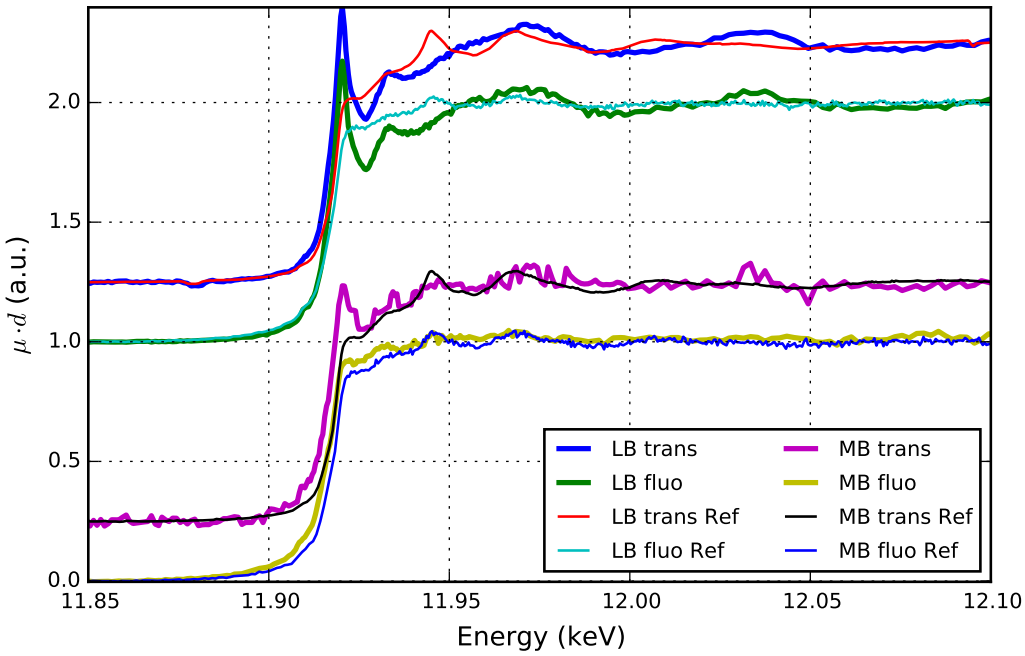

Figure 5.11.: Effect of beam size evident in XANES scans of $AuCl_3$ solution in a cuvette using a large beam (LB) and a micro focused beam (MB) in fluorescence (fluo) and transmission (trans) mode. Measurements of Au foil are denoted by Ref.

almost identical Au^{3+} spectra are obtained. The good data, resulting from a single scan, allows to clearly resolve spectral features and the characteristic white line of Au^{3+}.

In case of the microbeam, the spectrum found in fluorescence corresponds to metallic gold Au^0, while the transmission signal indicates some degree of oxidation and no clear assignment can be done. Overall, the data quality was lower as compared to the large beam measurement. This is likely sample related, since all reference spectra had a good quality. It would probably require multiple measurements to obtain comparable results. This was complicated by the formation of bubbles, which caused severe fluctuations in the spectra and moreover metal deposition on the cuvette walls at the position of the microbeam. These deposits are very likely the reason for the discrepancy between the fluorescence and transmission spectra.

Consequently, the large beam was used for further experiments, because undesired rapid beam induced gold reduction and deposition was avoided, no bubbles emerged, and finally better data quality was obtained from a single scan.

Experimental Limitations

For *in situ* experiments, the reaction has to run in fluid flow under simultaneous XAS measurement. This, unfortunately, means that experimental limitations and intrinsic incompatibilities of the experiment prevent further measurements, as detailed in the following.

To work under turbulent flow conditions, a flow of approximately 33 ml min^{-1} is required. This can be dosed by the pump, but limits the total duration of the experiment to about 3 minutes given a single filling of the two 50 ml syringes. If a very rapid data acquisition were used, *e.g.* below 10 s allowing 18 measurements, this would cause no problem. However, in order to acquire reasonably good data, including pre- and post-edge regions for normalization and good edge sampling to reveal spectral characteristics, around 6 minutes of measurement time are required.

A potential solution to this problem is the use of the continuous pumping mode using four syringes in total, where two are dosing and two are refilling at the same time. To this end, both syringe ports are used and equipped with spring-loaded ball check valves to block reverse flow during dosing and refilling respectively. This adds a new complication as additional force/pressure is needed to open the check valve and this in turn significantly alters the overall system performance. Due to limited pressure tightness of the plunger sealing in the glass syringe, air was able to enter the set up especially under high refilling rates. In some cases, at very high line back pressure and high dosing rate, fluids were also leaking through the plunger sealing. Furthermore, no smooth start of the dosing and transition between dosing syringes was observed, because the check valves opened and closed abruptly, causing varying pipeline pressures during operation. In addition, other mechanical problems caused the check valves to not close properly and thus allowed reverse flow and contamination of the syringe reservoirs.

Reduction of the flow rate, on the other hand, immediately leads to laminar flow, insufficient mixing of educts, non-flat flow profiles in the capillary, and of course extended total flow duration and thus allowing several *in situ* measurements. Ultimately, continuous mode rendered to be not working/applicable with the given material and only single run experiments with reduced volumetric flow rates had been conducted.

Capillary Flow Profile Scan

According to the experimental principle, different reaction times were accessed by scanning the flow at different positions along the capillary. A scan range of approx. 20 cm was achieved by mounting the capillary horizontally on the scanner table (*cf.* fig. 5.10).

The experiment was not run under completely turbulent conditions, due to the the reasons mentioned above. Therefore, the capillary was scanned in a first *in situ* test run perpendicular to the flow direction at a fixed distance of 10 cm from the mixer in the middle of the scan range to study the radial flow profile in the capillary.

The 15 capillary flow profile scans, shown in fig. 5.12, were recorded with a total flow of 4 ml min^{-1} using the PEEK cyclone mixer over almost 13 minutes. Data processing revealed movement of the capillary itself by around 0.5 mm. This movement needs to be compensated or it has to be prevented in order to reliably measure flow states in the capillary at fixed radial positions. By realigning the spectra based on the transmission signal, this compensation was easily achieved.

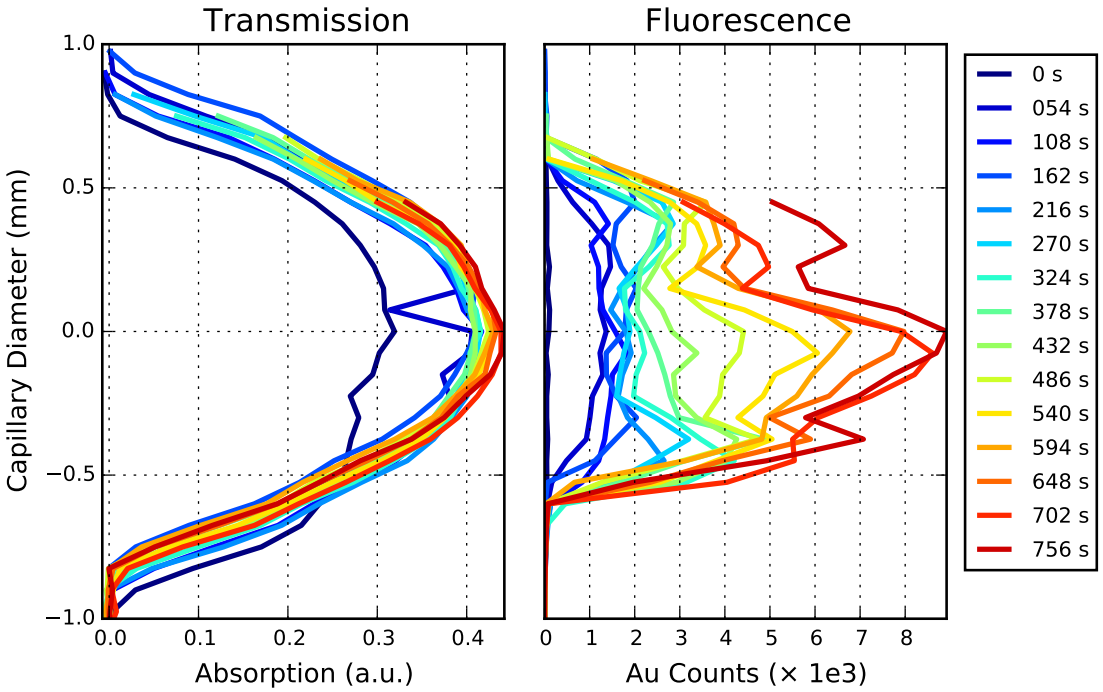

Figure 5.12.: Repeated scan across the capillary during slow flow from the syringe pump. A clear asymmetry between upper and lower half is evident in fluorescence, indicating a higher concentration of sedimented gold at the bottom of the capillary.

At the beginning of the experiments in fig. 5.12, with an empty capillary, the fluorescence spectrum was completely flat. The fluorescence signal of the second scan already shows that the capillary is then filled with gold solution, showing a single maximum in the capillary center. With increasing scan duration an asymmetric fluorescence signal is observed along the capillary diameter. This clearly indicates the enrichment of gold in the lower half of the capillary, whereas oxidized gold is still dominating the spectrum in the upper part. The most likely explanation for these results is the sedimentation of metallic gold at the bottom of the capillary, considering the prevailing low flow rate and horizontal capillary arrangement. This posed a severe problem as sedimentation lead to a reduction of the effective inner diameter of the capillary. This in turn caused a transition to asymmetric flow profiles where correlation of measurement positions to reaction times is not longer doable in a simple way.

In quantitative experiments, the formation of deposits in the capillary needs to be assessed to exclude the violation of experimental assumptions. The influence of, *e.g.*, flow speed and capillary orientation on the deposition behaviour should be studied. Vertical alignment of the observation capillary may prevent sedimentations, but may require additional efforts to achieve long scan ranges as a beam line set up is usually optimized to cover a maximum of lateral movement and provides only a minimum of vertical freedom. Such an adjusted setup was not scope of this work, as experiments in a free liquid jet can be also used to remove the influence of gold sediments from the experiment. This is demonstrated later in section 5.7.

Following Gold Reduction in Laminar Flow

Due to low flow rates, poor mixing, laminar flow, and deposits in the capillary, a simple mapping of spatial coordinates to reaction times was not possible. Nevertheless, we followed the gradual changes in the spectra as function of dosing time of the fluid to prove applicability of the detection concept and to test different mixer types.

In a first long test run a simple T-mixer (IDEX Health & Science, PEEK Tee P-728, 1.25 mm thru-hole) was used to asses mixing behaviour of $HAuCl_4$ and THPC with a total flow rate of $3\,\mathrm{ml\,min^{-1}}$. Scans across the capillary diameter showed a uniform gold distribution, indicating a good mixing of the two input streams. However, several XAS scans were acquired, probing the capillary cross-section and flow center, for about 135 minutes. Quite unexpected, no signal from metallic gold nanoparticles but only of seemingly unreacted Au^{3+} was found, although the typical color change to a red solution was observed in the waste container. This suggests, that no distinct reaction took place in the flow, although gold deposition and sedimentation was again observed at the measurement position after the end of the scan. Interestingly, the initial uniform gold profile was restored when a *fresh* position along the capillary was scanned. This confirms the 'no reaction hypothesis' from above, and further indicates a non-negligible impact of the X-ray beam on the reaction leading to the formation of metallic gold. This effect of X-ray induced reduction is well known in the community [253, 254].

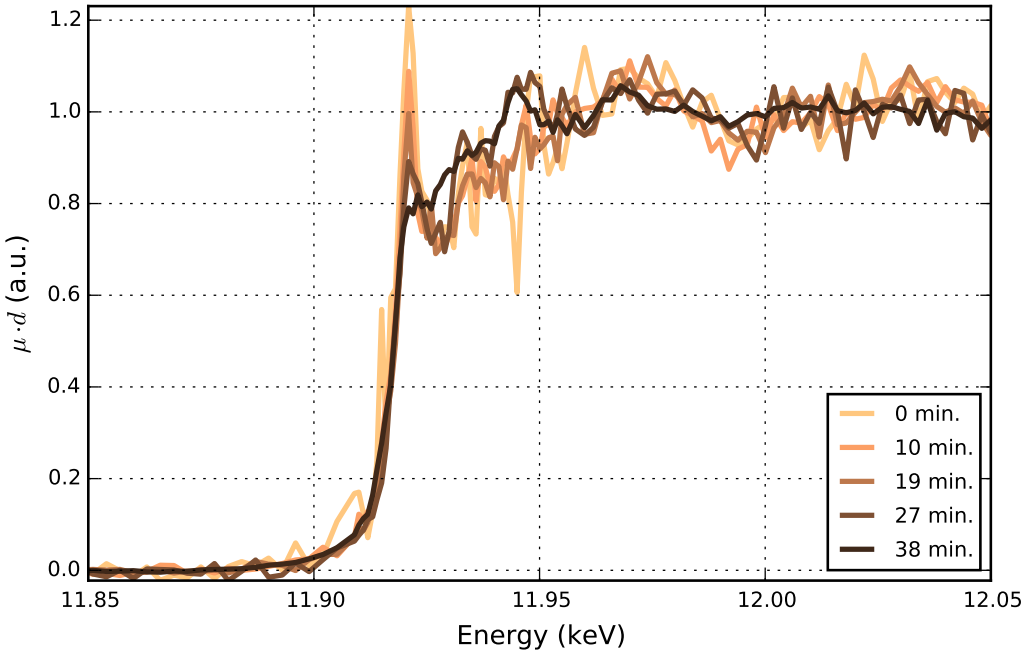

Figure 5.13.: XAS-spectra following the reduction of gold solution under slow laminar flow of $2\,\mathrm{ml\,min^{-1}}$ using a cyclone mixer.

A second test run, with syringes refilled with freshly prepared solutions and a PEEK cyclone mixer (IMVT), was done with a total flow of $2\,\mathrm{ml\,min^{-1}}$. The series of spectra in fig. 5.13 clearly shows that Au^{3+} solution is gradually reduced and probably reaches a Au^{1+} oxidation state near the end of experiment as can be seen from the 27 min trace. In the last scan metallic gold was obtained again, but the decreased noise level

strongly suggests that sedimented metal rather than suspended nanoparticles within the stream were the source of this signal. Thus, no reliable statement on the final oxidation state in the liquid can be given.

No follow-up experiment was done since the mixer got clogged due to low flow speed and the missing capability to flush the lines with water before shutting down the flow. However, the last experiment proves the technical feasibility of the measuring approach and suggests a better mixing of the cyclone-type mixer as compared to the T-type mixer even in laminar flow. Since some reaction and change in oxidation state was observed.

Summary and Conclusion to Syringe Pump Experiments

The syringe pump was able to dose liquids precisely and with constant rate. However, the combination of used equipment limited the expected performance. Mechanical problems of the check valves caused leaking and did not reliably prevent reverse flow, leading to a contamination of the fluid reservoirs. Furthermore, they introduced additional back pressure to the system, since they have to be pushed open. The glass syringes, needed since $HAuCl_4$ solutions are very corrosive, started leaking when the back pressure at the plungers became too high. High back pressures are very likely due to the experimental approach as it needs high flow rates, check valves, the microfluidic mixer, and eventually long and thin observation capillaries. In consequence, this prevented continuous flow operation. This means, that only the small amounts of liquid in the syringe bodies (2×50 ml) could be used. With a capillary of 1 mm inner diameter, where flow rates should be as high as $33\,\mathrm{ml\,min^{-1}}$, the observation time was therefore limited to 3 min. Results obtained under laminar flow suggest a better performance of cyclone-type mixers as compared to T-type mixers but at cost of a higher clogging tendency.

Surprisingly, at the used slow flow rates, the reaction was not always observed within the capillary scan range, although the solution turned dark brown in the waste bin, indicating the formation of gold nanoparticles.

On the other hand, the X-ray beam had verifiable impact on the reaction and led to deposition of metallic gold on the capillary walls and gold sedimentation at the beam position. This finding also needs to be considered in future experiments to prevent wrong conclusions.

Based on the experiments presented in this section, an improved setup is required using: sufficiently high flow rates in spite of the presence of high back pressure to reach turbulent flow conditions ($\mathrm{Re} > 2300$), continuous flow or at least longer dosing duration, line flushing with water at the end of the measurement, orientation of the capillary in vertical direction, improved XAS measurement, and perhaps other mixing devices.

A possible realization of such experiments is presented in the following section 5.7.

5.7. Fluidic Rack in situ Experiments

In this section results are presented, which were obtained using the specially designed fluidic rack, described in section 5.3.2. Its main purpose is to eliminate shortcomings observed during the syringe pump experiment, *cf.* section 5.6, and to provide a pulsation-free flow to finally realize the experimental approach, *cf.* section 5.2, using the same test reaction. Moreover, a new acquisition scheme, namely measurement in a free liquid jet, and the use of the custom-designed microfluidic chip, described in section 5.5, were tested.

Experimental Setup and Preparations at Beamline P06

Experiments were conducted at the beamline P06 [35]. The so-called micro hutch provides a micro focus capabilities and sufficient free space for installing the rack. Using the KB-mirrors, a sheet-like beam of $0.6 \times 1.3\,\mu m$ (v×h), extended in the horizontal plane, was adjusted. This shape was chosen to measure vertically aligned flows, thus the beam is not too much extended along the direction of the flow.

The default XAS scan speed of the beamline P06 was again too slow, taking several minutes, especially when using the default beamline control software `online`. Besides the software limitations, the undulator parameters prevented a very smooth motion synchronous with the monochromator. Therefore, a customized Python script (initial version from Edmund Welter, extended by Gerd Wellenreuther) was further modified by myself to coordinate fast XAS scans and decoupled rapid data acquisition with optional parallel scanning of stages if needed. This allowed a flexible combination of all the parameters mentioned to suit the experiment the best possible way.

For optimal results, parameters like scan speed, scan range, and sampling quality are adjusted using the Python script and dummy samples. Optimization yielded a minimal fluorescence acquisition time of 0.3 to 0.4 s with an energy scan speed of approximately $2\,eV\,s^{-1}$ covering ranges between 60 and 400 eV in 30 to 200 s easily. This allowed to obtain good XAS data in an acceptable amount of time and to save liquids. Thereby enlarging the length of experiments under continuous flow and thus allowing multiple measurements at different positions.

A shorter energy range was chosen sometimes in favor of short scan time. This is suitable for measurements of the Au L_3 edge of Au^{3+}, which features a pronounced white line. In general using such a short range is not advisable. By using a larger energy range, more data can be obtained from pre- and post-edge regions. This in turn facilitates a better and more robust normalization of spectra with distinct changes of the white line and features close to it. Thus, the energy range and scan parameters have to be adjusted specifically to the reaction under observation.

Options for Measuring the Liquid Flow

The reaction of $HAuCl_4$ with THPC was also followed within a free liquid jet and the microfluidic chip to check whether improved mixing in the built-in cyclone mixer of the chip and shorter duration from the point of mixing lead to an improved observation of the reaction.

Free Liquid Jet

In fig. 5.14 the setup for the free liquid jet is shown in operation at P06. The liquid was vertically emitted from the capillary into free space, where it was measured by the X-ray beam. Hence X-ray beam induced deposition on walls is no issue here.

The setup was inspired by experiments from other groups [245, 247]. The realization is quite simple. A syringe barrel was used to prevent spraying of liquids and a lid to fix and position the capillary inside. Windows have been cut into the barrel and sealed with Kapton® tape to exclude undesired beam interactions with the barrel material and to ease cleaning.

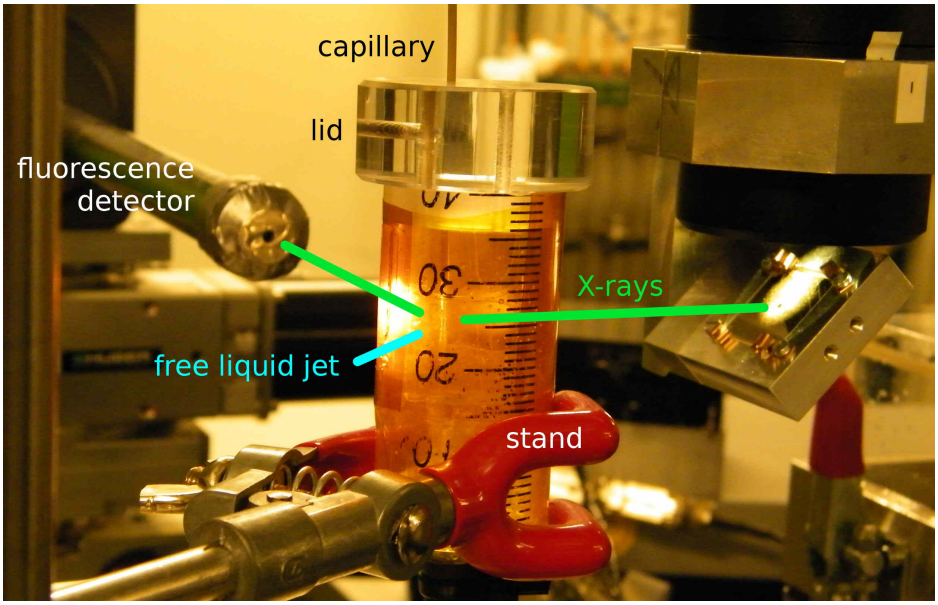

Figure 5.14.: The free liquid jet setup mounted and operated at the P06 beamline. The liquid flow can be seen between the 20 and 30 ml markers. X-rays enter from the right hand side and fluorescence from the stream is recorded by the detector in the rear left part of the image.

The jet was only used to measure the liquid stream leaving at the end of the capillary and of course did not include the mixer, which was positioned at the inlet of the capillary. In most cases a single cyclone was used for mixing, similar to the one used in the syringe setup in section 5.6.

Starting measurements with the free liquid jet is straight forward and just requires positioning of the jet in the X-ray beam. This was done by installing the stand for the barrel with the capillary lid (*cf.* fig. 5.14) and roughly pre-position the capillary exit. The capillary position was refined by moving the X-ray beam until the transmission signal was minimal. Once a transmission signal was found, the capillary was moved out of the direct beam. A jet was produced using a flow of water which was then centered within the beam.

Since only a thin Kapton® foil and air were absorbing the fluorescent radiation from the jet on its way to the detector, a low noise signal was obtained. The detector distance and orientation needed to be optimized for high count rates avoiding saturation of the the fluorescence detector at the same time.

Microfluidic Chip

The microfluidic chip, whose design is discussed in section 5.5 on page 102, was used for observation of the liquid directly after mixing without dead time and with high time resolution. In fig. 5.15 the chip is shown, mounted into its support on the scanning stages at the beamline P06. The lines for the liquids to and from the chip are mounted on the rear side, thus the front side remains free from obstacles for scanning.

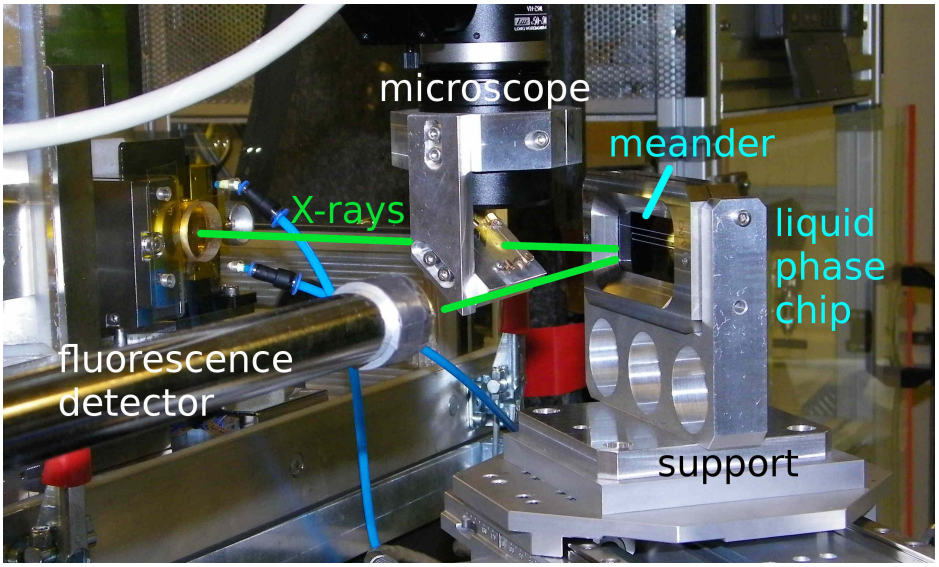

Figure 5.15.: The liquid phase chip mounted and operated at the P06 beamline. The dark chip with three light gray meander lines is mounted inside its support on top of a motor stage. The X-ray beam enters from the left hand side, passes through the 45° tilted microscope mirror and arrives at the chip. The tip of the fluorescence detector (lower left) is later moved closer to the chip to optimize count rates.

To measure the fluorescence, emerging from the fluid channel, the chip was inclined by 45° with respect to the incoming X-ray beam and the fluorescence detector to optimize detection, as seen in fig. 5.15. An additional linear stage, aligned with the chip, served for scanning the positions on the chip, allowing translations along the channel (x), while the vertical (z) position was adjusted by the sample z stage of the beamline.

In a first step, a chip coordinate system with respect to the beamline was needed to accurately position the flow channel in the X-ray beam. This was done by a coarse pre-alignment by eye and several line scans, using the two stages for x and z, across the chip and recording the transmission signal. A couple of coordinates was then saved for use in later measurements.

5.7.1. Experiments using the Liquid Phase Chip

To verify the experimental approach of rapid turbulent mixing followed by turbulent flow and reaction time mapping (*cf.* section 5.2 on page 97), the specially designed microfluidic chip was attached to the rack. This gave the opportunity to test the devices and to investigate the very early stage of the reaction.

Beam Induced Deposition Testing

As known from earlier experiments using the syringe pump, *cf.* section 5.6, beam induced gold deposition in capillaries is an issue. Thus it was necessary to check for similar problems in the liquid phase chip under turbulent conditions. Therefore, the chip was fed with $1.26\,\mathrm{L\,h^{-1}}$ of $HAuCl_4$ solution and $0.97\,\mathrm{kg\,h^{-1}}$ of water to yield a turbulent flow. A long series of acquisitions was then simulated by irradiating a fixed position of the fluid channel with X-rays and recording the fluorescence and transmission signals, as shown in fig. 5.16.

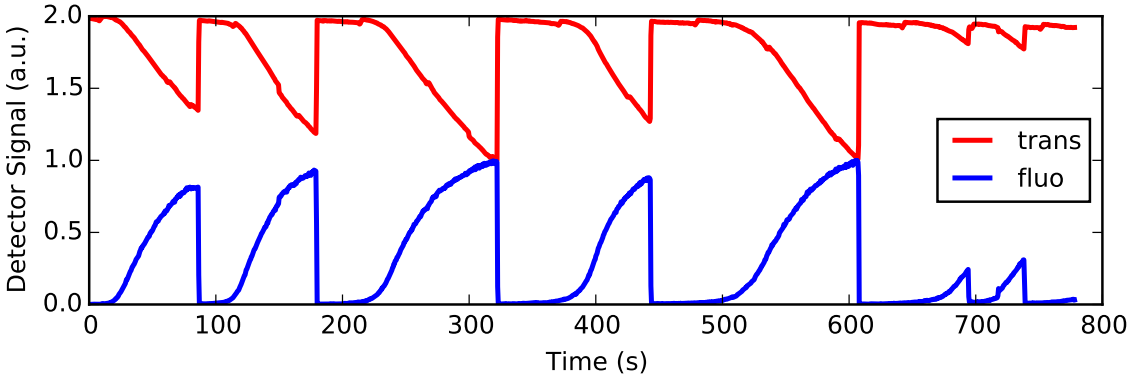

Figure 5.16.: Microfluidic Chip characterization: Beam induced Au deposition in the center of the channel close to the exit. A periodic growth and removal of the depositions by the turbulent flow of $HAuCl_4$ and water with in total $2.23\,\mathrm{L\,h^{-1}}$ was observed. Detector signals have been scaled and shifted for better visualization.

The formation of gold deposits is clearly evident from the change in transmission and fluorescence signals in fig. 5.16. Accumulation of metallic gold was accompanied by an increasing fluorescence signal and parallel decreasing transmission signal. Every once in a while, the deposit was removed by the turbulent flow and both signals turned back to their initial values. A test scan next to the original position confirmed a deposition free area, thus the observed behaviour is caused by the X-ray beam and locally confined.

Considering the available XAS scan protocols, requiring at least 30 s per scan, these results excluded a measurement at a fixed position.

Development of a Customized Scan Procedure

The beam induced local deposition of gold demands a *moving* acquisition, performing the XAS scan over a series of *fresh* positions in the flow channel. Manually controlled pre-tests with incremental changes of the scan position, perpendicular to the flow direction, justified this approach. It was implemented in the customized Python scan script to achieve a continuous position variation during the acquisition of XAS data.

The results of an experiment in this scanning mode, where 10 XAS scans at a fixed position along the flow direction were taken, is shown in fig. 5.17. Each line scan lasted 30 s with 0.3 s fluorescence sampling, while the next scan starts at the same position with a delay below one second. The first scan clearly shows an Au^{3+} spectrum and thus confirms the superiority of the new mode of operation.

However, the second scan, in the normalized plot, shows a reduction of intensity of the white line and indicates a change in gold oxidation state. Thus, the second scan is already affected by beam induced gold deposition, albeit the overall scan time is only 1 min. Most strikingly, this is evident in the raw fluorescence signal in the left panel of fig. 5.17, which dramatically increased with the number of scans.

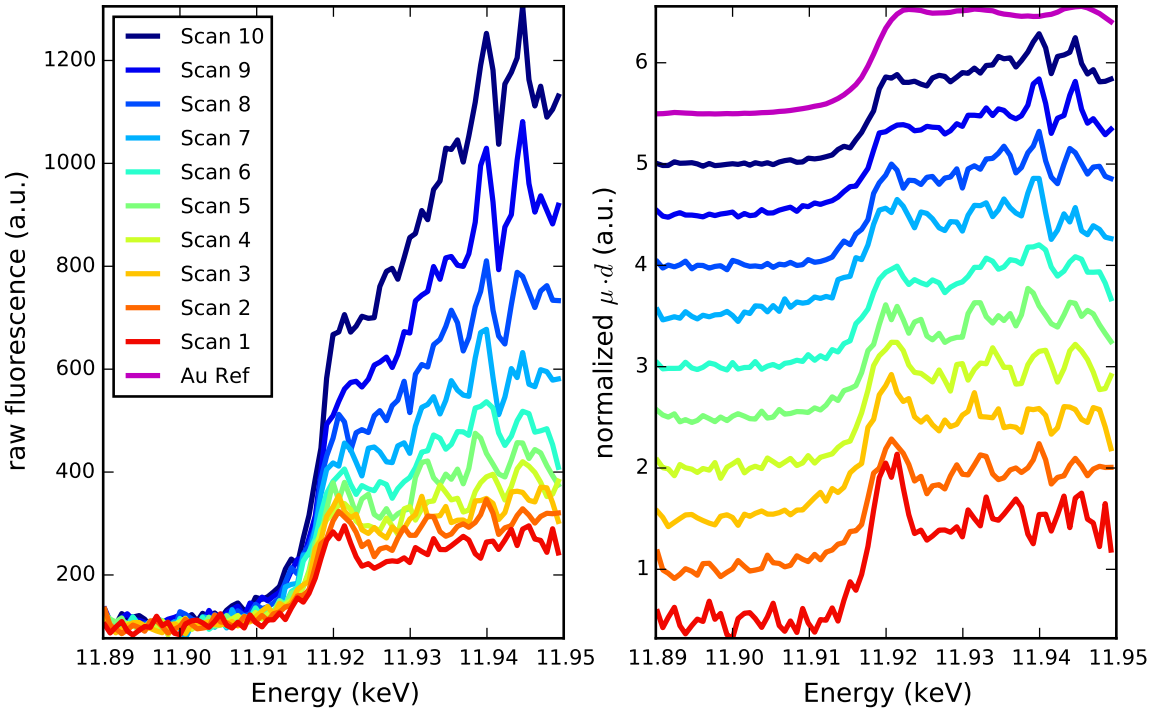

Figure 5.17.: Beam induced Au deposition during several repeated line scans across the same position of the microfluidic chip. Left: raw fluorescence, right: normalized and stacked absorption. Each scan takes 30 s with less than 1 s delay in between.

Additionally, a source of misinterpretation is visible here. The normalized data indicates a gold reduction. This is only true for the beam induced gold deposits but not for the remaining flowing liquid, since no reducing agent is present and separate scans on other positions still yielded an undisturbed Au^{3+} spectrum. In the present case, the deposited gold gradually started to dominate the fluorescence signal due to the increased concentration of gold within the beam area. Its oxidation state is not representative for the liquid flow. Had the reaction taken place in the liquid, the raw fluorescence and transmission signals would have remained rather constant in the pre- and post-edge region, because the overall concentration of gold would have been unchanged.

Due to this finding, only a single XAS scan with simultaneous position scan was done while the next scan was taken a bit (2 µm) further downstream. Obviously, this limits the number of scans possible on the chip. Moreover, it prevents repeated scans of a fixed reaction position translating to a specific reaction time, *e.g.* to study various fluid compositions.

Test Acquisitions of Au^{3+} and in situ Reaction

By using the line scan mode and a flow of gold solution and water through the chip, a reference spectrum of Au^{3+} was recorded first. Seven scans have been acquired without deposition problems and merged to improve statistics. For comparison, a reference spectrum, merged from four single measurements, using the free liquid jet is shown additionally in fig. 5.18.

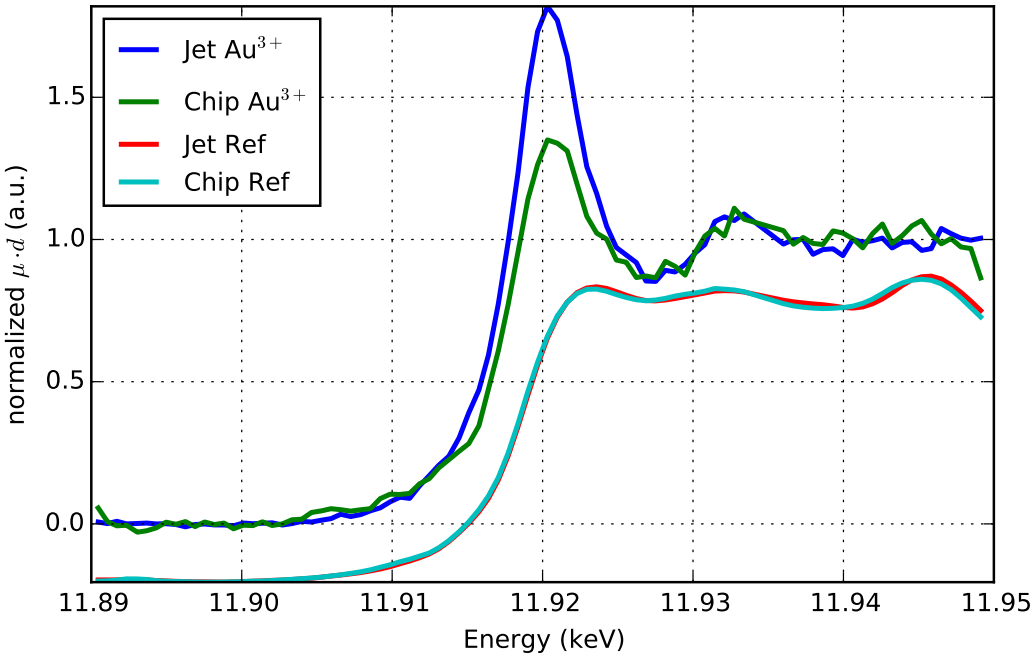

Figure 5.18.: Reference spectra of Au^{3+} solution recorded using the microfluidic chip and the free liquid jet for comparison. A pair of two Au^{3+} spectra is shown above a pair of metallic gold spectra shifted by -0.2.

In general, the spectra of Au^0 (Ref) and Au^{3+} (gold solution) were reproduced well in both systems. However, the white line of Au^{3+} in the chip was not as strong as in the jet, probably due to absorption by the chip material. The overall count rate using the chip was lower, which required to merge more scans, namely seven, as compared to the free liquid jet, where four scans were sufficient. This needs to be considered in the planning of the acquisition time of the XAS spectra to obtain comparable statistics.

To probe a wider range of reaction times, the microfluidic chip was then combined with a 50 cm long capillary at the outlet leading to the free liquid jet. The first 20 ms of the reaction progress were covered by four points on the chip. The first point was at the mixer outlet, corresponding to 2 ms of reaction, and the last point just before the chip outlet, corresponding to 20 ms of reaction, while the others were in between. The chip was fed with $1.26\,\mathrm{L\,h^{-1}}$ of Au^{3+} solution and $1.30\,\mathrm{kg\,h^{-1}}$ of THPC solution to ensure a turbulent flow. A later stage of the reaction, corresponding to around 40 ms, was then probed after the microfluidic chip within the free liquid jet.

At the last point, close to the chip outlet, the first scan already showed reduced gold which suggests a very rapid reaction. Likewise all other selected points also

showed Au^0 spectra. However, measuring the fluid in the free liquid jet yielded a Au^{3+} spectrum that indicates no significant reduction of the liquid. As it turned out by visual inspection, the entire fluid channel was gold coated after flowing the gold and THPC mixture through it. Due to this, no further measurements of the flow in the chip channels were possible, since fluorescence signals from the liquid were obscured by signals from the gold coated channel walls.

As the reaction was not completed after the liquid has left the chip, one can use the mixing capacity of the chip and in principle measure in the free liquid jet only. A variation of the observed reaction time is done by a change of the capillary length. An elongation of this capillary is, on the other hand, limited due to increasing back pressure, which prevents turbulent flow conditions. Due to this fact it is more reasonable to use the free liquid jet without the chip and achieve mixing by the single cyclone mixer made of PEEK with little intrinsic back pressure.

Summary Liquid Phase Chip: Design and Experiments

Considering the chip design and construction, the project was successful. The chip itself and the corresponding support construction are leak-tight at 12 bar input pressure, in order to achieve the calculated turbulent flow conditions, and allowed X-ray fluorescence and transmission experiments.

Experimental limitations arose mainly from gold deposition inside the chip channels disturbing or even preventing the measurement of the oxidation state of the gold in the liquid stream. The fixed observation time window, defined by the channel dimensions and flow rates, was given by the chip design. The target residence time needs to be estimated early in the design phase and requires at least an educated guess on the reaction velocities under investigation, in order to cover the relevant time scales.

Interference of signals from beam induced deposits are circumvented by a continuous sample movement during XAS acquisition. However, beam induced deposition occurred even with this technique and thus prevented repeated scans at a fixed chip (flow) position. This might be required to study the effects of various reaction parameters or to improve statistics by averaging several scans without decreasing temporal resolution, which is the case if scans are taken along the flow direction.

Complete coating of the channels by the reaction itself took place immediately, regardless of interaction with the X-ray beam. This gold layer dominated the fluorescence signals and therefore prevented to measure the oxidation state within the flow. Consequently, this is the major problem and needs to be addressed in future work.

Either a cleaning procedure has to be set up or deposition of gold has to be prevented, since the chip is no bulk ware and easily replaceable. For cleaning the microfluidic chip with aqua regia, fluidic ports made of titanium have been ordered. Deposition can also be prevented by a functionalization of the channel surface with a suitable material, *e.g.* silanization and adjustment of the pH value [239].

Furthermore, flow parameters that prevent contact of the liquid with the walls by establishing a protecting flow at the outside or allow the encapsulation of the reaction mixture in separate bubbles (segmented flow) [237] might be another way to reduce gold plating of the chip.

Depending on the reaction under investigation, application of a single use chip, cheap enough to be disposed after the experiment, might be an option too.

5.7.2. Experiments using the Free Liquid Jet

To avoid the deposition of gold, the gold reduction was then done by feeding a single cyclone mixer made of PEEK with two input streams from the fluidic rack and connecting the mixer outlet to a capillary leading to the free liquid jet, where the XAS measurements took place. Different reactions times were realized by adapting the length of the capillary.

Gold Reference Spectra

For this series of experiments and conditions a new set of reference scans was acquired to compare with later scan results. Besides the Au precursor solution, $HAuCl_4$, we used a AuCl pellet and a gold coated capillary to acquire the data shown in fig. 5.19.

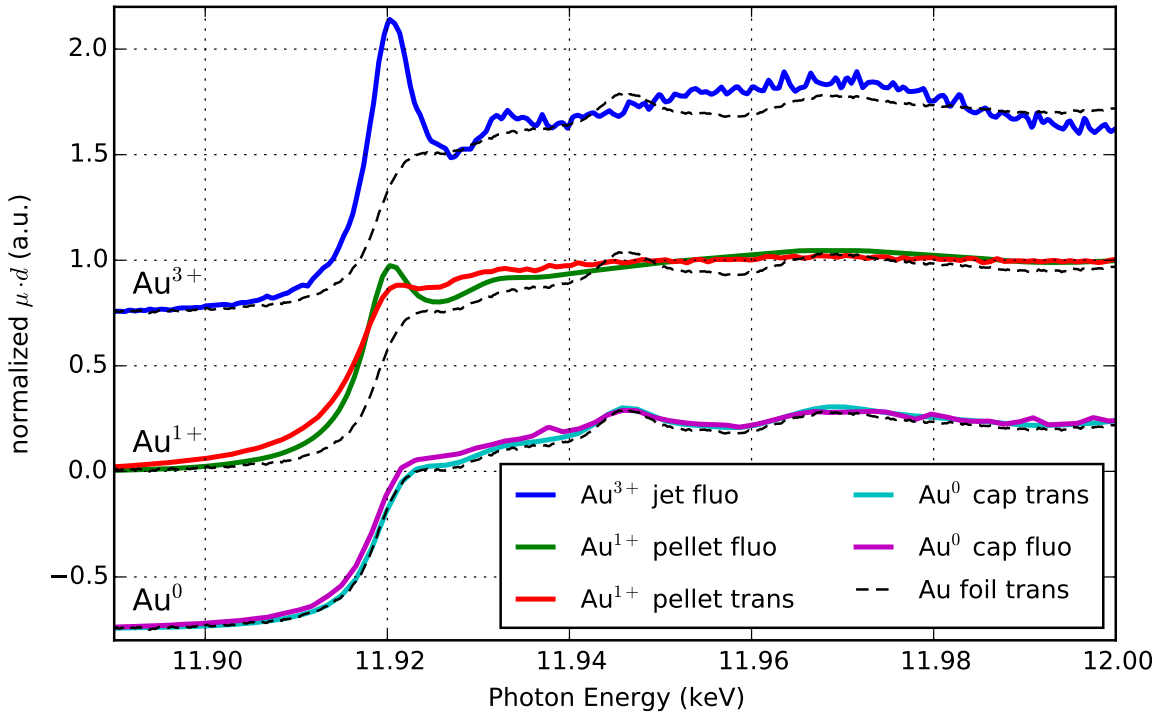

Figure 5.19.: Reference spectra of gold in different oxidation states. From top to bottom Au^{3+}, Au^{1+}, and Au^{0} spectra are shown in colored solid lines, which are supplemented by a black dashed line denoting the Au foil reference. Measurements are taken on the free liquid stream directly (jet), pressed powder sample (pellet), gold coated capillary (cap), or the metal gold foil reference (foil). Acquisition is either in fluorescence (fluo) or transmission (trans) mode.

In the near edge region presented in the spectra in fig. 5.19, the different gold oxidation states are most significantly distinguished by the intensity of the white line feature, which is therefore used as a fingerprint. A more careful inspection revealed an additional slight shift of the edge position for oxidized gold species with respect to the

metallic gold reference (dashed line). The spectra are in good agreement with results found in literature [255–257].

To asses the fluorescence and transmission signal quality and comparability, samples were measured in both modes except for Au^{3+}. Since the gold solution was measured in the jet only, to mimic later experiments, no transmission signal was obtained. Measurements using, solution in *e.g.* a cuvette, may be used instead if desired.

The transmission spectrum of Au^{1+}, obtained from the AuCl pellet, shows more details in comparison to the fluorescence spectrum that shows a weaker white line and is almost flat beyond that. This may cause problems in distinguishing Au^{1+} and Au^{0} spectra. However, a clear shift of the Au^{1+} edge position remains, which can be used as a marker. An example of following a gradual change from Au^{1+} to Au^{0} is for example found in [258]. The fluorescence and absorption spectra of Au^{0} from the gold coated capillary are almost identical and match the spectra of the Au reference foil very well.

Scan Along the Reaction Time Coordinate

By using various capillaries with different inner diameter (ID) and different length as feed to the jet, reaction times between 0.3 and 3 seconds were probed. The first three, blue shaded lines in table 5.1 state minimal flow rates to reach turbulent flow and are used to calculate the corresponding maximal capillary length, observation time, and pressure drop as reference.

Table 5.1.: Overview of calculated reference values and values used in the jet measurements. The column Reaction–Au^{x} reports the observed gold oxidation state and Flow–type gives the flow conditions either turbulent (T) or laminar (L). Annotations: *jet attached to chip outlet, †fresh THPC and clogging.

Capillary		Reaction		Flow			
ID (mm)	len. (m)	time (s)	Au^{x}	Au ($L\,h^{-1}$)	THPC ($L\,h^{-1}$)	type	Δp (bar)
0.50	1.0	0.20	–	1.65	1.65	T	11.3
0.75	3.0	0.95	–	2.50	2.50	T	9.9
1.00	8.0	3.23	–	3.50	3.50	T	10.0
0.75	1.0	0.27	3+	2.82	2.96	T	–
0.75	1.5	0.40	3+	2.95	2.89	T	–
1.00	0.5	0.52	3+	1.28	1.30	L	14.2*
1.00	3.0	1.41	3+	3.02	2.99	L	–
1.00	3.5	1.6–3	3+–0	3.26–1.12	3.17–1.39	L	14.2†
1.00	4.0	2.51	3+	2.40	2.07	L	6.8

As can be seen from table 5.1, almost each scan yielded spectra corresponding to Au^{3+}, except for one case, shown on page 125 as proof of principle. Notably, turbulent flow cannot be reached with a capillary of 1.00 mm ID and 3.5 m length, due to increasing back pressure. This limitation is explained in detail in the next section.

Experimental Upper Limit for the Observation Time

Basically two options are available to increase the residence time of the fluid in the capillary while maintaining turbulent flow conditions. Firstly, by increasing the length of the capillary, as done in the experiments discussed above, and secondly, by increasing the inner diameter of the capillary.

In the setup used, the maximum available pressures were 15 and 16 bar for the $HAuCl_4$ solution vessel and THPC vessel respectively. By replacing them for vessels with a higher maximum pressure, a longer capillary could be used while most other experimental parameters remain unchanged.

If the inner diameter is changed, a couple of parameters need to be adjusted in order to maintain a turbulent flow, as deduced in the following. Assume that the capillary radius r_1, being 1/2 of the inner diameter ID, is increased by a factor of x to obtain r_2. Accordingly, the circular capillary cross section area A, given by $\pi\, r^2$, increases quadratically.

$$r_2 = x \cdot r_1 \qquad \Rightarrow \qquad A_2 = x^2 \cdot A_1 \tag{5.2}$$

Now we have to consider the boundary condition of turbulent flow, which is expressed by an identical Reynolds number Re for both capillaries. Given the definition of $Re = \bar{v} \cdot d/\nu$ in pipes, where $\bar{v}$ is the mean fluid velocity, d is the tube diameter, and ν the kinematic viscosity we demand

$$Re_1 \overset{!}{=} Re_2 \qquad \Rightarrow \qquad \frac{\bar{v}_1 \cdot r_1}{\nu} \overset{!}{=} \frac{\bar{v}_2 \cdot r_2}{\nu} \qquad \Rightarrow \qquad \bar{v}_2 = x^{-1} \cdot \bar{v}_1 \tag{5.3}$$

After replacing r_2 we obtain the resulting average flow speed $\bar{v}_2$, which is smaller than $\bar{v}_1$. However, the resulting volumetric flow rate Q, given by $v \cdot A$, is calculated as

$$Q_2 = \bar{v}_2 \cdot A_2 = x^{-1} \cdot \bar{v}_1 \cdot x^2 \cdot A_1 \qquad \Rightarrow \qquad Q_2 = x \cdot Q_1 \tag{5.4}$$

and thus directly increases by factor x. In order to seamlessly scan the reaction time coordinate the same time t, given by $t = L \cdot A/Q$, needs to be accessed with both capillaries. By incorporating the respective parameters, a corresponding capillary length is determined.

$$\frac{A_1}{Q_1} L_1 \overset{!}{=} \frac{A_2}{Q_2} L_2 = \frac{x^2 \cdot A_1}{x \cdot Q_1} L_2 \qquad \Rightarrow \qquad L_2 = x^{-1} \cdot L_1 \tag{5.5}$$

By using the Hagen–Poiseuille equation for laminar flow, we may estimate changes in the pressure drop. Where η is the dynamic viscosity, equivalent to $\eta = \nu \cdot \rho$ using the kinematic viscosity ν and density ρ of the fluid.

$$\Delta p = \frac{Q \cdot L \cdot 8\eta}{\pi \cdot R^4} \Delta p = \frac{x \cdot Q_1 \cdot x^{-1} \cdot L_1 \cdot 8\eta}{\pi \cdot x^4 \cdot r_1^4} \qquad \Rightarrow \qquad \Delta p_2 = x^{-4} \cdot \Delta p_1 \tag{5.6}$$

This predicts a significant reduction of the pressure, as the radius is increased.

From these considerations, using a capillary with increased ID should increase the accessible observation time because the back pressure is no longer a limitation. However,

the volumetric flow rate is scaled by the same factor as the diameter and thus a big ID requires very high flow rates. Considering the total fluid volume of 4.5 L in both vessels, an increase of the capillary ID from 1 mm to 2 mm means an increase of the total flow rate from $7\,\mathrm{L\,h^{-1}}$ to $14\,\mathrm{L\,h^{-1}}$. This reduces the total run time of the experiment to a maximum of 19 min. Moreover, it leads to an very uneconomical operation, producing lots of "waste", especially if several time/positions scans are required.

Thus, increasing the diameter is not really feasible, or only for a single experiment. The length of the capillary is simply limited by the available maximum pressure resistance of the vessels and all fluidic parts involved. For the setup and experimental approach used, 1.0 mm ID, 3.5 m length, and 3 s residence time are the upper limit, *not* including the pressure drop caused by the fluidic rack and the mixer of approximately two to three bar.

Tests in Laminar Flow Regime for Extended Residence Times

As no reduction was observed in the short time accessible under turbulent flow conditions, the residence time was extended by using laminar flow and varying the educt ratios. They in turn influence reaction velocity so that a reaction might be observed within the time window accessible under laminar flow conditions.

Variation of Educt Ratio

The $HAuCl_4$-to-THPC ratio was varied from 0.1 to 10 to check whether reduction is triggered by other ratios of the two educts since a change in the educt ratio is directly connected to a change of reaction speed [259]. In principle, this may change the final particle size, but this was of minor concern within the scope of the experiment. The ratios were varied by changing the volume flow rate on each branch. Since, the pressure regulator on the vessels could not be adjusted precisely enough, the flow was reduced by an additional capillary in the gold feed to produce additional back pressure. A needle valve, already attached to the vessel, was used to change the flow in the THPC branch.

However, no reduction of gold was observed within the aforementioned range of educt ratios. It turned out, that the reduced concentration of gold in the solution at small $HAuCl_4$-THCP-ratios also decreases the fluorescence signal.

Gold Concentration Curve

Different flows allowed an easy and fast variation of the $HAuCl_4$-to-THPC ratio in the mixed stream. During an experiment with 1:10 (Au/water:water) flow ratio, using $0.36\,\mathrm{L\,h^{-1}}$ Au/water and $3.95\,\mathrm{kg\,h^{-1}}$ water, the gold/water branch was switched between dosing gold and water. However, in the setup used, the final ratio was not reached immediately but required some equilibration time as can be seen in fig. 5.20.

In the experiment shown in fig. 5.20, the gold flow was switched on at around 200 s. First changes in the jet were detected at around 300 s, a constant value was reached at around 500 s, almost 5 minutes after the change of reaction solution. Similarly, when switching from $HAuCl_4$ solution to water at around 800 s, some time passed until first

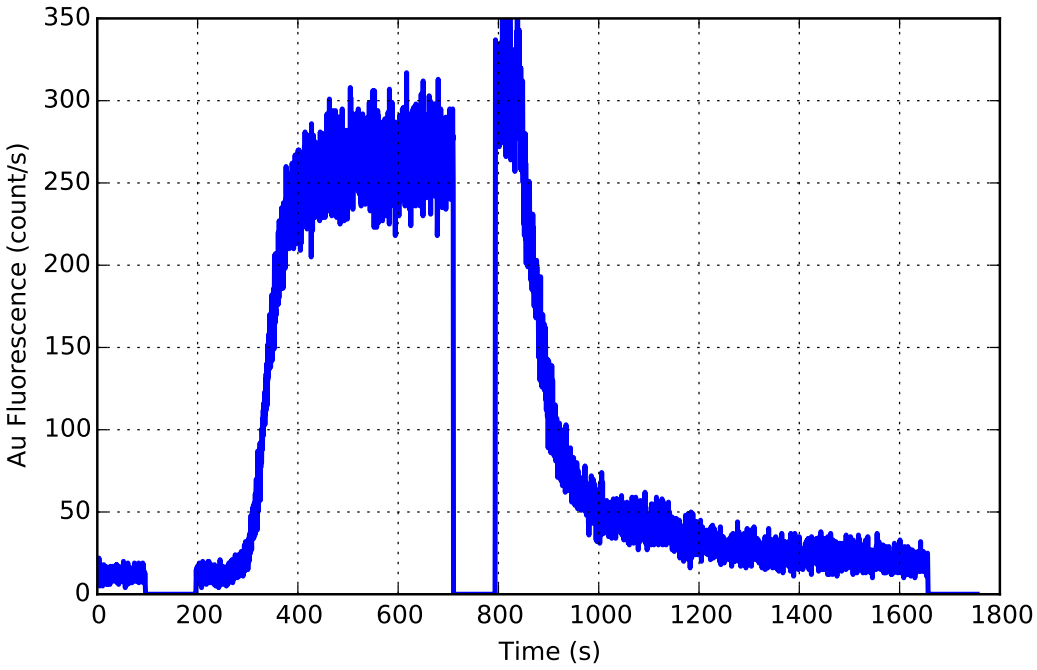

Figure 5.20.: Au Fluorescence intensity vs. reaction time under a gradual concentration change experiment with IMVT setup. The solution was switched from water (0–200 s) to a 1:10 solution ($HAuCl_4$/water:water) (200–800 s) and back to water. A considerable time delay between switching and stable fluorescence was observed. Since the switching could not be done from remote, the experiment had to be interrupted to enter the experimental hutch and switch manually, causing a region with zero counts in the fluorescence signal.

changes were detected. A final value was reached at around 1300 s, around 7.5 minutes after switching to water.

This delay imposes severe limitations on the experiment as any mixing done before the stable operation is reached are not done with the proper ratio leaving the mixture in an unknown condition. This delay can also lead to clogging of the mixer if inappropriate reactant ratios arrive. However, this effect seems to originate mainly from the extra delay capillary installed in the gold branch and from the fact that gold and water are used on the same line leading to the mixer. Consequently, before any gold is reaching the mixer, the prior capillary content has to be flushed away. The present laminar flow profile further delays the process.

At this point, no further analysis of the phenomenon is done as the phenomenon of *residence time distribution* is widely discussed in literature [260]. Nevertheless, future experiments should be tested for this effect, since the same effects are also expected for experiments with equal flow ratios.

This feature of the experiment can also be exploited to check whether a plug flow in the capillary as well as in the microfluidic chip is achieved [261]. In this case the delay should be almost zero. A simple improvement of the experiment would be the installation of a remote switching of the dosing as close as possible to the mixer and to have separated lines for each liquid, educts and water, up to this point.

Observation of Au Reduction: Proof of Principle

Despite of the above challenges, here a proof-of-principle scan series is shown, to demonstrate the ability to follow the change in the Au oxidation state. In fig. 5.21 the reduction process from Au^{3+} to Au^0 was followed using the free liquid jet setup. A laminar flow was used, composed from in average $1.5\,L\,h^{-1}$ gold precursor solution and $1.7\,kg\,h^{-1}$ THPC solution, mixed by a single cyclone and fed to a capillary of 1.0 mm ID and 3.5 m length resulting in a residence time of approximately 3 s.

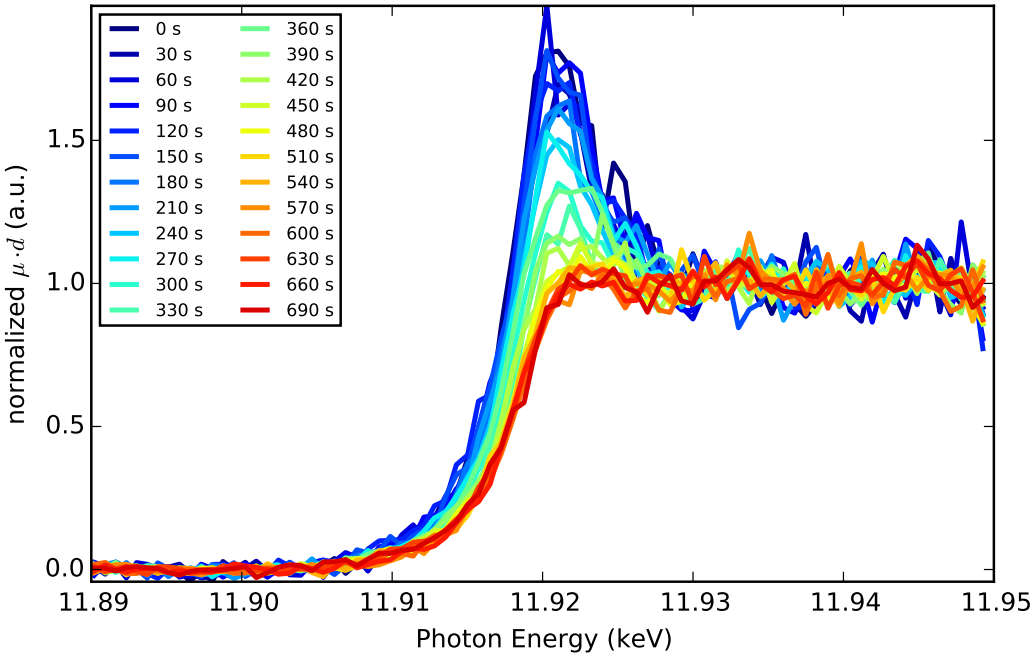

Figure 5.21.: Au precursor reduction as function of time using the free liquid jet at a fixed flow position. Fluorescence XAS scans taken every 30 s. Blue: spectrum at the begin of dosing showing the Au^{3+} white line, red: spectrum at the end of the acquisition showing $Au(_0)$.

The current experiment was done immediately after refilling fresh chemicals into the vessels. A flow of gold and water was used to adjust flow parameters. Finally, water was replaced by switching to THPC to start the reaction. Hence, the first spectra observed are from Au^{3+}, later spectra, taken each 30 s, show a gradual change toward Au^0. Please note, this data was taken at a fixed flow position, *i.e.* no scanning along the flow was performed.

Interestingly, it took relatively long until changes occurred if we consider a capillary residence time of 3 s and a scan time of 30 s. Ideally one would expect to find the final state of the reaction faster. However, at the end of this run the mixer was clogged by gold deposits. This indicates a very active and rapid reaction.

The observed high activity, leading to the reduction of gold, seemed to be related to the presence of fresh THPC in the reservoir. This hypothesis was supported by another short experiment, using fresh THPC yielding reduced gold and a clogged mixer. Moreover, this suggests that aging affects reactivity of the THPC solution. This hypothesis was further tested in a series of laboratory experiments presented in section 5.8 on page 128.

Summary Free Liquid Jet

The free liquid jet approach appears to be the best way of measuring X-ray sensitive liquids for several reasons. First of all, no beam induced deposition on the walls can occur, since no walls are in direct contact with the liquid during X-ray beam exposure. The free flowing liquid is always completely replaced, thus beam induced modifications are widely excluded. Altogether, this greatly simplifies the measurement and rules out major sources of error, like interference of signals from deposits and solution, in data acquisition and related data interpretation.

Moreover, the presented jet setup is relatively simple and cheap, as compared to the integrated observation lines in the microfluidic chip. It just requires maintaining the exit of a capillary at a fixed position to emit the liquid jet and some spraying and spill-over protection. Since the protecting window material can be freely chosen, *e.g.* thin Kapton® foil, the fluorescence signal can pass through it without significant intensity loss, which renders the setup ideal for fluorescence experiments. Last but not least, the jet is independent of the externally used mixer and thus renders the setup very versatile. This even allows to compare several mixer types and a selection of the most suitable mixer for a given reaction or set of fluidic parameters.

Since the capillary exit is fixed and the smooth liquid stream rapidly decayed into separate droplets, a long-ranged scan along the flow was not possible. This issue can be addressed by providing several external capillaries of different length connected to a switching valve, to allow changing the residence time from the mixer to the jet exit on the fly.

Conclusion to Fluidic Rack Experiments

The rack was able to deliver the liquids with high volumetric flow rates and with high pressure, as demanded by the experimental approach, thus enabling turbulent mixing and turbulent flow afterwards. Pressure driven fluid delivery worked very smooth and no pulsation or discontinuities were observed. It was able to operate the microfluidic chip, used for investigations of the very early reaction state, and the external cyclone mixer, for extended observation times. The additional water vessel, besides the two educt reservoirs, allowed flushing of lines if required and to pre-adjust flow rates. The applied pressures and flow rates on each branch are logged by an integrated computer, thereby allowing to check whether the required flow conditions are achieved/maintained within the duration of the experiment.

Inherent limitations are set by the design of the rack, regarding the finite volume of the liquid vessels and pressure resistance of these as well as other involved parts. Since refilling can only be done with unpressurized/vented vessels, uninterrupted continuous operation is not possible. An easier and faster way of re-filling as well as a more accurate estimate of the current liquid level in the vessels would greatly enhance handling.

For a given small flow channel or capillary cross section, the limited pressure resistance prevents increasing the volumetric flow rate to obtain higher Reynolds numbers or extending of the capillary length to obtain much longer residence times at a constant Reynolds number. Moreover, the standard pressure regulators (0 to 50 bar) used in the rack are not very well suited for precise pressure adjustments and should be replaced.

Several experimental logs revealed gradual changes of the initially set flow rates, which may alter mixing ratios and/or flow and mixer properties in general. Therefore, a precise, remote-controllable automatic flow control should be available to set and maintain desired flow conditions on each branch and switch between all three vessels, educts and water alike. Especially, beamline experiments would profit from a remote controlled flow as no direct interaction in the hutch is possible or only at the cost of interrupting the experiment. To avoid accidental clogging, a safe and reproducible start-up and shut-down protocol can then be implemented, which might also include automatic cleaning of lines.

However, the used experimental setup (rack, chip, jet) and adapted beamline XAS scan protocol can be used to investigate reactions in the anticipated manner and has proved to be in principle suitable to detect the reduction of Au^{3+} to gold nanoparticles. Apparently, significant deviations from lab batch experiments are present, that prevent a reproducible reaction. A hypothesis, derived on experimental observation, is the loss of THPC activity upon aging of the solution resulting in a delay of the reaction. This hypothesis was tested in dedicated laboratory experiments, shown in the next section.

5.8. Laboratory Tests for THPC Aging

In this section, the hypothesis of the influence of THPC aging on the ability to reduce Au^{3+} is discussed. This question was raised during synchrotron experiments in section 5.7. The same preparation protocol for the test solutions was used as presented in section 5.2.1, thus with identical concentrations and ratios esp. 1:1 for educt volumes. However, the reaction was carried out in water rinsed conventional beakers equipped with a magnetic stirrer, *i.e.* without any microfluidic device. Per definition, the aging time starts when NaOH is added to the THPC solution and ranges from the protocol-defined 2 min up to 180 min.

All experiments have been repeated three times in order to check reproducibility. Within the course of the reaction, the color change of the solution was captured by recording a video in order to determine relevant time scales (initial delay and duration) and their change with aging time. The resulting gold nanoparticles solutions were then investigated by UV-Vis to estimate size and amount of produced nanoparticles. Additionally, the pH of the aging THPC solution was monitored separately.

Reaction Delay and Duration with aged THPC

By analyzing the videos for each aging time and repetition, the delay between addition of aged THPC to the gold solution and the onset of color changes was determined. This reaction delay is shown in the top panel of fig. 5.22. Initially, the delay of the reaction is 1 s for fresh THPC. It increases to 2 s after 40 min of THPC aging, with a good reproducibility of the results across the three repetitions.

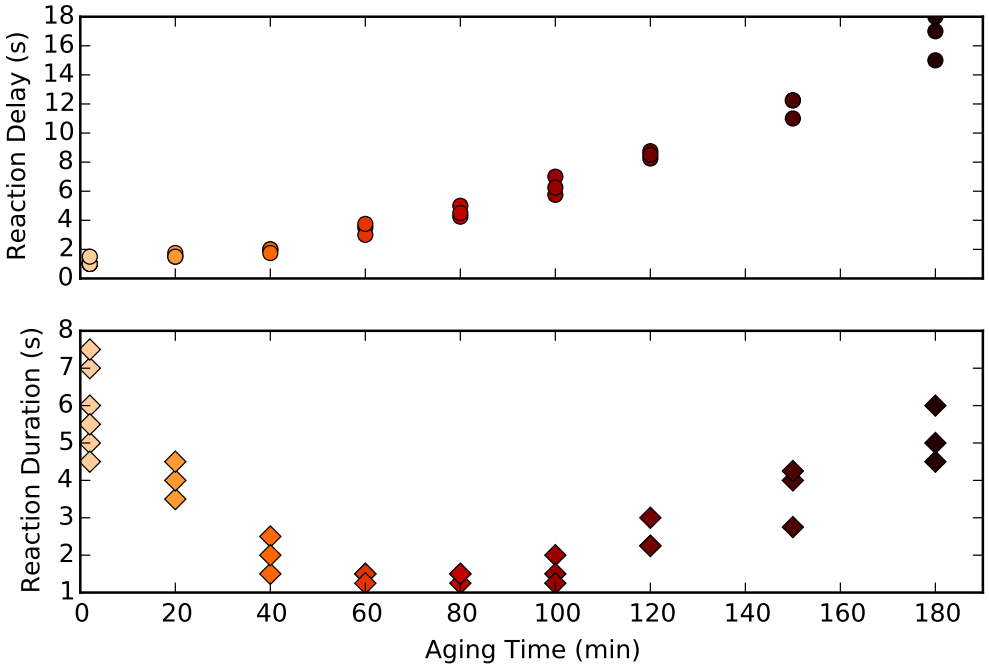

Figure 5.22.: Video analysis results of Au reaction with aged THPC. The reaction delay until the first color change (upper panel) and the duration of the coloring time (lower panel) is shown for each experiment (symbols).

After 60 min of THPC aging the delay is already larger than 3 s. This is the time scale covered in the beamline experiments, thereby confirming the hypothesis of THPC aging as the source of reaction inhibition. For longer aging times, the reaction delay further increased and finally reached 18 s after 3 hours of aging.

The lower panel in fig. 5.22 shows the observed duration of the reaction, taken from first color changes to a final constant appearance. Here a quite different behaviour was observed. While fresh and very old solutions resulted in long reaction durations of around 5 seconds, the shortest duration was found after 60 to 80 minutes of aging.

UV-Vis of AuNPs from aged THPC

The UV-Vis spectra of the above produced gold nanoparticle solution were investigated using a standard $10 \times 10\,\mathrm{mm}$ plastic cuvette. Every single product solution was measured and very good spectral reproducibility was found for a given aging step. Hence, and for clarity, averaged spectra are shown in fig. 5.23.

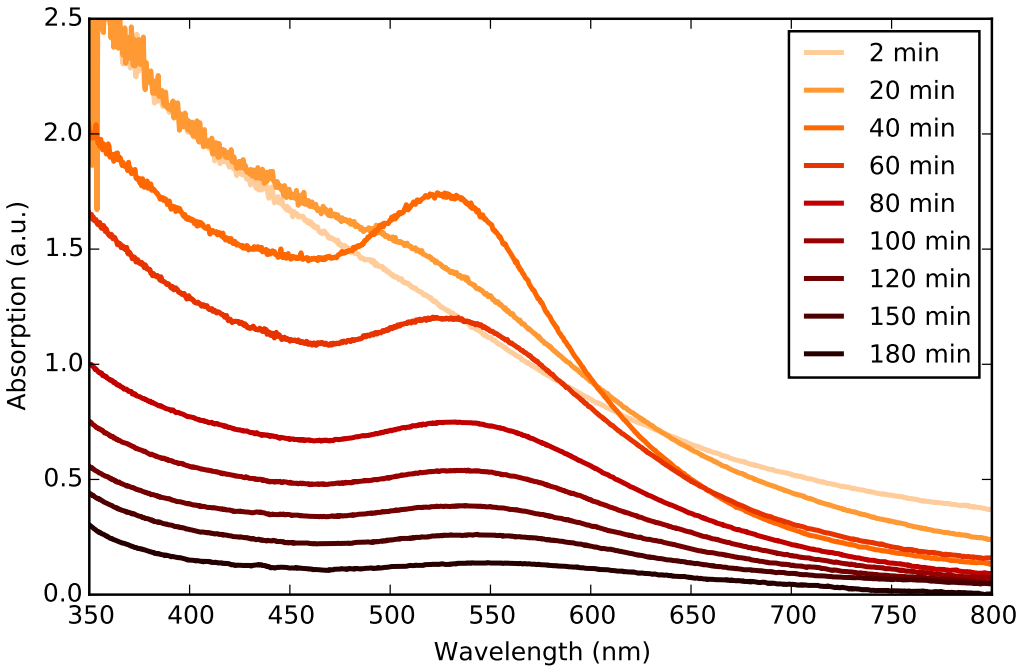

Figure 5.23.: UV-Vis absorption spectra of gold nanoparticle solutions obtained from aged THPC solutions. Each curve represents the average of multiple corresponding aging experiments.

The obtained UV-Vis absorption spectra underwent a significant alteration as function of THPC aging time. For 2 min aging a smooth and decaying spectrum with high absorption was obtained, indicating numerous and small nanoparticles. Already after 20 min, a small peak forms but the absorption remained comparable to the 2 min spectrum. The most pronounced peak was found for 40 min aging accompanied by a decreasing overall absorption. The observed peak formation is attributed to the presence of a surface plasmon resonance of the gold nanoparticles and indicates an increased size of the particles produced.

After 60 min of aging, the features of the 40 min curve were reproduced, but again with a decreased overall intensity. Thus with increasing aging time, evidently less

absorption was measured due to less formation of nanoparticles. Notably, it was possible to restore higher absorption signals in aged solutions by adding an excess of the same aged THPC solution. Overall, this also proves a deactivation of THPC.

The material of the vessel plays no role in THPC aging as was confirmed by experiments in stainless steel vessels. The results were very similar.

A possible deactivation reaction of THPC in alkaline conditions was proposed by Duff *et at.* [210]: $P(CH_2OH)_3 + 2\,H_2O \longrightarrow O_2P(CH_2OH)_3 + 2\,H_2$, where hydrogen is produced.

Changing pH value after THPC activation

In agreement to the above reaction, the pH of the THPC and NaOH solution was found to change over time, as can be seen in fig. 5.24. The pH value was monitored after addition of NaOH to the THPC solution using a calibrated pH meter. Initially, the pH was almost constant at around 11.8 for the first 40 minutes and started to drop more rapidly afterwards, finally reaching a pH of 10.6 after 95 minutes of aging.

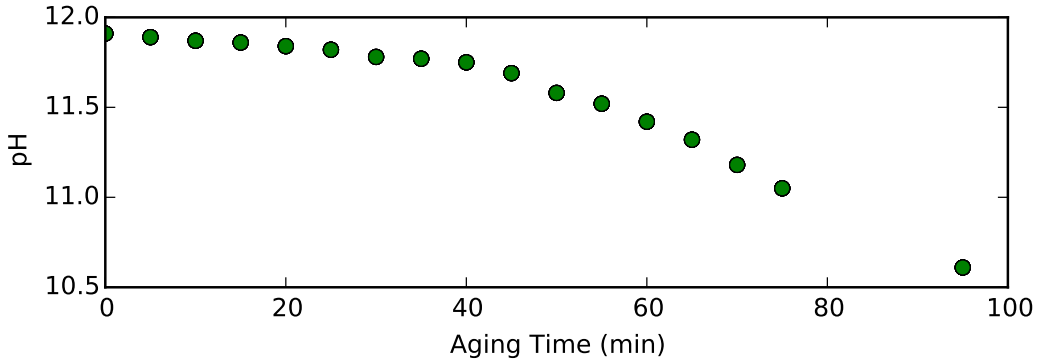

Figure 5.24.: Temporal evolution of the pH value of the THPC solution during aging.

Noticeable is the change in behaviour at around 40 minutes of aging, which was also observed in the UV-Vis spectra shown in fig. 5.23 and in the reaction delay and duration analysis shown in fig. 5.22 earlier. However, since this pH measurement was conducted independently from the above experiments a more dedicated and comprehensive study is required here.

Conclusion Laboratory Experiments

The lab experiments confirmed the aging of the THPC and NaOH solution equally in glass beakers and stainless steel vessels. As a direct result, the start of the reaction was delayed for several seconds with increasing aging time. Furthermore, the reaction efficiency was reduced and less nanoparticles are produced as the aging time increases. Moreover, a change of pH with aging time was found, which seems to correlate with the observed results. However, further studies are required to unravel the precise pH effects and other relevant reaction parameters. Both effects are very likely the reason for the partly missing reactivity of the solutions used during beamline experiments.

5.9. Overall Conclusion Liquid Phase Experiments

An experimental approach was presented to study the initial phase of the rapid AuNP formation by using THPC as reducing agent. The approach (section 5.2) utilized a rapid and thorough turbulent mixing as well as turbulent flow within the observation lines. This is important to sustain an unhindered reaction process and to obtain a plug flow, allowing a clear mapping of flow positions to reaction times.

It might preferentially be used for reactions with very short residence/reaction time. Otherwise, the demands in back pressure and/or flow rate become increasingly high and the setup becomes uneconomical. Alternative flow schemes might be better suited for longer observation times. This needs to be evaluated and adapted to the reaction of interest. The results of the current development are summarized in the following.

Fluid delivery using the syringe pumps offered precise liquid dosing even at low flow rates (page 112). High flow rates were possible for a short time only, due to the small volume of the syringes. Moreover, problems were encountered with continuous operation of the syringe pumps. Additionally, leaking of liquids at high back pressure was observed. Both issues are related to shortcomings of the currently used parts.

Advanced liquid dosing capabilities in terms of throughput and duration were provided by the fluidic rack, which was the key to realize the intended experimental approach (page 127). This was achieved by using pressurized vessels to overcome the flow resistance of tubings et cetera. Yet, a desirable improvement is a rack with fully remote-controllable flow controllers and flow switching.

Technically, the microfluidic chip design and the silicon based manufacturing has been proved to work (page 119). Solely the immediate coating of the channels with gold prevented access to the first two to 20 ms of the reaction. In all other respects the setup was fully working.

The free liquid jet, which is not prone to X-ray induced deposition that disturbed measurements in the other experimental setups, allowed the best performance for measurements of the liquid stream and easy operation, *cf.* page 126. The only drawback of the setup was the limitation of the accessible flow positions by the length of the capillary that is attached to the mixer. However, this issue can be addressed, *e.g.* by using capillaries of different length.

Although the reduction of $HAuCl_4$ solution with THPC was reproducibly conducted in lab experiments, it turned out to be more challenging in the continuous flow experiments, since the THPC solution starts aging immediately after addition of NaOH. This was manifested in reduced activity, elongated reaction duration, and increasing reaction delay as age of the solution increased. THCP aging therefore prevented reproducible and systematic investigations of the reduction reaction, especially because the onset of reaction was shifted beyond the experimentally accessible time domain of three seconds. Hence, future experiments should use continuously produced fresh THPC and NaOH mixtures for gold reduction.

By performing experiments with fresh THPC and NaOH solutions in continuous flow, the reaction should proceed like in the beaker. In a next step, AuNPs produced by batch and continuous flow techniques should be compared with respect to particle

size distribution and catalytic activity. Especially a possible influence of the turbulent flow is interesting, since this may indicate effects on the particle formation mechanisms. It is important to know whether results from continuous flow are valid for batch experiments or not. With a fully characterized experimental setup, the formation of other nanoparticles can be studied to gain new insights to kinetics and mechanisms and correlate nanoparticle properties to catalytic activity. For example copper and cobalt nanoparticles, as used for methanol synthesis [262, 263] and Fischer-Tropsch synthesis [264, 265] respectively. As already mentioned, this will very likely require tuning of some experimental parameters to adapt to the particular reaction.

By further use of THPC as reducing agent, mono-metallic nanoparticles from Pt, Pd, Rh, and Au, as well as alloys of them can be produced [212]. This offers a straightforward way to a multitude of interesting nanoparticle systems using the current setup. Copper nanoparticles (CuNP) have been prepared, very similar to the current AuNP synthesis, in a rapid reaction in water using $NaBH_4$ as reducing agent without gas protection [266]. Also large-scale, high-throughput synthesis was reported with controlled reduction [267], but further control of temperature and reaction in the minute-scale are required. This makes the experiments more challenging, since more parameters influence the CuNP synthesis result [268]. Cobalt nanoparticles (CoNP) have been prepared in a microfluidic synthesis [269] with improved control over the reaction, which required a more sophisticated microfluidic device. Furthermore, the produced CoNP solution was keep in N_2 atmosphere, which further increases complexity. This is in line with Lu *et al.* [270] stating: "synthesis of high-quality magnetic nanoparticles in a controlled manner, and detailed understanding of the synthetic mechanisms are still challenges to be faced in the coming years". Thus, interesting development and results can be expected.

Fast XAS beamlines should be considered for future experiments, preferentially using the free liquid jet, to realize a more efficient and economical setup. This is especially true if high flow rates are used. Moreover, conducting complementary techniques like SAXS and UV-vis in parallel would be beneficial to study size and shape of the produced nanoparticles. In addition to the comprehensive characterization of the reaction at lab scale, conditions expected during synchrotron experiments should be considered. This especially includes parameters which differ from the lab procedure for some reason, like solution aging in storage vessels. Alternative flow schemes, like for example segmented flow [223, 224], should be tested as supplement to the existing plug flow. This can be used to extend the observation duration. Thus this topic is presently further pursued in a new project at KIT ITCP.

6. Gas Phase Experiments

6.1. Introduction

The importance to characterize catalysts *in situ* and monitor them during reactions is nowadays a universally accepted fact and a commonly followed approach [16, 61, 137, 271]. This inherently demands the development of spectroscopic methods as well as suitable reaction cells with small dimensions and improved temperature control. Finally aiming to access the nanoscale as well as very short time scales with high spatial and temporal resolution.

So far, most used *in situ* setups are based on cm-sized setups or capillaries [21, 272–276]. However, this approach may suffer from problems, for example temperature gradients along the catalyst bed and feed gas by-pass, which may lead to flawed activity measurements [274].

An improved control over process parameters as well as better heat- and mass-transfer rates are expected for microreactors [277, 278]. By performing chemical process engineering in microreactors, it has been shown that various reaction system could be enhanced [278]. Hence, they are increasingly used in research to enhance spatial resolution, for example, and for syntheses in chemical industry [277–281]. An important aspect, with respect to industrial applications, is the easy upscaling by parallelization [282]. In chemistry related research, microreactors have been used as analytical tool in polymer and organic chemistry [283], biochemistry [284], and catalysis [278, 285–287].

Besides for process optimization, microreactors have also been used to solely monitor chemical reactions *in situ* or *operando* in combination with various complementary techniques like X-ray diffraction, X-ray absorption, UV-vis spectroscopy, and Raman spectroscopy [21, 229, 274, 285, 287–294]. Some studies in microreactors were also conducted in a spatially resolved manner to detect reaction gradients along the catalyst bed [22, 285, 293, 295]. Due to the small dimensions of microreactors, fast periodic temperature and/or gas composition changes are feasible, allowing to employ modulation excited spectroscopy, where the sensitivity is enhanced by phase sensitive detection of the system response to the perturbation [294, 296].

Most of the above-mentioned work was done in microreactors based on silicon, which is chemically inert, temperature stable, and can be well structured. A silicon based microreactor with external heating was used for sensitive testing of CO oxidation on Pt thin films successfully [297]. The fabrication of Si based chips with integrated Pt heater elements was reported by [286, 298].

Hence, the aim of this project was to develop and build an advanced Si-based gas phase microreactor device including a heater and a temperature readout, suitable for various spectroscopic methods, with XAS and XRD in the first place, and free from

the aforementioned limitations of glass capillary setups.

Thus, by making use of micro devices an improved control over experimental conditions and advantageous reaction conditions can be expected, which grants more detailed insight into catalytic gas phase reactions [277, 278].

Within the period of this thesis a first version of the device was finished and is now further developed within another project by Sina Baier. Hence, the purpose of this chapter is to provide documentation of the design and implementation, as well as to point to further improvements of the existing device.

6.2. Design Considerations

Up to now, many *in situ* gas phase experiments have been carried out using a thin glass capillary attached to gas lines and mounted on top of a gas blower for heating [21]. Although this approach was used successfully, it is still challenging and leaves room for improvements.

Referring to experiments carried out by myself, first of all, the handling of thin glass capillaries and leak-tight installation is delicate. Since both ends of the capillary were put into graphite ferrules and plugged into Swagelok® connectors fixed by a union nut. Any misalignment of the capillary in the ferrule or tensions while tightening the union nut, in order to seal the gas connector by the ferrule, will break the capillary.

Since heating is done by a hot gas stream from a massive gas blower, it cannot realize rapid temperature changes and the heating is dependent on the distance to the hot stream. Moreover, the temperature of the catalyst bed is not measured directly but by an external thermocouple between the gas blower and underneath the capillary.

The design of the new setup should be in a way that silicon wafer based chips, containing the sample, can be quickly exchanged and are mounted almost automatically gas-tight by the design of the support. In comparison to the external gas blower, the integrated heater should allow to rapidly change temperatures or to perform fast temperature ramps, since a direct heating is used and very little mass must be heated.

Besides the microdevice as reactor itself, a support for mounting, gas feeding, and electrical contact has to be designed. Additional, specific requirements arise from the following usage aspects, which constrain the design parameters.

Since X-ray spectroscopy is intended for later experiments, X-ray stable and transparent materials for photon energies above 10 keV are needed. These should be free from fluorescence yielding components to minimize background. Similarly, material that might also serve as potential catalyst, *e.g.* Pt, should not be used close to the sample region. The dimensions of the chip, especially thickness, need to allow detection of fluorescence signals from the sample including a geometry factor, since fluorescence signals are not detected at an angle of 90° but at 45° resulting in a longer path through the chip material. Furthermore, the sample compartment should be big enough to fill in the typical 100 µm large sieve fractions of catalyst powder and to hold enough sample to produce a reasonable absorption signal. Obviously, neither the chip nor the support should block the X-ray beam or the positioning of the detector.

From the catalytic point of view, stable (non-oscillating) and gradient free temperatures up to 550 °C are desired in the sample region. Furthermore, a built-in heater and a built-in temperature sensor for direct heating and temperature measurements and control are needed. Very important are a gas-tight fabrication of the chip and gas-tight connection to the support, allowing to precisely feed gases and collect products for analysis. Additionally, the materials used must be gas compatible/resistant, temperature stable, and catalytically inactive.

These requirements are well met by a support with external standard gas ports and internal connectivity to the silicon wafer based microreactor. Similarly, electrical contacts from the outside to the chip are required. In addition, suitable heater, temperature sensor, and temperature controller as well as a temperature calibration of the chip are needed. For practical reasons, an optically transparent cover should be used on the side of the channel to allow visual inspection of the catalyst bed and to perform optical spectroscopies.

6.3. Experimental Setup

The design specifications were worked out and adapted to technical possibilities in close collaboration with GeSiM GmbH that also manufactured the chips.

The realized setup consists of a free standing chip in a frame like support. Silicon wafers of 400 µm thickness were used as base material for the chip, where gas channels were produced by Si etching. Heating was realized via a Pt thin film layer similar to the Pt temperature sensor. A glass plate made of Borofloat 33 (Schott AG) on top of the channel functions as transparent cover.

Borofloat 33 is a boro-silicate-glass consisting of approximately 80 % SiO_2, 13 % B_2O_3, 4 % Na_2O, 2 % Al_2O_3, and traces of other oxides less than 0.1 %, thereby ensuring no fluorescence from elements within the glass. The thermal expansion coefficient is adapted to that of silicon ($3.3 \times 10^{-6}\,K^{-1}$, between 20 and 400 °C), UV transmission begins at about 300 nm, IR cut off at 3.5 μm; ref. index is 1.475 (Na D-line). Important for later heating experiments are the transformation temperature of 525 °C and the softening point of around 820 °C. Thus a temperature way above 515 °C should be avoided.

In fig. 6.1 the Si etching masks and layouts of metal deposits on the chip are shown. A single chip, fig. 6.1(h), is made from a 400 µm thick silicon wafer which is partially Pt coated, with 200 nm thickness, on the upper side and sealed by a 100 µm thick Borofloat glass on the lower side. The channels on the lower side of the chip, fig. 6.1(b), are 250 µm deep with an initial width of 1500 µm, to aid filling the sample, which later gradually narrows to the final width of 500 µm. On the upper side, fig. 6.1(a), a 13 mm long observation window is located, indicating the final sample position in the channel on the opposite side of the chip. It is etched another 110 µm deep to reduce the Si thickness to 40 µm, thus improving transmission experiments. In order to aid loading sample to the chip, the gas inlet has a larger diameter of 1.5 mm as compared to the

outlet with 0.8 mm. The loaded sample is stopped from entering the channel U-turn by a channel blocking structure consisting of blocks of 60 µm in size on a 100 µm raster. Thus, after this point only gas is flowing back to the outlet.

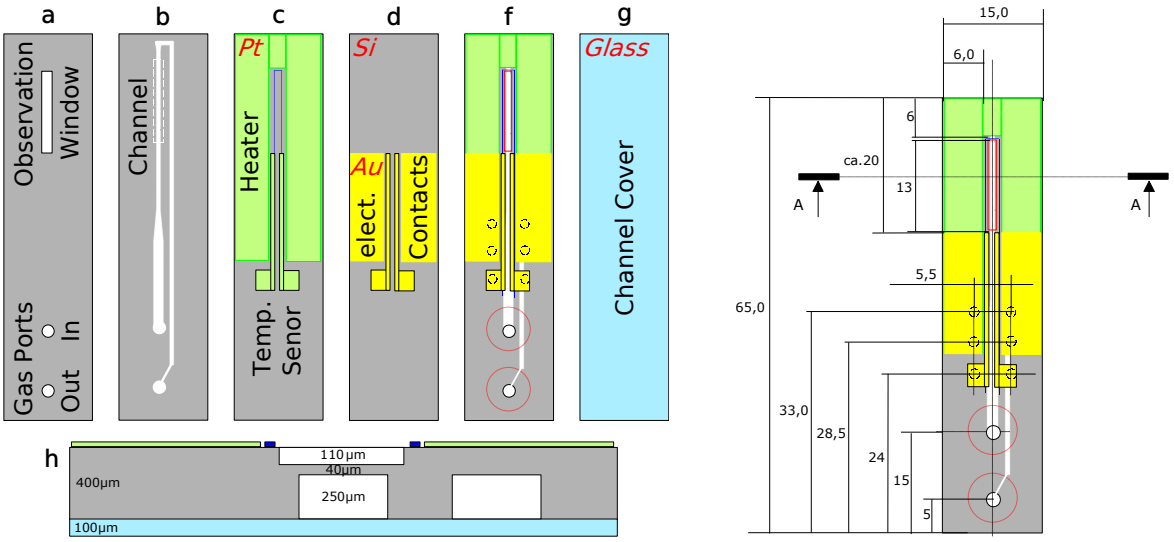

Figure 6.1.: Design and construction plan of the gas phase chip. Si chip etching masks for the **a** upper side and **b** lower side. Metal depositions masks for **c** platinum heater and temperature sensor and **d** electrical contacts both superimposed in **f**. The **g** Borofloat glass cover to close the lower side of the chip and **h** cross-section through the resulting chip along A-A, shown on the right hand side drawing which also includes the chip dimensions. Materials color codes: silicon (light gray), platinum (green), gold (yellow), and glass (light blue) are also denoted in red italic font.

A home made heater power supply and controller box was built by the electronic workshop of the institute. It contained a temperature controller (Eurotherm 2416) with serial interface (RS232) and was used to operate the controller by a custom LabView (National Instruments) program.

The power supply used for heating the chip was a simple constant current source, switched on and off several times a second. Initial test experiments using this source showed unstable performance and partially oscillating temperatures. Therefore, an improved power supply was used, utilizing a phase-fired controller which provides a continuous adjustment of the applied heating power. The superior performance in temperature stability and response, which are a key point for the control of the reaction, became immediately evident in test experiments.

The individual chips were mounted into a dedicated support device, shown in fig. 6.2, that provides mechanically stable and reproducible mounting, electrical contacts, and gas ports. For optional cooling of the support an additional port is present (gray), to flow pressurized air through the support base.

In total six electrical contacts, four for the heater and two for the temperature sensor, were realized by flexible legs, visible as golden pins in fig. 6.2. The gas connection was achieved by two cylindrical legs (brown), with screw nuts (blue) on the top and O-ring seals on the bottom end. The entire upper block (light blue) of the support is held by

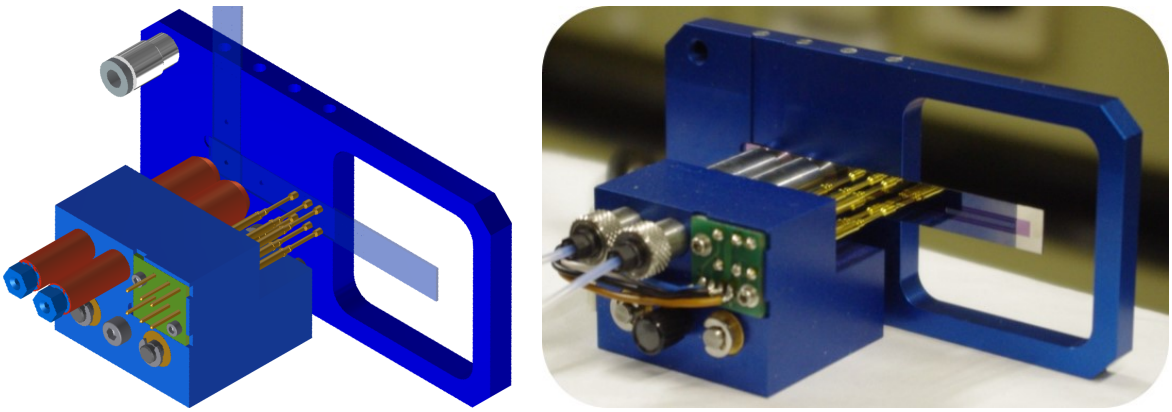

Figure 6.2.: Design drawing of the support and photo of the final product with a mounted gas phase chip. (Images by GeSiM and A. Rochet respectively)

springs in an upper position and has to be manually pushed down and fixed in this position by screws to mount the chips.

Temperature Calibration and Gradients

A temperature calibration was necessary, since no calibration curve $T(R)$, mapping a Pt sensor resistance R to a chip temperature T, was provided except two points at 20 and 500 °C.

A preliminary calibration was done for an empty chip without gas flow using the built-in heater operated with an adjustable power source with fixed 100 mA and $0-24$ V output. The heating power was adjusted manually to proceed in small temperature steps, which were measured by a thermocouple tip touching the chip surface in the center of the observation window as depicted in fig. 6.3.

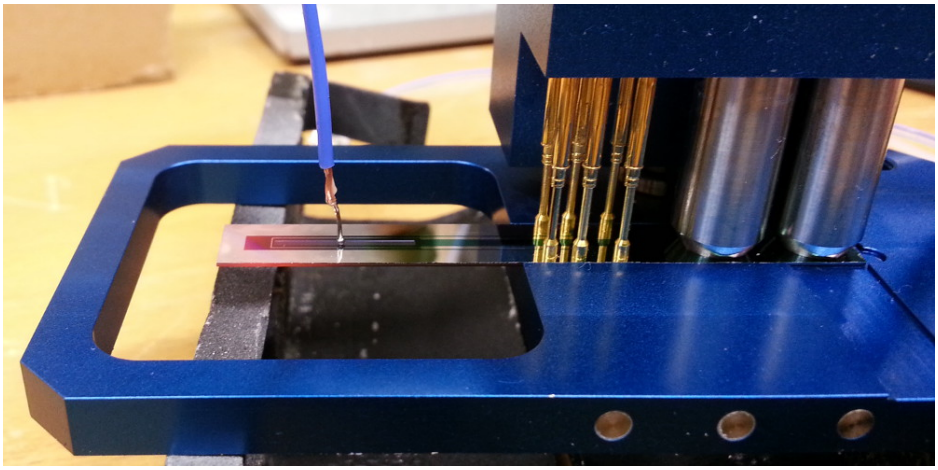

Figure 6.3.: Temperature calibration of a gas phase reactor chip using a thermocouple.

The resulting calibration curve in fig. 6.4 shows the resistance of the built-in temperature sensor and the corresponding externally measured temperature. As expected for a Pt sensor, the data was quite well reproduced by a linear fit, that provides the

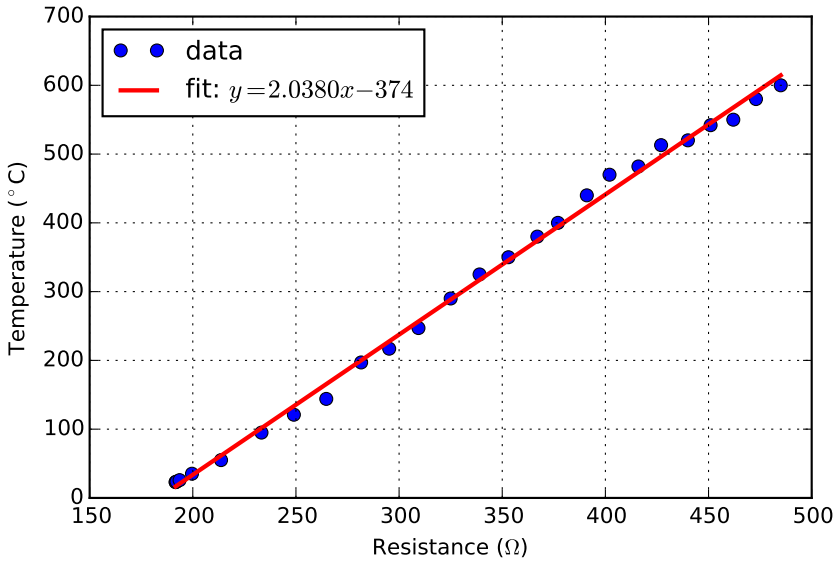

Figure 6.4.: Temperature calibration curve for a gas phase reactor chip.

desired functional description of the calibration curve

$$T(R) = 2.0380 \cdot R - 374\,.$$

Strictly speaking, this calibration is only valid for this particular chip, since variations have been observed within a batch of chips which might originate from the Pt depositions process. On the other hand, assuming linear behavior, the two provided points could be used to directly calculate the linear dependency. However, this should be checked carefully before conducting sophisticated experiments, especially when temperature gradients in the chip are expected as discussed in the next section.

During the temperature calibration run, a distinct temperature gradient on the chip was observed with bare eye, as shown in the left image of fig. 6.5. This is evident by

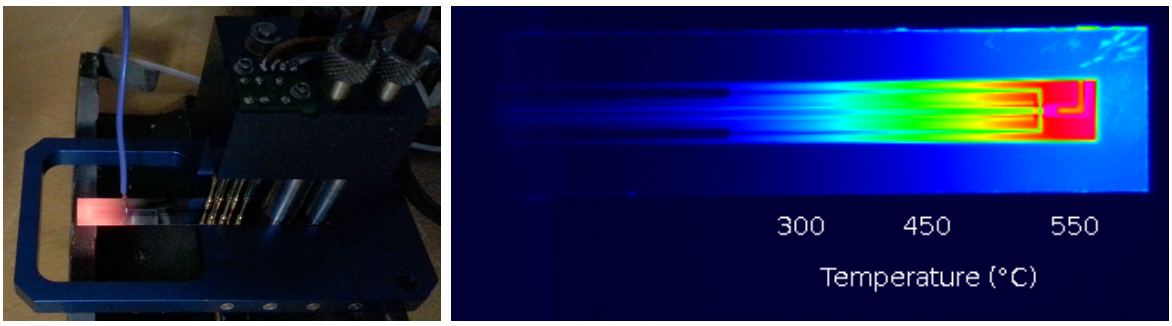

Figure 6.5.: Temperature profile of the actively heated chip (100 mA, 24 V). Left: Photograph of the chip during temperature calibration and testing showing a red glowing tip. Right: IR thermography image taken by a FLIR SC7000. Both images clearly show a distinct temperature gradient on the chip.

the red glowing tip of chip during heating, which was confirmed by a thermography image in the right pane of fig. 6.5, showing a rapid cooling from 550 to 300 °C within around 20 mm resulting in a gradient of approximately 12.5 K mm^{-1}. A gradient was expected, but its magnitude was hard to predict, since the coupling of the chip to the support was unknown. Such heat transfer parameters can be deduced from this experiment to perform more realistic simulations.

The observed temperature gradient poses a severe problem, as local overheating might damage the chip. Even more problematic is the influence on the catalyst and reaction properties. A constant temperature along the catalyst bed is needed to perform well-grounded experiments. Based on the improved input data, generated from this test, this issue was resolved in a second version of the gas phase chip.

6.4. First in situ Experiments

This chapter reports on the first experiments that were performed using the *in situ* device designed in this work. The performance of the device is critically evaluated and possible future directions are discussed. The experimental results presented here have been conducted by Amélie Rochet and Sina Baier, using a 4 wt.% Pt/Al_2O_3 catalyst, (*cf.* section 3.3.2 on page 25), and already utilized the second generation of the microreactor with an improved temperature profile. Only an excerpt is shown and more detailed analysis and further methodical compatibility tests will be available in an upcoming publication [299]. Synchrotron beamline test have been conducted at SUL-X (ANKA, Karlsruhe) [300, 301].

6.4.1. X-Ray Absorption Spectroscopy

The operability of the gas phase reactor for *in situ* X-ray absorption spectroscopy was tested by tracing the catalytic partial oxidation of methane to Syngas ($CH_4 + \frac{1}{2}O_2 \rightleftharpoons CO + 2H_2$). For this purpose the 100 to 200 µm sieve fraction of a 4 wt.% Pt/Al_2O_3 catalyst was used. A pre-mixed gas feed composed of CH_4/O_2 (6 %/3 %) in He flowed through the chip with a rate of 2.6 ml min^{-1}, while the temperature was ramped from room temperature to 450 °C with 5 °C min^{-1}.

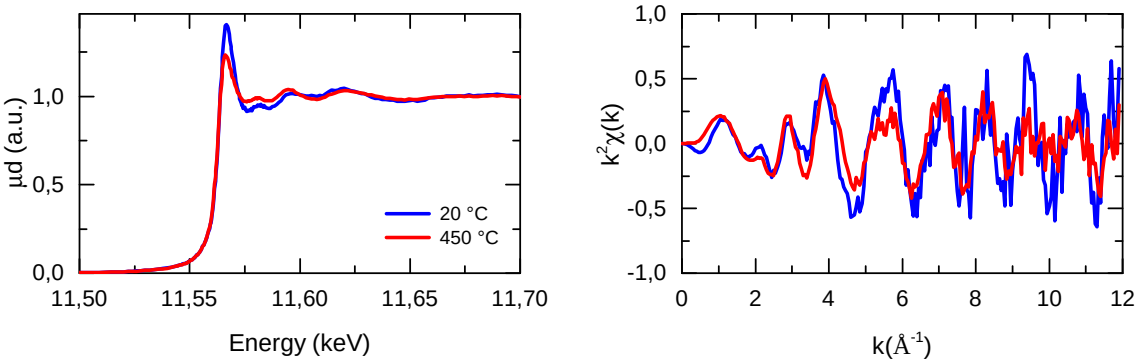

Figure 6.6.: X-ray absorption spectra of a 4 wt.% Pt/Al_2O_3 catalyst during catalytic partial oxidation of methane in the gas phase microreactor (left) with corresponding EXAFS signal (right).

Measurements of the Pt L_3 were performed using a 7 element Si(Li) fluorescence detector. According to the spectra shown in fig. 6.6, Pt was initially present as oxide at room temperature (blue). As the temperature was raised and after ignition of the reaction, Pt was slightly reduced (red). Upon cooling, and after extinction of the reaction, Pt was re-oxidized and the previous state was restored (blue). The corresponding EXAFS results, shown on the right in fig. 6.6, reveale a good data quality suitable for further analysis. Notably, measurements in transmission have also been successfully performed, but require samples with higher metal loading to obtain a decent edge jump.

This proves the ability of the microreactor to run controlled *in situ* reactions in combination with spectroscopic investigation.

6.4.2. X-Ray Diffraction

Another function test for XRD was performed at SUL-X, ANKA using a photon energy of 16 keV, a beam size of 100 × 100 µm, and 20 s exposure with a CCD detector 85 cm away from the sample. As expected for the empty chip, measured in the observation window, no distinct sharp diffraction peak was found (green line in fig. 6.7). Just one broad feature was observed around 2Θ=10°, which is attributed to the amorphous glass cover.

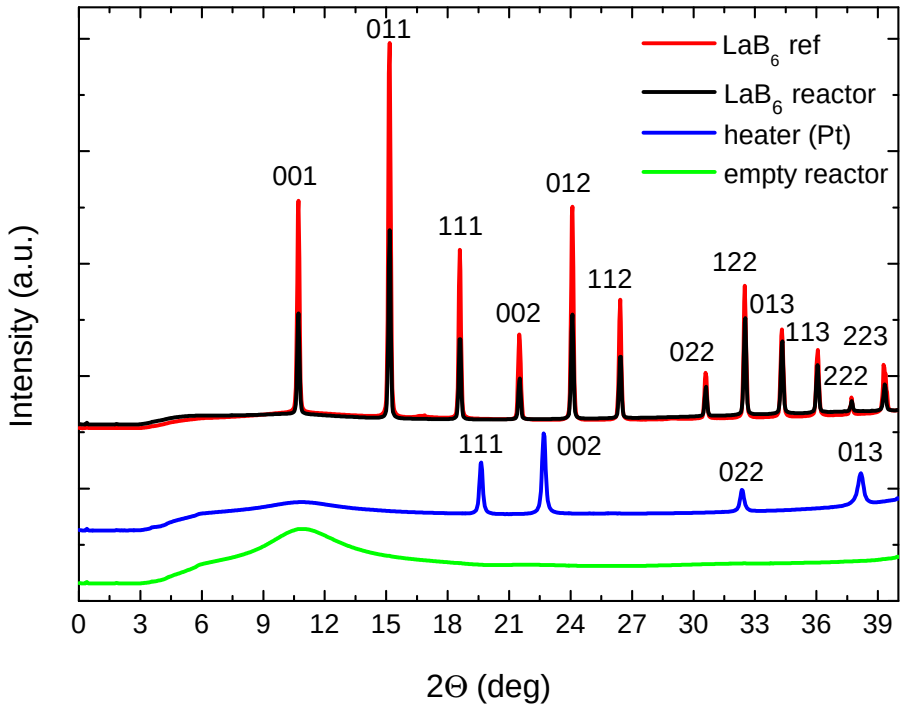

Figure 6.7.: X-ray diffractograms of the empty gas phase reactor in the observation window (green) and on the Pt heater (blue). LaB_6 reference in a capillary (red) and inside the chip (black).

Diffraction data from a LaB_6 standard powder was collected being mounted inside a conventional quartz glass capillary and inside the microreactor chip. This helps to assess the reproducibility and quality of diffraction data obtained from the chip.

Data from the capillary with 280 µm inner diameter and a 10 µm wall thickness is shown in red in fig. 6.7. All reflections have been indexed to the corresponding diffraction plane (hkl). The same sample, measured in the chip, yielded the black diffractogram shown in fig. 6.7.

As fig. 6.7 underlines, the corresponding black and red lines match, every peak was reproduced but with lower intensity in the chip due to higher absorption. This was even pronounced for small angles 2Θ due to the resulting extension of the distance the beam has to travel through the chip. Nevertheless, the chip works as expected and can be reliably used in future experiments. In situations without dedicated calibration samples, the deposited Pt heater layer on the chip may be used, which produces characteristic Pt diffraction peaks.

Additionally, the *in situ* measurement of catalytic partial oxidation of methane was repeated to capture changes in the diffraction pattern of the catalyst. However, since the catalyst preserved its initial, finely dispersed Pt nanoparticles no characteristic Pt reflections were observed and thus no plot of the data is shown here.

6.5. Conclusion & Outlook

A fully functional microdevice for *in situ* investigation of gas phase reactions has been designed, realized, and successfully tested. The chip is based on a silicon wafer, which has been processed to host a gas-tight channel structure. Furthermore, a resistive heater and temperature sensor based on Pt coatings are added to the chip surface. A tailored support ensures reproducible and easy mounting of chips in conjunction with leak free gas feeding and proper electrical contacts to the built-in heater and temperature sensor. The home-made power supply with integrated remote controllable temperature controller and phase-fired heating output permits stable and reliable operation.

The presented first design suffered from a strong temperature gradient of $12.5\,\mathrm{K\,mm^{-1}}$ at 550 °C measured by IR thermography. This was solved by optimization of the initial heater layout based on temperature simulations of the chip performed by Sina Baier. These were based on the parameters derived from the gradients of the first device generation. The second generation features a more advanced heater layout yielding an almost uniform temperature distribution across the length of the observation window and catalyst bed. The current temperature is limited to maximal 525 °C due to the transformation temperature of the glass cover, that would lead to the appearance of disturbing X-ray reflections.

The presented first tests using XRD have shown that no disturbing reflections originate from the reactor and that a LaB_6 diffraction pattern can be fully reproduced. Furthermore, the successful operation of the microreactor chip during *in situ* XAS experiments was demonstrated. The device can therefore by used with X-ray characterization techniques as well as with complementary optical spectroscopies and infrared thermography.

Within the current status of the project, the main development of the second version has successfully been finished [299]. The gas phase microreactor is ready for use in *in situ* experiments in a more controlled and reproducible way, thus enabling experimenters to gain new insights. Future chip versions may replace or skip the Borofloat glass to reach even higher temperatures, without deteriorating the reactor properties.

By exploiting the mechanical stability with a well protected catalyst bed inside the chip and a fast and precise temperature control it becomes possible to reproduce experimental conditions more reliably. This, as prerequisite, enables subsequent *in situ* measurements of the sample/reaction using potentially different experiments to correlate different techniques and thus gain complementary information. Especially the small dimensions of the catalyst bed allow full field measurements capable of capturing single grain effects with improved spatial resolution.

Part IV.

Final Remarks

7. Final Summary & Conclusion

An improved catalyst design and function will have a huge economical and environmental impact, since around 90 % of all products from industry make use of at least one catalyst. To gain such valuable new insights and deeper understanding is a challenging task due to the dynamic nature of catalysts. The interplay of several system properties spans different time and length scales [12, 13] and thus requires the most advanced experimental techniques and theoretical descriptions available [11].

In this work methods and devices were developed in order to extend and improve *in situ* catalysts characterization capabilities. Thus enabling new insight into reaction dynamics with high temporal and spatial resolution using microreactors and X-ray microscopy. In line with the structure of the thesis, the main aspects of the four areas of development are summarized in the following.

7.1. Overall Summary

Quasi *in situ* X-ray absorption micro-computed tomography (μ-CT) methodology and quantitative analysis was developed. This allowed to follow Pt sintering in single honeycomb exhaust gas catalyst channels during isothermal aging at 950 °C. Strong Pt sintering increased the absorption of individual voxels, evident by new features in the histogram. Assignment of these voxels, referred to as blobs, to Pt sintering was confirmed by EPMA. Consequently, the increased absorption was exploited to perform a segmentation of support and precious metal phase based on thresholding. This allowed rigorous quantitative analysis of a variety of properties of individual blobs and the entire blob ensemble.

The quantitative analysis yielded steadily increasing number, volume, and Pt content of the blobs as function of aging time. A correlated growth of volume and absorption was observed. Tracking of individual blob evolution was demonstrated and individually determined growth rates were used to cluster the blob ensemble into four different growth regimes. Utilizing volume renderings, Pt redistribution and agglomeration was directly followed over aging time with high spatial resolution.

Besides segmentation based analysis, a difference method and visual inspection/comparison was evaluated. These were used to qualitatively identify aging effects from quasi *in situ* μ-CT data, such as the formation of cracks in the washcoat and resulting material displacement.

Screening of several honeycomb samples by tomography revealed considerable variations in the washcoat loading and distribution. Therefore, μ-CT is a possible characterization method to improve catalyst preparation with respect to homogeneity and reproducibility of the washcoat. For this application lab CT devices are an interesting alternative. Moreover, it underlines the need for *in situ* studies in combination with

tomography to address spatial variations.

Imaging of metal nanoparticles by hard X-ray ptychography with chemical contrast was developed in collaboration with the group of Prof. Schroer. Experimental procedures and the analysis technique at beamline P06 (PETRA III at DESY) were advanced as a first step toward *in situ* studies. Imaging with chemical contrast and 10 nm resolution was demonstrated. This was achieved by providing a well-prepared and by electron microscopy pre-characterized set of model samples. The first set of samples consisted of Au nanoparticles and a Pt marker to develop a methodology to evaluate chemical contrast as function of energy while crossing the $Au\,L_3$ absorption edge. The second set of samples was prepared as a mix of Pt, Au, and Pd nanoparticles of different sizes to benchmark chemical contrast and resolution.

A liquid phase experiment was developed for *in situ* investigations of the early processes of the gold nanoparticle (AuNP) formation using THPC as reducing agent. Processes in the early phase govern the resulting AuNP shape and size distribution, which is essential for their physical properties. The approach is encompassing rapid mixing, continuous turbulent (plug) flow, and on-line measurements of the reaction mixture by XAS with high temporal resolution resulting from a mapping of acquisition position to reaction time. To this end, different fluidic storage and delivery setups as well as microfluidic mixers were tested, and various acquisition schemes were evaluated.

Experiments with fluidic storage and delivery setups showed that the syringe pump setup can dose the required fluids precisely but starts to leak as soon as the back pressure in the system becomes too high. Hence, no proper continuous mode could be realized. The second setup tested, the fluidic rack with hydrostatic pressure pumping, accomplished to dose liquids pulsation free even at high back pressure and with high flow rates although with less precise control of the flow conditions. However, in both cases, dosing time is limited by the fluid reservoir in the system.

For rapid mixing, a tailored microfluidic chip, made from silicon, with a triple cyclone mixer and an integrated observation channel was designed and built based on CFD simulations. In particular, the focus was laid on rapid mixing and turbulent flow, which hardly any device offers at the moment, hence it offers optimal mixing results for the targeted operation. The microfluidic chip and support construction were shown to be leak-tight and worked as desired. XAS measurements in the microfluidic device were possible but required continuous variation of the scan positions to minimize the effect from beam induced deposition. Nevertheless, immediate coating of the microfluidic chip with a gold layer during the reaction prevented measurements of the liquid underneath.

In addition a stand-alone single cyclone mixer was used, developed by IMVT KIT, with attached capillaries to investigate the fluid either directly or after feeding it into a free liquid jet. While deposition occurred in the capillary as well, it was of course not present in the free liquid jet. Hence, the jet proved to be the best way to measure X-ray sensitive liquids and offered best XAS signals. However, scanning along the liquid stream is more difficult using the jet.

In summary, the technical approach to access early reaction times with high temporal resolution was successfully realized. The fluidic rack, the microfluidic chip, and the free liquid jet are working as designed. However, experimental challenges like gold

coating in general and X-ray induced reduction of the $HAuCl_4$ solution in combination with deposition have to be solved. They prevent the measurement of the reaction process, which was not only evident in XAS measurements but will also hamper other characterization techniques.

Furthermore, deactivation of the reducing agent over time occurred. As dedicated lab experiments confirmed, the reaction was delayed beyond the experimentally accessible time and the reaction yield was considerably reduced as well. Steady production of fresh reducing agent solution may solve this problem.

An improved *in situ* gas phase microreactor was developed and built to overcome the limitations of the existing quartz glass capillary based setup. This includes mechanical stability, easy and reliable leak-tight mounting as well as improved temperature control. The microreactor is based on a structured silicon wafer and integrates a Pt heater as well as a Pt temperature sensor. First experiments using a Pt/Al_2O_3 catalyst and a LaB_6 reference confirmed full operability of the setup for on-line product analysis and compatibility to XAS and XRD. Similarly, Raman and IR thermography can also be used to study the sample inside the microreactor.

7.2. Overall Conclusion & Outlook

The present work has shown several ways to improve *in situ* spatial and temporal resolution for different fields in catalysis research. New insights have been gained as well as experience for further experimental developments and methodical improvements.

To push the limits of the methods further, higher resolution quasi *in situ* experiments on the washcoat aging can be obtained by studying small capillaries with samples of the washcoat only in μ-CT. This also allows to study the influence of temperature and gas atmosphere in more detail. Furthermore, changes of impregnated catalyst pellets can be studied starting from impregnation, calcination, and after usage in a catalytic reaction or aging. This will reveal changes in the metal distribution and help to improve coating properties for better catalytic performance.

As quasi *in situ* X-ray absorption micro-computed tomography is a non-destructive and spatially resolved technique, this allows to follow sample changes over time and to complement other more conventional characterization methods, especially by exploiting the quantitative abilities of the method. In XRD, for example, due to bulk averaging and samples usually taken post-mortem, often no precise information on the spatial distribution of phases of interest can be gained. In SEM limitations arise when the interior of a sample is of interest, since this requires destructive sample preparation like FIB-cutting. Moreover, *in situ* μ-CT experiments combined with parallel catalytic testing are reasonable and tempting in order to improve correlation between the two techniques. Especially correlative tomography is promising to relate complementary techniques across different length scales, which also includes higher spatial resolution.

Highest resolution is also expected from the use of *in situ* ptychography cells, exploiting the high penetration depth of hard X-rays, to follow changes of the catalysts

under more realistic conditions. This will allow to study sintering or alloying of nanoparticles under *in situ* conditions. Using the chemical contrast capabilities, changes in the oxidation state during reactions may be studied as well. Even an extension to 3D imaging is possible, allowing to study distribution and evolution of particles or pores within a small catalyst pellet for example.

Interesting new nanoparticles with defined properties can by obtained by the application of the liquid phase chip to optimize reaction conditions. By using THPC, nanoparticles from Pt, Pd, Rh, and Au as well as combinations of them can be obtained. This allows to study their formation mechanisms and kinetics, using the current setup. Cu or Co nanoparticles may be studied in a similar fashion, but very likely the microfluidic parts have to be adapted to the approximate course of the reaction to cover the relevant time frame. This includes possible initial reaction delays and the total duration of the reaction. Furthermore, temperature becomes an important synthesis parameter, which needs to be controlled as well. Current coating issues of microfluidic parts may be overcome in future by functionalization of the channel walls, different flow patterns or modifications of the complete setup, for example the utilization of the free liquid jet alone for measurements.

Finally, the catalytic reaction itself can then by studied *in situ* in the gas phase reactor. The small dimensions and improved control allow to study the sample/reaction in greater detail and with higher spatial resolution. This will enable subsequent reproducible experiments, which can be exploited to apply different characterization techniques, at the synchrotron or in the lab, and to correlate the results.

Although the individual techniques and devices have been developed/optimized separately for their special purpose, they may be combined now to cover a broader range in spatial and temporal resolution.

For example, μ-CT can be used to identify interesting sample regions, which can be further inspected by SEM or X-ray ptychography, even in 3D. Catalyst powders characterized in the gas phase microreactor may also be studied *in situ* by ptychography in future. Accordingly, tailored nanoparticles from the liquid phase setup may be used and studied by the above techniques. Thus a valuable contribution to the variety of characterization techniques was made.

Accordingly, special focus should be laid on the parallel acquisition of as many spectroscopic information and reaction data as possible to reduce ambiguities arising from variations of the actual reaction conditions present in different setups. These might be pressure, average temperature, temperature gradients, differences in lateral distribution of the catalytically active sites due to usage of different parts of the sample and many more.

By using the herein developed *in situ* methods and devices, more challenging questions can be addressed in future. However, these were only the first steps as there is always room and need for improvement. The author hopes that the current work inspires and enables future work in this direction.

Part V.

Bibliography & Appendix

Bibliography

[1] G. Ertl, H. Knözinger, F. Schüth, and J. Weitkamp, eds. *Handbook of Heterogeneous Catalysis*. Weinheim, Germany: Wiley-VCH Verlag GmbH & Co. KGaA, 2008. DOI: 10.1002/9783527610044 (cit. on p. 3).

[2] Z. Rui, S. Wu, H. Ji, and Z. Liu. "Reactivation and Reuse of Platinum-Based Spent Catalysts for Combustion of Exhaust Organic Gases". In: *Chemical Engineering & Technology* 38.3 (2015), pp. 409–415. DOI: 10.1002/ceat.201400467 (cit. on p. 3).

[3] J. Hagen. *Industrial Catalysis: A Practical Approach*. 2nd, completely rev. and extended ed. Weinheim: Wiley-VCH, 2006 (cit. on p. 3).

[4] R. Schlögl. "Ammonia Synthesis". In: *Handbook of Heterogeneous Catalysis*. Ed. by G. Ertl, H. Knözinger, F. Schüth, and J. Weitkamp. Weinheim, Germany: Wiley-VCH Verlag GmbH & Co. KGaA, 2008. DOI: 10.1002/9783527610044.hetcat0129 (cit. on p. 3).

[5] C. J. H. Jacobsen, S. Dahl, B. S. Clausen, S. Bahn, A. Logadottir, and J. K. Nørskov. "Catalyst Design by Interpolation in the Periodic Table: Bimetallic Ammonia Synthesis Catalysts". In: *Journal of the American Chemical Society* 123.34 (2001), pp. 8404–8405. DOI: 10.1021/ja010963d (cit. on p. 3).

[6] F. Besenbacher, I. Chorkendorff, B. S. Clausen, B. Hammer, A. M. Molenbroek, J. K. Nørskov, and I. Stensgaard. "Design of a Surface Alloy Catalyst for Steam Reforming". In: *Science* 279.5358 (1998), pp. 1913–1915. DOI: 10.1126/science.279.5358.1913 (cit. on p. 3).

[7] J. K. Nørskov et al. "Universality in Heterogeneous Catalysis". In: *Journal of Catalysis* 209.2 (2002), pp. 275–278. DOI: 10.1006/jcat.2002.3615 (cit. on p. 3).

[8] J. Greeley and M. Mavrikakis. "Alloy Catalysts Designed from First Principles". In: *Nature Materials* 3.11 (2004), pp. 810–815. DOI: 10.1038/nmat1223 (cit. on p. 3).

[9] J. K. Nørskov, T. Bligaard, J. Rossmeisl, and C. H. Christensen. "Towards the Computational Design of Solid Catalysts". In: *Nature Chemistry* 1.1 (2009), pp. 37–46. DOI: 10.1038/nchem.121 (cit. on p. 3).

[10] A. T. Bell. "The Impact of Nanoscience on Heterogeneous Catalysis". In: *Science* 299.5613 (2003), pp. 1688–1691. DOI: 10.1126/science.1083671 (cit. on pp. 3, 16).

[11] I. Chorkendorff and J. W. Niemantsverdriet. *Concepts of Modern Catalysis and Kinetics*. 2nd, rev. and enl. ed. Weinheim: Wiley-VCH, 2007 (cit. on pp. 3, 145).

[12] B. M. Weckhuysen. "Chemical Imaging of Spatial Heterogeneities in Catalytic Solids at Different Length and Time Scales". In: *Angewandte Chemie-International Edition* 48.27 (2009), pp. 4910–4943. DOI: 10.1002/anie.200900339 (cit. on pp. 3, 4, 81, 145).

[13] J.-D. Grunwaldt, J. B. Wagner, and R. E. Dunin-Borkowski. "Imaging Catalysts at Work. A Hierarchical Approach from the Macro- to the Meso- and Nano-Scale". In: *ChemCatChem Reviews* 5 (2013), pp. 62–80. DOI: 10.1002/cctc.201200356 (cit. on pp. 3, 4, 15, 16, 145).

[14] J. W. Niemantsverdriet. *Spectroscopy in Catalysis: An Introduction*. 3rd completely rev. and enl. ed. Weinheim and [Chichester]: Wiley-VCH and John Wiley, distributor, 2007. DOI: 10.1002/9783527611348 (cit. on p. 3).

[15] R. Schlögl. "Heterogeneous Catalysis". In: *Angewandte Chemie (International ed. in English)* 54.11 (2015), pp. 3465–3520. DOI: 10.1002/anie.201410738 (cit. on p. 3).

[16] B. M. Weckhuysen. "Snapshots of a Working Catalyst: Possibilities and Limitations of in Situ Spectroscopy in the Field of Heterogeneous Catalysis". In: *Chemical Communications* 2 (2002), pp. 97–110. DOI: 10.1039/b107686h (cit. on pp. 3, 133).

[17] J.-D. Grunwaldt and A. Baiker. "In Situ Spectroscopic Investigation of Heterogeneous Catalysts and Reaction Media at High Pressure". In: *Physical Chemistry Chemical Physics* 7.20 (2005), pp. 3526–3539. DOI: 10.1039/b509667g (cit. on p. 3).

[18] H. Topsøe. "Developments in Operando Studies and in Situ Characterization of Heterogeneous Catalysts". In: *Journal of Catalysis* 216.1-2 (2003), pp. 155–164. DOI: 10.1016/S0021-9517(02)00133-1 (cit. on p. 3).

[19] J. F. Haw. *In-Situ Spectroscopy in Heterogeneous Catalysis*. Weinheim, FRG: Wiley-VCH Verlag GmbH & Co. KGaA, 2002. DOI: 10.1002/3527601589 (cit. on p. 3).

[20] B. M. Weckhuysen. *In-Situ Spectroscopy of Catalysts*. Stevenson Ranch, Calif.: American Scientific Publishers, 2004 (cit. on p. 3).

[21] J.-D. Grunwaldt, M. Caravati, S. Hannemann, and A. Baiker. "X-Ray Absorption Spectroscopy Under Reaction Conditions: Suitability of Different Reaction Cells for Combined Catalyst Characterization and Time-Resolved Studies". In: *Physical Chemistry Chemical Physics* 6.11 (2004), pp. 3037–3047. DOI: 10.1039/B403071K (cit. on pp. 3, 133, 134).

[22] J.-D. Grunwaldt, B. Kimmerle, A. Baiker, P. Boye, C. G. Schroer, P. Glatzel, C. N. Borca, and F. Beckmann. "Catalysts at Work: From Integral to Spatially Resolved X-Ray Absorption Spectroscopy". In: *Catalysis Today* 145.3-4 (2009), pp. 267–278. DOI: 10.1016/j.cattod.2008.11.002 (cit. on pp. 3, 16, 133).

[23] J. Singh, C. Lamberti, and van Bokhoven, Jeroen A. "Advanced X-Ray Absorption and Emission Spectroscopy: In Situ Catalytic Studies". In: *Chemical Society Reviews* 39.12 (2010), pp. 4754–4766. DOI: 10.1039/c0cs00054j (cit. on p. 3).

[24] D. Ferri et al. "Synchrotron High Energy X-Ray Methods Coupled to Phase Sensitive Analysis to Characterize Aging of Solid Catalysts with Enhanced Sensitivity". In: *Physical Chemistry Chemical Physics* 15.22 (2013), pp. 8629–8639. DOI: 10.1039/C3CP44638G (cit. on p. 3).

[25] Y. Nagai et al. "In Situ Redispersion of Platinum Autoexhaust Catalysts: An on-Line Approach to Increasing Catalyst Lifetimes?" In: *Angewandte Chemie* 120.48 (2008), pp. 9443–9446. DOI: 10.1002/ange.200803126 (cit. on pp. 4, 72).

[26] B. M. Weckhuysen. "Preface: Recent Advances in the in-Situ Characterization of Heterogeneous Catalysts". In: *Chemical Society Reviews* 39.12 (2010), p. 4557. DOI: 10.1039/c0cs90031a (cit. on p. 4).

[27] P. Scherrer. "Bestimmung der Inneren Struktur und der Größe von Kolloidteilchen Mittels Röntgenstrahlen". In: *Göttinger Nachrichten Math Phys* 2 (1918), pp. 98–100 (cit. on pp. 8, 73).

[28] J. I. Langford and A. J. C. Wilson. "Scherrer After Sixty Years: A Survey and Some New Results in the Determination of Crystallite Size". In: *Journal of Applied Crystallography* 11.2 (1978), pp. 102–113. DOI: 10.1107/S0021889878012844 (cit. on p. 8).

[29] A. Monshi, M. R. Foroughi, M. R. Monshi, and A. Monshi. "Modified Scherrer Equation to Estimate More Accurately Nano-Crystallite Size Using XRD". In: *World Journal of Nano Science and Engineering* 02.03 (2012), pp. 154–160. DOI: 10.4236/wjnse.2012.23020 (cit. on p. 8).

[30] M. Newville. *Fundamentals of XAFS*. 2004. URL: http://xafs.org/Tutorials?action=AttachFile&do=get&target=Newville_xas_fundamentals.pdf (cit. on p. 8).

[31] G. Bunker. *Introduction to XAFS: A Practical Guide to X-Ray Absorption Fine Structure Spectroscopy*. Cambridge University Press, 2010 (cit. on p. 8).

[32] J.-D. Grunwaldt, S. Hannemann, J. Göttlicher, S. Mangold, M. A. Denecke, and A. Baiker. "X-Ray Absorption Spectroscopy on Heterogeneous Catalysts at the New XAS Beamline at ANKA". In: *Physica Scripta* 2005 (2005), p. 769. DOI: 10.1238/Physica.Topical.115a00769 (cit. on p. 8).

[33] K. Klementiev. *Xafsmass - a Program for Calculation of X-Ray Absorption*. ALBA synchrotron - Experiments Division. 2012. URL: http://www.cells.es/en/beamlines/bl22-claess/software (cit. on p. 8).

[34] D. Grolimund, A. Scheidegger, J. van der Veen, and R. Abela. *Layout of the Microxas Beamline at SLS*. Scientific Report 2011 Volume VIII. Swiss Light Source, Mar. 2002, pp. 56–57 (cit. on pp. 9, 107).

[35] C. G. Schroer et al. "Hard X-Ray Nanoprobe at Beamline P06 at PETRA III". In: *Nuclear Instruments and Methods in Physics Research Section A: Accelerators, Spectrometers, Detectors and Associated Equipment* 616.2—3 (2010), pp. 93–97. DOI: 10.1016/j.nima.2009.10.094 (cit. on pp. 9, 82, 87, 113).

[36] B. Ravel and M. Newville. "ATHENA, ARTEMIS, HEPHAESTUS: Data Analysis for X-Ray Absorption Spectroscopy Using IFEFFIT". In: *Journal of Synchrotron Radiation* 12.4 (2005), pp. 537–541. DOI: 10.1107/S0909049505012719 (cit. on p. 9).

[37] K. Wille. "Synchrotron Radiation Sources". In: *Reports on Progress in Physics* 54.8 (1991), pp. 1005–1067. DOI: 10.1088/0034-4885/54/8/001 (cit. on p. 9).

[38] D. H. Bilderback, P. Elleaume, and E. Weckert. "Review of Third and Next Generation Synchrotron Light Sources". In: *Journal of Physics B: Atomic, Molecular and Optical Physics* 38.9 (2005), S773–S797. DOI: 10.1088/0953-4075/38/9/022 (cit. on p. 9).

[39] S. Brunauer, P. H. Emmett, and E. Teller. "Adsorption of Gases in Multimolecular Layers". In: *Journal of the American Chemical Society* 60.2 (1938), pp. 309–319. DOI: 10.1021/ja01269a023 (cit. on p. 11).

[40] E. P. Barrett, L. G. Joyner, and P. P. Halenda. "The Determination of Pore Volume and Area Distributions in Porous Substances. I. Computations from Nitrogen Isotherms". In: *Journal of the American Chemical Society* 73.1 (1951), pp. 373–380. DOI: 10.1021/ja01145a126 (cit. on p. 11).

[41] W. Haiss, N. T. K. Thanh, J. Aveyard, and D. G. Fernig. "Determination of Size and Concentration of Gold Nanoparticles from UV-VIS Spectra". In: *Analytical Chemistry* 79.11 (2007), pp. 4215–4221. DOI: 10.1021/ac0702084 (cit. on p. 11).

[42] M. Votsmeier, T. Kreuzer, J. Gieshoff, and G. Lepperhoff. "Automobile Exhaust Control. Ullmann's Encyclopedia of Industrial Chemistry". In: *Ullmanns Encyclopedia of Industrial Chemistry*. Wiley-VCH, 2000, pp. 407–424. DOI: 10.1002/14356007.a03_189.pub2 (cit. on p. 15).

[43] R. M. Heck, R. J. Farrauto, and S. T. Gulati. *Catalytic Air Pollution Control: Commercial Technology*. 3rd ed. Hoboken and N.J: John Wiley, 2009 (cit. on p. 15).

[44] O. Deutschmann and J.-D. Grunwaldt. "Abgasnachbehandlung in Mobilen Systemen: Stand der Technik, Herausforderungen und Perspektiven Exhaust Gas Aftertreatment in Mobile Systems: Status, Challenges, and Perspectives". In: *Chemie Ingenieur Technik* 85.5 (2013), pp. 595–617. DOI: 10.1002/cite.201200188 (cit. on pp. 15, 16).

[45] H. Gandhi, G. Graham, and R. McCabe. "Automotive Exhaust Catalysis". In: *Journal of Catalysis* 216.1-2 (2003), pp. 433–442. DOI: 10.1016/S0021-9517(02)00067-2 (cit. on p. 15).

[46] M. V. Twigg. "Progress and Future Challenges in Controlling Automotive Exhaust Gas Emissions". In: *Applied Catalysis B: Environmental* 70.1-4 (2007), pp. 2–15. DOI: 10.1016/j.apcatb.2006.02.029 (cit. on p. 15).

[47] J. Kašpar, P. Fornasiero, and N. Hickey. "Automotive Catalytic Converters: Current Status and Some Perspectives". In: *Catalysis Today* 77.4 (2003), pp. 419–449. DOI: 10.1016/S0920-5861(02)00384-X (cit. on p. 15).

[48] G. C. Koltsakis and A. M. Stamatelos. "Catalytic Automotive Exhaust Aftertreatment". In: *Progress in Energy and Combustion Science* 23.1 (1997), pp. 1–39. DOI: 10.1016/S0360-1285(97)00003-8 (cit. on p. 15).

[49] S. Matsumoto. "Recent Advances in Automobile Exhaust Catalysts". In: *Environmental Catalysis and Eco-materials* 90.3–4 (2004), pp. 183–190. DOI: 10.1016/j.cattod.2004.04.048 (cit. on p. 15).

[50] G. Liu and P.-X. Gao. "A Review of NO_x Storage/Reduction Catalysts: Mechanism, Materials and Degradation Studies". In: *Catalysis Science & Technology* 1.4 (2011), p. 552. DOI: 10.1039/c1cy00007a (cit. on p. 15).

[51] Z. Liu and S. Ihl Woo. "Recent Advances in Catalytic $DeNO_x$ Science and Technology". In: *Catalysis Reviews* 48.1 (2006), pp. 43–89. DOI: 10.1080/01614940500439891 (cit. on p. 15).

[52] M. V. Twigg. "Catalytic Control of Emissions from Cars". In: *Catalysis Today* 163.1 (2011), pp. 33–41. DOI: 10.1016/j.cattod.2010.12.044 (cit. on p. 15).

[53] A. Russell and W. S. Epling. "Diesel Oxidation Catalysts". In: *Catalysis Reviews* 53.4 (2011), pp. 337–423. DOI: 10.1080/01614940.2011.596429 (cit. on pp. 15, 16, 71, 72).

[54] B. A. A. L. van Setten, M. Makkee, and J. A. Moulijn. "Science and Technology of Catalytic Diesel Particulate Filters". In: *Catalysis Reviews* 43.4 (2001), pp. 489–564. DOI: 10.1081/CR-120001810 (cit. on p. 15).

[55] R. M. Heck and R. J. Farrauto. "Automobile Exhaust Catalysts". In: *Hoelderich Special Issue* 221.1–2 (2001), pp. 443–457. DOI: 10.1016/S0926-860X(01)00818-3 (cit. on p. 15).

[56] D. Chatterjee, O. Deutschmann, and J. Warnatz. "Detailed Surface Reaction Mechanism in a Three-Way Catalyst". In: *Faraday Discussions* 119.1 (2001), pp. 371–384. DOI: 10.1039/b101968f (cit. on p. 15).

[57] T. A. Nijhuis, A. E. W. Beers, T. Vergunst, I. Hoek, F. Kapteijn, and J. A. Moulijn. "Preparation of Monolithic Catalysts". In: *Catalysis Reviews* 43.4 (2001), pp. 345–380. DOI: 10.1081/CR-120001807 (cit. on p. 15).

[58] P. Jiang, G. Lu, Y. Guo, Y. Guo, S. Zhang, and X. Wang. "Preparation and Properties of a γ-Al_2O_3 Washcoat Deposited on a Ceramic Honeycomb". In: *Surface and Coatings Technology* 190.2–3 (2005), pp. 314–320. DOI: 10.1016/j.surfcoat.2004.05.029 (cit. on p. 15).

[59] J.-D. Grunwaldt and A. Baiker. "In Situ Spectroscopic Investigation of Heterogeneous Catalysts and Reaction Media at High Pressure". In: *Physical Chemistry Chemical Physics* 7.20 (2005), pp. 3526–3539. DOI: 10.1039/B509667G (cit. on p. 15).

[60] B. M. Weckhuysen. "Chemical Imaging of Spatial Heterogeneities in Catalytic Solids at Different Length and Time Scales". In: *Angewandte Chemie-International Edition* 48.27 (2009), pp. 4910–4943. DOI: 10.1002/anie.200900339 (cit. on pp. 15, 91).

[61] B. M. Weckhuysen. "Determining the Active Site in a Catalytic Process: Operando Spectroscopy is More Than a Buzzword". In: *Phys. Chem. Chem. Phys.* 5.20 (2003), pp. 4351–4360. DOI: 10.1039/B309650P (cit. on pp. 15, 91, 133).

[62] E. S. J. Lox. "Automotive Exhaust Treatment". In: *Handbook of Heterogeneous Catalysis*. Wiley-VCH Verlag GmbH & Co. KGaA, 2008. DOI: 10.1002/9783527610044.hetcat0120 (cit. on p. 16).

[63] C. H. Bartholomew. "Mechanisms of Catalyst Deactivation". In: *Catalyst Deactivation* 212.1-2 (2001), pp. 17–60. DOI: 10.1016/S0926-860X(00)00843-7 (cit. on pp. 16, 66).

[64] P. Forzatti and L. Lietti. "Catalyst Deactivation". In: *Catalysis Today* 52.2–3 (1999), pp. 165–181. DOI: 10.1016/S0920-5861(99)00074-7 (cit. on pp. 16, 66, 72–74).

[65] J. Andersson, M. Antonsson, L. Eurenius, E. Olsson, and M. Skoglundh. "Deactivation of Diesel Oxidation Catalysts: Vehicle- and Synthetic Aging Correlations". In: *Applied Catalysis B: Environmental* 72.1-2 (2007), pp. 71–81. DOI: 10.1016/j.apcatb.2006.10.011 (cit. on p. 16).

[66] A. Winkler, D. Ferri, and R. Hauert. "Influence of Aging Effects on the Conversion Efficiency of Automotive Exhaust Gas Catalysts". In: *Catalysis Today* 155.1-2 (2010), pp. 140–146. DOI: 10.1016/j.cattod.2008.11.021 (cit. on p. 16).

[67] J. W. Niemantsverdriet. *Spectroscopy in Catalysis: An Introduction*. 3rd completely rev. and enl. ed. Weinheim: Wiley-VCH, 2007 (cit. on p. 16).

[68] A. Winkler, D. Ferri, and M. Aguirre. "The Influence of Chemical and Thermal Aging on the Catalytic Activity of a Monolithic Diesel Oxidation Catalyst". In: *Applied Catalysis B: Environmental* 93.1-2 (2009), pp. 177–184. DOI: 10.1016/j.apcatb.2009.09.027 (cit. on p. 16).

[69] F. Behafarid and B. Roldan Cuenya. "Towards the Understanding of Sintering Phenomena at the Nanoscale: Geometric and Environmental Effects". In: *Topics in Catalysis* 56.15-17 (2013), pp. 1542–1559. DOI: 10.1007/s11244-013-0149-4 (cit. on p. 16).

[70] J.-D. Grunwaldt and C. G. Schroer. "Hard and Soft X-Ray Microscopy and Tomography in Catalysis: Bridging the Different Time and Length Scales". In: *Chemical Society Reviews* 39.12 (2010), pp. 4741–4753. DOI: 10.1039/c0cs00036a (cit. on pp. 16, 81).

[71] T. L. Burnett et al. "Correlative Tomography". In: *Scientific Reports* 4 (2014). DOI: 10.1038/srep04711 (cit. on pp. 16, 78).

[72] F. Basile et al. "Combined Use of Synchrotron-Radiation-Based Imaging Techniques for the Characterization of Structured Catalysts". In: *Advanced Functional Materials* 20.23 (2010), pp. 4117–4126. DOI: 10.1002/adfm.201001004 (cit. on p. 16).

[73] L. Espinosa-Alonso, M. G. O'Brien, S. D. M. Jacques, A. M. Beale, K. P. de Jong, P. Barnes, and B. M. Weckhuysen. "Tomographic Energy Dispersive Diffraction Imaging to Study the Genesis of Ni Nanoparticles in 3D Within γ-Al_2O_3 Catalyst Bodies". In: *Journal of the American Chemical Society* 131.46 (2009), pp. 16932–16938. DOI: 10.1021/ja907329j (cit. on p. 16).

[74] F. Tariq, R. Haswell, P. D. Lee, and D. W. McComb. "Characterization of Hierarchical Pore Structures in Ceramics Using Multiscale Tomography". In: *Acta Materialia* 59.5 (2011), pp. 2109–2120. DOI: 10.1016/j.actamat.2010.12.012 (cit. on p. 16).

[75] E. K. Gibson, M. W. Zandbergen, S. D. M. Jacques, C. Biao, R. J. Cernik, M. G. O'Brien, M. Di Michiel, B. M. Weckhuysen, and A. M. Beale. "Noninvasive Spatiotemporal Profiling of the Processes of Impregnation and Drying Within Mo/Al_2O_3 Catalyst Bodies by a Combination of X-Ray Absorption Tomography and Diagonal Offset Raman Spectroscopy". In: *ACS Catalysis* 3.3 (2013), pp. 339–347. DOI: 10.1021/cs300746a (cit. on p. 16).

[76] M. Álvarez-Murga, P. Bleuet, and J.-L. Hodeau. "Diffraction/Scattering Computed Tomography for Three-Dimensional Characterization of Multi-Phase Crystalline and Amorphous Materials". In: *Journal of Applied Crystallography* 45.6 (2012), pp. 1109–1124. DOI: 10.1107/S0021889812041039 (cit. on p. 16).

[77] S. D. M. Jacques, M. Di Michiel, A. M. Beale, T. Sochi, M. G. O'Brien, L. Espinosa-Alonso, B. M. Weckhuysen, and P. Barnes. "Dynamic X-Ray Diffraction Computed Tomography Reveals Real-Time Insight Into Catalyst Active Phase Evolution". In: *Angewandte Chemie International Edition* 50.43 (2011), pp. 10148–10152. DOI: 10.1002/anie.201104604 (cit. on p. 16).

[78] C. G. Schroer et al. "Mapping the Chemical States of an Element Inside a Sample Using Tomographic X-Ray Absorption Spectroscopy". In: *Applied Physics Letters* 82.19 (2003), pp. 3360–3362. DOI: 10.1063/1.1573352 (cit. on p. 16).

[79] O. Lame, D. Bellet, M. Di Michiel, and D. Bouvard. "Bulk Observation of Metal Powder Sintering by X-Ray Synchrotron Microtomography". In: *Acta Materialia* 52.4 (2004), pp. 977–984. DOI: 10.1016/j.actamat.2003.10.032 (cit. on p. 16).

[80] D. Bernard, D. Gendron, J.-M. Heintz, S. Bordère, and J. Etourneau. "First Direct 3D Visualisation of Microstructural Evolutions During Sintering Through X-Ray Computed Microtomography". In: *Acta Materialia* 53.1 (2005), pp. 121–128. DOI: 10.1016/j.actamat.2004.09.027 (cit. on p. 16).

[81] P. Kočí, V. Novák, F. Štěpánek, M. Marek, and M. Kubíček. "Multi-Scale Modelling of Reaction and Transport in Porous Catalysts". In: *20th International Symposium in Chemical Reaction Engineering—Green Chemical Reaction Engineering for a Sustainable Future* 65.1 (2010), pp. 412–419. DOI: 10.1016/j.ces.2009.06.068 (cit. on p. 16).

[82] P. Kočí, F. Štěpánek, M. Kubíček, and M. Marek. "Modelling of Micro/Nano-Scale Concentration and Temperature Gradients in Porous Supported Catalysts". In: *19th International Symposium on Chemical Reaction Engineering - From Science to Innovative Engineering ISCRE-19* 62.18–20 (2007), pp. 5380–5385. DOI: 10.1016/j.ces.2006.12.033 (cit. on p. 16).

[83] P. Kočí, F. Štěpánek, M. Kubíček, and M. Marek. "Meso-Scale Modelling of CO Oxidation in Digitally Reconstructed Porous Catalyst". In: *Chemical Engineering Science* 61.10 (2006), pp. 3240–3249. DOI: 10.1016/j.ces.2005.12.008 (cit. on p. 16).

[84] V. Novák, P. Kočí, T. Gregor, J.-S. Choi, F. Štěpánek, and M. Marek. "Effect of Cavities and Cracks on Diffusivity in Coated Catalyst Layer". In: *SI: ICOSCAR-4* 216 (2013), pp. 142–149. DOI: 10.1016/j.cattod.2013.07.002 (cit. on pp. 16, 74, 77).

[85] V. Novák, P. Kočí, F. Štěpánek, M. Kubíček, and M. Marek. "Simulated Preparation of Supported Porous Catalyst and Evaluation of Its Reaction-Transport Properties". In: *Selected Papers from ESCAPE-20 (European Symposium of Computer Aided Process Engineering - 20), 6-9 June 2010, Ischia, Italy* 35.5 (2011), pp. 964–972. DOI: 10.1016/j.compchemeng.2011.01.039 (cit. on p. 16).

[86] V. Novák, E. Ortel, B. Winter, B. Butz, B. Paul, P. Kočí, M. Marek, E. Spiecker, and R. Kraehnert. "Prototyping of Catalyst Pore-Systems by a Combined Synthetic, Analytical and Computational Approach: Application to Mesoporous TiO_2". In: *Chemical Engineering Journal* 248 (2014), pp. 49–62. DOI: 10.1016/j.cej.2014.02.004 (cit. on pp. 16, 79).

[87] V. Novák, F. Štěpánek, P. Kočí, M. Marek, and M. Kubíček. "Evaluation of Local Pore Sizes and Transport Properties in Porous Catalysts". In: *International Symposium on Mathematics in Chemical Kinetics and Engineering* 65.7 (2010), pp. 2352–2360. DOI: 10.1016/j.ces.2009.09.009 (cit. on p. 16).

[88] K. Yamamoto, S. Oohori, H. Yamashita, and S. Daido. "Simulation on Soot Deposition and Combustion in Diesel Particulate Filter". In: *Proceedings of the Combustion Institute* 32.2 (2009), pp. 1965–1972. DOI: 10.1016/j.proci.2008.06.081 (cit. on p. 16).

[89] K. Yamamoto and T. Sakai. "Simulation of Continuously Regenerating Trap with Catalyzed Dpf". In: *Catalysis Today* 242 (2015), pp. 357–362. DOI: 10.1016/j.cattod.2014.07.022 (cit. on p. 16).

[90] A. C. Kak and M. Slaney. *Principles of Computerized Tomographic Imaging*. IEEE Press, 1988 (cit. on p. 17).

[91] T. M. Buzug. *Computed Tomography from Photon Statistics to Modern Cone-Beam Ct*. Berlin: Springer, 2008 (cit. on pp. 17, 20, 23).

[92] G. T. Herman. *Fundamentals of Computerized Tomography: Image Reconstruction from Projections*. 2nd. Advances in Computer Vision and Pattern Recognition. London: Springer, 2010 (cit. on p. 17).

[93] E. Maire and P. J. Withers. "Quantitative X-Ray Tomography". In: *International Materials Reviews* 59.1 (2014), pp. 1–43. DOI: 10.1179/1743280413Y.0000000023 (cit. on pp. 17, 78, 79).

[94] E. N. Landis and D. T. Keane. "X-Ray Microtomography". In: *Materials Characterization* 61.12 (2010), pp. 1305–1316. DOI: 10.1016/j.matchar.2010.09.012 (cit. on p. 17).

[95] J. Als-Nielsen and D. McMorrow. *Elements of Modern X-Ray Physics*. 2. ed. Hoboken: Wiley, 2011 (cit. on p. 18).

[96] F. Marone and M. Stampanoni. "Regridding Reconstruction Algorithm for Real-Time Tomographic Imaging". In: *Journal of Synchrotron Radiation* 19.Pt 6 (2012), pp. 1029–1037. DOI: 10.1107/S0909049512032864 (cit. on p. 21).

[97] A. Boubnov, A. Gänzler, S. Conrad, M. Casapu, and J.-D. Grunwaldt. "Oscillatory CO Oxidation Over Pt/Al_2O_3 Catalysts Studied by in Situ XAS and DRIFTS". In: *Topics in Catalysis* 56.1-8 (2013), pp. 333–338. DOI: 10.1007/s11244-013-9976-6 (cit. on pp. 25, 72).

[98] VSG3D. *Avizo Fire 8.1 - 3D Analysis Software for Materials Science* (cit. on pp. 28, 48).

[99] E. L. Ritman. "Micro-Computed Tomography-Current Status and Developments". In: *Annual review of biomedical engineering* 6 (2004), pp. 185–208. DOI: 10.1146/annurev.bioeng.6.040803.140130 (cit. on p. 33).

[100] G. Hofmann, A. Rochet, S. Baier, M. Casapu, S. Ritter, F. Wilde, M. Ogurreck, F. Beckmann, and J.-D. Grunwaldt. "Ageing Effects on Exhaust Gas Catalysts: Microscopic Changes Captured by X-Ray Tomography". In: *Journal of Physics: Conference Series* 499.1 (2014), p. 012017. DOI: 10.1088/1742-6596/499/1/012017 (cit. on pp. 37, 71, 184).

[101] G. Hofmann, A. Rochet, E. Ogel, M. Casapu, S. Ritter, M. Ogurreck, and J.-D. Grunwaldt. "Aging of a Pt/Al_2O_3 Exhaust Gas Catalyst Monitored by Quasi in Situ X-Ray Micro Computed Tomography". In: *RSC Adv.* 5 (9 2015), pp. 6893–6905. DOI: 10.1039/C4RA14007A (cit. on pp. 37, 184).

[102] S. Roy, A. K. Heibel, W. Liu, and T. Boger. "Design of Monolithic Catalysts for Multiphase Reactions". In: *Chemical Engineering Science* 59.5 (2004), pp. 957–966. DOI: 10.1016/j.ces.2003.12.001 (cit. on p. 43).

[103] A. Haibel, F. Beckmann, T. Dose, J. Herzen, M. Ogurreck, M. Müller, and A. Schreyer. "Latest Developments in Microtomography and Nanotomography at PETRA III". In: *Powder Diffraction* 25.02 (2010), pp. 161–164. DOI: 10.1154/1.3428364 (cit. on p. 47).

[104] A. Haibel et al. "Micro- and Nano-Tomography at the GKSS Imaging Beamline at PETRA III". In: *Proc. SPIE* 7804 (2010), 78040B. DOI: 10.1117/12.860852 (cit. on p. 47).

[105] I. Greving et al. "P05 Imaging Beamline at PETRA III: First Results". In: *Proc. SPIE* 9212 (2014). DOI: 10.1117/12.2061768 (cit. on p. 47).

[106] J. Schindelin et al. "Fiji: An Open-Source Platform for Biological-Image Analysis". In: *Nature Methods* 9.7 (2012), pp. 676–682. DOI: 10.1038/nmeth.2019 (cit. on p. 48).

[107] Enthought. *Enthought Canopy – Scientific and Analytic Python Deployment with Integrated Analysis Environment* (cit. on p. 48).

[108] H. Leclerc, J.-N. Périé, S. Roux, and F. Hild. "Voxel-Scale Digital Volume Correlation". In: *Experimental Mechanics* 51.4 (2011), pp. 479–490. DOI: 10.1007/s11340-010-9407-6 (cit. on pp. 51, 79).

[109] Q. Hu, Ley, M. Tyler, J. Davis, J. C. Hanan, R. Frazier, and Y. Zhang. "3D Chemical Segmentation of Fly Ash Particles with X-Ray Computed Tomography and Electron Probe Microanalysis". In: *Fuel* 116 (2014), pp. 229–236. DOI: 10.1016/j.fuel.2013.07.037 (cit. on p. 57).

[110] P. C. Flynn and S. E. Wanke. "A Model of Supported Metal Catalyst Sintering: I. Development of Model". In: *Journal of Catalysis* 34.3 (1974), pp. 390–399. DOI: 10.1016/0021-9517(74)90052-9 (cit. on p. 66).

[111] Y. Nagai, T. Hirabayashi, K. Dohmae, N. Takagi, T. Minami, H. Shinjoh, and S. Matsumoto. "Sintering Inhibition Mechanism of Platinum Supported on Ceria-Based Oxide and Pt-Oxide–Support Interaction". In: *Journal of Catalysis* 242.1 (2006), pp. 103–109. DOI: 10.1016/j.jcat.2006.06.002 (cit. on p. 66).

[112] C. H. Bartholomew. "Sintering Kinetics of Supported Metals: Perspectives from a Generalized Power Law Approach". In: *Studies in Surface Science and Catalysis: Catalyst Deactivation 1994 Proceedings of the 6th International Symposium*. Ed. by B. Delmon and G.F. Froment. Vol. Volume 88. Elsevier, 1994, pp. 1–18. DOI: 10.1016/S0167-2991(08)62726-3 (cit. on pp. 66, 72–74).

[113] D. Chan, S. Tischer, J. Heck, C. Diehm, and O. Deutschmann. "Correlation Between Catalytic Activity and Catalytic Surface Area of a Pt/Al_2O_3 DOC: An Experimental and Microkinetic Modeling Study". In: *Applied Catalysis B: Environmental* 156–157 (2014), pp. 153–165. DOI: 10.1016/j.apcatb.2014.03.009 (cit. on pp. 71–74).

[114] X. Chen, Y. Cheng, C. Y. Seo, J. W. Schwank, and R. W. McCabe. "Aging, Re-Dispersion, and Catalytic Oxidation Characteristics of Model Pd/Al_2O_3 Automotive Three-Way Catalysts". In: *Applied Catalysis B: Environmental* 163 (2015), pp. 499–509. DOI: 10.1016/j.apcatb.2014.08.018 (cit. on p. 71).

[115] J. Yang, V. Tschamber, D. Habermacher, F. Garin, and P. Gilot. "Effect of Sintering on the Catalytic Activity of a Pt Based Catalyst for CO Oxidation: Experiments and Modeling". In: *Applied Catalysis B: Environmental* 83.3–4 (2008), pp. 229–239. DOI: 10.1016/j.apcatb.2008.02.018 (cit. on p. 71).

[116] S. B. Simonsen, I. Chorkendorff, S. Dahl, M. Skoglundh, J. Sehested, and S. Helveg. "Direct Observations of Oxygen-Induced Platinum Nanoparticle Ripening Studied by in Situ TEM". In: *Journal of the American Chemical Society* 132.23 (2010), pp. 7968–7975. DOI: 10.1021/ja910094r (cit. on pp. 71, 72).

[117] S. B. Simonsen, I. Chorkendorff, S. Dahl, M. Skoglundh, K. Meinander, T. N. Jensen, J. V. Lauritsen, and S. Helveg. "Effect of Particle Morphology on the Ripening of Supported Pt Nanoparticles". In: *The Journal of Physical Chemistry C* 116.9 (2012), pp. 5646–5653. DOI: 10.1021/jp2098262 (cit. on p. 72).

[118] A. T. DeLaRiva, T. W. Hansen, S. R. Challa, and A. K. Datye. "In Situ Transmission Electron Microscopy of Catalyst Sintering". In: *Journal of Catalysis* 308 (2013), pp. 291–305. DOI: 10.1016/j.jcat.2013.08.018 (cit. on p. 72).

[119] J. Barbier, D. Bahloul, and P. Marecot. "Effect of Chloride on Sintering of Pt/Al_2O_3 Catalysts". In: *Catalysis Letters* 8.5-6 (1991), pp. 327–333. DOI: 10.1007/BF00764194 (cit. on p. 72).

[120] H. Lieske, G. Lietz, H. Spindler, and J. Völter. "Reactions of Platinum in Oxygen- and Hydrogen-Treated $Pt/\gamma\text{-}Al_2O_3$ Catalysts: I. Temperature-Programmed Reduction, Adsorption, and Redispersion of Platinum". In: *Journal of Catalysis* 81.1 (1983), pp. 8–16. DOI: 10.1016/0021-9517(83)90142-2 (cit. on p. 72).

[121] F. Le Normand, A. Borgna, T. F. Garetto, C. R. Apesteguia, and B. Moraweck. "Redispersion of Sintered Pt/Al_2O_3 Naphtha Reforming Catalysts: An in Situ Study Monitored by X-Ray Absorption Spectroscopy". In: *The Journal of Physical Chemistry* 100.21 (1996), pp. 9068–9076. DOI: 10.1021/jp960080m (cit. on p. 72).

[122] T. J. Lee and Y. G. Kim. "Redispersion of Supported Platinum Catalysts". In: *Journal of Catalysis* 90.2 (1984), pp. 279–291. DOI: 10.1016/0021-9517(84)90256-2 (cit. on p. 72).

[123] E. I. Altman and R. J. Gorte. "A Comparison of the Desorption of CO from Pt and Rh Particles on $\alpha\text{-}Al_2O_3(0001)$". In: *Surface Science* 195.3 (1988), pp. 392–402. DOI: 10.1016/0039-6028(88)90349-4 (cit. on p. 72).

[124] K. Arnby, A. Törncrona, B. Andersson, and M. Skoglundh. "Investigation of $Pt/\gamma\text{-}Al_2O_3$ Catalysts with Locally High Pt Concentrations for Oxidation of CO at Low Temperatures". In: *Journal of Catalysis* 221.1 (2004), pp. 252–261. DOI: 10.1016/j.jcat.2003.08.017 (cit. on pp. 72, 77).

[125] A. Papavasiliou, A. Tsetsekou, V. Matsouka, M. Konsolakis, I. V. Yentekakis, and N. Boukos. "Synergistic Structural and Surface Promotion of Monometallic (Pt) TWCs: Effectiveness and Thermal Aging Tolerance". In: *Applied Catalysis B: Environmental* 106.1-2 (2011), pp. 228–241. DOI: 10.1016/j.apcatb.2011.05.030 (cit. on p. 72).

[126] A. Papavasiliou, A. Tsetsekou, V. Matsouka, M. Konsolakis, and I. V. Yentekakis. "An Investigation of the Role of Zr and La Dopants Into $Ce_{(1-X-Y)}Zr_{(x)}La_{(y)}O_{(d)}$ Enriched γ-Al_2O_3 TWC Washcoats". In: *Applied Catalysis A: General* 382.1 (2010), pp. 73–84. DOI: 10.1016/j.apcata.2010.04.025 (cit. on p. 72).

[127] A. Papavasiliou, A. Tsetsekou, V. Matsouka, M. Konsolakis, I. V. Yentekakis, and N. Boukos. "Development of a Ce-Zr-La Modified Pt/γ-Al_2O_3 TWCs Washcoat: Effect of Synthesis Procedure on Catalytic Behaviour and Thermal Durability". In: *Applied Catalysis B: Environmental* 90.1-2 (2009), pp. 162–174. DOI: 10.1016/j.apcatb.2009.03.006 (cit. on p. 72).

[128] G. W. Graham, H.-W. Jen, W. Chun, H. P. Sun, X. Q. Pan, and R. W. McCabe. "Coarsening of Pt Particles in a Model NO_x Trap". In: *Catalysis Letters* 93.3/4 (2004), pp. 129–134. DOI: 10.1023/B:CATL.0000017065.47758.34 (cit. on p. 73).

[129] Y. Liu, D. Ma, X. Han, X. Bao, W. Frandsen, Di Wang, and D. Su. "Hydrothermal Synthesis of Microscale Boehmite and Gamma Nanoleaves Alumina". In: *Materials Letters* 62.8–9 (2008), pp. 1297–1301. DOI: 10.1016/j.matlet.2007.08.067 (cit. on p. 73).

[130] Y. Saito, T. Takei, S. Hayashi, A. Yasumori, and K. Okada. "Effects of Amorphous and Crystalline SiO_2 Additives on γ-Al_2O_3-to-α-Al_2O_3 Phase Transitions". In: *Journal of the American Ceramic Society* 81.8 (1998), pp. 2197–2200. DOI: 10.1111/j.1151-2916.1998.tb02608.x (cit. on p. 74).

[131] S. Huotari, T. Pylkkanen, R. Verbeni, G. Monaco, and K. Hamalainen. "Direct Tomography with Chemical-Bond Contrast". In: *Nature Materials* 10.7 (2011), pp. 489–493. DOI: 10.1038/nmat3031 (cit. on p. 78).

[132] P. J. Withers. "X-Ray Nanotomography". In: *Materials Today* 10.12 (2007), pp. 26–34. DOI: 10.1016/S1369-7021(07)70305-X (cit. on p. 78).

[133] A. Kyrieleis, V. Titarenko, M. Ibison, T. Connolley, and P. J. Withers. "Region-of-Interest Tomography Using Filtered Backprojection: Assessing the Practical Limits". In: *Journal of Microscopy* 241.1 (2011), pp. 69–82. DOI: 10.1111/j.1365-2818.2010.03408.x (cit. on p. 79).

[134] R. A. Ketcham. "Computational Methods for Quantitative Analysis of Three-Dimensional Features in Geological Specimens". In: *Geosphere* 1.1 (2005), p. 32. DOI: 10.1130/GES00001.1 (cit. on p. 79).

[135] R. Falcone, C. Jacobsen, J. Kirz, S. Marchesini, D. Shapiro, and J. Spence. "New Directions in X-Ray Microscopy". In: *Contemporary Physics* 52.4 (2011), pp. 293–318 (cit. on p. 81).

[136] J. C. Andrews and B. M. Weckhuysen. "Hard X-Ray Spectroscopic Nano-Imaging of Hierarchical Functional Materials at Work". In: *ChemPhysChem* 14.16 (2013), pp. 3655–3666. DOI: 10.1002/cphc.201300529 (cit. on p. 81).

[137] J.-D. Grunwaldt, J. B. Wagner, and R. E. Dunin-Borkowski. "Imaging Catalysts at Work: A Hierarchical Approach from the Macro- to the Meso- and Nano-Scale". In: *ChemCatChem* 5.1 (2013), pp. 62–80. DOI: 10.1002/cctc.201200356 (cit. on pp. 81, 91, 133).

[138] A. T. Bell. "The Impact of Nanoscience on Heterogeneous Catalysis". In: *Science* 299.5613 (2003), pp. 1688–1691. DOI: 10.1126/science.1083671 (cit. on p. 81).

[139] E. de Smit et al. "Nanoscale Chemical Imaging of a Working Catalyst by Scanning Transmission X-Ray Microscopy". In: *Nature* 456.7219 (2008), pp. 222–225. DOI: 10.1038/nature07516 (cit. on p. 81).

[140] I. D. Gonzalez-Jimenez et al. "Hard X-Ray Nanotomography of Catalytic Solids at Work". In: *Angewandte Chemie International Edition* 51.48 (2012), pp. 11986–11990. DOI: 10.1002/anie.201204930 (cit. on p. 81).

[141] F. Meirer, J. Cabana, Y. Liu, A. Mehta, J. C. Andrews, and P. Pianetta. "Three-Dimensional Imaging of Chemical Phase Transformations at the Nanoscale with Full-Field Transmission X-Ray Microscopy". In: *Journal of Synchrotron Radiation* 18.5 (2011), pp. 773–781. DOI: 10.1107/S0909049511019364 (cit. on p. 81).

[142] K. H. Cats et al. "X-Ray Nanoscopy of Cobalt Fischer-Tropsch Catalysts at Work". In: *Chemical Communications* 49.41 (2013), pp. 4622–4624. DOI: 10.1039/C3CC00160A (cit. on p. 81).

[143] Y.-C. K. Chen-Wiegart, W. M. Harris, J. J. Lombardo, W. K. S. Chiu, and J. Wang. "Oxidation States Study of Nickel in Solid Oxide Fuel Cell Anode Using X-Ray Full-Field Spectroscopic Nano-Tomography". In: *Applied Physics Letters* 101.25 (2012), pp. 253901–253904. DOI: 10.1063/1.4772784 (cit. on p. 81).

[144] Y. Liu, F. Meirer, P. A. Williams, J. Wang, J. C. Andrews, and P. Pianetta. "TXM-Wizard: A Program for Advanced Data Collection and Evaluation in Full-Field Transmission X-Ray Microscopy". In: *Journal of Synchrotron Radiation* 19.Pt 2 (2012), pp. 281–287. DOI: 10.1107/S0909049511049144 (cit. on p. 81).

[145] K. Jefimovs, J. Vila-Comamala, T. Pilvi, J. Raabe, M. Ritala, and C. David. "Zone-Doubling Technique to Produce Ultrahigh-Resolution X-Ray Optics". In: *Physical Review Letters* 99.26 (2007). DOI: 10.1103/PhysRevLett.99.264801 (cit. on p. 81).

[146] W. Chao, B. D. Harteneck, J. A. Liddle, E. H. Anderson, and D. T. Attwood. "Soft X-Ray Microscopy at a Spatial Resolution Better Than 15 nm". In: *Nature* 435.7046 (2005), pp. 1210–1213. DOI: 10.1038/nature03719 (cit. on p. 81).

[147] M. Dierolf et al. "Ptychography & Lensless X-Ray Imaging". In: *Europhysics News* 39.1 (2008), pp. 22–24. DOI: 10.1051/epn:2008003 (cit. on p. 81).

[148] H. N. Chapman and K. A. Nugent. "Coherent Lensless X-Ray Imaging". In: *Nature Photonics* 4.12 (2010), pp. 833–839. DOI: 10.1038/nphoton.2010.240 (cit. on p. 81).

[149] J. Miao, R. L. Sandberg, and C. Song. "Coherent X-Ray Diffraction Imaging". In: *IEEE Journal of Selected Topics in Quantum Electronics* 18.1 (2012), pp. 399–410. DOI: 10.1109/JSTQE.2011.2157306 (cit. on p. 81).

[150] C. G. Schroer et al. "Coherent X-Ray Diffraction Imaging with Nanofocused Illumination". In: *Physical Review Letters* 101.9 (2008), p. 090801. DOI: 10.1103/Physrevlett.101.090801 (cit. on p. 81).

[151] J. M. Rodenburg, A. C. Hurst, A. G. Cullis, B. R. Dobson, F. Pfeiffer, O. Bunk, C. David, K. Jefimovs, and I. Johnson. "Hard-X-Ray Lensless Imaging of Extended Objects". In: *Physical Review Letters* 98.3 (2007), p. 034801. DOI: 10.1103/PhysRevLett.98.034801 (cit. on p. 81).

[152] P. Thibault, M. Dierolf, A. Menzel, O. Bunk, C. David, and F. Pfeiffer. "High-Resolution Scanning X-Ray Diffraction Microscopy". In: *Science* 321.5887 (2008), pp. 379–382. DOI: 10.1126/science.1158573 (cit. on p. 81).

[153] K. A. Nugent. "Coherent Methods in the X-Ray Sciences". In: *Advances in Physics* 59.1 (2010), pp. 1–99. DOI: 10.1080/00018730903270926 (cit. on p. 81).

[154] A. Schropp, R. Hoppe, J. Patommel, D. Samberg, F. Seiboth, S. Stephan, G. Wellenreuther, G. Falkenberg, and C. G. Schroer. "Hard X-Ray Scanning Microscopy with Coherent Radiation: Beyond the Resolution of Conventional X-Ray Microscopes". In: *Applied Physics Letters* 100.25 (2012), p. 253112. DOI: 10.1063/1.4729942 (cit. on p. 81).

[155] M.-C. Daniel and D. Astruc. "Gold Nanoparticles: Assembly, Supramolecular Chemistry, Quantum-Size-Related Properties, and Applications Toward Biology, Catalysis, and Nanotechnology". In: *Chem. Rev.* 104.1 (2004), pp. 293–346. DOI: 10.1021/cr030698+ (cit. on pp. 81, 95, 96).

[156] M. De, P. S. Ghosh, and V. M. Rotello. "Applications of Nanoparticles in Biology". In: *Advanced Materials* 20.22 (2008), pp. 4225–4241. DOI: 10.1002/adma.200703183 (cit. on p. 81).

[157] M. Dierolf, P. Thibault, A. Menzel, C. M. Kewish, K. Jefimovs, I. Schlichting, K. v. König, O. Bunk, and F. Pfeiffer. "Ptychographic Coherent Diffractive Imaging of Weakly Scattering Specimens". In: *New Journal of Physics* 12.3 (2010), p. 035017. DOI: 10.1088/1367-2630/12/3/035017 (cit. on p. 81).

[158] M. Beckers, T. Senkbeil, T. Gorniak, M. Reese, K. Giewekemeyer, S.-C. Gleber, T. Salditt, and A. Rosenhahn. "Chemical Contrast in Soft X-Ray Ptychography". In: *Physical Review Letters* 107.20 (2011), p. 208101. DOI: 10.1103/PhysRevLett.107.208101 (cit. on p. 81).

[159] A. Schropp et al. "Non-Destructive and Quantitative Imaging of a Nano-Structured Microchip by Ptychographic Hard X-Ray Scanning Microscopy". In: *Journal of Microscopy* 241.1 (2011), pp. 9–12. DOI: 10.1111/j.1365-2818.2010.03453.x (cit. on p. 81).

[160] Y. Takahashi, A. Suzuki, N. Zettsu, Y. Kohmura, K. Yamauchi, and T. Ishikawa. "Multiscale Element Mapping of Buried Structures by Ptychographic X-Ray Diffraction Microscopy Using Anomalous Scattering". In: *Applied Physics Letters* 99.13 (2011), pp. 131905–3. DOI: 10.1063/1.3644396 (cit. on p. 81).

[161] W. Hoppe. "Beugung im Inhomogenen Primärstrahlwellenfeld. III. Amplituden- und Phasenbestimmung bei Unperiodischen Objekten". In: *Acta Crystallographica Section A* 25.4 (1969), pp. 508–514. DOI: 10.1107/S0567739469001069 (cit. on p. 82).

[162] O. Bunk, M. Dierolf, S. Kynde, I. Johnson, O. Marti, and F. Pfeiffer. "Influence of the Overlap Parameter on the Convergence of the Ptychographical Iterative Engine". In: *Ultramicroscopy* 108.5 (2008), pp. 481–487. DOI: 10.1016/j.ultramic.2007.08.003 (cit. on p. 82).

[163] A. M. Maiden and J. M. Rodenburg. "An Improved Ptychographical Phase Retrieval Algorithm for Diffractive Imaging". In: *Ultramicroscopy* 109.10 (2009), pp. 1256–1262. DOI: 10.1016/j.ultramic.2009.05.012 (cit. on p. 82).

[164] J. M. Rodenburg. "Advances in Imaging and Electron Physics". In: *Advances in Imaging and Electron Physics*. Ed. by Hawkes. Vol. 150. Elsevier, 2008. Chap. Ptychography and Related Diffractive Imaging Methods, pp. 87–184. DOI: 10.1016/s1076-5670(07)00003-1 (cit. on p. 82).

[165] D. Vaughan. *X-Ray Data Booklet*. Center for X-ray Optics and Advanced Light Source – Lawrence Berkeley National Laboratory. Oct. 2009. URL: http://xdb.lbl.gov/xdb-new.pdf (cit. on p. 86).

[166] R. Hoppe, J. Reinhardt, G. Hofmann, J. Patommel, J.-D. Grunwaldt, C. D. Damsgaard, G. Wellenreuther, G. Falkenberg, and C. G. Schroer. "High-Resolution Chemical Imaging of Gold Nanoparticles Using Hard X-Ray Ptychography". In: *Applied Physics Letters* 102.20 (2013), p. 203104. DOI: 10.1063/1.4807020 (cit. on pp. 88, 89, 184).

[167] M. Dierolf, A. Menzel, P. Thibault, P. Schneider, C. M. Kewish, R. Wepf, O. Bunk, and F. Pfeiffer. "Ptychographic X-Ray Computed Tomography at the Nanoscale". In: *Nature* 467.7314 (2010), pp. 436–439. DOI: 10.1038/nature09419 (cit. on p. 91).

[168] R. N. Wilke, M. Priebe, M. Bartels, K. Giewekemeyer, A. Diaz, P. Karvinen, and T. Salditt. "Hard X-Ray Imaging of Bacterial Cells: Nano-Diffraction and Ptychographic Reconstruction". In: *Optics Express* 20.17 (2012), pp. 19232–19254. DOI: 10.1364/OE.20.019232 (cit. on p. 91).

[169] M. Esmaeili, J. B. Fløystad, A. Diaz, K. Høydalsvik, M. Guizar-Sicairos, J. W. Andreasen, and D. W. Breiby. "Ptychographic X-Ray Tomography of Silk Fiber Hydration". In: *Macromolecules* 46.2 (2013), pp. 434–439. DOI: 10.1021/ma3021163 (cit. on p. 91).

[170] P. Trtik, A. Diaz, M. Guizar-Sicairos, A. Menzel, and O. Bunk. "Density Mapping of Hardened Cement Paste Using Ptychographic X-Ray Computed Tomography". In: *Cement and Concrete Composites* 36 (2013), pp. 71–77. DOI: 10.1016/j.cemconcomp.2012.06.001 (cit. on p. 91).

[171] M. Holler et al. "X-Ray Ptychographic Computed Tomography at 16 nm Isotropic 3D Resolution". In: *Scientific reports* 4 (2014), p. 3857. DOI: 10.1038/srep03857 (cit. on p. 91).

[172] H. F. Dam et al. "X-Ray Nanovision: Enabling Flexible Polymer Tandem Solar Cells by 3D Ptychographic Imaging". In: *Advanced Energy Materials* 5.1 (2015). DOI: 10.1002/aenm.201570004 (cit. on p. 91).

[173] T. K. Sau and A. L. Rogach. *Complex-Shaped Metal Nanoparticles*. Weinheim, Germany: Wiley-VCH Verlag GmbH & Co. KGaA, 2012. DOI: 10.1002/9783527652570 (cit. on p. 95).

[174] M. Brust, M. Walker, D. Bethell, D. J. Schiffrin, and R. Whyman. "Synthesis of Thiol-Derivatised Gold Nanoparticles in a Two-Phase Liquid-Liquid System". In: *Journal of the Chemical Society, Chemical Communications* 7 (1994), p. 801. DOI: 10.1039/c39940000801 (cit. on p. 95).

[175] N. R. Jana and X. Peng. "Single-Phase and Gram-Scale Routes Toward Nearly Monodisperse Au and Other Noble Metal Nanocrystals". In: *Journal of the American Chemical Society* 125.47 (2003), pp. 14280–14281. DOI: 10.1021/ja038219b (cit. on p. 95).

[176] C. M. Niemeyer. "Nanoparticles, Proteins, and Nucleic Acids: Biotechnology Meets Materials Science". In: *Angewandte Chemie International Edition* 40.22 (2001), pp. 4128–4158. DOI: 10.1002/1521-3773(20011119)40:22<4128::AID-ANIE4128>3.0.CO;2-S (cit. on p. 95).

[177] Y. Kim, J. Zhu, B. Yeom, M. Di Prima, X. Su, J.-G. Kim, S. J. Yoo, C. Uher, and N. A. Kotov. "Stretchable Nanoparticle Conductors with Self-Organized Conductive Pathways". In: *Nature* 500.7460 (2013), pp. 59–63. DOI: 10.1038/nature12401 (cit. on p. 95).

[178] E. Boisselier and D. Astruc. "Gold Nanoparticles in Nanomedicine: Preparations, Imaging, Diagnostics, Therapies and Toxicity". In: *Chemical Society Reviews* 38.6 (2009), pp. 1759–1782. DOI: 10.1039/b806051g (cit. on p. 95).

[179] K. Saha, S. S. Agasti, C. Kim, X. Li, and V. M. Rotello. "Gold Nanoparticles in Chemical and Biological Sensing". In: *Chemical Reviews* 112.5 (2012), pp. 2739–2779. DOI: 10.1021/cr2001178 (cit. on p. 95).

[180] X. Qian et al. "In Vivo Tumor Targeting and Spectroscopic Detection with Surface-Enhanced Raman Nanoparticle Tags". In: *Nature biotechnology* 26.1 (2008), pp. 83–90. DOI: 10.1038/nbt1377 (cit. on p. 95).

[181] A. Y. Sajjadi, A. Suratkar, K. Mitra, and M. S. Grace. "Short-Pulse Laser-Based System for Detection of Tumors: Administration of Gold Nanoparticles Enhances Contrast". In: *Journal of Nanotechnology in Engineering and Medicine* 3.2 (2012), p. 21002. DOI: 10.1115/1.4007245 (cit. on p. 95).

[182] G. Han, P. Ghosh, and V. M. Rotello. "Functionalized Gold Nanoparticles for Drug Delivery". In: *Nanomedicine (London, England)* 2.1 (2007), pp. 113–123. DOI: 10.2217/17435889.2.1.113 (cit. on p. 95).

[183] T. Stuchinskaya, M. Moreno, M. J. Cook, D. R. Edwards, and D. A. Russell. "Targeted Photodynamic Therapy of Breast Cancer Cells Using Antibody-Phthalocyanine-Gold Nanoparticle Conjugates". In: *Photochemical & photobiological sciences : Official journal of the European Photochemistry Association and the European Society for Photobiology* 10.5 (2011), pp. 822–831. DOI: 10.1039/c1pp05014a (cit. on p. 95).

[184] J. F. Hainfeld, D. N. Slatkin, and H. M. Smilowitz. "The Use of Gold Nanoparticles to Enhance Radiotherapy in Mice". In: *Physics in Medicine and Biology* 49.18 (2004), N309–N315. DOI: 10.1088/0031-9155/49/18/N03 (cit. on p. 95).

[185] M. Hübner, D. Koziej, J.-D. Grunwaldt, U. Weimar, and N. Barsan. "An Au Clusters Related Spill-Over Sensitization Mechanism in SnO_2-Based Gas Sensors Identified by Operando HERFD-XAS, Work Function Changes, Dc Resistance and Catalytic Conversion Studies". In: *Physical chemistry chemical physics : PCCP* 14.38 (2012), pp. 13249–13254. DOI: 10.1039/C2CP41349C (cit. on p. 95).

[186] S. D. Perrault and W. C. W. Chan. "In Vivo Assembly of Nanoparticle Components to Improve Targeted Cancer Imaging". In: *Proceedings of the National Academy of Sciences of the United States of America* 107.25 (2010), pp. 11194–11199. DOI: 10.1073/pnas.1001367107 (cit. on p. 95).

[187] J. Panyam, S. K. Sahoo, S. Prabha, T. Bargar, and V. Labhasetwar. "Fluorescence and Electron Microscopy Probes for Cellular and Tissue Uptake of Poly(d,l-Lactide-CO-Glycolide) Nanoparticles". In: *International Journal of Pharmaceutics* 262.1-2 (2003), pp. 1–11. DOI: 10.1016/S0378-5173(03)00295-3 (cit. on p. 95).

[188] D. Xi, S. Dong, X. Meng, Q. Lu, L. Meng, and J. Ye. "Gold Nanoparticles as Computerized Tomography (CT) Contrast Agents". In: *RSC Advances* 2.33 (2012), p. 12515. DOI: 10.1039/c2ra21263c (cit. on p. 95).

[189] D. Astruc, F. Lu, and J. R. Aranzaes. "Nanoparticles as Recyclable Catalysts: The Frontier Between Homogeneous and Heterogeneous Catalysis". In: *Angewandte Chemie International Edition* 44.48 (2005), pp. 7852–7872. DOI: 10.1002/anie.200500766 (cit. on p. 95).

[190] R. Coquet, K. L. Howard, and D. J. Willock. "Theory and Simulation in Heterogeneous Gold Catalysis". In: *Chemical Society Reviews* 37.9 (2008), p. 2046. DOI: 10.1039/b707385m (cit. on p. 95).

[191] B. Hvolbæk, T. V. Janssens, B. S. Clausen, H. Falsig, C. H. Christensen, and J. K. Nørskov. "Catalytic Activity of Au Nanoparticles". In: *Nano Today* 2.4 (2007), pp. 14–18. DOI: 10.1016/S1748-0132(07)70113-5 (cit. on p. 95).

[192] N. Lopez. "On the Origin of the Catalytic Activity of Gold Nanoparticles for Low-Temperature CO Oxidation". In: *Journal of Catalysis* 223.1 (2004), pp. 232–235. DOI: 10.1016/j.jcat.2004.01.001 (cit. on p. 95).

[193] M. Haruta, N. Yamada, T. Kobayashi, and S. Iijima. "Gold Catalysts Prepared by Coprecipitation for Low-Temperature Oxidation of Hydrogen and of Carbon Monoxide". In: *Journal of Catalysis* 115.2 (1989), pp. 301–309. DOI: 10.1016/0021-9517(89)90034-1 (cit. on p. 95).

[194] G. C. Bond and D. T. Thompson. "Catalysis by Gold". In: *Catalysis Reviews* 41.3-4 (1999), pp. 319–388. DOI: 10.1081/CR-100101171 (cit. on p. 95).

[195] M. Dekkers, M. Lippits, and B. Nieuwenhuys. "Supported Gold/MO_x Catalysts for NO/H_2 and CO/O_2 Reactions". In: *Catalysis Today* 54.4 (1999), pp. 381–390. DOI: 10.1016/S0920-5861(99)00201-1 (cit. on p. 95).

[196] M. Haruta and M. Daté. "Advances in the Catalysis of Au Nanoparticles". In: *Applied Catalysis A: General* 222.1-2 (2001), pp. 427–437. DOI: 10.1016/S0926-860X(01)00847-X (cit. on p. 95).

[197] A. S. K. Hashmi and G. J. Hutchings. "Gold Catalysis". In: *Angewandte Chemie International Edition* 45.47 (2006), pp. 7896–7936. DOI: 10.1002/anie.200602454 (cit. on p. 95).

[198] D. T. Thompson. "Using Gold Nanoparticles for Catalysis". In: *Nano Today* 2.4 (2007), pp. 40–43. DOI: 10.1016/S1748-0132(07)70116-0 (cit. on p. 95).

[199] P. Haider, B. Kimmerle, F. Krumeich, W. Kleist, J.-D. Grunwaldt, and A. Baiker. "Gold-Catalyzed Aerobic Oxidation of Benzyl Alcohol: Effect of Gold Particle Size on Activity and Selectivity in Different Solvents". In: *Catalysis Letters* 125.3-4 (2008), pp. 169–176. DOI: 10.1007/s10562-008-9567-5 (cit. on pp. 95, 96).

[200] R. Zanella. "Characterization and Reactivity in CO Oxidation of Gold Nanoparticles Supported on TiO_2 Prepared by Deposition-Precipitation with Naoh and Urea". In: *Journal of Catalysis* 222.2 (2004), pp. 357–367. DOI: 10.1016/j.jcat.2003.11.005 (cit. on p. 95).

[201] P. Zhao, N. Li, and D. Astruc. "State of the Art in Gold Nanoparticle Synthesis". In: *Coordination Chemistry Reviews* 257.3-4 (2013), pp. 638–665. DOI: 10.1016/j.ccr.2012.09.002 (cit. on p. 95).

[202] C. J. Murphy, T. K. Sau, A. M. Gole, C. J. Orendorff, J. Gao, L. Gou, S. E. Hunyadi, and T. Li. "Anisotropic Metal Nanoparticles: Synthesis, Assembly, and Optical Applications". In: *The journal of physical chemistry. B* 109.29 (2005), pp. 13857–13870. DOI: 10.1021/jp0516846 (cit. on p. 96).

[203] T. K. Sau and A. L. Rogach. "Nonspherical Noble Metal Nanoparticles: Colloid-Chemical Synthesis and Morphology Control". In: *Advanced materials (Deerfield Beach, Fla.)* 22.16 (2010), pp. 1781–1804. DOI: 10.1002/adma.200901271 (cit. on p. 96).

[204] T. K. Sau and C. J. Murphy. "Room Temperature, High-Yield Synthesis of Multiple Shapes of Gold Nanoparticles in Aqueous Solution". In: *Journal of the American Chemical Society* 126.28 (2004), pp. 8648–8649. DOI: 10.1021/ja047846d (cit. on p. 96).

[205] G. Frens. "Controlled Nucleation for the Regulation of the Particle Size in Monodisperse Gold Suspensions". In: *Nature Physical Science* 241.105 (1973), pp. 20–22. DOI: 10.1038/physci241020a0 (cit. on p. 96).

[206] J. Kimling, M. Maier, B. Okenve, V. Kotaidis, H. Ballot, and A. Plech. "Turkevich Method for Gold Nanoparticle Synthesis Revisited". In: *The Journal of Physical Chemistry B* 110.32 (2006), pp. 15700–15707. DOI: 10.1021/jp061667w (cit. on p. 96).

[207] J. Turkevich, P. C. Stevenson, and J. Hillier. "A Study of the Nucleation and Growth Processes in the Synthesis of Colloidal Gold". In: *Discussions of the Faraday Society* 11 (1951), p. 55. DOI: 10.1039/df9511100055 (cit. on p. 96).

[208] M. Brust, J. Fink, D. Bethell, D. J. Schiffrin, and C. Kiely. "Synthesis and Reactions of Functionalised Gold Nanoparticles". In: *Journal of the Chemical Society, Chemical Communications* 16 (1995), p. 1655. DOI: 10.1039/c39950001655 (cit. on p. 96).

[209] M. N. Martin, J. I. Basham, P. Chando, and S.-K. Eah. "Charged Gold Nanoparticles in Non-Polar Solvents: 10-Min Synthesis and 2D Self-Assembly". In: *Langmuir : the ACS journal of surfaces and colloids* 26.10 (2010), pp. 7410–7417. DOI: 10.1021/la100591h (cit. on p. 96).

[210] D. G. Duff, A. Baiker, and P. P. Edwards. "A New Hydrosol of Gold Clusters. 1. Formation and Particle Size Variation". In: *Langmuir* 9.9 (1993), pp. 2301–2309. DOI: 10.1021/la00033a010 (cit. on pp. 96, 98, 130).

[211] J.-D. Grunwaldt, C. Kiener, C. Wögerbauer, and A. Baiker. "Preparation of Supported Gold Catalysts for Low-Temperature CO Oxidation Via "Size-Controlled" Gold Colloids". In: *Journal of Catalysis* 181.2 (1999), pp. 223–232. DOI: 10.1006/jcat.1998.2298 (cit. on pp. 96, 98).

[212] J. L. Hueso, V. Sebastián, Á. Mayoral, L. Usón, M. Arruebo, and J. Santamaría. "Beyond Gold: Rediscovering Tetrakis-(hydroxymethyl)-Phosphonium Chloride (THPC) as an Effective Agent for the Synthesis of Ultra-Small Noble Metal Nanoparticles and Pt-Containing Nanoalloys". In: *RSC Advances* 3.26 (2013), p. 10427. DOI: 10.1039/c3ra40774h (cit. on pp. 96, 132).

[213] N. Pienack and W. Bensch. "In-Situ-Verfolgung der Bildung Kristalliner Feststoffe". In: *Angewandte Chemie* 123.9 (2011), pp. 2062–2083. DOI: 10.1002/ange.201001180 (cit. on p. 96).

[214] F. Wang, V. N. Richards, S. P. Shields, and W. E. Buhro. "Kinetics and Mechanisms of Aggregative Nanocrystal Growth". In: *Chemistry of Materials* 26.1 (2014), pp. 5–21. DOI: 10.1021/cm402139r (cit. on p. 96).

[215] N. T. K. Thanh, N. Maclean, and S. Mahiddine. "Mechanisms of Nucleation and Growth of Nanoparticles in Solution". In: *Chemical Reviews* 114.15 (2014), pp. 7610–7630. DOI: 10.1021/cr400544s (cit. on p. 96).

[216] E. E. Finney and R. G. Finke. "Nanocluster Nucleation and Growth Kinetic and Mechanistic Studies: A Review Emphasizing Transition-Metal Nanoclusters". In: *Journal of Colloid and Interface Science* 317.2 (2008), pp. 351–374. DOI: 10.1016/j.jcis.2007.05.092 (cit. on p. 96).

[217] J. E. Mondloch, E. Bayram, and R. G. Finke. "A Review of the Kinetics and Mechanisms of Formation of Supported-Nanoparticle Heterogeneous Catalysts". In: *Journal of Molecular Catalysis A: Chemical* 355 (2012), pp. 1–38. DOI: 10.1016/j.molcata.2011.11.011 (cit. on p. 96).

[218] Y. Sun. "Watching Nanoparticle Kinetics in Liquid". In: *Materials Today* 15.4 (2012), pp. 140–147. DOI: 10.1016/S1369-7021(12)70067-6 (cit. on p. 96).

[219] Y. Sun and Y. Ren. "In Situ Synchrotron X-Ray Techniques for Real-Time Probing of Colloidal Nanoparticle Synthesis". In: *Particle & Particle Systems Characterization* 30.5 (2013), pp. 399–419. DOI: 10.1002/ppsc.201300033 (cit. on p. 96).

[220] J. Becker, O. Schubert, and C. Sönnichsen. "Gold Nanoparticle Growth Monitored in Situ Using a Novel Fast Optical Single-Particle Spectroscopy Method". In: *Nano Letters* 7.6 (2007), pp. 1664–1669. DOI: 10.1021/nl070627g (cit. on p. 96).

[221] H.-G. Liao, K. Niu, and H. Zheng. "Observation of Growth of Metal Nanoparticles". In: *Chemical Communications* 49.100 (2013), pp. 11720–11727. DOI: 10.1039/C3CC47473A (cit. on p. 96).

[222] D. S. Sebba, D. A. Watson, and J. P. Nolan. "High Throughput Single Nanoparticle Spectroscopy". In: *ACS Nano* 3.6 (2009), pp. 1477–1484. DOI: 10.1021/nn9003346 (cit. on p. 96).

[223] V. S. Cabeza, S. Kuhn, A. A. Kulkarni, and K. F. Jensen. "Size-Controlled Flow Synthesis of Gold Nanoparticles Using a Segmented Flow Microfluidic Platform". In: *Langmuir : the ACS journal of surfaces and colloids* 28.17 (2012), pp. 7007–7013. DOI: 10.1021/la205131e (cit. on pp. 96, 132).

[224] A. M. Nightingale and J. C. Demello. "Segmented Flow Reactors for Nanocrystal Synthesis". In: *Adv Mater* 25.13 (2013), pp. 1813–1821. DOI: 10.1002/adma.201203252 (cit. on pp. 96, 132).

[225] N. Lorber et al. "Some Recent Advances in the Design and the Use of Miniaturized Droplet-Based Continuous Process: Applications in Chemistry and High-Pressure Microflows". In: *Lab Chip* 11.5 (2011), pp. 779–787. DOI: 10.1039/c0lc00058b (cit. on p. 96).

[226] J. P. McMullen and K. F. Jensen. "Rapid Determination of Reaction Kinetics with an Automated Microfluidic System". In: *Organic Process Research & Development* 15.2 (2011), pp. 398–407. DOI: 10.1021/op100300p (cit. on p. 96).

[227] S. Marre and K. F. Jensen. "Synthesis of Micro and Nanostructures in Microfluidic Systems". In: *Chemical Society Reviews* 39.3 (2010), pp. 1183–1202. DOI: 10.1039/b821324k (cit. on p. 96).

[228] A. Abou-Hassan, O. Sandre, and V. Cabuil. "Microfluidics in Inorganic Chemistry". In: *Angew Chem Int Ed Engl* 49.36 (2010), pp. 6268–6286. DOI: 10.1002/anie.200904285 (cit. on p. 96).

[229] J. Yue, J. C. Schouten, and T. A. Nijhuis. "Integration of Microreactors with Spectroscopic Detection for Online Reaction Monitoring and Catalyst Characterization". In: *Industrial & Engineering Chemistry Research* 51.45 (2012), pp. 14583–14609. DOI: 10.1021/ie301258j (cit. on pp. 96, 133).

[230] A. J. DeMello. "Control and Detection of Chemical Reactions in Microfluidic Systems". In: *Nature* 442.7101 (2006), pp. 394–402. DOI: 10.1038/nature05062 (cit. on p. 96).

[231] C.-X. Zhao, L. He, S. Z. Qiao, and A. P. J. Middelberg. "Nanoparticle Synthesis in Microreactors". In: *Chemical Engineering Science* 66.7 (2011), pp. 1463–1479. DOI: 10.1016/j.ces.2010.08.039 (cit. on p. 96).

[232] P. Watts and C. Wiles. "Micro Reactors: A New Tool for the Synthetic Chemist". In: *Organic & biomolecular chemistry* 5.5 (2007), pp. 727–732. DOI: 10.1039/b617327f (cit. on p. 96).

[233] P. R. Makgwane and S. S. Ray. "Synthesis of Nanomaterials by Continuous-Flow Microfluidics: A Review". In: *Journal of Nanoscience and Nanotechnology* 14.2 (2014), pp. 1338–1363. DOI: 10.1166/jnn.2014.9129 (cit. on p. 96).

[234] C.-H. Weng, C.-C. Huang, C.-S. Yeh, H.-Y. Lei, and G.-B. Lee. "Synthesis of Hexagonal Gold Nanoparticles Using a Microfluidic Reaction System". In: *Journal of Micromechanics and Microengineering* 18.3 (2008), p. 35019. DOI: 10.1088/0960-1317/18/3/035019 (cit. on p. 96).

[235] H. Tsunoyama, N. Ichikuni, and T. Tsukuda. "Microfluidic Synthesis and Catalytic Application of PVP-Stabilized, 1 nm Gold Clusters". In: *Langmuir* 24.20 (2008), pp. 11327–11330. DOI: 10.1021/la801372j (cit. on p. 96).

[236] J. Puigmartí-Luis. "Microfluidic Platforms: A Mainstream Technology for the Preparation of Crystals". In: *Chemical Society Reviews* 43.7 (2014), pp. 2253–2271. DOI: 10.1039/c3cs60372e (cit. on p. 96).

[237] J. Wagner, T. Kirner, G. Mayer, J. Albert, and J. M. Köhler. "Generation of Metal Nanoparticles in a Microchannel Reactor". In: *Chemical Engineering Journal* 101.1–3 (2004), pp. 251–260. DOI: 10.1016/j.cej.2003.11.021 (cit. on pp. 96, 119).

[238] J. Wagner and J. M. Köhler. "Continuous Synthesis of Gold Nanoparticles in a Microreactor". In: *Nano Letters* 5.4 (2005), pp. 685–691. DOI: 10.1021/nl050097t (cit. on p. 96).

[239] J. Wagner, T. Tshikhudo, and J. Kohler. "Microfluidic Generation of Metal Nanoparticles by Borohydride Reduction". In: *Chemical Engineering Journal* 135 (2008), S104–S109. DOI: 10.1016/j.cej.2007.07.046 (cit. on pp. 96, 119).

[240] S. Duraiswamy and S. A. Khan. "Dual-Stage Continuous-Flow Seedless Microfluidic Synthesis of Anisotropic Gold Nanocrystals". In: *Particle & Particle Systems Characterization* 31.4 (2014), pp. 429–432. DOI: 10.1002/ppsc.201300266 (cit. on p. 96).

[241] D. V. R. Kumar, A. A. Kulkarni, and B. L. V. Prasad. "Microfluidic Platform for Continuous Flow Synthesis of Triangular Gold Nanoplates". In: *Colloids and Surfaces A: Physicochemical and Engineering Aspects* 443 (2014), pp. 149–155. DOI: 10.1016/j.colsurfa.2013.10.047 (cit. on p. 96).

[242] J. M. Köhler, M. Held, U. Hübner, and J. Wagner. "Formation of Au/Ag Nanoparticles in a Two Step Micro Flow-Through Process". In: *Chemical Engineering & Technology* 30.3 (2007), pp. 347–354. DOI: 10.1002/ceat.200600388 (cit. on p. 96).

[243] C. V. Navin, K. S. Krishna, C. S. Theegala, and C. S. S. R. Kumar. "Lab-on-a-Chip Devices for Gold Nanoparticle Synthesis and Their Role as a Catalyst Support for Continuous Flow Catalysis". In: *Nanotechnology Reviews* (2013), pp. 1–26. DOI: 10.1515/ntrev-2013-0028 (cit. on p. 96).

[244] J. Polte, T. T. Ahner, F. Delissen, S. Sokolov, F. Emmerling, A. F. Thünemann, and R. Kraehnert. "Mechanism of Gold Nanoparticle Formation in the Classical Citrate Synthesis Method Derived from Coupled in Situ XANES and SAXS Evaluation". In: *Journal of the American Chemical Society* 132.4 (2010), pp. 1296–1301. DOI: 10.1021/ja906506j (cit. on p. 97).

[245] J. Polte, R. Erler, A. F. Thunemann, S. Sokolov, T. T. Ahner, K. Rademann, F. Emmerling, and R. Kraehnert. "Nucleation and Growth of Gold Nanoparticles Studied Via in Situ Small Angle X-Ray Scattering at Millisecond Time Resolution". In: *ACS Nano* 4.2 (2010), pp. 1076–1082. DOI: 10.1021/nn901499c (cit. on pp. 97, 114).

[246] J. Polte, X. Tuaev, M. Wuithschick, A. Fischer, A. F. Thuenemann, K. Rademann, R. Kraehnert, and F. Emmerling. "Formation Mechanism of Colloidal Silver Nanoparticles: Analogies and Differences to the Growth of Gold Nanoparticles". In: *ACS Nano* 6.7 (2012), pp. 5791–5802. DOI: 10.1021/nn301724z (cit. on p. 97).

[247] B. Abecassis, F. Testard, Q. Y. Kong, B. Francois, and O. Spalla. "Influence of Monomer Feeding on a Fast Cold Nanoparticles Synthesis: Time-Resolved XANES and SAXS Experiments". In: *Langmuir* 26.17 (2010), pp. 13847–13854. DOI: 10.1021/la1020274 (cit. on pp. 97, 114).

[248] B. Abecassis, F. Testard, O. Spalla, and P. Barboux. "Probing in Situ the Nucleation and Growth of Gold Nanoparticles by Small-Angle X-Ray Scattering". In: *Nano Lett* 7.6 (2007), pp. 1723–1727. DOI: 10.1021/nl0707149 (cit. on p. 97).

[249] K. Biswas, N. Varghese, and C. N. R. Rao. "Growth Kinetics of Gold Nanocrystals: A Combined Small-Angle X-Ray Scattering and Calorimetric Study". In: *Small (Weinheim an der Bergstrasse, Germany)* 4.5 (2008), pp. 649–655. DOI: 10.1002/smll.200700937 (cit. on p. 97).

[250] A. Kölbl, M. Kraut, and A. Wenka. "Design Parameter Studies on Cyclone Type Mixers". In: *Chemical Engineering Journal* 167.2-3 (2011). Special Issue - IMRET 11: 11th International Conference on Microreaction Technology, pp. 444–454. DOI: 10.1016/j.cej.2010.08.092 (cit. on pp. 101, 104).

[251] J. E. Mark. *Polymer Data Handbook*. New York: Oxford University Press, 1999 (cit. on p. 101).

[252] ANSYS, Inc. *Ansys Fluent 14* (cit. on p. 104).

[253] Y. Ohkubo, T. Nakagawa, S. Seino, J. Kugai, T. A. Yamamoto, H. Nitani, and Y. Niwa. "X-Ray-Induced Reduction of Au Ions in an Aqueous Solution in the Presence of Support Materials and in Situ Time-Resolved XANES Measurements". In: *Journal of Synchrotron Radiation* 21 (2014), pp. 1148–1152. DOI: 10.1107/s1600577514012703 (cit. on p. 111).

[254] A. Plech, V. Kotaidis, A. Siems, and M. Sztucki. "Kinetics of the X-Ray Induced Gold Nanoparticle Synthesis". In: *Physical chemistry chemical physics : PCCP* 10.26 (2008), pp. 3888–3894. DOI: 10.1039/b716599d (cit. on p. 111).

[255] R. E. Benfield, D. Grandjean, M. Kröll, R. Pugin, T. Sawitowski, and G. Schmid. "Structure and Bonding of Gold Metal Clusters, Colloids, and Nanowires Studied by EXAFS, XANES, and WAXS". In: *The Journal of Physical Chemistry B* 105.10 (2001), pp. 1961–1970. DOI: 10.1021/jp0028812 (cit. on p. 121).

[256] T. M. Salama, T. Shido, R. Ohnishi, and M. Ichikawa. "EXAFS/XANES, XRD, and UV-VIS Characterization of Intrazeolitic Gold(i) Prepared by Monolayer Dispersion of $AuCl_3$ Inside Na-Y Zeolite". In: *The Journal of Physical Chemistry* 100.9 (1996), pp. 3688–3694. DOI: 10.1021/jp951996g (cit. on p. 121).

[257] D. Tibiletti, A. Amieiro-Fonseca, R. Burch, Y. Chen, J. M. Fisher, A. Goguet, C. Hardacre, P. Hu, and D. Thompsett. "DFT and in Situ EXAFS Investigation of Gold/Ceria-Zirconia Low-Temperature Water Gas Shift Catalysts: Identification of the Nature of the Active Form of Gold". In: *The Journal of Physical Chemistry B* 109.47 (2005), pp. 22553–22559. DOI: 10.1021/jp054576s (cit. on p. 121).

[258] F. Hubert, F. Testard, A. Thill, Q. Kong, O. Tache, and O. Spalla. "Growth and Overgrowth of Concentrated Gold Nanorods: Time Resolved SAXS and XANES". In: *Crystal Growth & Design* 12.3 (2012), pp. 1548–1555. DOI: 10.1021/cg2016116 (cit. on p. 121).

[259] G. Wedler. *Lehrbuch der Physikalischen Chemie*. 5., vollst. überarb. und aktualisierte Aufl. Weinheim: Wiley-VCH, 2004 (cit. on p. 123).

[260] P. V. Danckwerts. "Continuous Flow Systems: Distribution of Residence Times". In: *Chemical Engineering Science* 2.1 (1953), pp. 1–13. DOI: 10.1016/0009-2509(53)80001-1 (cit. on p. 124).

[261] F. Trachsel, A. Günther, S. Khan, and K. F. Jensen. "Measurement of Residence Time Distribution in Microfluidic Systems". In: *Chemical Engineering Science* 60.21 (2005), pp. 5729–5737. DOI: 10.1016/j.ces.2005.04.039 (cit. on p. 124).

[262] S. Vukojević, O. Trapp, J.-D. Grunwaldt, C. Kiener, and F. Schüth. "Quasi-Homogeneous Methanol Synthesis Over Highly Active Copper Nanoparticles". In: *Angewandte Chemie* 117.48 (2005), pp. 8192–8195. DOI: 10.1002/ange.200503169 (cit. on p. 132).

[263] M. Behrens et al. "The Active Site of Methanol Synthesis Over $Cu/ZnO/Al_2O_3$ Industrial Catalysts". In: *Science* 336.6083 (2012), pp. 893–897. DOI: 10.1126/science.1219831 (cit. on p. 132).

[264] M. Trépanier, A. K. Dalai, and N. Abatzoglou. "Synthesis of CNT-Supported Cobalt Nanoparticle Catalysts Using a Microemulsion Technique: Role of Nanoparticle Size on Reducibility, Activity and Selectivity in Fischer-Tropsch Reactions". In: *Applied Catalysis A: General* 374.1-2 (2010), pp. 79–86. DOI: 10.1016/j.apcata.2009.11.029 (cit. on p. 132).

[265] H. Wang and Y. Kou. "Aqueous-Phase Fischer-Tropsch Synthesis Catalyzed by Cobalt Nanoparticles". In: *Chinese Journal of Catalysis* 34.10 (2013), pp. 1914–1925. DOI: 10.1016/S1872-2067(12)60674-3 (cit. on p. 132).

[266] T. M. D. Dang, T. T. T. Le, E. Fribourg-Blanc, and M. C. Dang. "Synthesis and Optical Properties of Copper Nanoparticles Prepared by a Chemical Reduction Method". In: *Advances in Natural Sciences: Nanoscience and Nanotechnology* 2.1 (2011), p. 15009. DOI: 10.1088/2043-6262/2/1/015009 (cit. on p. 132).

[267] Y. Lee, J.-R. Choi, K. J. Lee, N. E. Stott, and D. Kim. "Large-Scale Synthesis of Copper Nanoparticles by Chemically Controlled Reduction for Applications of Inkjet-Printed Electronics". In: *Nanotechnology* 19.41 (2008), p. 415604. DOI: 10.1088/0957-4484/19/41/415604 (cit. on p. 132).

[268] H.-t. Zhu, C.-y. Zhang, and Y.-s. Yin. "Rapid Synthesis of Copper Nanoparticles by Sodium Hypophosphite Reduction in Ethylene Glycol Under Microwave Irradiation". In: *Journal of Crystal Growth* 270.3-4 (2004), pp. 722–728. DOI: 10.1016/j.jcrysgro.2004.07.008 (cit. on p. 132).

[269] Y. Song, H. Modrow, L. L. Henry, C. K. Saw, E. E. Doomes, V. Palshin, J. Hormes, and C. S. S. R. Kumar. "Microfluidic Synthesis of Cobalt Nanoparticles". In: *Chemistry of Materials* 18.12 (2006), pp. 2817–2827. DOI: 10.1021/cm052811d (cit. on p. 132).

[270] A.-H. Lu, E. L. Salabas, and F. Schüth. "Magnetic Nanoparticles: Synthesis, Protection, Functionalization, and Application". In: *Angewandte Chemie (International ed. in English)* 46.8 (2007), pp. 1222–1244. DOI: 10.1002/anie.200602866 (cit. on p. 132).

[271] S. Zhang, L. Nguyen, Y. Zhu, S. Zhan, C.-K. Tsung, and F. Tao. "In-Situ Studies of Nanocatalysis". In: *Accounts of Chemical Research* 46.8 (2013), pp. 1731–1739. DOI: 10.1021/ar300245g (cit. on p. 133).

[272] A. Bansode, G. Guilera, V. Cuartero, L. Simonelli, M. Avila, and A. Urakawa. "Performance and Characteristics of a High Pressure, High Temperature Capillary Cell with Facile Construction for Operando X-Ray Absorption Spectroscopy". In: *Review of Scientific Instruments* 85.8 (2014), p. 8. DOI: 10.1063/1.4893351 (cit. on p. 133).

[273] B. S. Clausen, L. Grabæk, G. Steffensen, P. Hansen, and H. Topsøe. "A Combined QEXAFS/XRD Method for on-Line, in Situ Studies of Catalysts: Examples of Dynamic Measurements of Cu-Based Methanol Catalysts". In: *Catalysis Letters* 20.1-2 (1993), pp. 23–36. DOI: 10.1007/BF00772594 (cit. on p. 133).

[274] F. C. Meunier. "The Design and Testing of Kinetically-Appropriate Operando Spectroscopic Cells for Investigating Heterogeneous Catalytic Reactions". In: *Chemical Society Reviews* 39.12 (2010), pp. 4602–4614. DOI: 10.1039/b919705m (cit. on p. 133).

[275] G. Sankar, P. A. Wright, S. Natarajan, J. M. Thomas, G. N. Greaves, A. J. Dent, B. R. Dobson, C. A. Ramsdale, and R. H. Jones. "Combined QUEXAFS-XRD - a New Technique in High-Temperature Materials Chemistry - an Illustrative in-Situ Study of the Zinc Oxide-Enhanced Solid-State Production of Cordierite from a Precursor Zeolite". In: *Journal of Physical Chemistry* 97.38 (1993), pp. 9550–9554. DOI: 10.1021/j100140a002 (cit. on p. 133).

[276] B. Kimmerle, J.-D. Grunwaldt, A. Baiker, P. Glatzel, P. Boye, S. Stephan, and C. G. Schroer. "Visualizing a Catalyst at Work During the Ignition of the Catalytic Partial Oxidation of Methane". In: *The Journal of Physical Chemistry C* 113.8 (2009), pp. 3037–3040. DOI: 10.1021/jp810319v (cit. on p. 133).

[277] K. F. Jensen. "Microreaction Engineering – is Small Better?" In: *Chemical Engineering Science* 56.2 (2001), pp. 293–303. DOI: 10.1016/S0009-2509(00)00230-X (cit. on pp. 133, 134).

[278] K. Jähnisch, V. Hessel, H. Lowe, and M. Baerns. "Chemistry in Microstructured Reactors". In: *Angewandte Chemie-International Edition* 43.4 (2004), pp. 406–446. DOI: 10.1002/anie.200300577 (cit. on pp. 133, 134).

[279] L. Kiwi-Minsker and A. Renken. "Microstructured Reactors for Catalytic Reactions". In: *Catalysis Today* 110.1-2 (2005), pp. 2–14. DOI: 10.1016/j.cattod.2005.09.011 (cit. on p. 133).

[280] E. Klemm, H. Döring, A. Geisselmann, and S. Schirrmeister. "Microstructured Reactors in Heterogenous Catalysis". In: *Chemical Engineering & Technology* 30.12 (2007), pp. 1615–1621. DOI: 10.1002/ceat.200700311 (cit. on p. 133).

[281] W. Wibel, A. Wenka, J. J. Brandner, and R. Dittmeyer. "Measuring and Modeling the Residence Time Distribution of Gas Flows in Multichannel Microreactors". In: *Chemical Engineering Journal* 215-216 (2013), pp. 449–460. DOI: 10.1016/j.cej.2012.10.011 (cit. on p. 133).

[282] X. Liu, B. Unal, and K. F. Jensen. "Heterogeneous Catalysis with Continuous Flow Microreactors". In: *Catalysis Science & Technology* 2.10 (2012), pp. 2134–2138. DOI: 10.1039/C2CY20260C (cit. on p. 133).

[283] J. Vandenbergh, T. Tura, E. Baeten, and T. Junkers. "Polymer End Group Modifications and Polymer Conjugations Via "Click" Chemistry Employing Microreactor Technology". In: *Journal of Polymer Science Part a-Polymer Chemistry* 52.9 (2014), pp. 1263–1274. DOI: 10.1002/pola.27112 (cit. on p. 133).

[284] G. G. Mironov, A. D. St-Jacques, A. Mungham, M. G. Eason, R. A. Chica, and M. V. Berezovski. "Bioanalysis for Biocatalysis: Multiplexed Capillary Electrophoresis-Mass Spectrometry Assay for Aminotransferase Substrate Discovery and Specificity Profiling". In: *Journal of the American Chemical Society* 135.37 (2013), pp. 13728–13736. DOI: 10.1021/ja407486z (cit. on p. 133).

[285] E. Gross, X.-Z. Shu, S. Alayoglu, H. A. Bechtel, M. C. Martin, F. D. Toste, and G. A. Somorjai. "In Situ IR and X-Ray High Spatial-Resolution Microspectroscopy Measurements of Multistep Organic Transformation in Flow Microreactor Catalyzed by Au Nanoclusters". In: *Journal of the American Chemical Society* 136.9 (2014), pp. 3624–3629. DOI: 10.1021/ja412740p (cit. on p. 133).

[286] R. M. Tiggelaar, J. W. Berenschot, J. H. de Boer, R. G. P. Sanders, J. G. E. Gardeniers, R. E. Oosterbroek, A. van den Berg, and M. C. Elwenspoek. "Fabrication and Characterization of High-Temperature Microreactors with Thin Film Heater and Sensor Patterns in Silicon Nitride Tubes". In: *Lab on a Chip* 5.3 (2005), pp. 326–336. DOI: 10.1039/b414857f (cit. on p. 133).

[287] A. Urakawa, F. Trachsel, P. R. von Rohr, and A. Baiker. "On-Chip Raman Analysis of Heterogeneous Catalytic Reaction in Supercritical CO_2: Phase Behaviour Monitoring and Activity Profiling". In: *Analyst* 133.10 (2008), pp. 1352–1354. DOI: 10.1039/B808984C (cit. on p. 133).

[288] E. Cao, M. Sankar, S. Firth, K. F. Lam, D. Bethell, D. K. Knight, G. J. Hutchings, P. F. McMillan, and A. Gavriilidis. "Reaction and Raman Spectroscopic Studies of Alcohol Oxidation on Gold-Palladium Catalysts in Microstructured Reactors". In: *Chemical Engineering Journal* 167.2-3 (2011), pp. 734–743. DOI: 10.1016/j.cej.2010.08.082 (cit. on p. 133).

[289] F. Dionigi, M. G. Nielsen, T. Pedersen, O. Hansen, I. Chorkendorff, and P. C. K. Vesborg. "A Transparent Pyrex μ-Reactors-Reactor for Combined in Situ Optical Characterization and Photocatalytic Reactivity Measurements". In: *Review of Scientific Instruments* 84.10 (2013). DOI: 10.1063/1.4826495 (cit. on p. 133).

[290] K. Otto, W. H. Weber, G. W. Graham, and J. Z. Shyu. "Identification of Dispersed Platinum on Gamma-Alumina by Laser-Raman Spectroscopy". In: *Applied Surface Science* 37.2 (1989), pp. 250–257. DOI: 10.1016/0169-4332(89)90487-X (cit. on p. 133).

[291] G. Sankar, E. Cao, and A. Gavriilidis. "A Microstructured Reactor Based in Situ Cell for the Study of Catalysts by X-Ray Absorption Spectroscopy Under Operating Conditions". In: *Catalysis Today* 125.1-2 (2007), pp. 24–28. DOI: 10.1016/j.cattod.2007.01.068 (cit. on p. 133).

[292] B. Shelimov, J. F. Lambert, M. Che, and B. Didillon. "Initial Steps of the Alumina-Supported Platinum Catalyst Preparation: A Molecular Study by Pt-195 NMR, Uv-Visible, EXAFS, and Raman Spectroscopy". In: *Journal of Catalysis* 185.2 (1999), pp. 462–478. DOI: 10.1006/jcat.1999.2527 (cit. on p. 133).

[293] C. K. C. Tan, W. N. Delgass, and C. D. Baertsch. "Spatially Resolved in Situ FTIR Analysis of CO Adsorption and Reaction on Pt/SiO_2 in a Silicon Microreactor". In: *Applied Catalysis B: Environmental* 93.1-2 (2009), pp. 66–74. DOI: 10.1016/j.apcatb.2009.09.013 (cit. on p. 133).

[294] A. Urakawa, W. Van Beek, M. Monrabal-Capilla, J. R. Galán-Mascarós, L. Palin, and M. Milanesio. "Combined, Modulation Enhanced X-Ray Powder Diffraction and Raman Spectroscopic Study of Structural Transitions in the Spin Crossover Material [Fe(Htrz)2(trz)](BF4)+". In: *The Journal of Physical Chemistry C* 115.4 (2010), pp. 1323–1329. DOI: 10.1021/jp107206n (cit. on p. 133).

[295] S. Hannemann, J.-D. Grunwaldt, N. van Vegten, A. Baiker, P. Boye, and C. G. Schroer. "Distinct Spatial Changes of the Catalyst Structure Inside a Fixed-Bed Microreactor During the Partial Oxidation of Methane Over Rh/Al_2O_3". In: *Catalysis Today* 126.1-2 (2007), pp. 54–63. DOI: 10.1016/j.cattod.2006.08.065 (cit. on p. 133).

[296] D. Ferri, M. A. Newton, M. Di Michiel, G. L. Chiarello, S. Yoon, Y. Lu, and J. Andrieux. "Revealing the Dynamic Structure of Complex Solid Catalysts Using Modulated Excitation X-Ray Diffraction". In: *Angewandte Chemie International Edition* 53.34 (2014), pp. 8890–8894. DOI: 10.1002/anie.201403094 (cit. on p. 133).

[297] T. R. Henriksen, J. L. Olsen, P. Vesborg, I. Chorkendorff, and O. Hansen. "Highly Sensitive Silicon Microreactor for Catalyst Testing". In: *Review of Scientific Instruments* 80.12 (2009). DOI: 10.1063/1.3270191 (cit. on p. 133).

[298] R. M. Tiggelaar, P. v. Male, J. W. Berenschot, J. G. E. Gardeniers, R. E. Oosterbroek, M. H. J. M. d. Croon, J. C. Schouten, A. v. d. Berg, and M. C. Elwenspoek. "Fabrication of a High-Temperature Microreactor with Integrated Heater and Sensor Patterns on an Ultrathin Silicon Membrane". In: *Sensors and Actuators A: Physical* 119.1 (2005), pp. 196–205. DOI: 10.1016/j.sna.2004.09.004 (cit. on p. 133).

[299] S. Baier, A. Rochet, G. Hofmann, M. Kraut, and J.-D. Grunwaldt. "Lithographically Fabricated Silicon Microreactor for in Situ Characterization of Heterogeneous Catalysts – Enabling Correlative Characterization Techniques". In: *Review of Scientific Instruments* 86.6 (2015), p. 65101. DOI: 10.1063/1.4921775 (cit. on pp. 140, 142, 184).

[300] S. Mangold, R. Steininger, and T. Spangenberg. "High Throughput Data Acquisition at the XAS and SUL-X Beamline at ANKA". In: *Journal of Physics: Conference Series* 430 (2013), p. 12022. DOI: 10.1088/1742-6596/430/1/012022 (cit. on p. 140).

[301] S. Mangold, R. Steininger, T. d. S. Rolo, and J. Göttlicher. "Full Field Spectroscopic Imaging at the ANKA-XAS and SUL-X Beamlines". In: *Journal of Physics: Conference Series* 430 (2013), p. 12130. DOI: 10.1088/1742-6596/430/1/012130 (cit. on p. 140).

Acknowledgements

This work would not have been possible without the direct or indirect help of several people, whom I am going to thank in the following. Although prepared with greatest care, I probably forgot someone and want to say "thank you" nevertheless.

I wish to cordially thank, first and foremost, my supervisor Prof. Dr. Jan-Dierk Grunwaldt for offering this interesting and multifaceted Ph.D. thesis in the field of catalysis research in combination with synchrotron radiation experiments. His enduring support as well as the granted freedom and trust allowed and encouraged me to successfully conduct my research as well as to fulfill family obligations and finish writing this thesis.

In the "AK Grunwaldt" group, I express my gratitude to Dr. Maria Casapu and Elen Ogel for preparation and testing of the honeycomb catalysts as well as Jan Pesek for keeping care of the corresponding setups. I thank Dr. Amélie Rochet and Sina Baier for discussions, joining beamtimes, and for continuing the development of the second version of the gas phase microreactor. I thank Jörg Finsterle for construction of the gas phase chip heater and control software.

Thanks to Angela Beilmann for conducting BET measurements and Dr. Marina Tepluchin for help in setting up XRD measurements. I am grateful to Ghazal Tofighi for her interest and continuation of the liquid phase experiments as well as proof reading corresponding parts of the thesis. My former office colleague Dr. Gian Luca Chiarello I would like to thank for interesting discussions and the relaxed working atmosphere. Finally, I like to thank Fabian Hundemer for the dedicated investigation of THPC aging and AuNP characterization using UV-vis during his HiWi job and Martin Reichardt for the good collaboration and fruitful discussions during his Diploma work on AuNPs.

My deepest gratitude is expressed to Prof. Dr. Christian G. Schroer for being the co-referent of this thesis and for guiding my first steps in conducting tomography experiments and their reconstruction. I always appreciated his open minded, optimistic, and friendly attitude, that was especially valuable in preparing and conducting ptychography beamtimes.

I also like to stress the valuable support of his group in this respect. Dirk Samberg helped with construction ideas and accompanied the building of the liquid phase support constructions. Frank Seiboth, Dr. Jens Patommel, Stephan Ritter, Robert Hoppe, and Juliane Reinhardt are acknowledged for their constructive collaboration and tireless help during beamtimes. I very much appreciated the relaxed but professional working atmosphere as well as being part of running the beamline as a *power user*, which gave great insight to technical details, fun, and finally allowed us to conduct the envisioned experiments.

Special thanks are dedicated to Juliane Reinhardt. First for her friendship in general and moreover for a very frank and close collaboration. I appreciated her commitment and readiness to plan the experiments in detail, prepare samples in Denmark, and finally analyze the ptychographic data sets. Additionally, one must not to forget the proofreading of the entire thesis.

At the IMVT KIT, I like to thank Prof. Dr.-Ing. Roland Dittmeyer for support and advice in the liquid phase chip project, especially for increasing priorities in the IMVT workshop. Furthermore, Dr. Günter Rinke, Dr. Angela Ewinger, Anke Urban, Achim Wenka, and Sabine Heideker are thanked for design input on the mixer and chip layout as well as design and construction of the fluidic rack and of course for participation in the beamtime. I thank Dr. Andreas Kölbl for providing first PEEK mixers and Dr. Christin Hecht for help in finding suitable HPLC components in the vast assortment of the respective catalogs. Furthermore, for the preparation and measurement of EPMA on a honeycomb sample I like to thank Uta Gerhards.

Within the gas and liquid phase microreactor projects further thanks go to Dr. Andreas Jahn (IHM TUD) and Dr. Steffen Howitz (GeSiM) for constructive discussions and creative ideas in implementing our needs.

For discussions on ptychography cells and TEM measurements I acknowledge Dr. Christian Kübel and Dr. Di Wang respectively.

I am very grateful to Associate Prof. Dr. Christian D. Damsgaard (CEN DTU) for his open, constructive and motivating attitude as well as help, training, and support for conducting sample preparation and electron microscopy, using SEM and TEM, for ptychography samples.

Since much of my work is utilizing synchrotron light sources, I feel obliged to acknowledge the hard work of the staff working at these facilities, which allowed me to carry out my research.

At beamline P05 (Petra III, DESY), I like to thank Dr. Felix Beckmann, Dr. Fabian Wilde, Dr. Malte Ogurreck, Dr. Imke Greving, Dr. Julia Herzen, and Thomas Dose for support not only during the friendly user beamtime, which let me learn a lot about the beamline and tomography but also fruitful discussions and experimental support with tailored sample holders, allocation of an *ex situ* oven and help in customized reconstruction of tomographic data.

At beamline P06, I am grateful to Dr. Gerald Falkenberg, Dr. Gerd Wellenreuther, and Dr. Ulrike Bösenberg for fruitful discussions before and during the beamtimes with advice and for help in conducting the experiments in general. For the nanoprobe endstation, the group of Prof. Dr. Schroer is acknowledged once again.

Further support during various synchrotron beamtimes was provided by Dr. Camelia Borca (MicroXAS, SLS) and Dr. Stefan Mangold (XAS, ANKA), thank you.

I like to thank the Helmholtz Research School "Energy Related Catalysis" for granting a scholar ship and for providing interesting scientific exchange as well as interesting

soft skill courses. Further financial support for the projects was provided by the virtual institute VI-403 “In situ Nano-Imaging of Biological and Chemical Processes” and the BMBF-projects “X-ray microscopy” (05K10VK1) and “Nanoscopy” (05K13VK2). This allowed construction of the presented devices and acquisition of a tomography workstation as well as corresponding analysis software.

Last but not least I like to cardinally thank my parents for their trust and support, which allowed me to follow and realize my aims so far. Especially, I owe thanks to my two sons Cedric and Erik for providing a new perspective and joint rediscovery of the surrounding world as well as Sabine for her patience, encouragement, proofreading, critical discussion, and support during preparation of this work and in everyday life.

Scientific Contributions

Talks

2011/04 G. Hofmann and J.-D. Grunwaldt.
Opportunities of in situ Imaging of Chemical and Catalytic Processes.
Kick-off Meeting Virtuelles Institut VI-403 "In-situ Nano Imaging of Biological and Chemical Processes"
Göttingen, Germany

2011/11 G. Hofmann and J.-D. Grunwaldt. (invited)
Imaging in Catalysis Research: Towards Tomographic and Dynamic Studies using Synchrotron Radiation.
24th MAX-lab Usersmeeting
Lund, Schweden

2012/01 G. Hofmann and J.-D. Grunwaldt.
Imaging in Catalysis Research: Example Applications at P06.
HASYLAB Usersmeeting - Workshop on Nano Imaging
Hamburg, Germany

2012/07 G. Hofmann and J.-D. Grunwaldt.
X-Ray Computerized Tomography: A brief Introduction.
Helmholtz Research School for Energy-Related Catalysis, Summer School
Schwetzingen, Germany

2013/09 G. Hofmann and J.-D. Grunwaldt. (invited)
Ageing Effects on Exhaust Gas Catalyst: Microscopic Changes Captured by X-Ray Tomography.
22nd International Congress on X-Ray Optics and Microanalysis (ICXOM22)
Hamburg, Germany

2014/01 G. Hofmann and J.-D. Grunwaldt. (invited)
Quasi in situ X-Ray Tomography on Exhaust Gas Catalysts: Quantification of Ageing Effects.
DESY Photon Science Usersmeeting, Satellite Workshop – German Engineering Materials Science Centre (GEMS)
Hamburg, Germany

Publications

2013 R. Hoppe, J. Reinhardt, G. Hofmann, J. Patommel, J.-D. Grunwaldt, C. D. Damsgaard, G. Wellenreuther, G. Falkenberg, and C. G. Schroer.
High-Resolution Chemical Imaging of Gold Nanoparticles Using Hard X-Ray Ptychography.
Applied Physics Letters 102 203104 (2013), DOI: 10.1063/1.4807020.
[166], used in section 4.4 on page 87.

2014 G. Hofmann, A. Rochet, S. Baier, M. Casapu, S. Ritter, F. Wilde, M. Ogurreck, F. Beckmann, and J.-D. Grunwaldt.
Ageing Effects on Exhaust Gas Catalysts: Microscopic Changes Captured by X-Ray Tomography.
Journal of Physics: Conference Series 499 012017 (2014), DOI: 10.1088/1742-6596/499/1/012017.
[100], part of sections 3.6 and 3.8 on page 42 and on page 47.

2015 G. Hofmann, A. Rochet, E. Ogel, M. Casapu, S. Ritter, M. Ogurreck, and J.-D. Grunwaldt.
Aging of a Pt/Al_2O_3 Exhaust Gas Catalyst Monitored by Quasi in situ X-Ray Micro Computed Tomography.
RSC Advances 5 6893–6905 (2015), DOI: 10.1039/C4RA14007A.
[101], part of section 3.9 on page 54.

2015 S. Baier, A. Rochet, G. Hofmann, M. Kraut, and J.-D. Grunwaldt.
Lithographically Fabricated Silicon Microreactor for in situ Characterization of Heterogeneous Catalysts – Enabling Correlative Characterization Techniques.
Review of Scientific Instruments 86 065101 (2015), DOI: 10.1063/1.4921775.
[299], used in section 6.4 on page 140.

2015 J. Reinhardt, R. Hoppe, G. Hofmann, C. Baumbach, J. Patommel, S. Baier, A. Rochet, J.-D. Grunwaldt, C. D. Damsgaard, G. Falkenberg, and C. G. Schroer.
Imaging Catalysts by High-Resolution Hard X-Ray Ptychography Using an Opaque Beamstop.
Nano Letters, submitted.
Used in section 4.4 on page 87.

2015 G. Hofmann, G. Tofighi, G. Rinke, S. Baier, A. Ewinger, A. Urban, A. Wenka, S. Heideker, A. Jahn, R. Dittmeyer, and J.-D. Grunwaldt.
A Microfluidic Device for the Investigation of Rapid Gold Nanoparticle Formation in Continuous Turbulent Flow.
Journal of Physics: Conference Series, XAFS16, submitted.
based upon section 5.7 on page 113.

Posters

2012/09 G. Hofmann, J. Reinhardt, C. G. Schroer, and J.-D. Grunwaldt.
X-Ray Imaging in Catalysis with Chemical Contrast: Microscopic 3D Information on Structure, Morphology and Composition in Non-Destructive Manner.
HSC14 - HERCULES Specialized Courses: Neutrons and Synchrotron Radiation in Materials for Energy 2012
Grenoble, France

2013/01 G. Hofmann, J. Reinhardt, A. Rochet, C. G. Schroer, and J.-D. Grunwaldt.
X-Ray Microscopy and Imaging of Exhaust Gas Catalysts.
Hasylab, Usersmeeting 2013
Hamburg, Germany

2013/05 G. Hofmann, R. Hoppe, J. Reinhardt, C. G. Schroer, and J.-D. Grunwaldt.
Imaging Catalysts by Hard X-Rays: New Opportunities of X-Ray Tomography and Ptychography in the Nanoscale.
Bunsen Tagung 2013
Karlsruhe, Germany

2013/05 A. Rochet, G. Hofmann, S. Baier, and J.-D. Grunwaldt.
Importance of Spatial Resolution in Catalytic Reactors: Gradients in the Catalyst Structure during the Partial Oxidation of Methane.
Bunsen Tagung 2013
Karlsruhe, Germany

2013/10 A. Rochet, S Baier, G. Hofmann, and J.-D. Grunwaldt.
Gradients in the Catalyst Bed during the Partial Oxidation of Methane.
French GDR 2013
Lilli, France

2014/01 G. Hofmann, S. Baier, A. Rochet, E. Ogel, M. Casapu, and J.-D. Grunwaldt.
X-Ray Tomography as an Excellent Tool for Product Design of Catalysts and Capturing Aging Effects.
Hasylab, Usersmeeting 2014
Hamburg, Germany

2015/08 G. Hofmann, G. Tofighi, G. Rinke, S. Baier, A. Ewinger, A. Urban, A. Wenka, S. Heideker, A. Jahn, R. Dittmeyer, and J.-D. Grunwaldt.
Investigation of Rapid Gold Nanoparticle Formation in Continuous Flow by XAS.
XAFS16 2015
Karlsruhe, Germany

Curriculum Vitae

1995/09 – 2002/06	Abitur – Dr. Albert-Schweitzer-Gymnasium Vetschau/Spreewald, Deutschland
2002/06 – 2003/03	Wehrdienst Nienburg (Weser) und Hagenow, Deutschland
2003/10 – 2006/09	B.Sc. Physik mit Informatik – Universität Osnabrück *Untersuchung von Polyoxometallaten mit Hilfe der Röntgenphotoelektronenspektroskopie* Osnabrück, Deutschland
2006/09 – 2006/11	DESY Summer Student Hamburg, Deutschland
2007/10 – 2009/09	M.Sc. Physik – Goethe-Universität Frankfurt *Bau eines Mikrokalorimeters und Messung des Magnetokalorischen Effekts in* Cs_2CuCl_4 Frankfurt am Main, Deutschland
2009/10 – 2010/12	Wissenschaftlicher Mitarbeiter – Goethe-Universität Frankfurt Frankfurt am Main, Deutschland
2011/01 – 2015/07	Promotion – Karlsruher Institut für Technologie (KIT) *Development of Methods and Devices for Spatially and Temporally Resolved X-Ray Microscopy for Characterization in Heterogeneous Catalysis* Karlsruhe, Deutschland

Erklärung

Hiermit versichere ich, dass ich diese Arbeit selbständig verfasst und keine anderen als die angegebenen Quellen und Hilfsmittel verwendet habe sowie die wörtlich oder inhaltlich übernommenen Stellen als solche kenntlich gemacht, und die Satzung der Universität Karlsruhe (TH) zur Sicherung guter wissenschaftlicher Praxis beachtet habe.

Karlsruhe, den 2. Juni 2015